UNIVERSITY OF SOUTHAMPTON

FACULTY OF ENGINEERING AND PHYSICAL SCIENCES

SCHOOL OF CHEMISTRY

Computational Studies of Metallic Nanoparticles Applicable to Heterogeneous Catalysis

Author:
Lucas Garcia Verga

Supervisor:
Prof. Chris-Kriton Skylaris
Advisor:
Prof. Andrea E. Russell

A thesis submitted in fulfilment of the requirements
for the degree of Doctor of Philosophy in Chemistry

June 2019

UNIVERSITY OF SOUTHAMPTON

ABSTRACT

FACULTY OF ENGINEERING AND PHYSICAL SCIENCES

SCHOOL OF CHEMISTRY

Doctor of Philosophy

Computational Studies of Metallic Nanoparticles Applicable to Heterogeneous Catalysis

by Lucas Garcia Verga

Understanding the factors controlling a catalyst activity, selectivity, and stability is a complicated task with potential applications for a large number of technologies with high impact for our society. For example, optimised catalysts can have a central role to improve the durability, efficiency and decrease the cost of technologies such as fuel cells, which are devices able to convert the chemical energy from molecules into electricity by performing chemical reactions that are specific to the used fuel and the type of fuel cell. Fuel cell catalysts are commonly made from metallic nanoparticles on different types of supports, meaning that characteristics such as the nanoparticle composition, size, shape, composition of the support, electrolyte and many others can be simultaneously controlled to tune the catalyst towards a specific goal. The complexity involved in the catalyst optimisation makes the problem extremely exciting and challenging, requiring significant effort from many different research areas ranging from synthetic chemistry and electrochemistry to computational chemistry.

This thesis describes computational studies on metallic nanoparticles, focusing on nanoparticle size effects and its interplay with other variables that are important in the context of fuel cell catalysts such as the presence of support and adsorbate coverage effects. We also present a framework in ONETEP's linear-scaling DFT formalism for the implementation of local and angular momentum projected density of states (l-p-DOS), which is an important tool to study metallic nanoparticles used as catalysts. The four different bases used to project the density of states are tested, and its results are compared against other DFT code, helping to validate our l-p-DOS implementation. The results obtained for metallic nanoparticles show similar trends with all the implemented options, demonstrating the reliability of the method for such studies.

The ONETEP code with the implemented l-p-DOS functionality is used to perform a set of large-scale DFT calculations to study Pt nanoparticles isolated and supported on pristine graphene. The results show a weak metal-support interaction, with the adhesion energy per Pt atom decreasing with the nanoparticle size and being dominated by dispersion interactions for

larger nanoparticles. The interaction with the support induces geometric and electronic changes in the nanoparticle, with the inter-atomic distances expanding (contracting) for Pt facets close (far) to the support and with charge redistribution happening at the interface between Pt clusters and graphene. The changes in the geometric and electronic properties induced by the interaction with the support are size dependent, correlate with the interaction strength between cluster and support, and generate shifts in the d-band centres of the Pt nanoparticles. The isolated and supported nanoparticles were used to study how the nanoparticle size and presence of support alters the interaction of the nanoparticles with atomic oxygen, carbon monoxide, and ethanol. We show that nanoparticle size decreases strengthen the adsorption energies of O and CO, which can hinder the activity of these nanoparticles towards important reactions in the context of fuel cells. The size effect is observed to control the adsorption energies for O and CO to a larger extent than for ethanol. We also note that the presence of graphene weakens the adsorption energies for all adsorbates, with this effect being more significant for smaller nanoparticles. Finally, we study how the adsorbate coverage changes the adsorption of atomic oxygen on Pt nanoparticles and how coverage effects vary with the nanoparticle size. We observe that the increase in O coverage weakens the adsorption energies per O atom, with this effect being more significant for the larger simulated nanoparticles. These studies can help to understand different influences that the nanoparticle size can have by simulating non-trivial combinations of size and support effects and size and coverage effects which could have implications to designing more efficient catalysts for fuel cells and other applications.

Contents

Abstract iii

Contents v

List of Figures viii

List of Tables xiv

Declaration of Authorship xv

Acknowledgements xvi

Abbreviations xviii

1 Introduction and Motivation 1
1.1 Thesis Outline . . . 3

2 Theoretical Methods 5
2.1 Density Functional Theory . . . 5
2.1.1 Computational Quantum Mechanics . . . 5
2.1.2 DFT Foundations . . . 6
2.1.3 Exchange-Correlation Functionals . . . 9
2.1.4 Basis Set . . . 12
2.1.5 Pseudopotentials and the Projector Augmented Wave Method . . . 14
2.1.6 The ONETEP Program . . . 15
2.2 Density Functional Theory for Metallic Systems . . . 16
2.2.1 Electronic Smearing Schemes . . . 18
2.2.2 Density Mixing . . . 20
2.2.3 Ensemble DFT . . . 20
2.2.4 EDFT in ONETEP . . . 22

3 Computational Studies on Heterogeneous Catalysis 24
3.1 Reaction Mechanisms and Rates . . . 24
3.2 Electronic and Geometric Descriptors . . . 30
3.3 Strategies for Catalysts Design . . . 35
3.3.1 Catalyst Composition . . . 35
3.3.2 Nanoparticle Size and Shape . . . 39

3.3.3 Support Effects . . . 47

4 Atom and Angular Momentum Projected Density of States in ONETEP 52
4.1 Projected Density of States . . . 53
4.2 Projected Density of States in ONETEP . . . 54
4.2.1 Choice of Angular Momentum Resolved Basis . . . 55
4.2.2 Resolution of Identity and Construction of the Projected DOS . . . 57
4.3 Calculation Details . . . 59
4.4 Demonstration of the Method . . . 60
4.5 Conclusions . . . 67

5 Effects of a Graphene Support on Platinum Nanoparticles 69
5.1 Background . . . 70
5.2 Computational Details . . . 72
5.3 Two and Three Dimensional Pt Clusters Supported on Graphene . . . 74
5.4 Geometrical and Electronic Effects of the Graphene Support on Platinum Clusters 78
5.5 Conclusions . . . 88

6 Adsorption Properties of Platinum Nanoparticles: Support and Size Effects 90
6.1 Background . . . 91
6.2 Computational Details . . . 93
6.3 Adsorption on Isolated Pt Nanoparticles. . . . 96
6.4 Structural and Electronic Analysis for Adsorbates Interacting with Isolated Pt Nanoparticles. . . . 100
6.5 O, CO, and Ethanol Interacting with Pt Nanoparticles Supported on Graphene . 110
6.6 Conclusions . . . 114

7 DFT Calculation of Oxygen Adsorption on Platinum Nanoparticles: Coverage and Size Effects 116
7.1 Background . . . 117
7.2 Computational Details . . . 120
7.3 Coverage Effect: Methodology Calibration . . . 121
7.4 Interplay Between Nanoparticle Size and O Coverage . . . 128
7.5 Conclusions . . . 134

8 Conclusions 137
8.1 Further Work . . . 143

A Adsorption of O, CO, and Ethanol on Support Nanoparticles: Additional Results 145
A.1 O, CO, and Ethanol interacting with the Pt (100) facet of supported Pt nanoparticles . . . 145
A.2 Binding the Pt (100) facet on graphene . . . 146

B Structures for Different Adsorbate Coverages and Nanoparticle Sizes 148

Bibliography 151

List of Figures

1.1 Simplified structure of a PEMFC (Proton exchange membrane fuel cell) fed with hydrogen. . . . 2

2.1 Representation of the the Jacob's ladder of exchange-correlation functionals [1], where each ascending rung illustrates a class of XC functional with higher complexity, computational cost, and usually accuracy. . . . 10

2.2 Computational time per iteration against the number of atoms of Au nanoparticles of increasing size. The calculations were performed with the ensemble DFT as implemented in ONETEP [2]. Hamiltonian DD (DI) are the density dependent (independent) terms of the Hamiltonian. . . . 23

3.1 Reaction coordinate diagram for four possible reaction mechanism for WGS on a Pt(111) surface. The red and blue reaction mechanism involve the formation of a COOH intermediate, and the energetically preferred mechanism is indicated in red. Figure reprinted with permission from 3. Copyright 2008, American Chemical Society. . . . 28

3.2 Volcano plot for the ORR activity versus the adsorption energies of atomic oxygen. Figure reprinted with permission from 4. Copyright 2001, American Chemical Society. . . . 31

3.3 Alloyed-core@shell nanoparticle a) illustration and b) catalytic activity for the CO oxidation reaction. Figure b) shows a contour plot of the activity as a function of CO and O adsorption energies for different metallic clusters compared with pure Pt slab. Black dots represent monometallic slabs, blue triangles represent core-shell nanoparticles, while green points show the activity of AuPd@Pt nanoparticles with different Au/Pd ratios. Figure reprinted with permission from 5. Copyright 2015, American Chemical Society. . . . 38

3.4 Atomic oxygen adsorption energies for relaxed (filled circles) and unrelaxed (hollow hexagons) Pt and Au nanoparticles and surface slabs (horizontal lines). Results for Figure a) and b) were calculated on FCC adsorption sites, while c) uses edge adsorption sites. Figure reprinted with permission from 6. Copyright 2015, American Chemical Society. . . . 44

3.5 Contour plot of the catalytic activity with two different temperatures as a function of the CO and O adsorption energies, where red (blue) colors represent higher (lower) activities. The results were obtained for (111) (black), (211) (red), (532) (green) surfaces and for M_{12} (blue) and M_{55} (magenta) clusters. Figure reprinted with permission from 7. Copyright 2009, American Chemical Society. . . . 45

3.6 Fraction of adsorption sites with oxygen binding strength with a maximum difference of 0.2 eV to the optimum ORR binding strength as a function of the nanoparticle size. The oxygen binding strengths were calculated by the linear correlation between O adsorption and $\overline{CN}$ for experimentally observed nanoparticles (blue), truncated octahedra (green), cube-octahedra (red), and quasi-spherical (yellow) idealised nanoparticle models. Figure reprinted with permission from 8. Copyright 2017, American Chemical Society. 47

4.1 Total and projected density of states for a) an O atom in a singlet state and b) a CO molecule. Blue and red plots represent s and p bands, while black curves are obtained with the total DOS. 60

4.2 Angular momentum projected densities of states obtained with CASTEP (red) and ONETEP (black) with PAOs as the projection basis set. a), b), c) and d) show the s channel for CO, SiH_4, C_2H_2, and C_2H_4 molecules, while e), f), g) and h) show the p projected DOS for the same molecules. 63

4.3 Projected density of states (p-DOS) for different schemes implemented in ONETEP. a), c) and e) show, respectively, s p-DOS for CO, C_2H_4, and C_2H_6. b), d) and f) show the p projection for the same molecules. For all plots, different colors are used to represent each bases, where black, yellow, blue and green represent PAOs, SWs, C-SWs and CF-SWs. For c, d, e, f the CF-SWs calculated with 5 NGWFs for each hydrogen atom are represented as red segmented lines. 64

4.4 Angular momentum projected densities of states obtained with CASTEP (red) and ONETEP (black) with PAOs as the projection basis set. a), b), c), and d) present the d bands projected onto Pd and Pt atoms on (111) facets of Pd_{13}, Pt_{13}, Pt_{55} and Pt_{147} nanoparticles. 66

4.5 Density of states projected onto the d channels of Pt atoms in a (111) facet of a Pt_{147} nanoparticle where a) spans through all calculated energy levels and b) focus in the states near the Fermi level. For all plots, different colors are used to represent each bases, where black, yellow, blue and green represent PAOs, SWs, C-SWs and CF-SWs. 66

4.6 Calculated d-band centres using different projection schemes. a) shows the results for (111) facets of Pt nanoparticles against the nanoparticles sizes and for a Pt(111) slab. b) compares the calculated d-band centres with spherical waves bases (SWs, C-SWs, CF-SWs) to the same quantities obtained using PAOs, showing the d-band centres for the whole (111) facet of Pt nanoparticles of increasing size, the exposed facet of the Pt (111) slab, and the (111) facet of Pd_{13} (square symbols). The d-band centres are calculated using the occupancy-weighted l-p-DOS and focusing on the states near the Fermi-level to exclude the variations for the low energy levels illustrated in figure 4.5. For all plots, different colors are used to represent each bases, where black, yellow, blue and green represent PAOs, SWs, C-SWs and CF-SWs. 67

5.1 Initial geometries used for a) Pt_4, b) Pt_{13}, and c) Pt_{55}, clusters constructed as monolayers; d) Tetrahedral Pt_4, e) Icosahedral (Ih) Pt_{13}, and f) Cuboctahedral (Oh) Pt_{55}. Cuboctahedral shapes were used on Pt_{13}, Pt_{55}, Pt_{147}, and Pt_{309} clusters. 73

5.2 Formation energy per Pt atom, E_{FOR}/n, for different Pt clusters interacting with the graphene support. Ih (Oh) refers to Icosahedral (Cuboctahedral) symmetries. The cuboctahedral facet in contact with the graphene is indicated between brackets. Simulations containing dispersion interactions are represented by dashed lines. Vertical dashed lines were plotted to delimit the number of Pt atoms in the systems. 75
5.3 Cohesive energies, E_{COH}/n for different Pt clusters. Ih (Oh) refers to Icosahedral (Cuboctahedral) symmetries. Simulations containing dispersion interactions are represented by dashed lines. Vertical dashed lines were plotted to delimit the number of Pt atoms in the systems. 76
5.4 Adhesion energy per Pt atom in contact with the graphene support. The systems were ordered according to the number of Pt atoms in contact with the graphene. Ih (Oh) refers to Icosahedral (Cuboctahedral) symmetries, the cuboctahedral facet in contact with the graphene is indicated between brackets. Simulations containing dispersion interactions are represented by dashed lines. 77
5.5 Optimised geometries for (a) Pt_{13} monolayer (b) Cuboctahedral Pt_{13} with the (100) facet and (c) the (111) facet interacting with graphene, and (d) Cuboctahedral Pt_{309} with the (111) facet in contact with the support. The numbers are the average Pt-Pt bond lengths for each Pt layer, while numbers between brackets represent the average bond lengths in the unsupported nanoparticles. Gray (green) spheres represent platinum (carbon) atoms. 79
5.6 Adhesion energy per Pt atom in contact with the graphene support versus the average percentage of Pt-Pt bond length expansion in the nanoparticle facet in contact with the graphene sheet, where the black line is only a guide to the eye. 81
5.7 Changes in the electronic densities of supported Pt_{55} nanoparticles, where a) and b) show electronic density difference plots (Isosurface at 0.01e/Å^3), where blue (red) represents accumulation (depletion) of electrons, and c) and d) presents the Mulliken charges for each atom plotted as a colour scale. Figures a) and c) represent a cuboctahedral Pt_{55} with the (100) facet in contact with the graphene, while b) and d) represent the same system with the (111) facet interacting with the support. Green (gray) spheres represent carbon (platinum) atoms. Figure reproduced from ref. 9. 82
5.8 Average percentage of Pt-Pt bond length expansion in the nanoparticle facet in contact with the graphene versus the charge difference per Pt atom in the same nanoparticle facet, where the black line is only a guide to the eye. 83
5.9 Atom and angular momentum projected density of states (l-p-DOS) plots for cuboctahedral nanoparticles interacting with the graphene support: (a), (b), (c), and (d) represents the p-bands of the graphene support interacting with Pt_{13}, Pt_{55}, Pt_{147}, and Pt_{309} cuboctahedral nanoparticles, while (e), (f), (g), and (h) represents the d-bands of different Pt facets for the same systems. Dashed lines indicate the d-band centre of each facet. For the plots of the p-band of graphene, black (red) lines indicate systems before (after) the interaction with the Pt cluster, with the inset showing in detail the occupied states with higher energy, i.e, close to the Fermi level. For the plots showing the d-band of platinum facets, black lines indicate the (111) facet in isolated Pt clusters, while red (blue) lines indicate the Pt (111) facets which are closest (farthest) from the support. Figure reproduced from ref 9. 84

5.10 d-band centre from the closest (C) and farthest (F) Pt facets from the graphene support, considering Pt cuboctahedral nanoparticles with a) the (100) facet and b) the (111) facet in contact with the support. The results are presented for: i) isolated Pt systems: isolated Pt cluster with the geometry obtained during the optimisation in vacuum; ii) Deformed Pt systems: isolated Pt clusters with the geometry obtained after the interaction with the graphene support and; iii) Interacting Pt systems: the whole Pt/graphene system. 86

6.1 Adsorption sites for (a) Pt(111) facet of a Pt_{147}, where 1 to 3 represent top adsorption sites located on the vertex, edge and centre of the nanoparticle facet, 4 to 6 are bridge sites also located on the vertex, edge and centre of the (111) facet, and 7 and 8 are HCP sites locate on the vertex and edge of the Pt(111) facet and 9 is an FCC site. Figure (b) shows a similar adsorption site distribution for the (100) facet of a Pt_{147}, and (c) illustrates the initial configuration of an ethanol molecule on the Top-V site of Pt_{147}. For each adsorption site, we also present the generalised coordination number which was calculated as proposed by Calle-Vallejo *et al.* [10]. 95

6.2 Adsorption energies for oxygen (red), carbon monoxide (blue), and ethanol (black) interacting with the (111) facet of Pt_{13}, Pt_{55}, and Pt_{147} on different adsorption sites. The letters V, E, and C represent adsorption sites in the vertex, edge and centre of a nanoparticle facet. 97

6.3 Adsorption energies for oxygen (red), carbon monoxide (blue), and ethanol (black) interacting with the (100) facet of Pt_{13}, Pt_{55}, and Pt_{147} on different adsorption sites. The letters V, E, and C represent adsorption sites in the vertex, edge and centre of a nanoparticle facet. 99

6.4 Adsorption energies for oxygen (red), carbon monoxide (blue), and ethanol (black) interacting with different top sites on (111) facets versus the generalised coordination number relative to each adsorption site. Circles, squares, and triangles represent Pt_{13}, Pt_{55}, and Pt_{147} nanoparticles. 101

6.5 Adsorption energies for oxygen (red), carbon monoxide (blue), and ethanol (black) interacting with different adsorption sites on (111) facets versus the generalised coordination number relative to each adsorption site, where a) presents all adsorption sites on a (111) facet, while b) and c) presents bridge and hollow sites. 102

6.6 Differences between the adsorption energies of O, CO and ethanol obtained using geometry optimised nanoparticles and those obtained using unrelaxed Pt nanoparticles created with bond lengths from experimental Pt bulk. The letter V represents adsorption sites in the vertex of the nanoparticle facet. 104

6.7 Adsorption energies for oxygen, carbon monoxide, and ethanol interacting with the (111) facet of Pt_{13}, Pt_{55}, and Pt_{147} on different adsorption sites. Red (black) circles are adsorption energies obtained with the rPBE (rVV10) functional. The letters V, E, and C represent adsorption sites in the vertex, edge and centre of a nanoparticle facet. 105

6.8 Electronic density differences plots for O, CO and ethanol interacting with Pt_{13}, Pt_{55}, and Pt_{147} nanoparticles (Isosurface at 0.02e/ $Å^3$), where blue (red) represents electron accumulation (depletion). The numbers associated with each plot are overall Mulliken charge differences calculated for each adsorbate, where a negative number represents adsorbate receiving electrons. We show the results for O interacting in the HCP-V adsorption site and CO and ethanol adsorbed on TOP-V sites. 106

6.9 Local and angular momentum projected density of states (l-p-DOS) of the d-band of Pt atoms in the interacting region of the (111) facet. Figure a), b), and c) show the density of states for Pt_{13} interacting with O, CO, and ethanol. Figure d), e), and f) show O, CO, and ethanol interacting with Pt_{147}. 108
6.10 Adsorption energies for oxygen, carbon monoxide, and ethanol interacting with the (111) facet of Pt_{13}, Pt_{55}, and Pt_{147} on different adsorption sites. Black dots are adsorption energies obtained with isolated Pt nanoparticles and red triangles are the adsorption energies for Pt nanoparticles supported on graphene. The letters V, E, and C represent adsorption sites in the vertex, edge and centre of a nanoparticle facet. 111
6.11 Adsorption energies for O (red), CO (blue) and ethanol (black) on isolated (filled circles) and supported (open squares) Pt nanoparticles. The adsorption sites used for these plots are the ones presented in figure 6.10. The continuous (segmented) lines are linear regressions obtained for isolated (supported) systems. 112

7.1 Radial distribution functions g(r) for "Relaxing Pt" and "Freezing Pt" approaches for 3 different oxygen coverages on Pt_{55}. Filled blue (black) curves represent Pt (O) g(r) functions for the "Freezing Pt" calculations. Red (green) curves represent Pt (O) g(r) functions for "Relaxing Pt" calculations. The atom in the centre of the Pt nanoparticle is used as the reference for the g(r) in all the calculations. 124
7.2 Final geometries for the 1 ML oxygen coverage on a Pt_{55} nanoparticle obtained with different geometry optimisation approaches, where a) and b) show the Pt nanoparticle covered with O from different angles for the "Relaxing Pt" strategy, while c) and d) show the same system from different angles for the "Freezing Pt" approach. Silver and red balls represent Pt and O atoms. 125
7.3 Illustration of the systems used to obtain a) E_{O_m/Pt_n} b) E_{REF}, where the E_{REF} structure is obtained by excluding the O atoms from the facet we are interested to study 127
7.4 Adsorption energies per O atom E_{ADS} (black circles) and adsorption energy averages $\overline{E}_{ADS}$ for initial (red squares) and final (blue triangles) O configurations for several O coverages on Pt_{55}, Pt_{147}, and Pt_{309} nanoparticles. 131
7.5 Density of states projected on the d-band of surface Pt atoms of cuboctahedral a) Pt_{55}, b) Pt_{147}, and c) Pt_{309} nanoparticles with different O coverages. Figure d) shows the calculated d-band centre for each nanoparticle size as a function of the O coverage. 133

A.1 Adsorption energies for O, CO, and ethanol interacting with the (100) facet of Pt_{13}, Pt_{55}, and Pt_{147} on different adsorption sites. The letters V, E, and C represent adsorption sites in the vertex, edge and centre of a nanoparticle facet. Black dots are adsorption energy values calculated for isolated nanoparticles and red open squares are the same values calculated for Pt nanoparticles supported on pristine graphene. 146
A.2 Adsorption energies for oxygen interacting with the adsorption sites in the (111) and (100) facets of Pt_{13}, Pt_{55}, and Pt_{147}, where the letter V represents adsorption sites in the vertices of a nanoparticle facet. Black dots are adsorption energy values calculated for isolated nanoparticles. Red and green dots are the adsorption energies calculated for Pt nanoparticles bound to graphene via the (111) and (100) facet. 147

B.1 Pt_{55} nanoparticle interacting with different coverages of atomic oxygen, where a), b), c) show initial O configuration and d), e), f) show the O configuration after geometry optimisations. Silver (red) balls represent Pt (O) atoms. 148
B.2 Pt_{147} nanoparticle interacting with different coverages of atomic oxygen, where a), b), c), d), e), and f) show initial O configuration and g), h), i), j), k), and l) show the O configuration after geometry optimisation. Silver (red) balls represent Pt (O) atoms. 149
B.3 Pt_{309} nanoparticle covered with atomic oxygen on different coverages, where a) to g) show initial O configuration and h) to n) show the O configuration after geometry optimisation. Silver (red) balls represent Pt (O) atoms. 150

List of Tables

4.1 Charge spilling parameter, presented as percentages, for calculations performed with CASTEP and different angular momentum resolved bases in ONETEP. . 62

5.1 Comparison of adhesion energy E_{AD} (eV), formation energy E_{FOR} (eV), and average distance between Pt-C and Pt-Pt for Pt_n clusters ($n = 1-4$) interacting with the graphene support. 74

5.2 Average Pt-Pt bond length for each Pt layer on cuboctahedral Pt nanoparticles with the (100) facet interacting with a graphene support. The results are presented for all the Pt layers, where the first one is the closest to the graphene support. Results in brackets were obtained for the same facets in an isolated nanoparticle. 80

5.3 Average Pt-Pt bond length for each Pt layer on cuboctahedral Pt nanoparticles with the (111) facet interacting with a graphene support. The results are presented for all the Pt layers, where the first one is the closest to the graphene support. Results in brackets were obtained for the same facets in an isolated nanoparticle. 80

6.1 Atomic distances between Pt-O, Pt-C, C-O, and C-H, from the CH_3 group for O, CO, and Ethanol adsorbed on Pt nanoparticles. 109

7.1 Oxygen adsorption energies for different values of coulomb-cutoff radius. . . . 121

7.2 The effect of Pt nanoparticle relaxation: Adsorption energies for Pt nanoparticles interacting with atomic O with and without geometry optimising the Pt nanoparticles during the interaction with the adsorbate. In both cases, we present the adsorption energies per O atom for each coverage. 123

7.3 Covering the whole nanoparticle vs hemispherical coverage: Adsorption energies per O atom for Pt_{55} interacting with atomic O at different coverages with the whole Pt_{55} surface and only one hemisphere covered with O 126

7.4 Relaxing all O atoms vs Relaxing only the atoms on a specific facet: Adsorption energies per O atom for Pt nanoparticles interacting with atomic O at different coverages, where we show adsorption energies for all O atoms E_{ADS} calculated with equation 7.3 and adsorption energies for a single facet $^{\star}E_{ADS}$ calculated with equation 7.5 128

7.5 Number of O atoms present on each type of adsorption site for different nanoparticle sizes and oxygen coverages. Numbers outside (inside) brackets represent the number of O atoms placed on a particular type of adsorption site before (after) the geometry optimisations. 129

7.6 Adsorption energies for a single O atom interacting on different adsorption sites and nanoparticle sizes, where NE and NC are non-existent and non-computed adsorption sites. 131

Declaration of Authorship

I, Lucas Garcia Verga, declare that this thesis titled, 'Computational Studies of Metallic Nanoparticles Applicable to Heterogeneous Catalysis' and the work presented in it are my own. I confirm that:

- This work was done wholly or mainly while in candidature or a research degree at this University.
- Where any part of this thesis has previously been submitted for a degree or any other qualification at this University or any other institution, this has been clearly stated.
- Where I have consulted the published work of others, this is always clearly attributed.
- Where I have quoted from the work of others, the source is always given. With the exception of such quotations, this thesis is entirely my own work.
- I have acknowledged all main sources of help.
- Where the thesis is based on work done by myself jointly with others, I have made clear exactly what was done by others and what I have contributed myself.
- Parts of the work presented in this thesis haven been published in academic journals and as a book chapter [9, 11–13] and my contribution has been clearly state in those chapters.

Signed:

Date:

Acknowledgements

These last four years have been an exciting and challenging time that will always be an important part of my life and it is a great pleasure to thank everyone involved in this journey.

I would like to acknowledge the *Conselho Nacional de Desenvolvimento Científico e Tecnológico - Brasil* (CNPq: 206419/2014-7), which has funded my four years of research.

I would like to thank my supervisor Prof. Chris-Kriton Skylaris for accepting me in his group, guiding my research, keeping me focused, helping me to become a better researcher, and for all the support during these four years.

Thanks to my academic advisor, Prof. Andrea E. Russell, for her suggestions and insights regarding our research and all the encouragement and support.

Thanks to Valerio Vitale, Max Phipps, Jacek Dziedzic, Frank Longford, Ben Lowe, and Jolyon Aarons for welcoming me and making me feel part of the group since the first day. Thank you all for being great friends, creating such a great environment inside and outside the office, and for being such a great source of help and knowledge in all the time I needed.

Thanks to Gabriele Boschetto, James Womack, Tom Ellaby, and Gabriel Bramley for your friendship, for all your insights to my research, your help when I needed for research and personal questions, and for our long and funny conversations over lunch and coffee breaks. Thanks to Gabriel for helping me proofreading this thesis. I would also like to thank all the new members of Skylaris group Han Chen, João Morado, Dimitris Mathas, Rebecca Clements, Catriona Gibbon, Jamie Whipham, Bastien Belzunces, and Marjan Famili. You make the office an enjoyable place to be.

Thanks to Ana, Anderson, Bia, Fábio, Karla, Laura, Luísa, Márcio, Marcos, Pedro, Pri, Rafael, Renata, and all the Brazillian friends I have found in Southampton for such great time and good company. I have never imagined that I would learn so much about the culture of other parts of Brazil while in Southampton. Our friendship has made the past four years to fly by. I would especially like to thanks Anderson, Luísa, and Laura for being such a great part of our life in UK, and to Pedro for being such a special friend that has helped me to overcome many difficulties in my work and personal matters.

Thanks to Dr Francisco Carlos Lavarda for believing in me and for encouraging me to pursue a PhD. A special thanks to Dr Pablo Venegas Urenda for giving me my first opportunity in academia, for all his scientific guidance, for his help during these last eight years, and for being not only a great supervisor but a great friend.

Thanks to Léo, Camila, Gui, Laís, Juninho and all my other friends for always caring for us and for keeping in contact during all this time.

Thanks to Flor, Val, and Joara for becoming part of my family and for supporting us in our journey.

Thanks to my aunt "Tia Kuka" one of the most independent, happy, and brave person I have ever met. You have always encouraged me to pursue my dreams and you will always be a part of who I am.

Thanks to my parents Cláudia and Edson, and to my sister Fernanda. Your visits to the UK, your support, and our long conversations about almost everything have helped me to endure this challenging time by constantly reminding me that I have a place filled with unconditional love.

Finally, thanks to my wife Juliane for being by my side, for being brave and face all the difficulties with me, for bringing joy and light even in my worse moments, and for being my partner in every moment of my life. You bring the best of me, and you are the reason for everything I do, without you this journey would not have been possible.

Abbreviations

DFT	**D**ensity **F**unctional **T**heory
ONETEP	**O**rder **N** **E**lectronic **T**otal **E**nergy **P**ackage
NGWF	**N**on-orthogonal **G**eneralised **W**annier **F**unction
EDFT	**E**nsemble **D**ensity **F**unctional **T**heory
XC Functional	E**x**change **C**orrelation Functional
LDA	**L**ocal **D**ensity **A**pproximation
GGA	**G**eneralised **G**radient **A**pproximation
LCAO	**L**inear **C**ombination of **A**tomic **O**rbitals
PAW	**P**rojector **A**ugmented **W**ave
FOE	**F**ermi **O**perator **E**xpansion
[L]-(P)-DOS	[**L**ocal] - (Angular momentum **P**rojected) - **D**ensity **O**f **S**tates
[C](F)-SW	[**C**ontracted] (**F**itted) **S**pherical **W**ave
PAO	**P**seudo **A**tomic **O**rbitals
[PEM](FC)	[**P**roton **E**xchange **M**embrane] (**F**uel **C**ell)
DEFC	**D**irect **E**thanol **F**uel **C**ell
AEM	**A**nion **E**xchange **M**embrane
EOR	**E**thanol **O**xidation **R**eaction
ORR	**O**xygen **R**eduction **R**eaction
WGS[R]	**W**ater **G**as **S**hift [**R**eaction]
HER	**H**ydrogen **E**volution **R**eaction
PES	**P**otential **E**nergy **S**urface
MEP	**M**inimum **E**nergy **P**ath
NEB	**N**udged **E**lastic **B**and
[L](Q)ST	[**L**inear] (**Q**uadratic) **S**ynchronous **T**ransit
BEP	**B**rønsted **E**vans **P**olanyi
MAE	**M**ean **A**bsolute **E**rror

ADF-STEM	**A**nnular **D**ark **F**ield **S**canning **T**ransmission **E**lectron **M**icroscopy
ML	**M**ono**l**ayer
MD	**M**olecular **D**ynamics

This thesis is dedicated to my wife, Juliane.

Chapter 1

Introduction and Motivation

Rationally designing optimised catalysts is a central research challenge in chemistry due to their importance to a wide range of applications with high impact for society. The catalyst activity, selectivity and stability are key variables to perform the CO_2 reduction, conversion of biomass to hydrogen and other fuels, sulphur removal from combustible fuels, and other chemical processes crucial in our drive for sustainability. The main technological focus for this thesis is the study of metallic nanoparticles that are applicable as catalysts for fuel cells, which might play an important role for lowering pollutant emissions by producing clean electricity safely and efficiently. These characteristics of fuel cells make them attractive for a wide range of applications, from small portable devices to decentralised power plants.

A fuel cell converts chemical energy stored in a molecule into electricity by performing a set of chemical reactions which are specific for type of each fuel cell. As an example, figure 1.1 illustrates a simplified structure of a proton-exchange membrane fuel cell (PEMFC) fed with hydrogen gas. This fuel cell consists of a membrane separating two porous electrodes that are connected by an external circuit. The anode breaks the H_2 molecule into $H^+ + e^-$, the electrons flow through the external circuit generating electricity, while H^+ is transported through the proton exchange membrane to the cathode. The unused fuel can be recycled and fed again to the anode. In the cathode, oxygen molecules react with the electrons coming from the external circuit and with the hydrogen protons to form water.

Fuel cells can be fed with a wide variety of fuels which are easier to produce, store and transport as compared with hydrogen gas. Alcohol fuel cells are interesting examples that have been attracting considerable attention due to advantages they have demonstrated over hydrogen fuel cells [14–16]. Methanol is one of the most studied fuels for alcohol fuel cells. In the ideal methanol oxidation reaction, CO_2 and water are formed. Although, if the anodic reaction is not

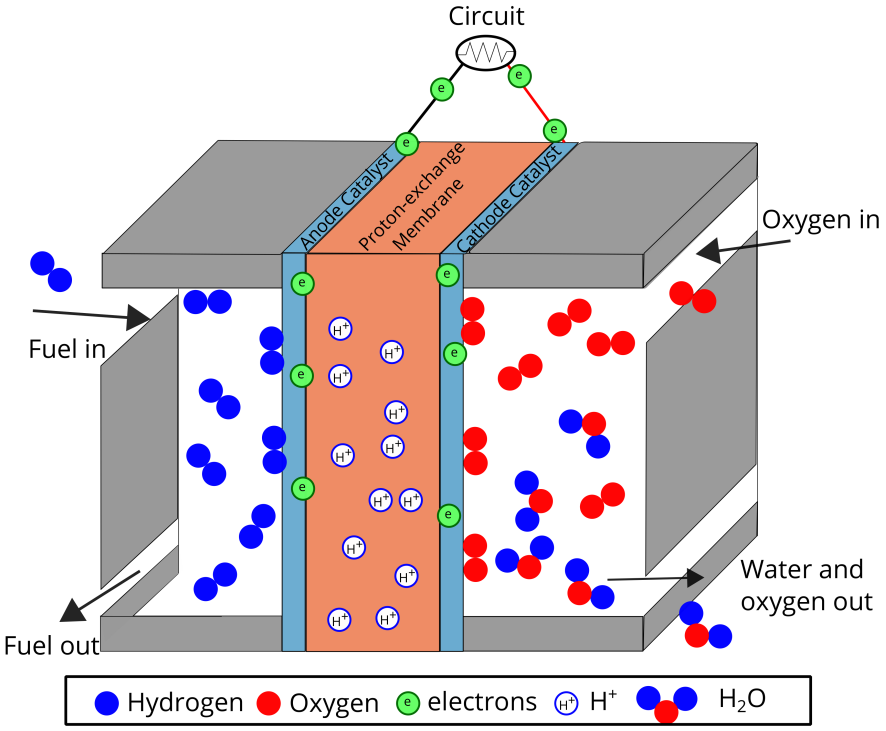

FIGURE 1.1: Simplified structure of a PEMFC (Proton exchange membrane fuel cell) fed with hydrogen.

complete, formaldehyde, CO, and formic acid can be generated as byproducts, poisoning the catalyst surface and decreasing the efficiency of the fuel cell. Moreover, methanol itself is a nonrenewable, toxic, volatile and flammable substance, which could generate issues if applied to portable devices [17].

Ethanol is another interesting fuel option for fuel cells. The main ethanol production comes from fermenting agricultural products, such as sugar-cane and corn. It has a high energy density and lower toxicity when compared with methanol [17], and it is a fuel easy to handle, transport and distribute. In the direct ethanol fuel cells (DEFCs), the ideal ethanol oxidation reaction also produces just CO_2 and water as byproducts. As compared with the scheme from figure 1.1, if a PEM-based fuel cell is fed with ethanol, the anode will receive an aqueous solution of ethanol which is oxidised, generating electrons, protons, and carbon dioxide. Similar to the hydrogen fuel cell, the protons will diffuse through the proton-exchange membrane, and the electrons will flow through the external circuit. In the cathode, oxygen reduction reaction combines protons, electrons and oxygen received from the environment to produce water.

In the PEM-based fuel cell, the anodic ethanol oxidation reaction happens in an acidic environment, which reduces the number of options for anode catalysts and can lower the fuel cell performance due to the difficulty to perform the EOR. There are, however, other types of designs

for fuel cells that can make use of an alkaline media in the anode to facilitate the EOR, allowing to use the reaction environment as an additional variable to tune the fuel cell efficiency. Anion-exchange membrane (AEM)-based fuel cell is an example of such fuel cells design, where the membrane allows the movement of anions, being suitable for alkaline environments.

Another option to indirectly power a fuel cell with ethanol is using an ethanol steam reforming reactor to produce hydrogen that can be purified and fed to a hydrogen fuel cell [18]. This option increases the complexity of the fuel cell but avoids the complications associated with storing and distributing hydrogen gas. Efficient catalysts for the ethanol oxidation reaction (EOR), for the oxygen reduction reaction (ORR), and for the ethanol steam reforming are ongoing problems that need to be addressed in order to improve the durability, stability and efficiency of the fuel cells and to decrease the overall cost of the technology.

Metallic nanoparticles are widely used in such catalysts, where characteristics such as the nanoparticle size, shape, and composition can be controlled to tune the catalyst activity. These nanoparticles are also commonly dispersed over supports that can directly or indirectly participate in the chemical reactions. All these variables can be concomitantly controlled and might affect each other, making catalysts optimisations an exciting and challenging task. The complexity of this problem has been motivating research to understand how each parameter can control the catalyst activity, selectivity and durability, in which computational studies can be powerful tools to provide insights about the physical phenomenon at an atomic level.

In this thesis, we focus our research on nanoparticle size effects and its interplay with other variables that are important in the context of heterogeneous catalysis, such as the presence of support and the adsorbate coverage. We present large-scale density functional theory (DFT) calculations to study how the non-trivial combination of such effects can alter the interaction between nanoparticle surfaces and adsorbates, searching for insights that might help designing new catalysts.

1.1 Thesis Outline

This section presents how the various chapters in the thesis are connected and provides a short description of the content of each chapter. Chapter 2 brings a brief introduction to the central concepts behind DFT, an overview of the linear-scaling DFT approach based on the formalism of the ONETEP program, and some considerations about DFT calculations for metallic

systems. Chapter 3 introduces the computational catalysis field, treating the main approximations and concepts commonly employed in such studies and discussing important research outcomes from the literature. Chapter 4 describes the theoretical framework within ONETEP's formalism to obtain local (atom-projected) and angular momentum projected density of states, which is an important tool for computational studies of metallic catalysts, allowing the calculation of d-band centres that are useful electronic descriptors to explain and predict a surface catalytic activity. These computational tools are employed in chapter 5 to study the interaction of Pt nanoparticles of increasing size with pristine graphene and investigate how the interaction between a nanoparticle and the support changes with the nanoparticle size. The supported and unsupported nanoparticles from chapter 5 are used to investigate the adsorption properties of platinum nanoparticles interacting with atomic oxygen, carbon monoxide and an ethanol molecule in chapter 6, providing insights about the interplay between nanoparticle size and support effects. The nanoparticle size is also studied together with the adsorbate coverage effects on chapter 7, where we assess possible strategies to deal with this complicated problem using DFT and perform a study about the interplay of these effects for the oxygen adsorption energies. For each chapter from 4 to 7 we comment on the main outcomes for that particular study; however, we also discuss the main findings from the thesis on chapter 8 which includes general recommendations for future work.

Chapter 2

Theoretical Methods

This chapter is a brief introduction to density functional theory, including an overview of linear-scaling DFT within ONETEP's formalism and concepts necessary for DFT calculations on metallic systems. A version of this review was also published as part of a book chapter [11]:

Lucas Garcia Verga and Chris-Kriton Skylaris. Chapter 8 - DFT Modeling of Metallic Nanoparticles. In Stefan T. Bromley and Scott M. Woodley, editors, Computational Modelling of Nanoparticles, volume 12 of Frontiers of Nanoscience, pages 239 - 293. Elsevier, 2018.

in which, I was responsible for writing and revising the text, and Prof. Chris-Kriton Skylaris was responsible for additional corrections and revisions.

2.1 Density Functional Theory

2.1.1 Computational Quantum Mechanics

The origin of quantum mechanics dates from the beginning of the twentieth century, when classical physics started failing to predict and explain microscopic phenomena, such as the photoelectric effect, atomic spectroscopy, and the black-body radiation. The development of quantum mechanics was essential to unveil the underlying physics of problems inherent to the atomic scale, and it is the foundation of a significant part of what we call modern technology.

The description of a non-relativistic quantum state and how it varies in time can be made with the Schrödinger's equation which is presented in equation 2.1 in atomic units.

$$\hat{H}\Psi = i\frac{\partial \Psi}{\partial t}, \tag{2.1}$$

where i is the unit imaginary number, Ψ is the wavefunction of the quantum system, and $\hat{H}$ is the Hamiltonian operator. For a time-independent Hamiltonian, we can separate the time and position dependencies of the wavefunction and obtain a time-independent Schrödinger equation as presented in equation 2.2:

$$\hat{H}\psi = E\psi, \tag{2.2}$$

where E is the energy eigenvalue associated with the Hamiltonian operator acting on the stationary eigenstate, ψ. The time dependence can be expressed by adding a phase factor to the stationary wavefunction. However, analytically solving the time-independent Schrödinger equation is only possible for simple systems, making approximations and numerical solutions crucial to the application of the theory on questions of technological interest.

Density functional theory (DFT) is one of the main tools currently used to solve the time-independent Schrödinger's equation, combining moderate computational cost and high accuracy. Scientists have been employing DFT in several areas, such as physics, chemistry, engineering and material sciences and the impact of DFT in science and technology is clear from the remarkable citation statistics of its original work [19, 20]. From now on, this chapter will briefly present some fundamental aspects of DFT to enable the discussions about the information that is possible to obtain with such calculations and about our applications on metallic nanoparticles.

2.1.2 DFT Foundations

For multi atomic systems, which are the centre of computational quantum chemistry investigations, if a nucleus α is located at $\mathbf{R}_\alpha$ and an electron i is located at $\mathbf{r_i}$, we can write the Hamiltonian for the Schrödinger's equation as:

$$\hat{H} = -\frac{1}{2}\sum_i {\nabla_i}^2 - \frac{1}{2}\sum_\alpha \frac{{\nabla_\alpha}^2}{m_\alpha} - \sum_{i,\alpha}\frac{Z_\alpha}{|\mathbf{r_i}-\mathbf{R}_\alpha|} + \frac{1}{2}\sum_i\sum_{j\neq i}\frac{1}{|\mathbf{r_i}-\mathbf{r_j}|} + \frac{1}{2}\sum_\alpha\sum_{\beta\neq\alpha}\frac{Z_\alpha Z_\beta}{|\mathbf{R}_\alpha-\mathbf{R}_\beta|}, \tag{2.3}$$

where the first two terms are, respectively, the kinetic energies of electrons and nuclei. The third term represents the Coulomb attraction between nuclei and electrons, the fourth term describes

the electron-electron interaction and the last term represents the nuclei-nuclei interaction. M_α and Z_α are the mass and atomic number of a nucleus α.

As the nuclei masses are much larger than that of the electrons, electrons mean speed is orders of magnitude higher than that of the nuclei, and their movements can be treated into distinct time scales. Thus, it is possible to simplify the solution of the Schrödinger equation for multi atomic systems by making use of the Born-Oppenheimer approximation, considering nuclei as static particles during the movement of electrons. Under this approximation, the problem from equation 2.3 becomes easier by making the nuclei kinetic energy zero and the nuclear repulsion a constant, creating an electronic Hamiltonian:

$$\hat{H}_{elec} = -\frac{1}{2}\sum_i {\nabla_i}^2 - \sum_i \sum_\alpha \frac{Z_\alpha}{|\mathbf{r_i} - \mathbf{R}_\alpha|} + \frac{1}{2}\sum_i \sum_{j \neq i} \frac{1}{|\mathbf{r_i} - \mathbf{r_j}|} \tag{2.4}$$

The solution of the time-independent Schrödinger's equation with the electronic Hamiltonian results in an electronic wavefunction, ψ_{elec}, which is associated with an electronic energy E_{elec}. The total energy of the system can be obtained by summing the electronic energy and the internuclear repulsion energy.

$$E_{total} = E_{elec} + \frac{1}{2}\sum_\alpha \sum_\beta \frac{Z_\alpha Z_\beta}{|\mathbf{R}_\alpha - \mathbf{R}_\beta|} \tag{2.5}$$

To systematically search for the solutions of Schrödinger's equation for a given system, one can make use of the variational principle. The variational principle states that an approximate solution or trial wavefunction, ϕ, different from the exact ground-state wavefunction, ψ_0, will have an associated energy that is higher than the ground-state energy.

The Hamiltonian is a Hermitian operator and its eigenvectors form an orthogonal set, which can be used to expand the trial function. Thus, let's assume a trial wavefunction ϕ expanded in terms of the eigenvectors ψ_n, as generalised in equation 2.6,

$$\phi = \sum_n C_n \psi_n, \tag{2.6}$$

where ϕ is the trial wavefunction linearly expanded in terms of the ψ_n true solutions of the Schrödinger equation, and C_n are coefficients of the linear combination. According to the variational principle, the energy obtained with a trial function, ϕ, different from the ground state wavefunction, ψ_0, is higher than the ground state energy, E_0:

$$E = \frac{\langle \phi | \hat{H} | \phi \rangle}{\langle \phi | \phi \rangle} = \frac{\sum_n \sum_m C_n C_m \langle \psi_n | \hat{H} | \psi_m \rangle}{\sum_{n'} \sum_{m'} C_{n'} C_{m'} \langle \psi_{n'} | \psi_{m'} \rangle} = \frac{\sum_n |C_n|^2 E_n}{\sum_{n'} |C_{n'}|^2} = \sum_n |C_n|^2 E_n \tag{2.7}$$

where the $|C_0|^2$ associated to ψ_0 is given by:

$$|C_0|^2 = 1 - \sum_{n \geq 1} |C_n|^2 \tag{2.8}$$

From equations 2.7 and 2.8, and by the definition that ψ_n are the solutions of the Schrödinger equation with ψ_0 being the ground state wavefunction, we can see that the energy associated to trial wavefunction is higher than the ground state energy.

$$E = \sum_n |C_n|^2 E_n = E_0 |C_0|^2 + \sum_{n \geq 1} |C_n|^2 E_n = E_0 + \sum_{n \geq 1} |C_n|^2 (E_n - E_0) \geq E_0 \tag{2.9}$$

Therefore, the search for the solution of Schrödinger's equation can happen through a variational method, where the trial wavefunction is changed to minimise the total energy of a given system, knowing that the true ground-state solution will act as the lower limit.

Density Functional Theory searches for the ground-state properties of a system by shifting the emphasis away from the wavefunctions to the electronic density as the key quantity using the Hohenberg-Kohn theorems, consequently reducing the complexity of the problem. The first Hohenberg-Kohn theorem establishes that the external potential and the ground state electronic density have a one-to-one relation. Thus, as the electronic Hamiltonian is determined by the number of electrons and the external potential, the electronic density can be used as a fundamental variable.

The second Hohenberg-Kohn theorem states that the functional for the total energy, which depends on the electronic density, respects the variational principle, i.e, only the ground-state electronic density will minimise the total energy of the system. Thus, the Hohenberg-Kohn theorems show that it is possible to describe the Hamiltonian of an electronic system with an universal functional of the electronic density, however, it does not provide a final form of such functional.

Kohn-Sham DFT brings a useful approach to construct part of the unknown functional by reintroducing the wavefunctions explicitly. However, the many body problem is now changed to a system of N non-interacting particles. The ground-state energy functional using Kohn-Sham DFT can be written as:

$$E_{KS}[n] = T_s[n] + \int \upsilon_{ext}(\vec{r})n(\vec{r})d\vec{r} + V_H[n] + E_{XC}[n], \tag{2.10}$$

where the first term is the independent particle kinetic energy, the second is the external potential, which is usually composed by the nuclei-electron interaction and, the third term is the Coulomb electron-electron interaction, and the final term is the exchange-correlation energy. By reintroducing wavefunctions, the kinetic energy can be described as:

$$T_s[n] = -\frac{1}{2}\sum_{i=1}^{N}\int \psi_i{}^*(\vec{r})\nabla^2\psi_i(\vec{r})d\vec{r}, \tag{2.11}$$

where ψ represents single particle non-interacting wavefunctions.

The electron-electron interaction can be defined as a functional of the electronic density:

$$V_H[n] = \frac{1}{2}\int d\vec{r}\int \frac{n(\vec{r})n(\vec{r'})}{|\vec{r}-\vec{r'}|}d\vec{r'}, \tag{2.12}$$

where n is the electronic density, which can be defined in terms of the single particle wavefunctions:

$$n(\vec{r}) = \sum_{i=1}^{N}|\psi_i(\vec{r})|^2 \tag{2.13}$$

Thus, using the Kohn-Sham formalism, we end up with a system of non-interacting wavefunctions associated with an electronic density. Except for the exchange-correlation term, the entire energy functional has a direct dependence on the electronic density, n, or the single particle non-interacting wavefunctions. As the system respects the variational principle, it is possible to search for an optimum set of wavefunctions to minimise the total energy by using a self-consistent procedure, and if a good approximation for the exchange-correlation functional is given, the obtained result should be the ground state charge density and energy of the interacting system, allowing the study of ground state properties of any multi atomic system.

2.1.3 Exchange-Correlation Functionals

The exchange-correlation (XC) functional in Kohn-Sham theory is unknown and includes a correction term for the difference between the kinetic energies of the interacting and non-interacting systems. Due to the unknown form of the XC functional, an important area for

DFT research is developing and testing the accuracy, computational efficiency and transferability of XC functionals. In general, as the sophistication of the method to create the exchange-correlation functional increases, usually, so it does the accuracy and computational cost.

This relation between the different levels of computational cost and accuracy of the XC functional can be illustrated by the "Jacob's ladder" [1] of XC functionals, where each rung represents a more accurate and costly functional. The XC functionals vary from local density approximation (LDA), which depends only on the local values of the electronic density to double-hybrids, where a portion of Hartree-Fock exchange and a perturbative second-order correlation are used. Figure 2.1 illustrates the so-called "Jacob's ladder" of XC functionals. Moving to the following "rung" up the ladder is equivalent to move to a more costly, complex and usually accurate XC functional.

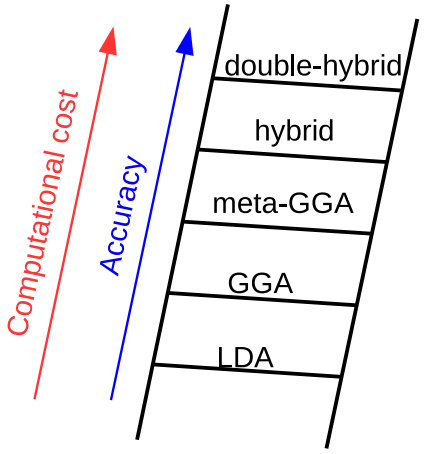

FIGURE 2.1: Representation of the the Jacob's ladder of exchange-correlation functionals [1], where each ascending rung illustrates a class of XC functional with higher complexity, computational cost, and usually accuracy.

As illustrated in figure 2.1, local density approximation (LDA) functionals are the simplest exchange-correlation functionals used in DFT calculations. For LDAs, the XC functional depends only on the local values of the electronic density, and the exchange-correlation energy can be computed as an integral of the exchange-correlation energy density from the homogeneous electron gas model as follows:

$$E_{XC}^{LDA}[n] = \int n(\vec{r})\varepsilon_{XC}(n(\vec{r}))d\vec{r}, \tag{2.14}$$

where ε_{XC} is the exchange-correlation energy per electron for an homogeneous electron gas of density $n(\vec{r})$. This term can be separated in an exchange and a correlation contribution. The exchange energy for an homogeneous electron gas is known exactly, as shown in equation 2.15.

$$\varepsilon_X(n(\vec{r})) = -\frac{3}{4}\left(\frac{3n(\vec{r})}{\pi}\right)^{\frac{1}{3}} \tag{2.15}$$

Meanwhile, the correlation energy is responsible for the main variations between different LDA functionals and can be calculated from expressions for high and low electronic density limits and from results for intermediate electronic density values obtained from accurate quantum mechanical calculations, such as quantum Monte Carlo techniques. Despite being a simple approach, LDA functionals can be good approximations depending on the studied system.

Other classes of XC functionals of increasing complexity and generally higher computational cost and accuracy are also available and widely used in DFT calculations. The next rung in the "Jacobs ladder" is the generalised gradient approximation (GGA), which includes the gradient of the electronic density as another variable to the local value of the electronic density to build the XC functional.

$$E_{XC}^{GAA}[n] = \int n(\vec{r})\varepsilon_{XC}(n(\vec{r}), \vec{\nabla} n(\vec{r}))d\vec{r} \tag{2.16}$$

The GGA functionals are widely used in production calculations with DFT. Similarly to the LDA functionals, there are several theoretical formulations for GGA functionals available, parametrised to different classes of materials and with different levels of accuracy and transferability. The Perdew-Burke-Ernzerhof, or PBE functional [21] is an example of a GGA functional widely used for many applications, that together with some re-parametrisations such as RPBE [22], parametrised to improve the adsorption energies of for adsorbates interacting with transition-metal surfaces, and PBEsol [23], parametrised to improve the description of densely packed solids and their surfaces, form one of the main classes of XC functionals applied to the study of metallic nanoparticles.

The next rung of the ladder are the meta-generalised-gradient approximations (meta-GGAs), which includes the kinetic energy density as an additional parameter to the local value and gradient of the electronic density in the formulation of the XC functional. The following rungs are hybrid functionals, where a portion of the exact exchange energy from Hartree-Fock theory is used to construct the functional and double-hybrid functionals, where a portion of HF exact exchange and a perturbative second-order correlation are used in the construction of the functional. As no universally optimal XC functional exists, each approach needs to be assessed for the system and properties of interest before choosing an appropriate XC functional.

2.1.4 Basis Set

Kohn-Sham DFT re-introduces the idea of non-interacting particles wavefunctions, requiring a computationally efficient basis set to represent these complicated mathematical functions accurately. Each basis set has advantages and disadvantages, and the choice is typically associated with the system under study. Usually, careful convergence tests and comparisons with more expensive calculations or experimental results are needed to define the size of the basis set necessary to carry on research with DFT. Two widely established classes of basis set on DFT calculations are Gaussian and plane waves basis set. Generally, Gaussian basis sets are more used for relatively small molecules, while the plane-wave basis set performs better for periodic and extended systems.

The Gaussian basis sets are constructed under the Linear Combination of Atomic Orbitals (LCAO) ansatz, where the molecular orbitals, ψ_i, are expanded in terms of linearly combined basis functions, θ_α, with expansion coefficients, $C_{\alpha i}$.

$$\psi_i(\vec{r}) = \sum_\alpha \theta_\alpha(\vec{r}) C_{\alpha i} \tag{2.17}$$

Under the LCAO approach, using STOs, that resemble atomic orbitals, as basis functions θ_α seems a suitable option. However, Gaussian functions are more computationally efficient. Thus, a commonly adopted approach for density functional theory calculations is to use contracted Gaussian (CG) functions as basis functions, which combines Gaussian functions to generate a set of θ_α able to reproduce Slater-type orbitals.

The accuracy and computational cost are usually controlled by changing the size of the basis set. A minimal basis set uses only one function for each atomic orbital, being the cheapest, simplest, and least accurate basis set. More expensive and accurate basis sets, such as double-zeta, triple-zeta and quadruple-zeta basis are obtained by using two, three or four basis functions per atomic orbital, respectively. As most of the chemically relevant information comes from the valence electrons, a strategy to improve the computational efficiency with atom centred basis sets is to increase the size of the basis only for the valence orbitals, creating split-valence basis sets. Variational freedom can also be increased by adding polarisation and diffuse functions. The first includes functions with higher angular momentum than the valence orbitals of each atom, while the second expands the functions to regions far away from the nucleus as compared to the regular basis functions.

If the system is placed inside a simulation box periodically repeated in space, we can

naturally introduce plane waves as possible basis set to expand the Kohn-Sham wavefunctions. Let assume a simulation cell with volume Ω defined by primitive lattice vectors $\vec{a}_1$, $\vec{a}_2$, and $\vec{a}_3$, where any lattice vector can be written as:

$$\vec{R} = N_1\vec{a}_1 + N_2\vec{a}_2 + N_3\vec{a}_3, \tag{2.18}$$

where, N_i are any integer numbers. According to Bloch's theorem we can write the eigenstates for a periodic Hamiltonian as a function with the same periodicity of the potential modulated by a plane wave, ensuring the periodicity of the electronic density.

$$\psi_{n,\vec{k}}(\vec{r}) = e^{i\vec{k}\cdot\vec{r}}\mu_{n,\vec{k}}(\vec{r}), \tag{2.19}$$

where $\vec{k}$ are wave vectors and n is a band index. As the μ is a periodic function, we can further expand it in terms of a Fourier Series:

$$\mu_{n,\vec{k}}(\vec{r}) = \sum_{\vec{G}} c_{n,\vec{k}}(\vec{G})e^{i\vec{G}\cdot\vec{r}} = \mu_{n,\vec{k}}(\vec{r}+\vec{R}) = \sum_{\vec{G}} c_{n,\vec{k}}(\vec{G})e^{i\vec{G}\cdot(\vec{r}+\vec{R})}, \tag{2.20}$$

where the sum will run over the wave vectors $\vec{G}$ that respect the condition imposed by the periodicity $\vec{G}\cdot\vec{R} = 2\pi M$, with M being any integer number. Any reciprocal lattice vector $\vec{G}$ can be constructed by reciprocal lattice primitive vectors $\vec{b}_1$, $\vec{b}_2$, and $\vec{b}_3$, which can be defined from the real lattice primitive vectors as:

$$\vec{a}_i \cdot \vec{b}_j = 2\pi\delta_{i,j} \tag{2.21}$$

From equation 2.19 and 2.20 we can show that the plane waves can be used as a basis set:

$$\psi_{n,\vec{k}}(\vec{r}) = \sum_{\vec{G}} c_{n,\vec{k}}(\vec{G})e^{i(\vec{G}+\vec{k})\cdot\vec{r}}, \tag{2.22}$$

From equation 2.19 and 2.20 it is also easy to show that the vectors $\vec{k}$ differing by a reciprocal lattice vector $\vec{k}' = \vec{k} + \vec{G}$ should provide equivalent results. As a consequence we can represent the periodic system only using functions for the wave vector $\vec{k}$ within the first Brillouin zone.

Thus, for a periodic system, the wavefunction for each band can be expanded as a sum of an infinite number of $\vec{G}$ vectors for an infinite number of $\vec{k}$ vectors within the first Brillouin zone. In practical calculations, we can move from an infinite sum and control these two parameters

until we have obtained the accuracy we expect from our calculation. The number of $\vec{G}$ is controlled by the kinetic energy cutoff parameter, which can be systematically increased, allowing more plane waves to the basis set until convergence to the desired physical observable.

Meanwhile, the number of k-points can be controlled by dividing the Brillouin zone into a mesh of k-points, replacing the infinite number of $\vec{k}$ points to a finite number that is controlled as a calculation input. As the $\vec{k}$ vectors are constrained to the Brillouin zone, increasing a simulation cell size decreases the number of k-points that need to be calculated to obtain a same accuracy, and both quantities, simulation cell size and number of k-points, need to be considered together when testing the calculation convergence.

2.1.5 Pseudopotentials and the Projector Augmented Wave Method

As the electronic wavefunctions rapidly vary close to the atom's core, an accurate description of such regions using plane-wave basis set would require a large set of functions or equivalently a very large kinetic energy cutoff, increasing the calculation cost. Moreover, the core electrons are almost unaffected by the chemical environment, with the valence electrons being responsible for most of the chemical bonding.

A method to avoid these difficulties in practical calculations is modelling only valence electronic states with the plane wave basis functions while keeping core states frozen. The influence of the core states can be combined with the nuclei interaction to form an effective potential or as commonly called, a pseudopotential. The generated pseudopotential has to reproduce the potential for the valence region, which is defined as a region outside the core radius used in the pseudopotential generation.

A different approach to treat the same problem is using the projector augmented wave or PAW method [24]. PAW performs a linear transformation between all-electron and pseudo-wavefunctions, presented in equation 2.23. The linear transformation maps all-electron wavefunctions to the pseudo-wavefunctions inside a spherical core region centred on the atom, ensuring that both wavefunctions will have the same characteristics outside the core region. The pseudo-wavefunction is smoother inside the core region, it can be well described by plane waves, optimised *in situ*, and used to recover the behaviour of an all-electron wavefunction.

$$|\psi_n\rangle = |\tilde{\psi}_n\rangle + (|\varphi_v\rangle - |\tilde{\varphi}_v\rangle)\langle\tilde{p}^v|\tilde{\psi}_n\rangle, \tag{2.23}$$

where, the all-electron wavefunction $|\psi_n\rangle$ is expressed based on the pseudo wavefunction $|\tilde{\psi}_n\rangle$,

pre-defined projectors $|\tilde{p}^{v}\rangle$, and all-electron waves $|\varphi_v\rangle$ and pseudo waves $|\tilde{\varphi}_v\rangle$) localised within the core radius. Thus, PAW offers the possibility of performing calculations with similar computational efficiency as the pseudopotential approach, with a high degree of transferability and provides information about the wavefunctions near the nuclei which can be important for some calculations.

2.1.6 The ONETEP Program

The increase in the computational efficiency of DFT codes has been allowing calculations on systems containing hundreds of atoms, which increases the importance of DFT on modern science and technology. However, in conventional DFT codes, the cost of the calculation scales cubically with the number of atoms, which is a bottleneck to the application of DFT on systems with thousands of atoms, such as large nanoparticles, which increases the interest in linear-scaling DFT methods, i.e., where the computational cost scales linearly with the number of atoms.

Generally, linear-scaling DFT approaches are obtained by exploiting the concept of nearsightedness of electronic matter [25]. The idea behind this concept is that the external electronic potential affects the electronic properties locally, i.e., the changes that a perturbation in the electronic potential at some point in space causes in the electronic properties at another place decays to zero with the increase in the distance between these two points. Comprehensive reviews of such methods can be found in the literature [26, 27] and implementations of such approaches can be found on programs such as ONETEP [28], SIESTA [29], OPENMX [30], CONQUEST [31] and BIGDFT [32].

The ONETEP code is an example of such linear-scaling DFT formulation, which achieves the linear-scaling computational cost with the number of atoms by exploring the nearsightedness of the electronic matter together with a spatial truncation of the molecular orbitals. In ONETEP, the density matrix is constructed with non-orthogonal generalised Wannier functions (NGWFs) ϕ_α and a sparse density kernel matrix $K^{\alpha\beta}$, which represents the one-particle reduced density matrix in the set of duals of the NGWFs.

$$\rho(\mathbf{r},\mathbf{r}') = \sum_{\alpha\beta} \phi_\alpha(\mathbf{r}) K^{\alpha\beta} \phi^*_\beta(\mathbf{r}') \tag{2.24}$$

The sparsity of the density kernel matrix $K^{\alpha\beta}$ can be controlled by a single cut-off parameter that makes elements from $K^{\alpha\beta}$ zero, if they are separated by a distance greater than the

given cut-off. In practical calculations, the kernel cutoff needs to be tested, as the decay function associated with the nearsightedness of the electronic matter is dependent on the system under study. For example, for insulating materials, the decay is exponential and much more rapid than the algebraic decay obtained with metallic systems. Thus, the usage of the nearsightedness needs to be carefully controlled to obtain better scaling while maintaining acceptable levels of accuracy in the calculations.

The localisation constraint for the NGWFs is also controlled by a single parameter, the NGWF radius, which defines the spherical volume of each atom-centred NGWF. The sparsity of the density kernel matrix together with the spatial cut-off imposed to the NGWFs provides a density matrix where the information scales linearly with the system size. In ONETEP, each NGWF is expanded in terms of a primitive basis set of periodic cardinal sine functions (psinc),$D_i(\mathbf{r})$, [33]:

$$\phi_\alpha(\mathbf{r}) = \sum_i D_i(\mathbf{r}) C_{i\alpha}, \tag{2.25}$$

where the index i runs over all grid points inside the NGWF localization sphere. The psinc functions are related to plane waves via a Fourier transform. Thus, as the NGWFs are optimised *in situ* and the number of the psinc functions can be controlled by a single parameter, ONETEP allows the same systematic improvement of the basis set as a plane wave DFT code. As the NGWFs are optimised *in situ* the algorithm follows a self-consistent two nested loops approach, where one loop minimises the total energy functional iteratively varying the matrix elements of the density kernel with fixed NGWFs, while the other loop minimises the total energy varying the NGWFs.

2.2 Density Functional Theory for Metallic Systems

Modelling metallic nanoparticles with density functional theory is challenging and computationally demanding, as some particularities of metallic systems make regular DFT algorithms inefficient for large-scale calculations. As previously shown in equations 2.10, 2.11, and 2.13, the Kohn-Sham equations are built with the idea of single particle non-interacting wavefunctions ψ_i, which are used to calculate the electron kinetic energies and are linked to the electronic density. The electrons are expected to fill the electronic states in increasing order of energy up to the Fermi level, following the Aufbau principle. More general expressions can be

obtained by explicitly introducing the concept of orbital occupation, re-writing equations 2.11 and 2.13 as:

$$T[n] = -\frac{1}{2}\sum_i f_i \int \psi_i^*(\vec{r})\nabla^2\psi_i(\vec{r})d\vec{r}, \tag{2.26}$$

$$n(\vec{r}) = \sum_i f_i|\psi_i(\vec{r})|^2, \tag{2.27}$$

where f_i is the orbital occupancy, which is equal to zero (one) if the orbital is unoccupied (occupied). If the calculation is non-spin-polarised, each occupied ψ_i state has two electrons and f_i for occupied states should be equal to two.

During the energy optimisation, the differences in the energies of the electronic states vary, which is not a problem for materials with a bandgap, such as insulators. However, for metallic systems, the states near the Fermi level are too close in energy and the variations in the energies of electronic states with respect to each other may lead to discontinuous changes in the occupancy of the states and in the total energy of the system, making the energy minimisation algorithms unstable. To solve this problem, it is possible to employ the idea of using a continuous function of fractional occupancies that can be controlled by a finite electronic temperature, as the one employed in Mermin's formulation of finite temperature DFT [34].

By using the canonical ensemble treatment for the electrons, we change the functional to be minimised, from the total energy to a Helmholtz free energy functional A.

$$A[T,\varepsilon_i,\psi_i] = \sum_i f_i\langle\psi_i|\hat{T}|\psi_i\rangle + \int \upsilon_{ext}(\vec{r})n(\vec{r})d\vec{r} + E_H[n] + E_{XC}[n] - TS[\{f_i\}], \tag{2.28}$$

where ε_i are the energy eigenvalues, ψ_i the electronic wavefunctions associated to an occupancy f_i, T is a constant finite electronic temperature, S is the electronic entropy term which depends on the occupancy. $\hat{T}$, υ_{ext}, E_H and E_{XC} are the terms commonly present in Kohn-Sham DFT. As T is constant and f_i can be obtained as a function of the eigenvalues ε_i, the functional A is dependent only on ε_i and ψ_i.

In general, linear-scaling DFT methods allow the calculation of systems with thousands of atoms. However, as described before, these methods rely on the nearsightedness of electronic matter to construct sparse matrices and obtain the linear-scaling computational cost. For insulators and materials with a bandgap the electronic density matrix elements decay exponentially

within the distance between two points, while for metallic systems, this decay is slower hindering the application of such methods [35]. Here, we will outline some of the main differences that need to be taken into account to perform DFT calculation on metallic systems, introduce commonly used methods for large-scale DFT calculation on metals and promising approaches which can reduce the scaling of these calculations with the number of atoms.

2.2.1 Electronic Smearing Schemes

In the previous section, we have addressed the reasons for the instabilities of standard DFT methods applied to metallic systems and the need of using a finite electronic temperature to control the distribution of fractional occupancies for the electronic states. The distribution of electrons in different energetic states at thermodynamic equilibrium can be obtained by the Fermi-Dirac distribution, meaning that the electronic occupancy f_i can be calculated as:

$$f_i^{FD}(\varepsilon_i) = \left(1 + \exp\left[\frac{\varepsilon_i - \mu}{k_B T}\right]\right)^{-1}, \tag{2.29}$$

where μ is the chemical potential, k_B the Boltzmann constant, and ε_i are the energy eigenvalues. The distribution becomes a Heaviside step function at zero Kelvin, with discontinuous integer occupancies. For the Fermi-Dirac distribution, the entropy associated with the electronic temperature depends on the occupancies f_i and is given by:

$$S[\{f_i\}] = -k_B \sum_i [f_i \ln(f_i) + (1 - f_i)\ln(1 - f_i)] \tag{2.30}$$

In practice, as f_i is dependent on the ε_i, all the terms from equation 2.28 are dependent on the energy eigenvalues and electronic wavefunctions, and the minimum of the Helmholtz functional can be obtained self-consistently.

The electronic temperature works as a parameter to control the convergence of the algorithm and has to be carefully tested to improve the computational efficiency while maintaining relative energies and other properties comparable with those obtained for zero Kelvin. Moreover, the non-zero temperature also implies that the number of states that need to be calculated will be higher than those from regular DFT.

As the electronic temperature is only employed to improve the calculation convergence, if one is not interested in the thermal distribution, any other sigmoidal distribution converging to a Heaviside step function can be used. One of the main advantages of Fermi-Dirac occupation is the physical correspondence of the smearing to an actual thermal distribution associated to the

temperature T, while one of the major disadvantages is that the function decay is slow, adding a significant number of extra states with small occupancies to the calculation.

There are several schemes to calculate the electronic occupancies with different benefits and downsides. One example of a distribution function commonly used to perform DFT calculations on metallic systems is the "Gaussian smearing scheme", where the error function is used to calculate the occupancies:

$$f_i{}^G(\varepsilon_i) = \frac{1}{2}\left[1 - \mathrm{erf}\left(\frac{\varepsilon_i - \mu}{\sigma}\right)\right], \tag{2.31}$$

where the smearing width σ is a generalisation of the temperature T with no physical meaning. This distribution function is also monotonic, sigmoidal and smooth. However, the function tails off quicker than the Fermi-Dirac distribution and the number of calculations of extra states slightly occupied is reduced. As this electronic temperature is only a numerical tool to improve the algorithm convergence, the entropic term and consequently the Helmholtz free energy functional become a generalised functional.

DFT calculations of metallic systems frequently use this approach. The energies obtained with the smeared occupancies can be extrapolated to an unsmeared limit by applying a post hoc correction at the end of the calculation [36]. Meanwhile, forces and stresses are calculated with the smeared results and should be reliable if the smearing width is chosen to be a value able to improve the calculation convergence while resembling the zero Kelvin system.

Other approaches such as the Methfessel-Paxton Hermite polynomial smearing [37] and the Marzari-Vanderbilt "cold smearing" [38] are also available to perform calculations with metallic systems. Similarly to the Gaussian smearing scheme, the smearing widths of these distributions are not related to a physical temperature and the functional to be minimised is a generalised free energy. As one can imagine, each approach has its own characteristics that need to be considered before choosing the smearing method for a specific DFT calculation. For instance, for the Methfessel-Paxton Hermite polynomial smearing, the dependence of the occupancies on the smearing width is quartic and the results can be used without extrapolation to zero smearing width, but the method can result on negative occupancies. Here, all the calculations are performed using a Fermi-Dirac occupancy smearing.

2.2.2 Density Mixing

A common approach to solve the Kohn-Sham equations in DFT is the usage of the direct inversion in the iterative subspace (DIIS), which is a iterative method first described by Pulay [39, 40] and first implemented for DFT calculations by Kresse and Furthmüller [41] which has been playing a major role as an electronic energy minimisation tool for metallic systems.

Usually, the minimisation is performed by introducing an initial set of wavefunctions and charge density which are used to calculate occupancies and the energies. The wavefunctions are iteratively optimised for a fixed charge density. The optimised wavefunctions generate an output charge density that can be used on a new minimisation step. The usage of the output density from a step as the initial charge density for the following one introduces instabilities in the method which are usually decreased with the density mixing scheme. The Pulay mixing scheme is commonly used as an approach to obtain a better input for the charge density based on the results of the initial charge densities and residual vectors from previous iterations:

$$n_{in}{}^{opt}(\vec{r}) = \sum_i \alpha_i n_{in}{}^{i}(\vec{r}) \tag{2.32}$$

where α_i are obtained minimizing the norm of the residual vector and are constrained to:

$$\sum_i \alpha_i = 1 \tag{2.33}$$

As it happens for any method applied to metals, a smearing function is chosen and the smearing widths tested. For practical calculations, an additional preconditioner is applied to the charge densities to damp long-range wave-vectors, improving the algorithm stability and efficiency.

2.2.3 Ensemble DFT

Despite the success of iterative methods based on the charge density mixing for the treatment of metallic systems, the electronic occupancies receive a non-self-consistent treatment, and the method is considered non-variational, and the algorithm is unstable depending on the employed preconditioner and charge mixing scheme. The formulation of a stable variational method that ensures progressive lower energies towards the ground state for DFT calculations on metallic systems helps to solve some the problems defined for iterative methods.

Marzari, Vanderbilt and Payne [42] proposed a scheme to perform DFT calculations for metallic systems, which in the literature is often referred to as Ensemble DFT or EDFT. The EDFT approach follows the same ideas of the previous method concerning the addition of extra bands partially occupied due to an electronic distribution based on a finite (generalised) temperature within a continuous and smooth distribution function.

The optimisation of the Helmholtz free energy functional from equation 2.28 within the EDFT approach is obtained with respect to the wavefunctions and electronic occupancy, optimising the wavefunction occupancies for every step of the wavefunction optimisation. The electronic occupancies are used in the calculation of the electronic density calculated as:

$$n(\vec{r}) = \sum_{ij} f_{ij} \psi_i^*(\vec{r}) \psi_j(\vec{r}) \tag{2.34}$$

The occupancies f_{ij} are computed in the basis of the orbitals ψ_i, imposing that the trace of the occupancy matrix needs to be equal to the number of occupied states. This change of representation allows the Helmholtz free energy functional to be projected as:

$$G[T, \{\psi_i\}] = \min_{\{f_{ij}\}} A[T, \{\psi_i\}, \{f_{ij}\}] \tag{2.35}$$

Within this formalism, G is invariant to unitary transformations of $\{\psi_i\}$, the f_{ij} are defined in the minimisation of A and remain constant during the optimization of G. This approach allows the functional minimisation to be performed in two nested loops, where the inner loop minimises A, optimising the occupancies with fixed wavefunctions and the outer loop minimises G, updating the wavefunctions. In the Marzari, Vanderbilt and Payne [42] approach, the outer loop minimisation is performed as a direct conjugate gradient method with the molecular orbitals subject to orthonormality constrains. To avoid the broad spectrum near zero occupancy a preconditioning scheme is applied to calculate the search directions together with the regular the kinetic energy preconditioning.

Freysoldt, Boeck and Neugebauer [43] also formulated a similar method to the Marzari, Vanderbilt and Payne EDFT to perform DFT calculation on metallic systems. In this case, the algorithm follows the same ideas of the previous method, but differently from Marzari and Vanderbilt they employ the non-diagonal matrix representation to the orbital energies, and the line search in the inner loop is performed in the space of the Hamiltonian matrices.

Both approaches are stable and variational methods to minimise the Helmholtz free energy functional, solving the problems of non-self-consistent occupancies from the density mixing iterative method and providing accurate forces. For both EDFT methods, the inner loop step contains diagonalisations of the Hamiltonian matrix, which scales cubically with the number of atoms. Nowadays, EDFT and charge density mixing methods are well-established algorithms used to treat metallic systems, widely applied to DFT calculations on metallic systems, such as extended surfaces and nanoparticles.

2.2.4 EDFT in ONETEP

Following the original formulations of iterative methods with charge density mixing and EDFT methods to treat metallic systems, significant effort has been made to find alternative approaches to reduce prefactors and scaling of the algorithms. Reduced scaling algorithms could allow the simulation of systems more significant in the point of view of technological applications, with calculations able to account, for example, for the nanoparticle size and shape effects, interactions with supports, and changes induced in the nanoparticle due to the interaction with other molecules.

The implementation of the EDFT method in the linear-scaling DFT code ONETEP [2] is an example of an implementation of a variational DFT method for metals with reduced scaling. To solve the Helmholtz free energy functional, the implementation of EDFT in ONETEP follows the ideas of two nested loops from Marzari, Vanderbilt and Payne [42], with the inner loop search in the space of Hamiltonian matrices as proposed by Freysoldt, Boeck and Neugebauer [43].

The ONETEP implementation of EDFT uses a minimum set of NGWFs, characteristic from the ONETEP code, which are variationally optimised in terms of psinc funtions. The localisation constraint of NGWFs makes the matrix representation of the Hamiltonian sparse, allowing the usage of efficient sparse algebra routines to achieve linear-scaling computational cost for most parts of the algorithm, which was demonstrated to be able to calculate Au nanoparticles with up to 2057 atoms [2]. The algorithm was tested in the original paper against a similar direct minimisation scheme in the plane wave DFT CASTEP code [44]. The tests showed the ability of the implementation to provide similar free energy results for a Cu fcc-bulk and to converge to the plane-wave geometries and density of states results for a Pt_{13} cluster.

Similarly to the original EDFT implementations, the diagonalisation of the Hamiltonian matrix has a cubic scaling cost, hindering a fully linear-scaling EDFT algorithm. The usage of localised functions reduces the dimensions of the Hamiltonian and consequently alleviates the

computational cost associated with the diagonalisation operations. Figure 2.2 shows for a set of Au nanoparticles, that parts of the code are linear-scaling, while the diagonalisation grows cubically, showing the size range where such operations control the overall method scaling.

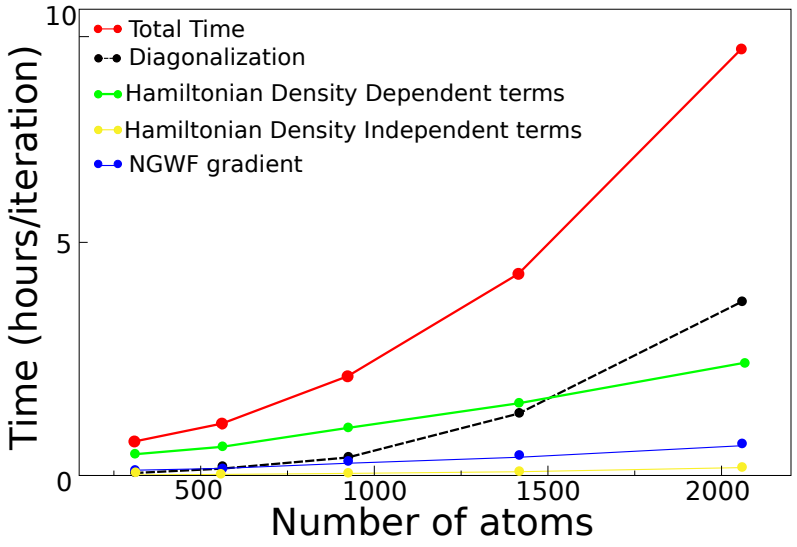

FIGURE 2.2: Computational time per iteration against the number of atoms of Au nanoparticles of increasing size. The calculations were performed with the ensemble DFT as implemented in ONETEP [2]. Hamiltonian DD (DI) are the density dependent (independent) terms of the Hamiltonian.

As the diagonalisation of the Hamiltonian matrix is the main overhead of the EDFT method, an idea to achieve reduced scaling methods for metallic systems is to avoid the cubic-scaling diagonalisation operations during the self-consistent calculations. The Fermi Operator Expansion (FOE) approach, first presented by Goedecker and Colombo [45], is an example of such approaches. In this work, we perform all of our calculations with the EDFT method previously described. However, we encourage the reader to consult a recent and comprehensible review on DFT methods for metals with emphasis in the operator expansions approach [46] and the paper describing the recent implementation of a linear-scaling DFT formulation for metallic systems using the fermi operator expansion in the ONETEP code [47], which in the near future could be helpful for performing DFT calculations on other complex metallic structures important to a wide range of applications.

Chapter 3

Computational Studies on Heterogeneous Catalysis

This chapter introduces some of the main approximations, concepts and computational tools used to study metallic nanoparticles applied to heterogeneous catalysis with DFT calculations. It also discuss important outcomes from the literature that are relevant to this thesis. Sections of this review were also published as part of a book chapter. [11]:

Lucas Garcia Verga and Chris-Kriton Skylaris. Chapter 8 - DFT Modeling of Metallic Nanoparticles. In Stefan T. Bromley and Scott M. Woodley, editors, Computational Modelling of Nanoparticles, volume 12 of Frontiers of Nanoscience, pages 239 - 293. Elsevier, 2018.

in which, I was responsible for writing and revising the text, and Prof. Chris-Kriton Skylaris was responsible for additional corrections and revisions.

3.1 Reaction Mechanisms and Rates

The search for active and selective catalysts is a central question for several industrial processes, and it is crucial in the development of new technologies. Biofuels production, high-temperature lubricants, water splitting, and conversion of biomass to other valuable chemicals are a few examples of chemical processes that are relevant to our society and that are intrinsically related to the catalyst efficiency [48]. Efficient catalysts are also important for improving technologies such as fuel cells, that might help us to mitigate environmental problems and move

away from fossil fuels by efficiently generating electricity via electrochemical reactions that can be performed with different fuels obtained from renewable sources.

Understanding how each characteristic of a catalyst alters reaction mechanisms and rates for chemical reactions is essential to search for better catalysts. In that sense, computational studies can be powerful tools to search for rate-limiting steps in a chemical reaction and generate insights that can lead to improved catalysts. However, computationally studying a chemical reaction happening at a catalyst surface can be an extremely challenging task that might demand exploring complex potential energy surfaces (PES) to search for energetically stable clusters and nanoparticles and to obtain the geometries of reactants, products and transition states for chemical reactions on the catalytic surface.

Describing the catalytic activity for a given chemical reaction often requires studying the activation barriers and reaction rates for each reaction step. These quantities can be calculated by computing the energy difference between the transition state and the energies of the reactant and products for forward and reverse activation barriers. The geometries for the reactants and products on a catalyst surface can be obtained using the energies, forces and Hessian matrix of a system to search for an energetic local minimum in the PES, which can be done using an appropriate geometry optimisation algorithm [49]. Meanwhile, the transition state is obtained by searching in the PES for a saddle point between the reactant and product minima.

The search for transition states is much more complex than the geometry optimisations of the reactants and products. The transition state structure has to be a maximum in only one direction, the direction related to the transition from a given reactant to a product, and a minimum in all other perpendicular directions. Several methods for locating transition states have been developed and tested during the years [50–58], with different levels of accuracy and computational cost. The methods are also able to provide different information. In some cases, the algorithm searches only for the transition state structure, while in other cases it focuses on the minimum energy path (MEP), obtaining intermediate structures along the reaction path where any point in the path is an energetic minimum in all directions except in the one where the transition occurs.

The type of input data necessary for the transition state search algorithm can be used to separate the different algorithms in different classes. In some methods, the search for the transition state occurs using local information of the PES and usually its first and second derivatives. These methods usually rely on one initial structure, close enough to the transition state, while no other information about reactants and products are necessary. Another class of algorithms are the ones that require the geometry of reactants and products as inputs, restraining the search

for the transition state between the two geometries. Here, we briefly present three methods used within DFT calculations to search for transition states and minimum energy paths, detailed analysis and discussions about the different algorithms can be found in the literature [59, 60] and in computational quantum chemistry textbooks [61].

The nudged elastic band (NEB) [50–52] is a method frequently used in the search for transition state structures and minimum energy paths between two states. The NEB algorithm searches for the MEP, by discretising the reaction path with a set of structures linked by spring forces. A sensible initial set of configurations can be created by generating structures from interpolations between products and reactants. The resultant forces F_i^{NEB} for the "NEB" path are composed by the perpendicular components of the atomic forces on each image in relation to a unit vector tangent to the path and by the parallel components of the "spring forces".

The NEB images are relaxed along these resultant force vectors, until F_i^{NEB} converges to absolute values below a given threshold. If the reaction path has only one transition state, the saddle point in the converged path is considered the transition state. As NEB searches for the reaction path, the transition state structure is an approximation, which can be refined with a secondary NEB calculation or with another method. The reformulation of the method, known as climbing image NEB (CI-NEB) [53], removes the spring forces for the highest energy image of the path, allowing this structure to move up to the saddle point by and obtaining a result closer to the transition state structure.

If one is interested only in the transition state structure, different methods can be applied. An example is the linear and quadratic synchronous transit methods, respectively known as LST and QST, formulated by Halgren and Lipscomb [55] and generalised by Govind *et al.* [56]. In the LST method, a set of trial structures is generated by linearly interpolating the geometries of the reaction reactants and products. The maximum energy between these structures is a first approximation of the transition state structure, which is refined and energy minimised along a direction orthogonal to the reaction path. If necessary, a quadratic interpolation (QST) between reactant and product can also be used to search for the transition state.

For systems in which the reactant or product structures are unknown, methods such as the dimer method [54] are advantageous. These methods search for the transition states using only an initial structure guess, relying on the local information of the PES and its first and second derivatives, which can be expensive to calculate due to the need of computing and diagonalising the Hessian matrix. The dimer method avoids the direct calculation of the Hessian matrix by determining the direction along which the energy should be maximised using two symmetrically

displaced images, and it can be an additional tool to search for transition states.

There are several examples in the literature of studies on important chemical reactions such as CO_2 reduction [62], oxygen reduction reaction and oxygen dissociation [63–66], and alcohol decomposition reactions [67–72] over metallic surfaces using DFT calculations and transition state search methods. Alcohol decomposition reactions over metallic systems are particularly interesting and challenging systems to be treated with DFT calculations. The applications related to these calculations are connected with the usage of the biomass as a source of hydrogen for fuel cells and are interesting systems to study different reaction steps such as C-C, C-H, O-H, and C-O bond breaking, which are also important to other technologies.

For the steam reforming of ethanol, computational studies with DFT calculations have indicated that ethanol is favourably dehydrogenated in the first reaction steps, with C-C and C-O bond breaking happening only for more dehydrogenated species [70, 71, 73, 74]. Sutton and Vlachos [71] have calculated reaction and activation energies of reaction steps involved in the ethanol decomposition on close-packed surfaces of Co, Ni, Pd, Pt, Rh, and Ru. They have observed that the dehydrogenation steps are favoured over C-O and C-C bond breaking for all the studied metallic surfaces. The order of the dehydrogenation, however, varied depending on the metallic surface and was different from some experimental observations. For example, the authors show that a decomposition via acetaldehyde with α-C-H and O-H bond breaking should be favourable for Rh(111) surfaces, while other theoretical [74] and experimental data [75] show that a decomposition with β-C-H is preferred in such catalysts. However, most of the theoretical and experimental results also point to CH_xCO as precursors of C-C cleavage, generating adsorbed CO and CH_x that should be further reformed to increase H_2 production.

Carbon monoxide can poison fuel cell electrodes by blocking active sites on the catalyst surface. Thus, to use the H_2 obtained from steam reforming of ethanol in hydrogen fuel cells, it is necessary to increase the H_2/CO ratio, by decreasing the CO concentration of the gas stream before feeding it to fuel cell anode. In that sense, studying catalysts for the water gas shift reaction (WGS) is also necessary to ensure an appropriate CO content in the gas stream. This reaction mechanism over metallic surfaces has also been extensively studied with DFT calculations [3, 76–82] and it is another good example of how computational studies can help to understand reaction mechanisms relevant for catalyst design. For example, for Pt(111) surfaces, Grabow *et al.* [3] investigated possible reaction paths for the WGS reaction by calculating 17 elementary reaction steps using the CI-NEB method for the transition states, and combining the DFT results with a microkinetic model. Figure 3.1 summarises the relative energies of intermediate states

calculated with DFT.

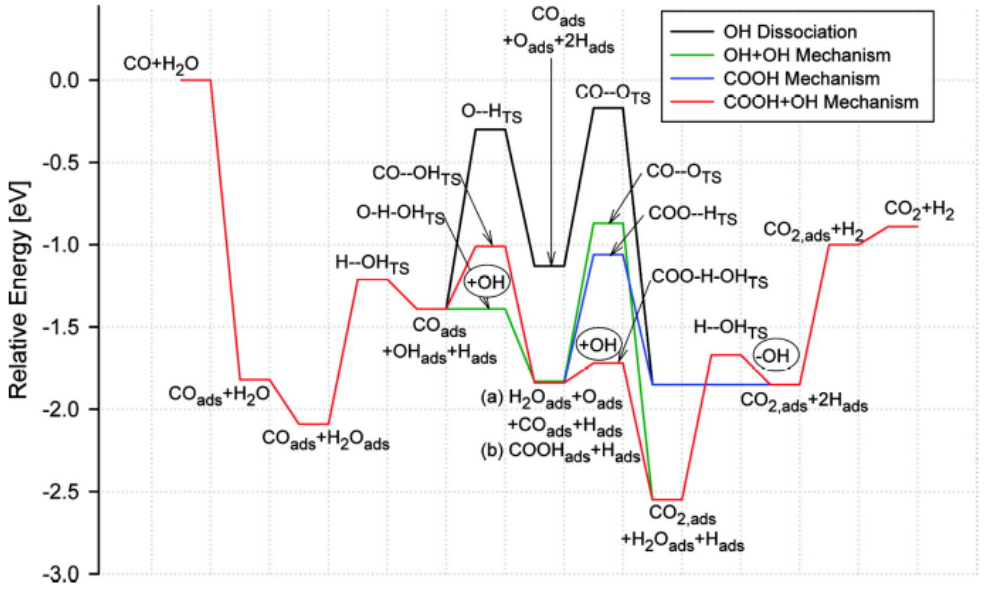

FIGURE 3.1: Reaction coordinate diagram for four possible reaction mechanism for WGS on a Pt(111) surface. The red and blue reaction mechanism involve the formation of a COOH intermediate, and the energetically preferred mechanism is indicated in red. Figure reprinted with permission from 3. Copyright 2008, American Chemical Society.

Figure 3.1 illustrates the competition of four possible reaction paths for the WGS reaction over a Pt(111) surface. For two of those paths, namely OH+OH dissociation and OH dissociation, CO is oxidised by atomic oxygen. For the other two paths, OH oxidises CO, and COOH is as an intermediate. The OH dissociation path is the less likely to happen due to the high activation energy for the second O-H bond breaking on H_2O, and the COOH paths are slightly favoured over the CO oxidised by O paths.

The analysis based on the DFT calculations favours the COOH+OH mechanism in terms of activation energies. These conclusions did not account for adsorbate coverage, temperature and pressure effects, which were included in the microkinetic model created using the DFT results. On the other hand, the results from the microkinetic model show that the small OH coverage on the surface hinders the energetically preferred path and that most of the CO_2 production comes from the COOH mechanism with the direct $\mathrm{COOH} \longrightarrow \mathrm{CO_2} + \mathrm{H}$ decomposition step. These findings lead the authors to suggest additional H_2O in the feed as a possible way to increase OH coverage and facilitate the low-energy decomposition path.

The water activation competed as one of the reaction steps likely to be rate determining in the work of Grabow *et al.* [3] and similar conclusions were also drawn for DFT calculations

on Pt(111) and Pd(111) used as catalysts for the WGS reaction [76]. The reaction barriers calculated for Pt were lower than the ones for Pd catalysts and again, carboxyl formation played an important role, and the water dissociation competed as the rate-determining reaction step depending on the reaction conditions. General conclusions of these theoretical studies are consistent with experimental observations. For instance, the lower reaction barriers calculated for Pt as compared with Pd, agrees with experimental findings showing higher WGS activity for Pt/Al_2O_3 as compared with Pd/Al_2O_3 [83].

However, some differences in the proposed reaction mechanisms and rate-determining steps can appear when comparing experimental and theoretical findings. For example, the theoretical study of Grabow *et al.* [3] indicates formate as a spectator species, which was consistent with experimental findings for the reverse WGS [84]. Meanwhile, experimental studies for WGS on Pt/Al_2O_3 and Pt/CeO_2 indicates formate as an active species and the formate decomposition as a likely rate-determining step depending on reaction conditions [83, 85, 86]. Moreover, the comparison with experimental data in the work from Clay *et al.* [76] shows discrepancies in some kinetic parameters when comparing the Pt(111) and Pd(111) calculations with the experimental Pt and Pd catalysts supported on Al_2O_3, which indicates that the support activity might also play an important role in the reaction and the need to include it in the model.

Despite the valuable information that the transition state structures and the minimum energy paths from DFT calculations can provide, the cost of such calculations hinders DFT of studying and testing a more significant number of metallic nanoparticles and surfaces as possible catalysts or to increase the complexity of the model. An alternative way to study a chemical reaction is focusing on the interaction of the catalyst surface with reactants, intermediate states, and products coupled to thermodynamics concepts to analyse different reactions steps and propose reaction mechanisms and rate-limiting steps for the studied chemical reaction.

For example, in the context of electrochemical reactions with proton-coupled-electron transfers, i.e., reaction steps $A^* + H^+ + e^- => AH^*$, it is possible to use DFT results to calculate the necessary overpotential to make a reaction mechanism thermodynamically accessible. A common approach to deal with this problem is to make use of the so-called computational hydrogen electrode [4]. The model consists on considering the applied electrode potential in relation to the reversible hydrogen electrode, in which the reaction $2(H^+ + e^-) => H_2$ is in equilibrium for all temperatures and values of pH at zero voltage. Using this model, one can calculate the chemical potential of the proton-electron pair based on the chemical potential of a

H_2 molecule and the applied potential, and use its value to calculate the change in the free energy during a reaction step. A reaction mechanism will only be thermodynamically accessible at the electrode potential that allows all the reaction steps to be exergonic, and these results can be used to determine the most likely reaction mechanism for a given chemical reaction.

The thermodynamic analysis about the interaction between a catalyst surface and adsorbates provides a powerful tool to obtain reaction mechanisms and general insights about the chemical reactions happening at the surface, however, such analysis will not directly provide information about the reaction kinetics that could be obtained calculating activation barriers using the transition state structures. To further reduce the computational cost in this area and expand the ability of DFT to analyse more catalysts or simulate more complicated systems, other approaches have been developed to link the catalytic activity of a certain catalyst surface or nanoparticle with properties which are less expensive to calculate with DFT than the transition state structures. In the next section, we outline some concepts commonly used together with DFT calculations to decrease the computational cost and describe the catalytic activity of a metallic surface, to a certain extent, without explicitly determining reaction paths and transition state structures.

3.2 Electronic and Geometric Descriptors

The Sabatier's principle is one of the concepts commonly used in the search for optimum catalysts [87]. The idea behind the concept is the existence of an optimal "bonding strength" between the catalyst surface and the atoms and molecules involved in the reaction. If the bonding between the catalyst and the adsorbates is too weak, the surface will not be able to bind and activate the reactants. Meanwhile, if the bond is too strong, it will hinder the products' desorption and consequently reduce the catalyst efficiency. Thus, Sabatier's principle qualitatively indicates the existence of descriptors, which are specific for each reaction and predict the activity of different catalysts, leading to volcano-type relationships between the catalyst activity and the descriptor.

Researchers have been using this concept together with DFT calculations to determine catalytic activity descriptors for chemical reactions and applying the descriptors as a tool to search for optimum catalysts. As an example, Nørskov *et al.* [4], have modelled the oxygen reduction reaction on several transition and noble metal surfaces using the CHE and observed a correlation between the activity of the surface and the atomic oxygen adsorption energies in the catalyst surfaces, which resulted in the volcano plot in figure 3.2. However, finding an efficient

parameter or set of parameters to describe the reaction is not an easy task, and other approaches are usually applied to identify good descriptors for a given reaction.

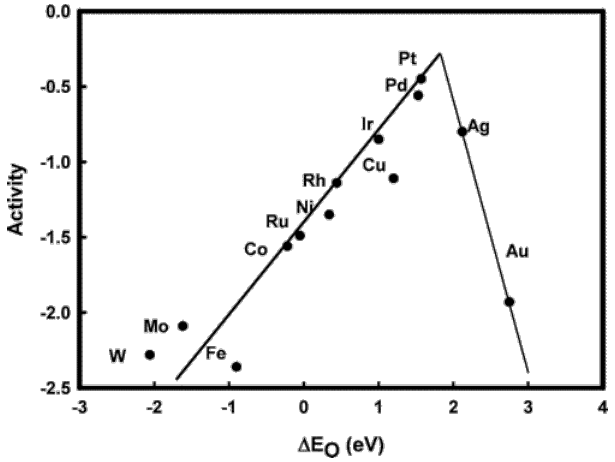

FIGURE 3.2: Volcano plot for the ORR activity versus the adsorption energies of atomic oxygen. Figure reprinted with permission from 4. Copyright 2001, American Chemical Society.

The Brønsted-Evans-Polanyi (BEP) principle [88, 89] is another concept that is usually applied together with DFT calculations to study reaction steps on metallic surfaces and nanoparticles. The BEP principle states that the change in the activation energy for a given reaction step linearly correlates to the change in the reaction energy. Thus, the adsorption energies of reactants and products for the intermediate reaction steps would be enough information to obtain the activation energies. These results could be coupled to microkinetic models [90] to study the reaction on a catalyst surface without the computational cost associated with the search for transition state structures.

There are several examples in the literature testing BEP relations with DFT calculations for different reactions [91–94]. In general, they observe that the linear relations are independent of the chemical composition of the metallic surface and transferable to similar adsorbates, i.e., the same linear equation can describe the correlation between activation energies and reaction energies for different reaction steps on surfaces composed by different metals. This universality of the BEP relations happens when the transition state structures for these reactions are very similar for different adsorbates.

As an example, Wang *et al.* [93, 94] observed linear trends for a set of chemical reactions based on C-C, C-O, C-N, N-O, N-N, and O-O dissociation, calculated on different metallic surfaces. The results show an associated mean absolute error (MAE) of 0.35 eV obtained with the universal trend. However, the parameters of the linear equation and the associated error of the trend change depending on the subset of the data that is being used. For example, if only CH_X-O

bonds, with $0 \leq X \leq 3$, are considered, the MAE drops to 0.25 eV, and if an even smaller set, such as only C-O bond breaking is used, the error can be as small as 0.13 eV. Thus, the authors indicated a clear trade-off between the accuracy and the universality of these linear relations. The computational benefits of the BEP relations make this approach an important part of the computational search for efficient catalysts. However, as for any other semi-qualitative approximation, a researcher should carefully assess the results considering possible errors introduced by the BEP relation for each particular case [95].

Another approach used to reduce the computational cost when studying metallic surfaces, clusters and nanoparticles applied to heterogeneous catalysis are the relationships between the adsorption energies obtained for different adsorbates. This type of approximation is a powerful tool to investigate metallic surfaces as catalysts. A set of adsorption energies for single atoms and small molecules interacting with a surface can be used to predict the adsorption energies of intermediate states of a reaction, which can be used to compute reaction and activation energies for different reaction steps via BEP relations. Thus, using both concepts together can dramatically reduce the computational cost to obtain reaction mechanisms, rates and rate determining steps for a chemical reaction. For example, the work from Abild-Pedersen *et al.* [96] showed the existence of a correlation between the adsorption energies of AH_x adsorbates and the adsorption energies of atoms A, with A=C, O, N, and S, interacting with different closed-packed and stepped metallic surfaces. For both, stepped and closed-packed surfaces, the slope obtained for the fitted equation was close to $\gamma = (x_{max} - x)/x_{max}$, where x_{max} is the maximum number of bonds that the atom A which is in contact with the metal surface can form in an isolated molecule.

Over the years, the scaling relationships for adsorption energies have been applied to different types of adsorbates. An example is the study of glycerol reforming, where the researchers estimated the adsorption energies of several intermediate species on a Pt surface using the adsorption energies of carbon, oxygen, glycerol and a subset of intermediate species obtained from DFT calculations [97]. In a different work, the authors have expanded the relationships to predict the adsorption energies of intermediate species on different metallic surfaces using only O, CO and the adsorption energies of intermediate species previously calculated for a Pt surface [98]. The combination of scaling relationships and BEP relations allowed them to compute the kinetics and thermochemistry of this chemical reaction without the need of computing all the possible transition state structures, greatly reducing the computational cost for the overall study [97, 98].

The links established between adsorption energies of single atoms or group of atoms with the activation and reaction energies are useful not only to decrease the computational cost for the study but also to help to determine parameters to be used as "bond strength" descriptor for Sabatier's principle volcano plots or activity maps [87]. Given the importance of the adsorption of atoms and molecules for catalytic applications, some theoretical approaches have been developed to link the electronic and geometric properties of metallic surfaces or nanoparticles to the adsorption energies of adsorbates. Describing the adsorption on a surface with descriptors based on the geometric or electronic properties of the surface can reduce even more the computational cost in the screening of possible catalysts for chemical reactions. Moreover, understanding the factors that control the bond strengths of key adsorbates can provide insights about possible routes to tune the catalyst performance.

The d-band centre is one example of a bonding strength descriptor that is widely used in studies of heterogeneous catalysis. As proposed by Nørskov *et al.* [4, 99, 100], the d-band model describes the bond formation between an adsorbate and a transition-metal surface using information from the d-band of a metallic surface that can be readily accessed through DFT calculations. The interaction between the adsorbate's valence states and a metallic surface happens through the coupling of the adsorbate's states with the s states of the surface, which shifts and broadens the adsorbate's valence state, and through the formation of bonding and antibonding states between the adsorbate's state and the d states of the metallic surface.

The contribution of the metallic s states to the interaction with an adsorbate is very similar for all transition-metal surfaces, due to the delocalised, half-filled characteristics of their s bands. Meanwhile, the d-bands are more localised, and most of the differences in the adsorption energies are considered to depend on the filling of the metal-adsorbate antibonding states, which can be evaluated through the energy of the antibonding state in relation to the Fermi level. As the antibonding states are always higher in energy than the d-band energies, the authors proposed that a good description of the energy of the antibonding state, and consequently the bonding strength, is the energetic centre of the occupied d-band state with respect to the Fermi level. Thus, the d-band model allows the prediction of the bonding strength, where a surface with a higher d-band centre in relation to the Fermi level binds the adsorbate more strongly.

Other descriptors for atomic and molecular bonding on transition metal surfaces have also been developed and tested in different situations. The generalised coordination number developed by Calle-Vallejo *et al.* [10, 101] is an example. In this case, the descriptor is computed with a bond counting strategy, i.e., directly from the geometries of the nanoparticles and surfaces

without the need for electronic structure calculations. The generalised coordination number $\overline{CN}$ is calculated as follows:

$$\overline{CN}(i) = \sum_{j=1}^{n_i} cn(j)/cn_{max} \tag{3.1}$$

where the n_i nearest neighbour j from the adsorption site i are counted with a weight of $cn(j)/cn_{max}$, with $cn(j)$ being the coordination number of each first neighbour and cn_{max} being the maximum number of first neighbour in the bulk. For example, $cn_{max} = 12$ for a top adsorption site in an FCC crystal. The generalised coordination number can also be computed for other adsorption sites such as hollow and bridges or materials with different crystalline structures by changing cn_{max}.

Calle-Vallejo *et al.* [101] compared the generalised coordination number against the coordination number as possible descriptors for adsorption energies. They have computed adsorption energies on adsorption sites with different generalised coordination numbers but with the same coordination number 9 on different nanoparticles and on an extended Pt(111) surface. While the generalised coordination number grew with the system size, following the changes in the adsorption energies of OH, the coordination number remained the same. The generalised coordination numbers also correlated with the adsorption energies of OOH for different adsorption sites on six Pt nanoparticles and the extended Pt(111) surface. The generalised coordination number is a purely geometric descriptor, computed without performing electronic structure calculations, which reduces the computational cost to test possible catalysts for nanoparticles with similar chemical composition.

Other approaches, such as the one proposed by Aarons *et al.* [8] also describes the adsorbate-surface interaction without computing the adsorption energies. In this case, the authors correlated the adsorption energies of atomic oxygen on different adsorption sites of Pt nanoparticles with the values of the electronic density on an electrostatic potential isosurface. Another example of a quantity that can be used as a catalytic descriptor is the orbitalwise coordination number [102], where the coordinative saturation of an adsorption site and its ability to form bonds via a specific orbital are estimated considering bond counting arguments and considering interatomic interactions to assess the local coordination. Thus, using any of these descriptors, one can correlate adsorption energies, reaction and activation energies, and properties of the catalysts, helping to understand and test possible reaction mechanisms and new catalysts.

3.3 Strategies for Catalysts Design

So far, we have presented some of the main concepts and tools used together with DFT calculations to study metallic surfaces, clusters and nanoparticles applied to heterogeneous catalysis. These strategies can be helpful to understand the mechanisms of chemical reactions at the catalyst surface an also propose strategies to improve the catalyst activity, selectivity and stability. The efforts to design new catalysts involve understanding how the catalyst composition, the nanoparticle size and shape, the presence of ligands in the nanoparticle surface, the reaction conditions, the presence and the composition of the support, and several other characteristics affect the catalyst for each specific reaction, making the area challenging and exciting. In the next sections, we present selected studies aiming to illustrate how catalysts can be modified through different routes and how DFT can be useful to search for improved metallic catalysts.

3.3.1 Catalyst Composition

The chemical composition of the metallic catalyst is one of the first considerations that need to be tuned for each chemical reaction. In general, an optimum catalyst for a given application has to be active, selective and stable under specific reaction conditions. For example, in the context of direct ethanol fuel cells, the anodic reaction of ethanol oxidation can be performed under acidic or alkaline environment, depending on the type of fuel cell, and the optimum catalyst composition can be different for each case. For an acidic media, platinum and platinum-based alloys are commonly indicated as excellent catalysts for the ethanol oxidation reaction [103–105]. Meanwhile, for alkaline environments, palladium and palladium-based alloys are commonly indicated as possible candidates to replace Pt-based catalysts due to their lower cost and high performance under these reaction conditions [103, 104, 106].

In acidic environment, Pt catalysts are found to be able to break the C-C bond in ethanol molecules, which could lead to complete ethanol oxidation to CO_2 [107–111]. However, the CO_2 yield for ethanol oxidation on Pt catalysts is rather small as compared to C2 products such as acetaldehyde and acetic acid, which considerably reduces the fuel cell efficiency. Computational studies have helped to explain the relatively low formation of C1 products from the ethanol oxidation reaction by showing how the presence of OH and O on the catalyst surface can affect the C-C bond break [112]. The computational results demonstrate that the presence of OH and O adsorbed species increases the reaction barrier for the C-C bond cleavage [112], which explains the CO formation for low applied potentials commonly observed experimentally

[108–111]. However, platinum surfaces are also easily poisoned by adsorbed CO, and the adsorbed OH species are necessary to further oxidise CO to CO_2, meaning that the OH coverage needs to be controlled to avoid inhibiting the C-C bond break while allowing CO oxidation.

Alloying Pt catalysts with other metals such as Ru and Sn can improve the catalyst activities on acidic media. The enhanced catalytic activity obtained with the addition of Ru to Pt catalysts is commonly explained due to an increase in OH adsorption, which is necessary to avoid surface poisoning [105]. A similar effect is observed when alloying Pt catalyst with Sn. However, in both cases the selectivity towards C1 products does not increase with the addition of the co-catalysts, showing that the increase in activity should be explained due to more efficient reactions towards C2 products rather than more complete oxidation to CO_2.

The importance of adsorbed OH species for the ethanol oxidation reaction can also be observed by studies comparing the catalyst activity on different pH values. Lai *et al.* [111] have demonstrated significant increases for the EOR on Pt catalysts for alkaline electrolytes. However, as previously said, in alkaline media other compositions such as Pd-based catalysts can be considerable options against Pt catalysts. For example, Ma *et al.* [106] compared carbon-supported Pt and Pd catalysts in alkaline media and demonstrated a superior activity for Pd catalysts towards the ethanol oxidation reaction. Similar to Pt catalysts, the activity of Pd-based catalysts can also be improved by alloying them with other metals that could help to alleviate CO poisoning [104].

The catalyst composition is also a key variable for improving the activity towards the ORR happening at the cathode of DEFCs. As demonstrated in figure 3.2, platinum catalysts are predicted with DFT calculations to be close to the activity peak of a volcano plot obtained from monometallic catalysts [4], indicating Pt as a suitable candidate for the ORR. The volcano plot from the calculations performed by Nørskov shows that an improved catalyst for ORR could be obtained by slightly weakening the adsorption energies of atomic oxygen on the catalyst surface [4]. Interestingly, the exploration of this concept has lead to the discovery of alloys such as Pt_3Y and Pt_3Sc [113] and near-surface alloys such as Cu/Pt(111) [114] which are improved catalysts for the ORR as compared to Pt(111), as demonstrated theoretically and experimentally.

Computational investigations about the effect of the chemical composition for a metallic catalyst can also be found for other types of metallic nanoparticles and chemical reactions. The work on O_2 dissociation, which a crucial step for the ORR, on platinum-based truncated octahedra nanoparticles from Jennings *et al.* [115], is one example. In this study, M@Pt core-shell clusters were created with different transition-metal cores and used to compute O_2 adsorption,

activation energies for O_2 dissociation, and the electronic and geometric effects induced by the addition of the second element. In general, the authors observed that clusters with late (early) transition-metal cores had lower (higher) dissociation barriers.

The low dissociation barriers were associated with the distortions on (111) facets of small metallic clusters, which happened for pure Pt and for bimetallic clusters where the Pt-M interaction was relatively weak. The authors did not assess the stability of the bimetallic clusters; however, the comparison of the Pt-M interaction with the Pt-Pt interaction was used as an indication of the cluster stability and the metals from group 9 were indicated as promising candidates for core elements in the core-shell clusters. They have observed that the Pt-M interactions for this class of metals were slightly stronger than Pt-Pt interactions, but not strong enough to inhibit the favourable distortions in the (111) facet that lowered the activation energies. Moreover, this group of metals as the nanoparticle core induced downshifts in the d-band centre, which also helps the oxygen desorption step in the oxygen reduction reaction.

Another case of a study trying to tune catalytic activity by changing the composition of the catalyst with bimetallic nanoparticles is a recent computational screening for core-shell nanoparticles tested for the oxygen reduction (ORR) and hydrogen evolution reactions (HER) [116]. The study used O and H adsorption energies on bimetallic truncated octahedra nanoparticles with 79 atoms as descriptors for the catalytic activity for ORR and HER. The authors have also calculated segregation energies as the difference between the nanoparticle energies in the core-shell configuration and nanoparticles with one atom from the core and one atom from the shell exchanged. The segregation energies were calculated with and without the adsorbates, to observe the nanoparticle in both conditions. In terms of catalytic activity, the authors observed that the choice of the shell was a key factor, with Pt, Pd, Ag and Ir being the most active shells for ORR. For other nanoparticle shells, the oxygen binding was too strong or too weak as compared with the -1.24 eV value obtained as a peak for the volcano plot. The high activity of Ag shelled nanoparticles can be particularly interesting for industrial applications due to the low cost of Ag as compared with Pt [116].

This type of study on the effects of the chemical composition for nanoalloys applied to heterogeneous catalysis is not restricted to bimetallic structures or core-shell nanoparticles. However, increasing the number of elements in the nanoparticle or considering different nanoalloy patterns, also increases the complexity and the computational cost of the study. Nonetheless, it is possible to cite examples of complex nanoalloys studied with DFT calculations, such as the study of alloy-core@shell nanoparticles from Zhang and Henkelman [5], which employed DFT

calculations to assess the catalytic activity of a nanoparticle composed of a random bimetallic core covered with a noble metal shell for CO oxidation, which can be important in the context of indirectly using ethanol to power fuel cells using ethanol steam reforming to generate H_2.

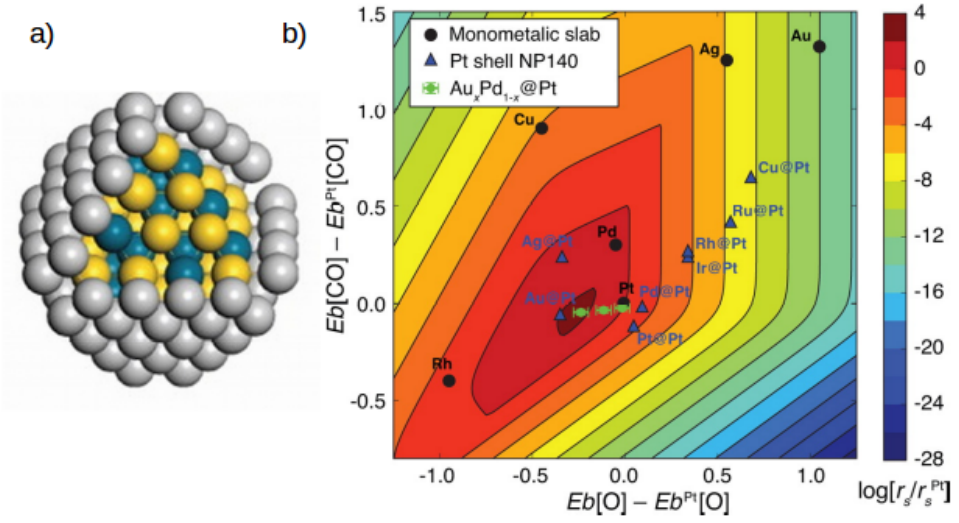

FIGURE 3.3: Alloyed-core@shell nanoparticle a) illustration and b) catalytic activity for the CO oxidation reaction. Figure b) shows a contour plot of the activity as a function of CO and O adsorption energies for different metallic clusters compared with pure Pt slab. Black dots represent monometallic slabs, blue triangles represent core-shell nanoparticles, while green points show the activity of AuPd@Pt nanoparticles with different Au/Pd ratios. Figure reprinted with permission from 5. Copyright 2015, American Chemical Society.

The authors have compared random alloyed FCC crystals covered with a Pt or Pd monolayer and truncated octahedra M_{140} with the same composition. These structures were assessed as catalyst candidates for the HER and CO oxidation reactions, using atomic and molecular adsorption energies, BEP relations and microkinetic models [5]. For the alloy-core@shell nanoparticles and slabs, the authors have observed a linear relationship between the binding energies of adsorbates and the shifts in the surface's d-band centre. The d-band centre changes were also linearly correlated with the changes in the alloy-core composition. Figure 3.3 shows an illustration of a nanoparticle with a random PdAu core and a Pt shell and an activity map for the CO oxidation on different catalytic surfaces [5].

As shown in figure 3.3 b), Au@Pt, Ag@Pt and AuPd@Pt nanoparticles are possible candidates as CO oxidation catalysts. Moreover, the activity of AuPd@Pt nanoparticles was between the activities of Pd@Pt and Au@Pt core-shell nanoparticles [5]. This relation is a consequence of the linear relationship between the surface's d-band centre and the alloy-core composition and can be used as a guide to predict alloy-core@shell nanoparticles by linearly interpolating the results of regular core-shell structures, showing another route to tune the catalyst by changing its composition that can be further explored with the aid of DFT calculations.

3.3.2 Nanoparticle Size and Shape

In addition to the catalyst composition, understanding the impact of the nanoparticle size and shape in the catalyst activity, selectivity and durability is of great importance for catalyst design. First of all, controlling the nanoparticle size helps to ensure an appropriate surface-to-volume ratio, increasing the active area and reducing the loading of expensive metals in the catalyst. Also, as a material size decreases, new properties emerge due to the changes in the geometric and electronic structures of the nanomaterial, which are caused by variations in the surface-to-volume ratio, interfacial effects, quantum confinement of electrons, among other effects, making the nanoparticle size an important variable in the search for optimum catalysts. The nanoparticle size and morphology also control the number and type of available adsorption sites and active facets, which can affect how the nanoparticle interacts with adsorbates and change the activity and selectivity of the catalyst.

Controlling the nanoparticle size and shape with a uniform dispersion of nanoparticles over supports is an extremely active and challenging research area. Despite the ongoing challenges to generate scalable methods to finely tune the metallic nanoparticle size in industrial levels, the advances in experimental techniques in this area have been enabling studies to help unveil the impact of these variables in the catalytic activity [117]. Meanwhile, computationally defining an energetically stable or metastable nanoparticle shape for given nanoparticle size and composition is also challenging and an important part for studies on metallic nanocatalysts. An initial guess for a nanoparticle/cluster structure can be geometry optimised with DFT calculations by calculating atomic forces and using them to search for an energetic local minimum in the potential-energy surface. However, the local minimum structures obtained with geometry optimisation schemes are generally dependent on the initial guess, while searches for the global minimum can be much more complicated [118].

The algorithms for global optimisation of clusters and nanoparticles can be coupled with DFT or with less expensive descriptions of the PES such as empirical potentials. Usually, Monte-Carlo and molecular dynamics methods based on simulated annealing approaches, Basin hopping methods, and genetic algorithms are used as tools for global minimum searches of metallic nanoparticle structures [118], with the overall efficiency of the minimisation relying on the model used to create, select and modify the structures of the nanoparticles and the accuracy and computational efficiency of the tool used to describe the PES. An alternative strategy which is commonly employed in the computational study of metallic nanoparticles is to generate and optimise a set of initial guesses, which can be created based on characteristics of the studied

system. The energies obtained after the optimisation of the initial guesses can be compared to obtain a putative global minimum. This kind of strategy, however, provides a biased search that can hinder global minimisation.

Global optimisations of metallic nanoparticles with DFT calculations are relatively scarce in the literature due to the computational cost associated with the calculations. However, some examples can be found for metallic clusters. For Au_n clusters with $n \leq 20$, a global optimisation with a DFT - Basin hopping approach, has shown the formation of Au_{20} tetrahedron clusters in gas-phase [119]. The energy obtained with the optimum geometry from the DFT-based algorithm was found to be 1.28 eV lower than the energy from the most stable structure found with a global optimisation performed with an empirical potential. The stability of the cluster was explained in terms of electronic structure characteristics inherent of gold clusters in this particular size, which could only be captured with electronic structure simulations, showing the relevance of DFT-based global optimisations to find global minimum geometries for clusters with specific size and composition [119]. More recently, the same method was applied to an Au_{40} cluster, which was also found to be stable with a twisted pyramid structure [120].

On the other hand, the approach of testing several configurations is more frequently used to assess the stability of clusters and small nanoparticles. Usually, these calculations are focused on structures considered sensible, which normally retain bulk-like aspects, are symmetrical, such as Wulff constructions, and are built by accounting for bonding characteristics of the metal and maximising the presence of stable facets. For gold structures, it was observed that a cuboctahedral symmetry is more stable for Au_{13} while the icosahedral one is more stable for Au_{55} [121]. For rhodium clusters, the energetic difference between cuboctahedral and icosahedral structures was calculated to be small, with icosahedral being slightly more stable for Rh_{13} and Rh_{55} [122]. Similar studies were also performed for other metallic nanoparticles such as Ru [123], Pd [124–126], Pt [127], and other metallic systems [128]. These results also show the existence of stable 2D structures for small clusters, generally smaller than ten atoms, which can be explored to increase the catalyst surface area. Moreover, these studies show a general trend of stronger cohesive energies with increasing cluster size, converging to bulk values.

For metallic nanoparticles applied on heterogeneous catalysis, the need for finding the global minimum geometry instead of a metastable structure should be carefully assessed by the researcher. These calculations, especially global minimum methods based on DFT, can be much more expensive than simple geometry optimisations. Moreover, the global minimum geometry can be different from the ones that are relevant for catalytic applications due to the different

experimental conditions such as solvent, temperature, support, and adsorbate concentration, on which the nanoparticle will be used. For example, recent studies have shown that the energy differences and relative stabilities among isomers can change due to the presence of ligands or reactants adsorbed on the clusters. For instance, Sun and Sautet [129] demonstrated that the global minimum of a Pt_{13} obtained in gas-phase is not similar to the global minimum obtained for a Pt_{13} covered with 18 or 26 H atoms. For an isolated Pt_{13}, they have obtained an open structure with low symmetry and average coordination number of 4.2 as the global minimum, while under high H coverage, the global minimum is a bulk-like cuboctahedral cluster, and the energy of the first isomer in a non-cuboctahedral shape is 1.63 eV higher than the global minimum.

Despite these difficulties on experimentally controlling the nanoparticle size and shape and computationally determining the energetic stability of the nanoparticles, the importance of these effects for the catalytic activity makes computational and experimental studies in this area indispensable for in the search for improved catalysts. As already exemplified, the nanoparticle morphology is crucial to control the available metallic facets in a catalyst, which is an important variable to be tuned for each reaction. For example, for the ethanol oxidation reaction, both experimental and theoretical studies have been showing that the catalyst activity and selectivity are structure sensitive, with different available Pt facets being preferred for the EOR in different reaction environments[58, 110, 130–133].

Colmati *et al.* [110] showed experimentally that under an acidic media the main product obtained on Pt(111) surfaces after the ethanol oxidation is acetic acid, and suggested that C-C bond breaking is only possible on Pt(111) electrodes with the presence of defects due to the low CO, and consequently CO_2 formation observed for such electrodes. On the other hand, the C-C bond breaking is easier for Pt(100) at low potentials, with its surface being readily poisoned by adsorbed CO, and for Pt(110) at any potential, with the formation of acetic acid from acetaldehyde presenting lower rates as compared with the other facets [110].

These results agree with theoretical findings from DFT calculations for the ethanol oxidation reaction on different Pt surfaces such as the work from Wang and Liu [58] which shows that the C-C bond breaking is easier for Pt(100) facets as compared to Pt(111). The computational results also show that acetic acid and CO_2 originate from CH_3CO and that the selectivity towards each product is controlled by the catalyst activity for the reaction $CH_3CO + OH \longrightarrow CH_3COOH$, which is favoured on Pt(111) facets. Meanwhile, for Pt(100) facets, CH_3CO is dehydrogenated favouring the C-C bond cleavage [58].

Similarly, other reactions such as the water dissociation reaction, which is important for the WGS and EOR, are also found to be structure sensitive, strengthening the importance of shape-controlled nanoparticles. For example, DFT calculations on water dissociation on different Pt surfaces have shown that steps and kinks adsorption sites can affect activation energy barriers, showing that the site coordination can affect the catalytic activity of a surface [79]. More specifically, for Pt(111) Pt(100), and Pt(211) surfaces, the computed values of the water dissociation activation energies were smaller than the water adsorption energies, while Pt(110) and Pt(321) surfaces presented lower activation energies, indicating the importance of low coordinated adsorption sites for this reaction.

These studies help to illustrate the importance of the nanoparticle structure on heterogeneous catalysis research, with the presence of stepped and kinked adsorption sites causing significant changes in the catalyst activity. As the ratio between different adsorption sites also depends on the nanoparticle size, controlling this variable is also relevant when dealing with metallic nanoparticles. For example, similar studies on the water dissociation were also carried out for Pt nanoparticles ranging from Pt_{13} to Pt_{140} [81]. The results from the calculations show negligible variations on the adsorption energies of water molecules for different nanoparticle sizes, with a clear adsorption preference at low coordinated top sites. On the other hand, the activation energies increase with the nanoparticle size towards the value obtained for Pt(111) extended surface. Similarly to what was observed for Pt(111) slabs, for larger nanoparticles, the absolute values of reaction barriers were larger or equal to that obtained for water adsorption energies, while water dissociation was favourable for smaller nanoparticles.

The size of the nanoparticle is also found to be relevant for reactions such as the EOR and ORR, with both experimental and theoretical studies pointing to strong size dependence in the catalytic properties of platinum clusters and nanoparticles with a diameter between 1 and 3 nm. For the EOR, Perez *et al.* [134] observed an activity peak obtained for Pt nanoparticles of 2.6 nm. The authors pointed that possible explanations for the increase in activity with decreasing nanoparticle size were involved with the increase in the concentration of low-coordinated sites, which could facilitate the dissociative adsorption of ethanol and increase the OH presence in the surface to act as a promoter for the reaction. At the same time, for nanoparticles smaller than 2.6 nm, the increase in adsorbed OH could block sites to adsorb ethanol. Meanwhile, for the ORR, Pt nanoparticles with a diameter between 2 and 2.5 nm have been indicated as optimum catalysts sizes [135–139]. Nevertheless, some recent experimental work [140–142] have been able to show promising results using metallic subnanoclusters ($\leq$ 1nm) as catalysts, with high surface

areas, good CO tolerance and high catalytic activity depending on the Pt cluster structure.

One advantage of computationally studying metallic nanoparticles is the ability to isolate the impact of the nanoparticle size, shape and composition more easily than with experimental studies. To a certain extent, it is possible to assess how each change in the nanoparticle affects the geometric and electronic properties and consequently, the catalytic activity, and how the interplay between those effects take place. The studies from Nørskov and coworkers [6, 143, 144] on the effects of nanoparticle size for O and CO adsorption, which are important descriptors for catalytic activity, on Au_n and Pt_n cuboctahedra nanoparticles with $13 \leq n \leq 1415$, are examples of size effects studies performed with DFT calculations. The authors simulated a single adsorbate interacting with cuboctahedral nanoparticles of increasing size on similar adsorption sites. They have calculated the adsorption energies on geometry optimised and non-optimised metallic nanoparticles, allowing to separate some of the electronic and geometric effects caused by changing the nanoparticle size.

The authors demonstrated that the adsorption energies on metallic nanoparticles converge to the slab value for Pt nanoparticles with more than 147 atoms and gold nanoparticles larger than 561 atoms [6, 143, 144]. They have observed that for nanoparticles smaller than a certain size, the adsorbate interacts indirectly with atoms in the vertices and edges of the nanoparticles. Platinum nanoparticles screened this effect better than gold, justifying its quicker convergence to slab values. Moreover, they have observed that the modifications in the metallic bond lengths due to the change in the nanoparticle size are not as important to control the adsorption energies as the changes in the adsorption sites coordination and the electronic effects. They also observed that the changes in the bond lengths are more relevant for FCC (111) adsorption sites than for edge (211) and that this effect can be reproduced on calculations for stressed slabs [6].

Figure 3.4 shows that, as an overall trend, the decrease of the nanoparticle size increases the adsorbate binding strength. However, as the nanoparticle size reduces, the metallic bond lengths decrease, which, according to the d-band model, generates a downshift in the d-band centre that should create a weakening in the adsorption energies. This result can be observed by comparing in figure 3.4 the results for relaxed and unrelaxed nanoparticles. Thus, there is a competition between the electronic and geometric changes induced in the nanoparticle caused by the size effects. A clear exception to the size effect trend is the Au_{55} nanoparticle, which binds oxygen weaker than larger Au nanoparticles. The authors explain this effect as a consequence of the electronic shell effects. As 58 electrons is an electronic closed shell, the acceptance of electrons should be easier for Au_{55} nanoparticle, but the donation should be more difficult,

interfering with the interaction between the nanoparticle surface and these adsorbates.

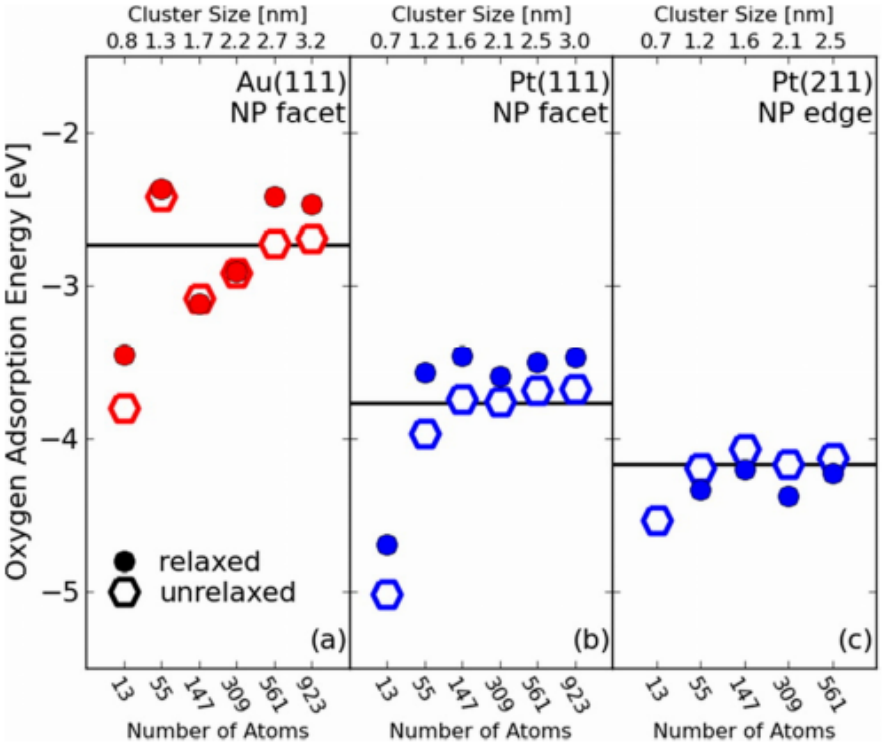

FIGURE 3.4: Atomic oxygen adsorption energies for relaxed (filled circles) and unrelaxed (hollow hexagons) Pt and Au nanoparticles and surface slabs (horizontal lines). Results for Figure a) and b) were calculated on FCC adsorption sites, while c) uses edge adsorption sites. Figure reprinted with permission from 6. Copyright 2015, American Chemical Society.

In the literature, the size effects are also computationally studied with other types of adsorbates. For example, despite the problems faced to correctly predict with DFT the CO adsorption on certain metallic surfaces [145], CO is another adsorbate commonly used to assess properties of metallic catalysts. CO is an important intermediate for some reactions and a molecule that can hinder the catalytic activity by blocking active sites due to the strong adsorption in the surface for other reactions.

In terms of size effects, Rösch and coworkers [146–149] carried out a series of studies about the CO adsorption on Pt and Pd nanoparticles of increasing size. They have observed two intersecting trends for the adsorption energies as a function of the number of Pt and Pd atoms in the nanoparticles [148, 149]. Up to a certain size, which was indicated to be around 200 atoms for Pt and 50 atoms for Pd nanoparticles, the increase in the number of atoms of the nanoparticle weakens the CO adsorption energies, which was associated to shifts of the surface's d-band centre as a consequence of changes in the ratio between atoms with lower and higher coordination. This trend was obtained for small nanoparticles. However, in this size

range, the authors also observed strong variations in the adsorption energies due to the non-scalable behaviour associated with significant changes in geometries of clusters with different sizes. Above the critical size, the CO adsorption energies showed an opposite trend, with the increase in the nanoparticle size leading to stronger adsorption energies, which was explained based on the expansion of the atomic distances in the metallic nanoparticle facet [148, 149].

Another example of size effects studied with DFT calculations is the work carried out by Jiang *et al.* [7], which assessed the catalytic activity of M_{12}, M_{55} clusters and closed-packed, stepped and kinked surfaces for the catalytic oxidation of CO. The calculations tested scaling relationships between adsorbates and BEP relations and were used as parameters for a microkinetic model. Figure 3.5 shows the catalytic activity calculated with the microkinetic model as a function of the O and CO binding strength for two different temperatures, where red (blue) colours represent higher (lower) activities.

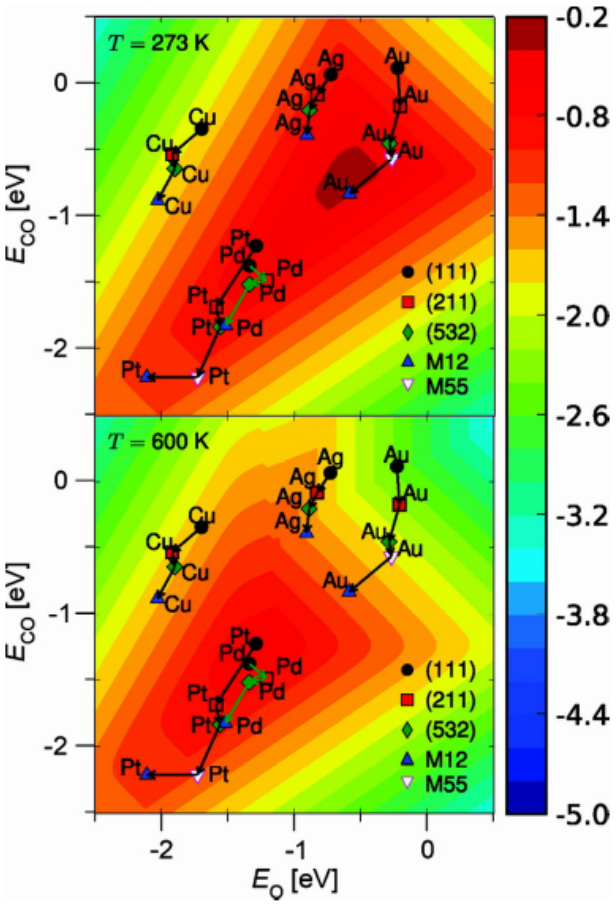

FIGURE 3.5: Contour plot of the catalytic activity with two different temperatures as a function of the CO and O adsorption energies, where red (blue) colors represent higher (lower) activities. The results were obtained for (111) (black), (211) (red), (532) (green) surfaces and for M_{12} (blue) and M_{55} (magenta) clusters. Figure reprinted with permission from 7. Copyright 2009, American Chemical Society.

Figure 3.5 shows that the calculated rate of CO oxidation is also structure and size dependent. For gold and silver catalysts, the metallic clusters have higher catalytic activity followed by stepped and kinked surfaces, with the activity increasing with decreasing cluster size. For Pt and Pd catalysts the trend was the opposite. At low temperatures, small Au clusters had the highest activity rates, while for higher temperatures Pt and Pd were more active. These effects happened due to the difference in the bonding strength of different clusters and as a consequence of changing the coordination number of the active sites.

This high dependence of the adsorption energies and, consequently, the catalytic activity of nanoparticles on the surface geometry makes the usage of idealised structures another point that needs to be carefully assessed when comparing theoretical and experimental data. As discussed before, computationally defining stable nanoparticle and clusters to study heterogeneous catalysis can be a challenging task and, even if the global minima is found, it is not easy to state that the nanoparticle will be similar to that used in reaction conditions. Recently, Aarons *et al.* [8] showed with a combined theoretical and experimental work, how the morphological differences from nanoparticle models and commercial catalysts could affect the description of the catalytic activity. They have introduced a method to construct models of Pt nanoparticles from high-resolution annular dark-field scanning transmission electron microscopy (ADF-STEM) data, using the image intensities to determine the number of atoms for each atomic column in the 2D projection of the nanoparticles. These geometries were further refined with genetic algorithm and geometry relaxations with an empirical force field.

The authors have calculated O adsorption energies on different adsorption sites for Pt nanoparticles and a Pt(111) slab using DFT calculations and used these results to parametrise the O adsorption dependence on the generalised coordination numbers. They have computed the generalised coordination number distribution for the experimental nanoparticles and cuboctahedra, quasi-spherical and truncated octahedra models with different sizes and, using the parametrisation of adsorption energies versus the generalised coordination number, compared the distribution of "optimum" adsorption sites for each nanoparticle model. Figure 3.6 shows the evolution with the nanoparticle size of the fraction of adsorption sites within a maximum difference of 0.2 eV from the optimum O adsorption energy for the ORR.

By exploring the Sabatier's principle and the generalised coordination number, Aarons *et al.* have managed to evaluate large Pt nanoparticle structures obtained from experimental data without explicit DFT calculations [8]. They have observed that the experimental nanoparticles have rougher surfaces than the truncated octahedra nanoparticles, which helps to increase the

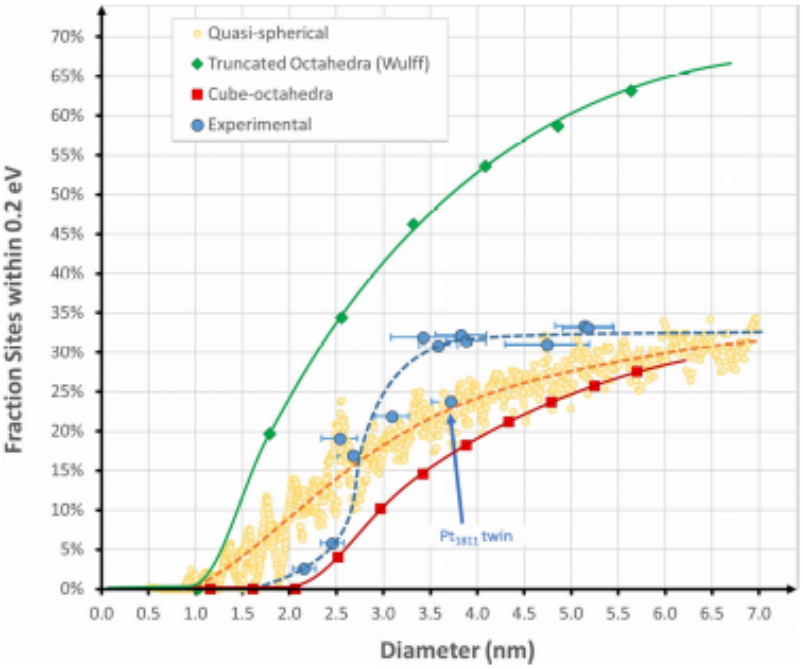

FIGURE 3.6: Fraction of adsorption sites with oxygen binding strength with a maximum difference of 0.2 eV to the optimum ORR binding strength as a function of the nanoparticle size. The oxygen binding strengths were calculated by the linear correlation between O adsorption and $\overline{CN}$ for experimentally observed nanoparticles (blue), truncated octahedra (green), cube-octahedra (red), and quasi-spherical (yellow) idealised nanoparticle models. Figure reprinted with permission from 8. Copyright 2017, American Chemical Society.

number of adsorption sites with stronger O-binding and reduces the fraction of adsorption sites with optimum activity. In general, the study provides insights for the size and shape dependence for ORR and for the differences between experimental and theoretical data, which can be taken into account when comparing both results.

3.3.3 Support Effects

Up to now, we have illustrated how the nanoparticle size, shape and composition can control the catalyst performance. The nanoparticles are usually dispersed over support materials that can participate in the chemical reaction directly or by modifying the nanoparticle electronic and geometric properties. The last effect is directly related to the nanoparticle-support interaction, which depends on characteristics of the nanoparticle, such as size, shape and composition and properties of the support. Controlling this interaction is also essential for catalyst design to avoid nanoparticle sintering, helping to maintain the nanoparticle size and the durability of the catalyst over time.

In addition to a metal-support interaction that improves properties of the catalyst towards a specific reaction, the support also has to possess a surface area large enough to allow for

nanoparticle dispersion and present properties such as high electrical conductivity and stability in the reaction conditions that it would be used. Metal oxides, metal carbides, and carbon-based supports are commonly studied for state-of-the-art catalysts for different reactions taking place at the anode and cathode of fuel cells. Each support has advantages and disadvantages and will interact with each nanoparticle differently, allowing an extra variable that can be used to tune a catalyst for a specific reaction. As the support is supposed to affect the nanoparticle geometric and electronic properties and to participate directly and indirectly in the chemical reaction, DFT calculations on the support-nanoparticle interaction and how it changes with the size and composition of the nanoparticle can be extremely useful to explore new catalysts.

For example, Daio *et al.* [150] compared the interaction of Pt clusters with a graphene support and a $SnO_2(100)$ support, showing that the interaction between the metal oxide support and the Pt nanoparticle is much stronger than the one obtained when graphene is used as the support. As a consequence, the bond length strains in the nanoparticle that were induced by the interaction with $SnO_2(100)$ were almost 80% larger than the ones generated by the interaction with graphene. The authors have also calculated activation barriers for an oxygen molecule dissociation on a relaxed and on a strained platinum slab designed to mimic the effect of the support. They have observed a reduction of the activation barriers from 0.52 eV to 0.39 eV as an effect of the Pt lattice strain, helping to strengthen the idea that is possible to control the catalytic properties of a catalyst by using the support effects.

This strong interaction between Pt nanoparticle and SnO_2 was also observed experimentally. For example, in experimental comparisons, it was observed that the SnO_2 supported Pt nanoparticles could achieve similar catalytic activities for the ORR as the commercial Pt/C ones, with the Pt/SnO_2 catalyst being much superior to the Pt/C in terms of catalyst durability. The improved durability of the catalysts made from SnO_2 supported nanoparticles was ascribed to the increases in the nanoparticle size after catalytic tests observed for the Pt/C system that was considerably larger than the ones observed for Pt/SnO_2 [151], which can be correlated with the theoretical studies pointing to stronger metal-support interactions for such systems [150].

The study of Pt_{55} nanoparticles on α-Al_2O_3 (0001), rutile SnO_2 (100), monoclinic ZrO_2 (111), and rutile TiO_2 (100) surfaces [152] is another example of DFT calculations applied to investigate support effects. The authors have observed that the density of states of the Pt cluster becomes more continuous after the interaction, that the Pt_{55} structure deforms due to the interaction with the metal oxide surface, and that the charges in Pt atoms in the surface changes with atoms gaining and losing electrons depending on their positions in relation to

the support. Moreover, the authors have also calculated the O binding strength on different adsorption sites of the supported Pt_{55} clusters [152]. They have observed that the adsorption energies for nanoparticles supported on ZrO_2 and TiO_2 are similar to the unsupported result when comparing only bridge sites, while for α-Al_2O_3 and SnO_2 supports the adsorption energies are stronger than the unsupported case for the adsorption sites near support. The large difference in the adsorption energies for similar adsorption sites depending on the proximity of the support indicates that the kinetics of chemical reactions can be drastically different for the top of the nanoparticle and near the nanoparticle/support interface.

Metal-oxides, metal-nitrides and metal-carbides supports were also studied via DFT calculations as possible corrosion-resistant supports for Pt deposition for catalysis applications. Xia *et al.* [153] calculated the interaction between platinum layers and several materials that are commonly studied as supports, including rutile MO_2(M = Ti, Ru, Ir), modified TiO_2 surfaces and TiX (X= O, N, C) structures. They have observed a favourable formation of a Pt skin for low coverages of Pt on rutile supports and a strong tendency of Pt to stay in subsurface sites for TiN and TiC supports. Moreover, they have demonstrated that surface modifications to the supports, such as metal doping or reductions, enhance the Pt wetting of the support, which could help the Pt films to be more stable over the support and avoid the formation of large Pt nanoparticles. The authors have also observed a convergence of density of states patterns with increasing overlayer thickness, showing a screening effect from the Pt layers to the electronic modifications induced by the support.

Xia *et al.* [154] also studied how different supports could change the adsorption energies of atomic oxygen on Pt slab models with 4 Pt overlayers supported on different substrates. They have observed changes in the oxygen adsorption energies and d-band centre shifts of the exposed Pt film as a consequence of lattice strains caused by the mismatch between the support and the Pt structures. The changes in the oxygen adsorption energies have demonstrated that the support can help to control the Pt growth and consequently influence the catalytic properties of the catalytic material. Through the oxygen adsorption energies and the calculations to assess the wetting ability of the surfaces, the authors have indicated metal-carbides such as TiC and WC as well as TiO as promising supporting materials for Pt deposition for applications in fuel cells as catalysts for the oxygen reduction reaction.

Other materials such as graphene, graphite, carbon nanotubes and carbon black are examples of carbon-based supports that are also commonly used on fuel cells applications. For

instance, graphene has a large surface area, high electrical conductivity and is thermally stable, but defect-free graphene is known to interact weakly with Pt nanoparticles which could lead to nanoparticle agglomeration [155–157]. DFT calculations performed to study the metal-graphene interaction have also been showing the weak interaction of pristine graphene with metallic clusters and the importance of dispersion interactions to models these systems [150, 158–161]. In addition to graphene, DFT have also been employed to study other types of carbon-based supports such as graphite [162, 163] and carbon nanotubes [164] interacting with metallic clusters and nanoparticles, showing similar results concerning the weak metal-support interactions, the importance of the dispersion interactions, and changes in the geometries and electronic properties of the metallic nanoparticles comparable to results obtained with graphene.

Several DFT studies have been performed to also suggest and understand ways of increasing the nanoparticle-support interaction such as including point defects or doping the support [150, 158–161, 164–166]. For instance, computational results show that point defects can act as binding sites for Pt clusters and nanoparticles, significantly increasing their interaction and being able to tune the nanoparticle properties towards specific reactions [159–161, 165].

Similarly, in situ transmission electron microscopy (TEM) analysis performed on Pt nanoparticles dispersed over few-layer graphene supports have demonstrated the importance of defects and oxygenated functional groups to stabilize the Pt nanoparticles [167]. For example, the observed density of Pt nanoparticles was superior near the edges of the support, where more defects and functional groups could be found, than in the flat surfaces [167]. Moreover, when comparing the average size of the Pt nanoparticles supported on few-layer graphene and carbon nanotubes obtained with the same method, they have observed that the few-layer graphene presented nanoparticles that were five times smaller than the ones found on carbon nanotubes [167].

Thus, the inherent characteristics of graphene and the ability to tune the metal-support interaction with defects and functionalization of the support make nanoparticles supported on graphene-based materials a promising class of catalysts. For example, it is possible to find in the literature examples of graphene-supported Pt-based [168] and Pd-based [169] nanoparticles synthesized and applied as catalysts for the ethanol oxidation reaction. The measurements for Pt supported nanoparticles show an increase in the catalytic activity of graphene-supported Pt as compared with graphite and carbon black supports [168]. Moreover, for Pd-based nanoparticles, the comparison of Pd nanoparticles supported on graphene-oxide and Pd/C commercial catalysts, have demonstrated that the graphene-oxide support increases the activity and stability

of the catalyst for EOR under alkaline media [169].

From the examples presented in this chapter, it is clear how challenging it can be to rationally design an optimise catalyst for a chemical reaction. The multi-variable character of the search and the fact that each variable such as size, shape, composition, reaction environment, support can affect and be affected by each other increase the number of options for improving catalysts and, at the same time, the complexity of the field. Thus, we understand that further investigations on how the interplay of such effects changes the catalyst surfaces of metallic nanoparticles could be extremely helpful to build additional knowledge that can lead to advances in the design of new catalysts.

Chapter 4

Atom and Angular Momentum Projected Density of States in ONETEP

This chapter describes the theoretical framework used in the implementation of an atom-projected and angular momentum projected density of states (l-p-DOS) in the ONETEP code. The l-p-DOS is an important tool for obtaining electronic descriptors and will be used throughout this thesis. This work is also described in a manuscript in preparation that should be submitted at some point before or after the examination of this thesis:

L. G. Verga, J. Aarons, N. Hine and C.-K. Skylaris. Atom-projected and angular momentum resolved density of states in the ONETEP code, manuscript in preparation, 2019.

in which, my participation was developing and analysing the tests for the method, writing the manuscript and helping with the debugging of the code and with a small part of the code development. The majority of the code was developed by Dr. Jolyon Aarons, which also helped to write the section about the formalism of l-p-DOS in ONETEP. Dr. Nicholas Hine and Prof. Chris-Kriton Skylaris supervised the work and participated in the corrections of the manuscript.

Abstract

Local and angular momentum projected density of states (l-p-DOS) are invaluable sources

of information that can be obtained from density functional theory calculations. We describe a theoretical framework within ONETEP's linear-scaling DFT formalism that allows the calculation of local (atom-projected) and angular momentum projected density of states. We describe four different bases that can be used for projecting the DOS with angular momentum resolution and perform a set of tests to compare them. We validate the results obtained with ONETEP's l-p-DOS against the plane-wave DFT code CASTEP. Comparable results between ONETEP's and CASTEP's charge spilling parameters are observed when we use pseudo-atomic orbitals as the projection basis set. In general, the charge spilling parameters show remarkably low values for projections using non-contracted spherical waves as the angular momentum resolved basis. We also calculate the d-band and d-band centres for Pt atoms in (111) facets of cuboctahedral Pt nanoparticles of increasing size, which is an example of l-p-DOS application commonly used as an electronic descriptor in heterogeneous catalysis and which will be used throughout this thesis. Interestingly, the different projection bases lead to similar conclusions, showing the reliability of the implemented method for such studies. The implementation of this method in a linear-scaling framework such as ONETEP provides another tool for analysing the electronic structure of complex nanostructured materials.

4.1 Projected Density of States

As discussed in chapter 2, DFT calculations have been playing an important role in scientific development over the last decades. The applicability of DFT to so many different areas has motivated the development of different formalisms and implementations of DFT to provide users with computationally efficient codes for different systems. One of the first considerations one has to make when choosing an appropriate DFT code to study a specific system is the basis set used to represent the single particle wave functions. For some cases, using functions that are not atomic-like orbitals can be more computationally efficient to describe the system and solve the Kohn-Sham equations. A good example is the widely used plane wave DFT formalism, where the basis set that can be improved systematically, being extremely efficient to deal with periodic and extended systems.

However, atom-like basis sets are necessary to calculate certain properties of the electronic structure, and projection schemes are often required to allow the calculation of the desired quantity. The pioneer work from Sanchez-Portal [170, 171] is a good example of such projections schemes, where the eigenfunctions obtained with a plane wave DFT code were projected

onto localised atomic-like-orbitals, which allowed local quantities such as atomic charges or local density of states to be computed. Additionally to built-in functionalities in many plane-wave DFT codes, projection schemes can also be found in post-processing codes, such as LOBSTER [172], which uses the projection to compute several local properties.

The local (atom projected) density of states (l-DOS) and the angular momentum projected density of states (p-DOS) are useful tools to obtain information and insights for relevant applications. In the field of heterogeneous catalysis, the density of states projected onto the d-band of metallic surfaces is widely used to obtain electronic descriptors such as the d-band centres presented in chapter 3. In the following chapters of this thesis, we use local and angular momentum projected density of states (l-p-DOS) to support our analysis on isolated and supported Pt nanoparticles. Here, we explain the idea behind the l-p-DOS implementation in ONETEP and we present our choices for angular momentum resolved bases. We show test cases for general use and test cases focused on metallic nanoparticles, comparing different angular momentum resolved basis sets used to construct the l-p-DOS and comparing the results obtained with ONETEP to similar calculations from the CASTEP plane-wave code [44].

4.2 Projected Density of States in ONETEP

The density of states (DOS) is a function of the energy, ε, that can be defined as:

$$\rho(\varepsilon) = \sum_i \langle \psi_i \,|\, \psi_i \rangle \, \delta(\varepsilon - \varepsilon_i), \tag{4.1}$$

In the ONETEP formalism, we can express this in terms of NGWFs as

$$\rho(\varepsilon) = \sum_i M_i^{\dagger\alpha} \left\langle \phi_\alpha \,\middle|\, \phi_\beta \right\rangle M^\beta_{\ i} \, \delta(\varepsilon - \varepsilon_i), \tag{4.2}$$

Thus, to construct an angular momentum projected density of states from ONETEP's NGWFs, we first need to define an angular momentum resolved basis, project the eigenfunctions obtained with the NGWFs to this representation and construct a weights matrix that allows summation over particular angular momentum and atoms to decompose the total DOS. In the following sections, we show the possible choices of angular momentum resolved basis and the methodology used to construct l-p-DOS implemented in ONETEP.

4.2.1 Choice of Angular Momentum Resolved Basis

The angular momentum resolved basis functions are constructed having the form of spherical harmonics, $Z_{l,m}(\Omega)$ multiplied by a radial part, where Ω stands for the angular dependence (solid angle). The form of the radial part is where we have some flexibility. Provided we choose functions which capture enough of the NGWF character with a small spilling parameter and a small number of basis functions in the set, the set will be considered adequate. The definition of a "small" spilling parameter and the number of basis functions considered to be too many or too few is arbitrary and will be explored from now on.

We have explored four options of the angular momentum resolved basis, where three of them are based on Spherical Waves (SW) basis sets. Firstly, we have a non-contracted, full set of SWs; a contracted set with unity contraction weights (C-SWs), a contracted set with contraction weights defined through an inner product with each NGWF, our so-called fitted set (CF-SWs); and finally a set of pseudo-atomic orbitals (PAOs) which is the only set not based on SWs. The pseudo-atomic orbitals are used as an initialisation scheme for the optimised NGWFs, so may represent a low spilling option for the projection of the NGWFs.

We choose the Spherical Wave (SW) basis as an option for our functions so that we can tune the size of the basis systematically to reduce the amount of spilling to the appropriate levels for the application of each calculation. As listed before, this leaves us with some choice, however, in how (or if) we choose to contract the basis functions. Contraction is desirable mainly because our SW basis is not only resolved in the azimuthal quantum number, l, giving the desired angular momentum resolution, but also in magnetic quantum number m and implicitly in the principal quantum number, through the Bessel functions, j_l. The number of basis functions in this set may be prohibitive for practical calculations, and we can contract over m and j_l.

The spherical waves are generated on the same equispaced grid as we use for NGWFs and are defined as

$$\chi_{Ak_{nl}lm}(\vec{r}) = j_l(k_{nl}r)Z_{l,m}(\Omega)H(a-r), \tag{4.3}$$

where H is a Heaviside step function which cuts off any contribution to the spherical waves outside of a radius, a.

Contracted Spherical Waves (C-SWs) are defined in terms of the SWs as

$$\chi_{Alm}(\vec{r}) = \sum_{k_{nl}} \omega_{Ak_{nl}lm}\chi_{Ak_{nl}lm}(\vec{r}), \tag{4.4}$$

where $\omega_{Ak_{nl}lm}$ are the contraction coefficients which for C-SWs are set to 1.

The contraction coefficients can also be set to fit the NGWFs, generating a set of angular momentum resolved functions that we call Contracted and Fitted Spherical Waves (CF-SWs). However, in the case that we fit to the NGWFs, we instead take a set of l and m_l CF-SWs on every NGWF of every atom, rather than one set per atom. This typically increases the size of the spherical wave basis by a factor of 4 for atoms up to (and including) the third row of the periodic table and up 13 for heavy transition metal atoms. In this case, the CF-SWs are defined as

$$\chi_{\alpha lm}(\vec{r}) = \sum_{k_{nl}} \omega_{\alpha k_{nl} lm} \chi_{Ak_{nl}lm}(\vec{r}), \tag{4.5}$$

where contraction coefficients $\omega_{\alpha k_{nl}lm}$ which best fit the NGWF ϕ_α can be calculated by taking the inner product of each NGWF with each SW on the same center:

$$\omega_{\alpha k_{nl}lm} = \langle \phi_\alpha \,|\, \chi_{Ak_{nl}lm} \rangle \,. \tag{4.6}$$

It is possible in this approach that contraction coefficients on an NGWF sum to zero, which will lead to a non-positive definite overlap matrix, if left untreated. One approach to overcome this problem would be to remove this CF-SW from the set, but instead we opt to leave it in place, recording its index and dealing with it in the resolution of identity, as we explain in the next section.

Another option that we have is to use pseudoatomic orbitals (PAOs) as our angular momentum resolved basis. PAOs are solutions to the atomic Kohn-Sham equation and have the form:

$$\varphi_n(\mathbf{r}) = \sum_\nu c_{n,\nu} B_{l_n,\nu}(r) Z_{l_n m_n}(\Omega), \tag{4.7}$$

where $c_{n,\nu}$ are a set of coefficients obtained by solving the Kohn-Sham equation for each atom species with spherical localisation constraints using the same cutoff radius as the one used for the NGWFs. Since the PAOs are used for the initialisation of NGWFs [173], to also use them as the angular momentum resolved basis requires no extra calculations associated with the generation of the set. The number of PAOs per atom, N, is the same as the number of NGWFs, typically a number associated with subshell-filling (i.e. 1,4,9,13,...).

4.2.2 Resolution of Identity and Construction of the Projected DOS

Once we have chosen an angular momentum resolved basis and constructed it, we can then construct an identity operator. This can be expressed in terms of the functions and inverse overlap as

$$\hat{1} = |\chi_{\alpha lm}\rangle \Lambda^{\alpha lm,\beta l'm'} \left\langle \chi'_{\beta l'm'} \right|, \tag{4.8}$$

which for a good enough set of $\chi_{\alpha lm}$,

$$\langle \phi_\alpha | \hat{1} | \phi_\beta \rangle \approx \langle \phi_\alpha | \phi_\beta \rangle. \tag{4.9}$$

Inserting this identity operator into the expression for the density of states from equation 4.2, we get the expression

$$\rho(\varepsilon) \approx \sum_i M_i^{\dagger\alpha} \langle \phi_\alpha | \chi_{\alpha lm} \rangle \Lambda^{\alpha lm,\beta l'm'} \left\langle \chi'_{\beta l'm'} \right| \phi_\beta \rangle M^\beta{}_i \, \delta(\varepsilon - \varepsilon_i), \tag{4.10}$$

Defining the DOS in terms of this identity operator allows us to exploit the angular momentum dependence of $|\chi_{\alpha lm}\rangle$, by selectively summing over particular angular momentum components l and m to create angular momentum projected DOS.

To calculate the angular momentum projected density of states, we firstly rewrite equation 4.10 in terms of a weights matrix, $W_{\alpha lm,i}$:

$$\rho(\varepsilon) = \sum_{\alpha,l,m,i} W_{(\alpha,l,m),i} \delta(\varepsilon - \varepsilon_i), \tag{4.11}$$

where $W_{\alpha lm_l,i}$ is defined to be the Hadamard product of two matrices defined as a left and a right part of the identity matrix expression in equation 4.10, such that

$$W_{\alpha lm,i} = R^{\alpha lm}{}_i \circ T_{\alpha lm,i} \tag{4.12}$$

and under the condition that

$$\sum_{\alpha lm} W_{\alpha lm,i} = M_i^{\dagger\alpha} \langle \phi_\alpha | \chi'_{\alpha lm} \rangle \Lambda^{\alpha lm,\beta l'm'} \left\langle \chi'_{\beta l'm'} \right| \phi_\beta \rangle M^\beta{}_i. \tag{4.13}$$

The effect is to change the order of operations with respect to equation 4.10, so that instead of producing an element in the identity matrix by multiplying each element of a row in

the $\mathbf{R}^T$ matrix by each element of a column in the $\mathbf{T}$ matrix and summing all products in the row and column pair, we instead construct an element in the $\mathbf{W}$ matrix by taking the elementwise product of $\mathbf{R}$ and $\mathbf{T}$ and summing over the elements in the columns of $\mathbf{W}$. This allows for the final sums to be taken over restricted sets of indices, as we require.

For instance, the angular momentum projected density of states can be written as

$$\rho_l(\varepsilon) = \sum_{\alpha m,i} W_{\alpha lm,i}\delta(\varepsilon - \varepsilon_i), \tag{4.14}$$

or the local angular momentum projected density of states can be written as

$$\rho_{\mathscr{S},l}(\varepsilon) = \sum_{\alpha(\mathscr{S}),m,i} W_{\alpha lm,i}\delta(\varepsilon - \varepsilon_i), \tag{4.15}$$

where $\alpha(\mathscr{S})$ means the subset of α centered on the set of atoms, $\mathscr{S}$.

Finally, the ${R^{\alpha lm}}_i$ and $T_{\alpha lm,i}$ matrices can be defined in many ways. In our implementation, we have decided to define the matrices using a symmetric decomposition achieved by taking the Löwdin decomposition of $\Lambda^{\alpha lm,\beta l'm'}$, which can be expressed in terms of its eigenpairs,

$$\mathbf{\Lambda Q} = \lambda \mathbf{Q}, \tag{4.16}$$

as:

$$\mathbf{\Lambda}^{\frac{1}{2}} = \mathbf{Q}\lambda^{\frac{1}{2}}\mathbf{Q}^T, \tag{4.17}$$

where $\mathbf{Q}$ is the matrix of eigenvectors of $\mathbf{\Lambda}$ and $\lambda^{\frac{1}{2}}$ is the diagonal matrix of square-rooted eigenvalues of $\mathbf{\Lambda}$.

The $\mathbf{T}$ matrix in the symmetric decomposition may then be expressed as

$$T_{\alpha lm,i} = \left(\mathbf{\Lambda}^{\frac{1}{2}}\right)_{\alpha lm}^{\beta l'm'} \left\langle \chi'_{\beta l'm'} \middle| \phi_\beta \right\rangle {M^\beta}_i, \tag{4.18}$$

where $T_{\alpha lm,i}$ has invariant indices in this case, and $W_{\alpha lm,i}$ from Eq.4.12 can be defined as its elementwise square

$$W_{\alpha lm,i} = T^2_{\alpha lm,i}. \tag{4.19}$$

For all the implemented angular momentum resolved basis, we can define the spilling parameter s, as

$$s = \sum_i^{N_{MO}} \left\{ 1 - \sum_{\alpha lm} W_{\alpha lm,i} \right\} / N_{\mathrm{MO}}, \tag{4.20}$$

this helps to quantify how good the angular momentum projected basis is in terms of the accuracy of the identity operator. We will use the spilling parameter later in the paper to assess the quality of our sets.

The problem of having basis functions with zero weight leading to eigenvalues of zeros in the C-SW overlap matrix, discussed in section 4.2.1 may be dealt with by not inverting $\Lambda_{\alpha lm_l,\beta l'm'}$ to form $\Lambda^{\alpha lm,\beta l'm'}$ or $\left(\mathbf{\Lambda}^{\frac{1}{2}}\right)^{\alpha lm,\beta l'm'}$, but instead by taking its eigenvalue decomposition

$$\mathbf{\Lambda}^{-\frac{1}{2}} = \mathbf{Q} f(\lambda) \mathbf{Q}^T, \qquad f(\lambda) = \begin{cases} 0 & \lambda < 0 \\ \lambda^{-\frac{1}{2}} & \lambda >= 0 \end{cases}, \tag{4.21}$$

which is equivalent to dropping basis functions which lead to non-positive definite overlap matrices. This operation requires a diagonalisation, however, if we need to avoid this, we can drop basis functions with zero weights and use an iterative inversion or Löwdin algorithm.

The projected weights allows us to construct various types of DOS. For example, to construct the DOS for the p electrons of a subset of atoms, we can add up all the weights for $l' = 1$ and restrict the summation to the select atoms.

Up to now, the expressions were derived for the case of norm-conserving pseudopotentials. In the case of PAW calculations, equation 4.1 becomes

$$\rho(\varepsilon) = \sum_i \langle \tilde{\psi}_i | \hat{\tau}^\dagger \hat{\tau} | \tilde{\psi}_i \rangle \delta(\varepsilon - \varepsilon_i), \tag{4.22}$$

where $\hat{\tau}$ is the PAW operator and $\tilde{\psi}_i$ are the smooth valence wavefunctions and the derivation of the l-p-DOS will follows the same ideas.

4.3 Calculation Details

We performed our simulations with the ONETEP [28] and CASTEP [44] codes. For metallic systems in ONETEP, we used the ensemble DFT method, as implemented by Serrano and Skylaris [2]. For all calculations, we adopted PBE [21] as our exchange-correlation functional. The ONETEP calculations were conducted using the projector augmented wave (PAW) method [24], as implemented in ONETEP by Hine [174] while in CASTEP the calculations were conducted with ultrasoft pseudopotentials[175]. For all the calculations, we have used the GBRV library for ultrasoft and PAW potentials [176]. We have used the OptaDOS [177] code to post-process the results from CASTEP calculations and obtain the l-p-DOS data, and used the mid-gap level from ONETEP calculations as zero for all l-p-DOS plots.

In ONETEP, we set the psinc basis set [33] kinetic energy cutoff to 550 eV for geometry optimisations and 850 eV for properties calculations, with the NGWFs radii set to be 9.0 a_0. For CASTEP, the kinetic energy cutoff was equal to 450 eV. We performed our simulations under periodic boundary conditions, with a minimum vacuum gap of 10 Å between the borders of the simulation box and any simulated atom. The structures used to compute the projected density of states were optimised in ONETEP, where the geometries were relaxed with a convergence threshold of 0.002 Ha/a_0 on the atomic forces. The only exceptions are the Pt slabs and nanoparticles. For these cases, the structures were constructed with bond lengths from the optimised Pt bulk geometry. For all the calculations, the SWs, C-SWs, and CF-SWs were created using a total of 16 functions per magnetic quantum number m per atom.

4.4 Demonstration of the Method

We start the demonstration of the method by showing in figure 4.1 the total and the projected density of states for an O atom on a singlet state and a CO molecule using the non-contracted SWs projection basis. For the O atom, it is simple to observe that the density of states was successfully projected to s and p orbitals. For the CO molecule, the total DOS shows the existence of four peaks, representing the occupied molecular orbitals formed by the valence electrons. The last and the first two peaks represent σ orbitals formed by hybridised sp orbitals and are described in our angular momentum projected density of states as a sum of s and p contributions. The third peak is two times more intense, as it represents two degenerate π molecular orbitals which are, fully projected as a p band, illustrating the results we can obtain with the implementation of the angular momentum projected density of states.

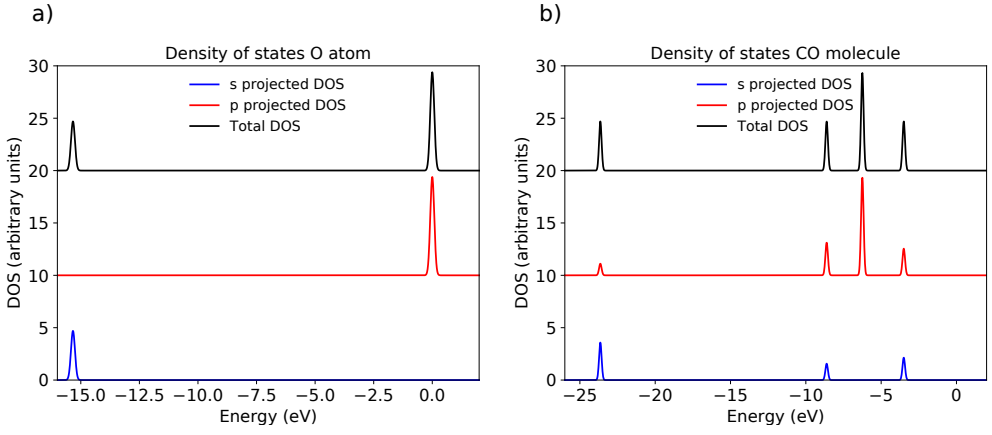

FIGURE 4.1: Total and projected density of states for a) an O atom in a singlet state and b) a CO molecule. Blue and red plots represent s and p bands, while black curves are obtained with the total DOS.

For a more rigorous testing of the methods, we have calculated a reformulation of the spilling paramenter presented before in equation 4.20, which measures the ability of the basis to represent the calculated states. Here, we aim to compare our bases against CASTEP's charge spilling parameter, which is obtained by restraining the spilling parameter calculation to the occupied bands [171]. In a general form, to also deal with fractional occupancies, we can write the charge spilling parameter as

$$s_q = 1 - \left\{ \sum_i \sum_{\alpha lm} f_i W_{\alpha lm,i} / \sum_i f_i \right\}, \tag{4.23}$$

where f_i are the occupancies and $W_{\alpha lm,i}$ the weights matrix as defined in equation 4.13.

To compare the angular momentum resolved bases, we present in table 4.1 the charge spilling parameter for different systems. We have calculated the l-p-DOS for a CO molecule, a set of hydrocarbons, a silane molecule, a $LiPF_6$ compound in the C_{4v} symmetry, a set of cuboctahedral metallic nanoparticles (Pt and Pd) and a platinum slab with 320 atoms and a (111) facet exposed. We performed the calculations using all the available l-p-DOS bases in ONETEP, namely: i) non-contracted spherical waves (SWs); ii) Contracted spherical waves (C-SWs); iii) Contracted and fitted to the NGWFs spherical waves (CF-SWs) and; iv) Pseudoatomic orbitals (PAOs).

Table 4.1 shows a general trend on the charge spilling parameters with SWs $<$ PAOs $\leq$ CASTEP $<$ CF-SWs $<$ C-SWs. The small values obtained with SWs were expected due to the large size and flexibility of the basis. The results obtained with PAOs in ONETEP and CASTEP indicate that the implementation in both codes is comparable and that we should also expect similar results for l-p-DOS plots. Table 4.1 also shows that determining the contraction coefficients by fitting the C-SWs to the NGWFs contributes to reducing the spilling parameter as compared with contraction of spherical waves using unit weights. For the calculations with metallic nanoparticles, all the pDOS options, with the exception of C-SWs, show similar values of charge spilling parameters, indicating that the projected density of states obtained with these approaches should also be comparable to each other.

We compare in figure 4.2 the projected density of states obtained with CASTEP and the ones obtained with PAOs in ONETEP for small molecules. Figure 4.2 a), b), c), and d) show, respectively, the density of states projected onto s states for CO, SiH_4, C_2H_2, and C_2H_4, while figure 4.2 e), f), g), and h) show the p projection for the same molecules. Similarly to the results obtained for the charge spilling parameters, here, we see a remarkable agreement between ONETEP and CASTEP results. The pDOS similarity in both codes helps to validate

TABLE 4.1: Charge spilling parameter, presented as percentages, for calculations performed with CASTEP and different angular momentum resolved bases in ONETEP.

System	SWs (%)	C-SWs (%)	CF-SWs (%)	PAOs (%)	CASTEP (%)
CO	0.19	26.78	6.45	1.59	1.66
C_2H_2	0.04	17.92	16.47	1.77	1.89
C_2H_4	0.03	13.55	7.44	1.83	1.91
C_2H_6	0.02	11.02	6.96	1.70	1.78
SiH_4	0.08	11.82	10.11	2.40	2.79
$LiPF_6$	0.30	17.62	7.87	0.94	0.90
Pd_{13}	0.00	19.73	0.28	0.08	0.10
Pt_{13}	0.01	22.70	0.41	0.06	0.13
Pt_{55}	0.01	19.28	0.17	0.07	0.11
Pt_{147}	0.00	17.83	0.01	0.07	0.10
Pt(111)	0.00	15.75	0.05	0.06	0.08

the implementation of the projected density of states in ONETEP.

Meanwhile, figure 4.3 compares all the implemented angular momentum resolved basis, testing the results for CO, C_2H_4 and C_2H_6. Figure 4.3 a), c) and e) show, respectively, the density of states of CO, C_2H_4 and C_2H_6 projected onto s channels, while b), d) and f) shows the projections for p channels of the same molecules.

In general, the projections with all the angular momentum resolved bases are similar. The generation of the non-contracted spherical waves set is unbiased and, as demonstrated with the charge spilling parameters, provides an almost complete projection of the calculated bands for a wide range of systems. In this sense, the similarity of the pDOS obtained with PAOs and non-contracted SWs reinforces the idea that PAOs are viable options to obtain angular momentum projected density of states.

The main differences arise when calculating systems with atoms with valence shells composed by different values of azimuthal quantum numbers. The spherical waves basis is constructed with the same maximum l for every atom in the system. For example, for a hydrocarbon, the SWs are constructed with s and p functions for carbon and hydrogen atoms. Meanwhile, the PAOs are constructed by default in ONETEP to initialise the NGWFs, which results on basis with s and p character for carbon atoms and only s character for hydrogen, generating small variations in the pDOS peaks as compared to SWs.

For example, in the carbon monoxide tests in figure 4.3 a) and b), both oxygen and carbon atoms have s and p orbitals for all projection schemes and the computed pDOS for all approaches is almost identical. Meanwhile, for C_2H_4 and C_2H_6, some variations are observed depending on the chosen basis set, where the projections performed with non-contracted spherical waves show more p character as compared to the PAOs projection for the lowest energy peaks on both

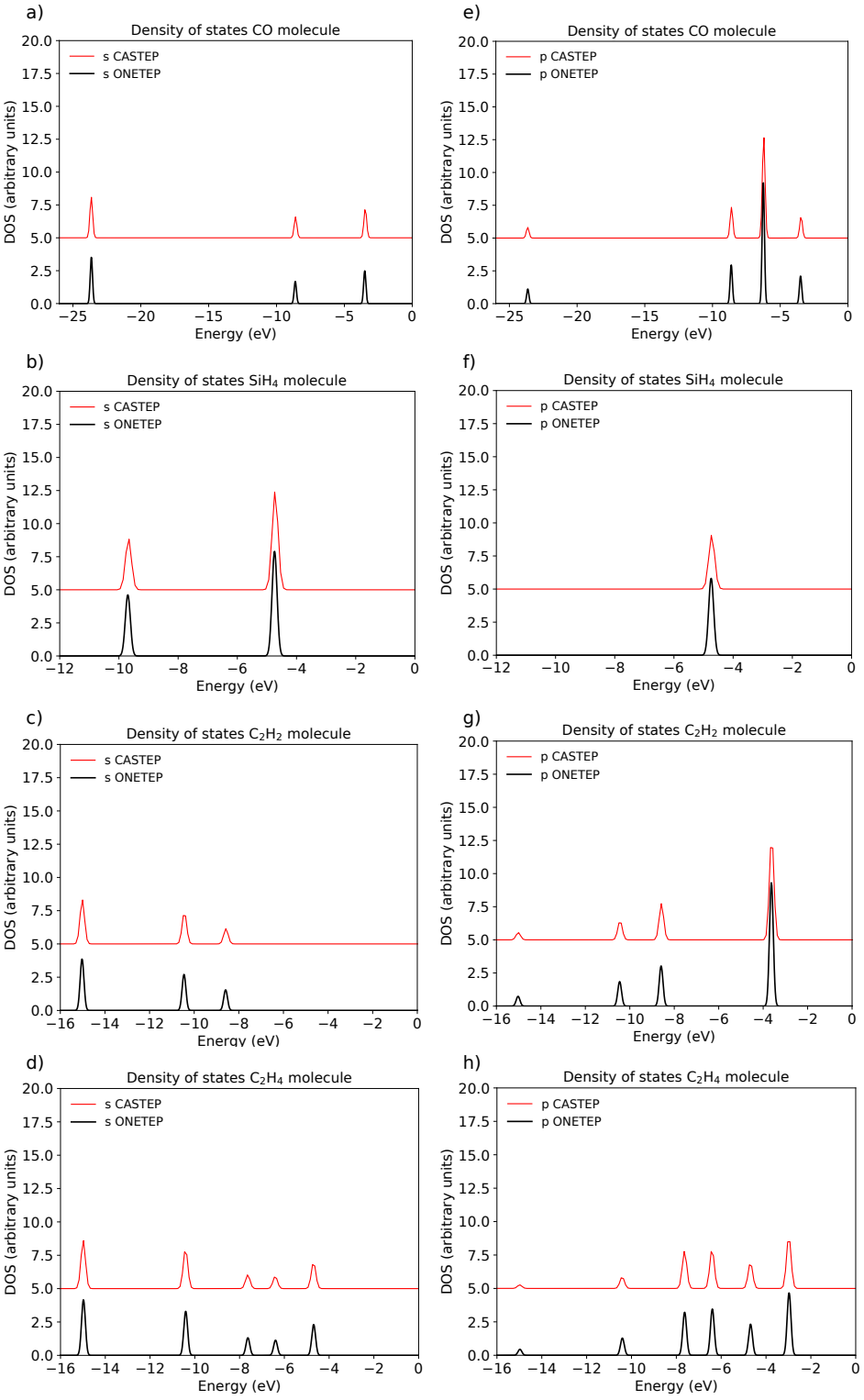

FIGURE 4.2: Angular momentum projected densities of states obtained with CASTEP (red) and ONETEP (black) with PAOs as the projection basis set. a), b), c) and d) show the s channel for CO, SiH_4, C_2H_2, and C_2H_4 molecules, while e), f), g) and h) show the p projected DOS for the same molecules.

hydrocarbons.

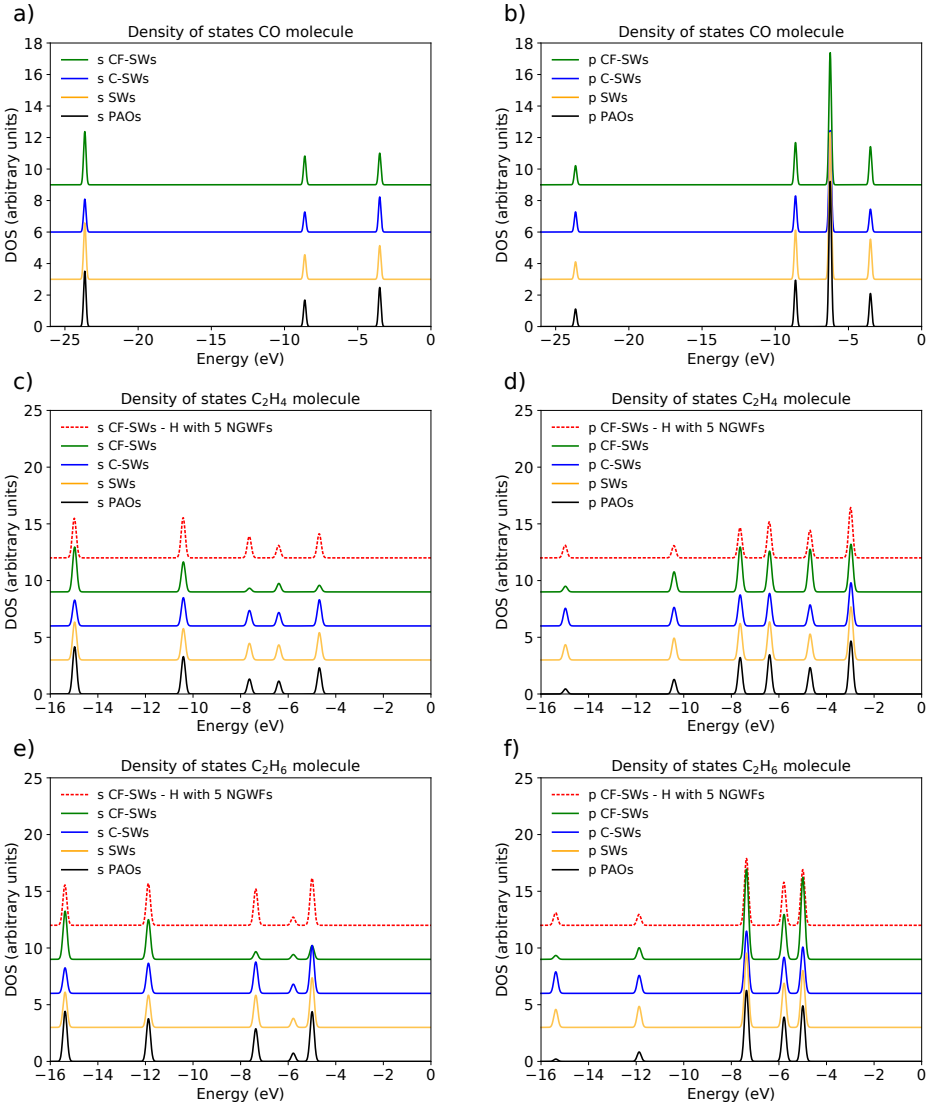

FIGURE 4.3: Projected density of states (p-DOS) for different schemes implemented in ONETEP. a), c) and e) show, respectively, s p-DOS for CO, C_2H_4, and C_2H_6. b), d) and f) show the p projection for the same molecules. For all plots, different colors are used to represent each bases, where black, yellow, blue and green represent PAOs, SWs, C-SWs and CF-SWs. For c, d, e, f the CF-SWs calculated with 5 NGWFs for each hydrogen atom are represented as red segmented lines.

From all the contracted spherical waves schemes, the CF-SWs is the one that presents larger variations from PAOs and non-contracted SWs. We attribute that to the difficulty of fitting a spherical wave basis composed with s and p functions to a single NGWF. To test if the number of NGWFs was a problem, we have tested the effect of including five NGWFs to hydrogen atoms to initialise them with s (2 NGWFs) and p (3NGWFs) character. As a result, the calculated charge spilling parameters decrease from 7.44% to 3.69% for C_2H_4 and from 6.97% to 2.34% for C_2H_6, and the overall behaviour observed with non-contracted spherical waves is recovered.

As briefly commented in the introduction and discussed on chapter 3, angular momentum projected density of states is an invaluable tool for theoretical investigations in the field of heterogeneous catalysis. In this area, describing the interaction between the catalyst surface and adsorbates is essential to explain and predict catalytic activities. As proposed by Nørskov *et al.* [99, 100], properties from the localised d-band of transition metals can be used as electronic descriptors of the interaction strength between and adsorbate and the catalyst's surface. Moreover, due to the connection between the d-band centre and the surface composition, crystallographic orientation, site coordination and nanoparticle sizes, studies with such descriptors can be used to search for routes to catalysts optimisations.

Here, to test our methods for this application, we have decided to compute cuboctahedral platinum nanoparticles of increasing size, ranging from Pt_{13} to Pt_{561} and a Pt slab with a (111) facet exposed. We have also computed a Pd_{13} cluster as an additional test. Increasing the nanoparticle size affects the surface's Pt-Pt bond lengths and the ratio between uncoordinated and coordinated sites, generating shifts in the d-band centres that translate in a weakening in the interaction with adsorbates. Here, we are not considering the changes in the Pt-Pt bond lengths with increasing nanoparticle sizes. We compute Pt nanoparticles created with Pt bulk bond lengths to isolate the electronic effects to the geometrical changes due to size effects. Similarly to the tests with small molecules, here, we start showing in figure 4.4 the l-p-DOS obtained with ONETEP and CASTEP.

Again, we observe a remarkable similarity between ONETEP and CASTEP results for the l-p-DOS plots, which helps to validate the implementation of the projected density of states and shows how the results compare for metallic systems. Figure 4.5 a) and b) present the density of states projected onto the d channels of Pt atoms in a (111) facet of a Pt_{147} nanoparticle, where the first plot spans through all calculated energy levels and the second focuses on the states near the Fermi level which will be used to calculate the d-band centres. These plots show that d-bands calculated with all the implemented bases are similar. The overall shape of the d-band near the Fermi level remain almost unchanged for all bases, with only small variations in the peaks intensities. The main differences appear for low energy levels, where additional d projected states are observed for spherical wave based approaches. In practice, as the energy levels near the Fermi level are the important region for this application and these results are similar for all bases, this should not affect the overall applicability of any of the schemes for the purpose of this thesis.

Figure 4.6 a) shows the d-band centres calculated with different approaches for the (111)

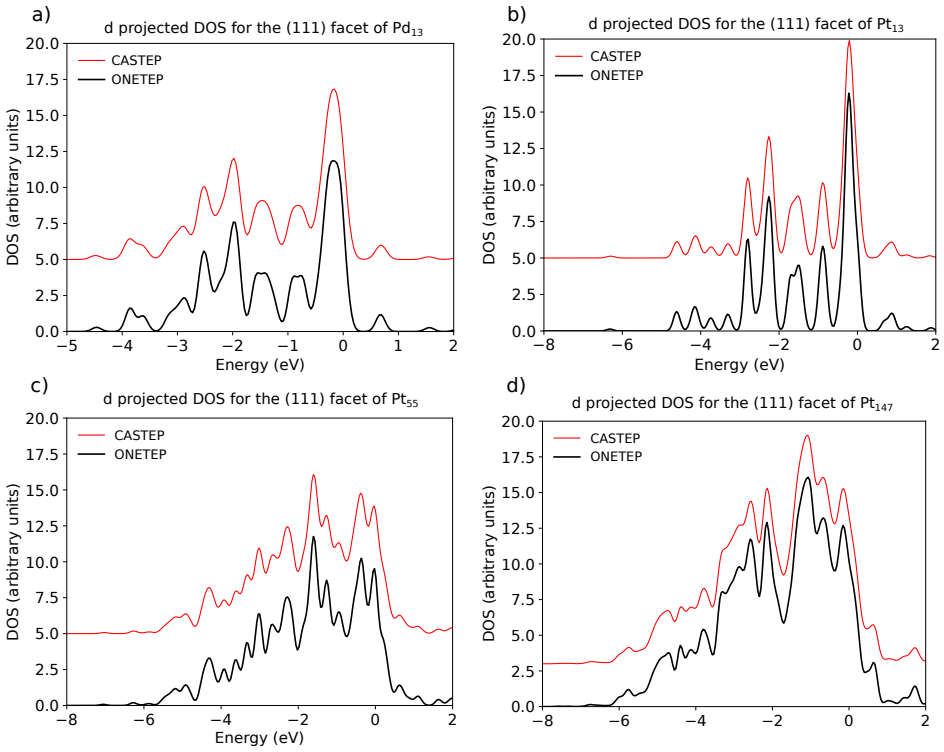

FIGURE 4.4: Angular momentum projected densities of states obtained with CASTEP (red) and ONETEP (black) with PAOs as the projection basis set. a), b), c), and d) present the d bands projected onto Pd and Pt atoms on (111) facets of Pd_{13}, Pt_{13}, Pt_{55} and Pt_{147} nanoparticles.

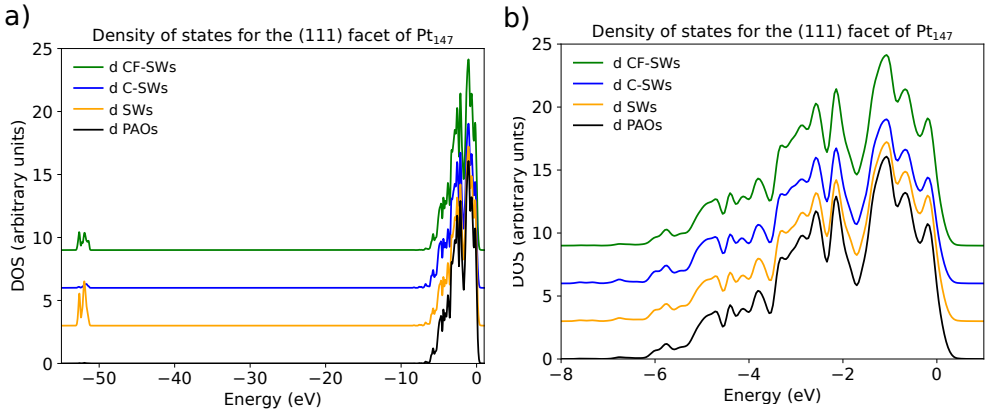

FIGURE 4.5: Density of states projected onto the d channels of Pt atoms in a (111) facet of a Pt_{147} nanoparticle where a) spans through all calculated energy levels and b) focus in the states near the Fermi level. For all plots, different colors are used to represent each bases, where black, yellow, blue and green represent PAOs, SWs, C-SWs and CF-SWs.

facet of the nanoparticles against the nanoparticles sizes. The d-band centres are calculated using the occupancy-weighted l-p-DOS and focusing on the states near the Fermi-level, i.e., excluding the variations for the low energy levels illustrated in figure 4.5. As we increase the nanoparticle size, the d-band centre moves away from the Fermi-level, which according to the d-band theory should describe a weaker interaction with adsorbates.

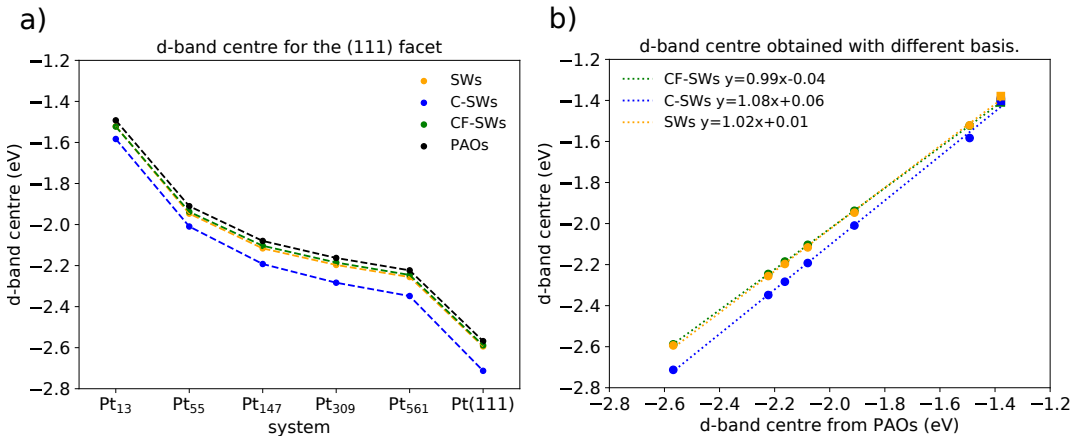

FIGURE 4.6: Calculated d-band centres using different projection schemes. a) shows the results for (111) facets of Pt nanoparticles against the nanoparticles sizes and for a Pt(111) slab. b) compares the calculated d-band centres with spherical waves bases (SWs, C-SWs, CF-SWs) to the same quantities obtained using PAOs, showing the d-band centres for the whole (111) facet of Pt nanoparticles of increasing size, the exposed facet of the Pt (111) slab, and the (111) facet of Pd_{13} (square symbols). The d-band centres are calculated using the occupancy-weighted l-p-DOS and focusing on the states near the Fermi-level to exclude the variations for the low energy levels illustrated in figure 4.5. For all plots, different colors are used to represent each bases, where black, yellow, blue and green represent PAOs, SWs, C-SWs and CF-SWs.

Figure 4.6 b) shows how the calculated d-band centres with spherical waves bases (SWs, C-SWs, CF-SWs) compare to the same quantities calculated using PAOs. We show the d-band centres for the whole (111) facet of Pt nanoparticles of increasing size, the exposed facet of the Pt (111) slab, and the (111) facet of Pd_{13}. As observed, the small changes in the projected density of states plots are not crucial for the calculated d-band centres, and similar trends and conclusions could be obtained with any method.

4.5 Conclusions

In this chapter, we described the underlying theoretical framework for the implementation of angular momentum projected density of states within ONETEP's formalism and presented four options of angular momentum resolved bases that were implemented in ONETEP to obtain l-p-DOS. The first three are based on spherical waves, with a non-contracted set of SWs; a contracted set with unity contraction weights (C-SWs), and a contracted set where the contraction weights are determined via inner products with the NGWFs (CF-SWs). Pseudo-atomic orbitals (PAOs) are used for the fourth basis set, which is also the initialisation of NGWFs in ONETEP.

We performed tests on several systems to assess how the projection varies with changes in the basis sets and how the ONETEP's results compare to CASTEP's l-p-DOS. We have calculated the density of states for a CO and a silane molecule, a set of hydrocarbons, a $LiPF_6$

compound, metallic nanoparticles of different sizes, and one platinum slab with 320 Pt atoms. In terms of charge spilling parameter, s_q, we observed a similar trend for all tested systems, with SWs $<$ PAOs $\leq$ CASTEP $<$ CF-SWs $<$ C-SWs. In general, we have observed remarkably small charge spilling parameters for calculations with the non-contracted SWs basis. For PAOs, the charge spilling parameters obtained with ONETEP and CASTEP were almost identical, and for contracted SWs basis, the option with contraction weights obtained by fitting the NGWFs presented lower s_q values than the one with unit contraction weights.

Despite some differences in the charge-spilling parameter, the l-p-DOS results are comparable between the implemented approaches and between the two tested codes. The more evident differences arise with systems composed by atoms with different values of azimuthal quantum numbers in the valence shell, where the main differences appear for l-p-DOS obtained with CF-SWs as compared to the other options. This difference can be reduced by adding NGWFs in the ONETEP basis set to allow a better fitting between NGWFs and SWs. Moreover, for metallic nanoparticles of increasing size, the d-bands near the Fermi level, which is commonly used as a descriptor in the heterogeneous catalysis field, remain almost unaltered between different approaches, showing the robustness of the implemented method for such studies. We expect that the availability of these methods in a linear-scaling framework such as ONETEP will help the analysis of the electronic structure of complex nanostructured materials.

Chapter 5

Effects of a Graphene Support on Platinum Nanoparticles

This chapter presents our studies about the interaction between platinum clusters and nanoparticles with graphene. We performed the calculations with a set of clusters and nanoparticles to study how the interaction changes with the system size. This work was also published as a manuscript on "Physical Chemistry Chemical Physics - PCCP " [9].

L. G. Verga, J. Aarons, M. Sarwar, D. Thompsett, A. E. Russell, and C.-K. Skylaris. Effect of Graphene Support on Large Pt Nanoparticles. Phys. Chem. Chem. Phys., 18:32713–32722, 2016.

in which, I participated in all the stages of the work. Dr. J. Aarons participated in the development and application of the l-p-DOS functionality. All the other authors participated with corrections and ideas for the manuscript, with the whole work being supervised by Prof. Chris-Kriton Skylaris.

Abstract

State-of-the-art catalysts are often made of supported metallic clusters and nanoparticles, increasing the surface area and decreasing the loading of the catalytic material and therefore the overall cost. Thus, it is important to understand factors controlling the interaction between

nanoparticles and supports and how the support can change the geometries and electronic properties of nanoparticles. Here, we employ large-scale DFT calculations to simulate platinum structures with up to 309 atoms interacting with single layer graphene supports with up to 880 carbon atoms. We compute the adhesion, cohesion and formation energies of two and three-dimensional Pt structures interacting with the support. We include dispersion interactions via a semi-empirical dispersion correction and a vdW functional. We show that three-dimensional Pt clusters are more stable than the two-dimensional ones when interacting with the support and that the difference between their stabilities increases with the system size. Also, the dispersion interactions are more pronounced as we increase the nanoparticle size, being essential to a reliable description of larger systems. We observe inter-atomic expansion (contraction) on the closest (farthest) Pt facets from the graphene sheet and charge redistribution with the overall charge being transferred from the platinum clusters to the support. The Pt-Pt expansion, which is related to the charge transfer in the system, correlates with the adhesion energy per Pt atom in contact with the graphene. These, and other electronic and structural observations show that the effect of the support cannot be neglected. Our study provides for the first time, to the best of our knowledge, quantitative results on the non-trivial combination of size and support effects for nanoparticles sizes which are relevant to catalyst design.

5.1 Background

Platinum and platinum-based alloys are widely studied as excellent catalysts for several chemical reactions involved in different types of fuel cells [178, 179]. However, the high cost of Pt, the inadequate global supply, and the slow kinetics of the ORR in pure Pt catalysts, has been stimulating the development of different approaches to decrease the platinum loading in the catalyst, increase its surface area and decrease the overall cost of the catalyst while maintaining or improving its activity and selectivity. Using metallic nanoparticles, clusters or monolayers dispersed over supports can help to circumvent these difficulties by increasing the Pt surface-to-volume ratio in the catalyst [155, 178, 180].

Carbonaceous materials such as graphene, graphite, carbon black and carbon nanotubes are commonly used as catalysts supports on fuel cells applications. Among these materials, graphene is receiving special attention due to some inherent advantages of its structure. First of all, the two-dimensional shape of graphene enables a surface area higher than other forms of carbon. Secondly, some of its characteristics, such as high electrical conductivity and good

thermal stability makes graphene a promising material for fuel cell applications [155]. Unfortunately, the interaction between platinum clusters and pristine graphene is relatively weak, which can cause loss of catalytic surface, due to the agglomeration of Pt particles [156]. Also, as the number of the atoms on platinum nanoparticles increases the interactions per Pt atom in contact with the graphene support decrease, leading to difficulties in growing Pt monolayers over graphene supports [157].

Studies aiming to understand the interaction between metallic systems and carbon-based supports and the efficiency of these catalysts for fuel cell applications are widely present in the literature [150, 155–160, 162, 164–166, 181–184]. One interesting example is the work by Maiti and Ricca [164], where Au, Pt and Pd atoms, monolayers, multilayers, and clusters interacting with graphene supports were studied via DFT simulations. According to their results, only small Pt subnanoclusters are able to wet a graphene surface. Okazaki-Maeda *et al.* [158] also investigated the interaction between Pt_n clusters with ($n \leq 13$) and graphene supports using *ab-initio* simulations, achieving similar conclusions to Maiti and Ricca, and showing that 3D clusters are unequivocally more stable over graphene when the cluster has more than 10 Pt atoms, which also agrees with the findings from Xiao and Wang [127] for isolated platinum clusters. Furthermore, other studies such as the work of Schneider *et al.* [166] and Ramos-Sanchez and Balbuena [162] showed that the interaction between platinum clusters and carbonaceous supports have a significant contribution from van der Waals interactions.

Recently, graphene supports with point defects have also attracted attention from the scientific community. From a theoretical point of view, Fampiou and Ramasubramaniam [159] studied Pt_n ($n \leq 13$) clusters interacting with pristine graphene and other types of defective graphene sheets using DFT and simulations with empirical potentials. They have demonstrated that point defects can act as binding traps for Pt clusters, increasing the strength of the interaction. As a consequence, their work not only helps to elucidate the graphene-metal interaction but also helps to guide defect engineering in supports for fuel cells.

In addition to the support effects in the catalytic activity, the optimum size of Pt nanoparticles for different catalysts and how the nanoparticle size affects the nanoparticle/support interaction are still ongoing questions. Therefore, in this chapter, we present our calculations treating several sizes of platinum clusters over graphene with large-scale DFT calculations using the ONETEP code. First of all, we validate our calculations against the literature, simulating Pt_n clusters with (n = 1 - 4) and comparing with the work from Fampiou and Ramasubramaniam[159]. Secondly, aiming to check if the stability of platinum monolayers differs significantly from the

ones obtained with 3D structures, we simulate Pt_n systems (n = 1 - 55) constructed as two and three-dimensional structures on graphene supports. Additionally, we simulate cuboctahedral Pt_n with (n = 147, 309), which represents Pt nanoparticles with diameters close to 1.7 nm and 2.2 nm respectively, enabling us to see how the support and size effects can act together to change the properties of platinum nanoparticles and how the interaction nanoparticle-support is affected by the nanoparticle size. We finish this chapter discussing aspects of our work which could be relevant to catalyst design.

5.2 Computational Details

The calculations were carried out using the EDFT method in the ONETEP code [2, 28]. The projector augmented wave (PAW) method [24] was used to describe core electrons. We adopted the generalised gradient approximation with the PBE [21], RPBE [22], and one vdW functional, the rVV10 [185, 186], as our exchange-correlation functionals. We also included the empirical dispersion correction proposed by Grimme [187] in the PBE and RPBE functionals, generating two variations here called PBE-D2 and RPBE-D2. The parameters used in the empirical dispersion correction were the same as the values proposed by Grimme for the carbon atoms [187], while for platinum atoms, the dispersion coefficient C_6 and the van der Walls radius R_0 were taken from the literature [162]. The universal scaling factor S_6, was also obtained from the literature, being equal to 0.75 for the PBE functional [187] and 1.25 for the RPBE functional [162].

We set the kinetic energy cutoff to 550 eV for geometry optimisations and 850 eV for total energy and properties calculations. For each Pt (C) atom, we have assigned 12 (4) NGWFs with 9.0 a_0 radii. The NGWF conjugated gradient optimisation preconditioning parameter k_0 [188] used in our simulations was equal to 2.5 $a_0{}^{-1}$, and the geometry optimisations were performed until the forces on all atoms were below 0.005 Ha/a_0. We have used the C-SWs method implemented in ONETEP to perform the l-p-DOS analysis and obtain d-band centres. The nanoparticles (monolayers) were constructed with initial Pt-Pt distances of 2.80 Å (2.60 Å) [127] in the configurations shown in figure 5.1, where the cuboctahedral shape was used for Pt_{13}, Pt_{55}, Pt_{147}, and Pt_{309}. Orthorhombic simulation boxes were built allowing periodicity to the graphene sheet and a minimum gap of 10 Å between the borders and Pt atoms. Two-dimensional clusters were studied up to 55 Pt atoms.

We computed: i) the adhesion energies E_{AD}; ii) the formation energies E_{FOR}; and iii) the cohesive energies of a free Pt cluster E_{COH}, which are defined as follows:

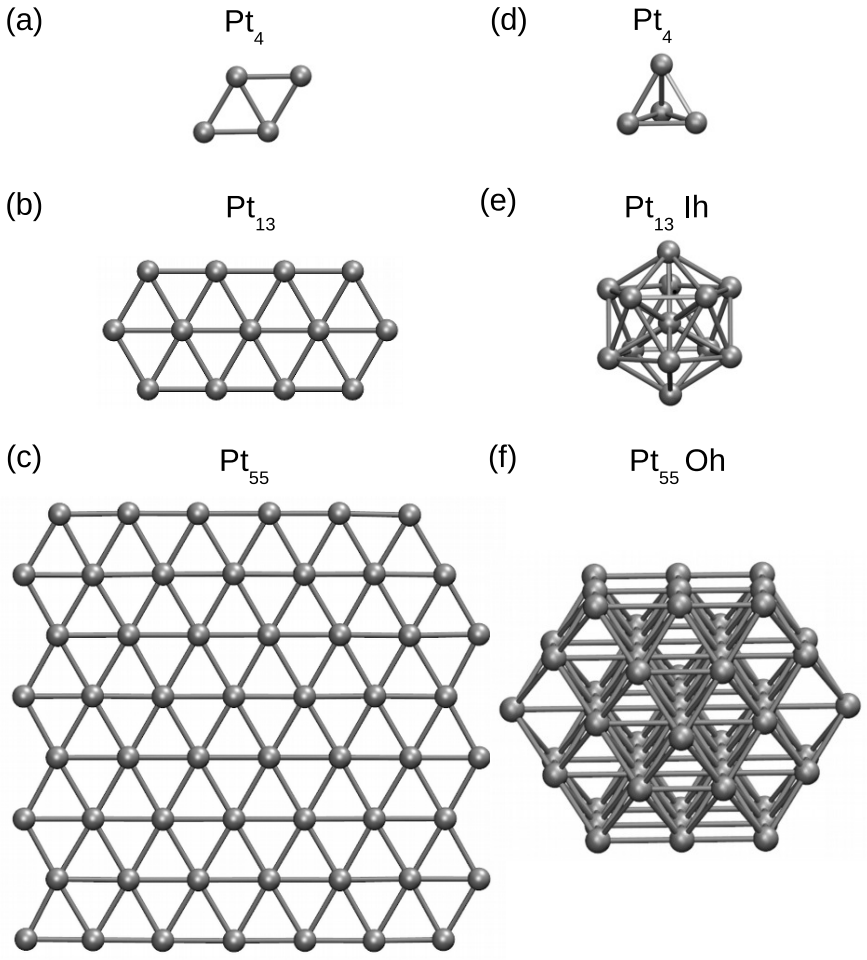

FIGURE 5.1: Initial geometries used for a) Pt_4, b) Pt_{13}, and c) Pt_{55}, clusters constructed as monolayers; d) Tetrahedral Pt_4, e) Icosahedral (Ih) Pt_{13}, and f) Cuboctahedral (Oh) Pt_{55}. Cuboctahedral shapes were used on Pt_{13}, Pt_{55}, Pt_{147}, and Pt_{309} clusters.

$$E_{AD} = E_{Pt_n/graph} - (E_{graph} + E_{Pt_n}) \tag{5.1}$$

$$E_{FOR} = E_{Pt_n/graph} - (E_{graph} + n * E_{Pt}) \tag{5.2}$$

$$E_{COH} = E_{Pt_n} - n * E_{Pt} \tag{5.3}$$

where, n is the number of Pt atoms, E_{Pt} is the energy of a single Pt atom, E_{graph} is the energy of the graphene sheet, E_{Pt_n} is the energy of the Pt structure and $E_{Pt_n/graph}$ is the energy of the platinum structure bound to the graphene sheet. E_{graph} and E_{Pt_n} are obtained, respectively, after geometry optimisations from the isolated graphene and Pt cluster, while $E_{Pt_n/graph}$

is obtained after the geometry optimisation of the interacting system.

5.3 Two and Three Dimensional Pt Clusters Supported on Graphene

Initially, we validate our calculations against the literature using Pt_n with (n = 1 - 4) nanoclusters interacting with graphene using the PBE exchange-correlation functional. Table 5.1 compares our results and the ones from Fampiou and Ramasubramaniam [159].

TABLE 5.1: Comparison of adhesion energy E_{AD} (eV), formation energy E_{FOR} (eV), and average distance between Pt-C and Pt-Pt for Pt_n clusters ($n = 1 - 4$) interacting with the graphene support.

Fampiou and Ramasubramaniam [159]	E_{AD}(eV)	E_{FOR}(eV)	Pt-Pt(Å)	Pt-C(Å)
Pt atom at bridge site	-1.57	-1.57	-	2.10
Pt_2	-0.78	-4.58	2.38	2.25
Triangular Pt_3	-1.35	-8.64	2.49	2.22
Tetrahedral Pt_4	-1.13	-12.07	2.60	2.14
ONETEP	E_{AD}(eV)	E_{FOR}(eV)	Pt-Pt(Å)	Pt-C(Å)
Pt atom at bridge site	-1.64	-1.64	-	2.10
Pt_2	-0.95	-4.83	2.37	2.23
Triangular Pt_3	-1.17	-8.92	2.49	2.26
Tetrahedral Pt_4	-1.24	-12.46	2.59	2.20

As we can see in table 5.1, our results agree with the ones obtained in the literature. The methodology used in our work to calculate E_{AD} is slightly different from the methodology used by Fampiou and Ramasubramanian. In their strategy, E_{Pt_n} is calculated by removing the carbon atoms from the Pt-graphene system and minimising the remaining structure. Meanwhile, we calculate E_{Pt_n} from geometry optimisations of platinum clusters initialised with bulk-like Pt-Pt distances of 2.80 Å. Both strategies are valid choices, but they can change the result from E_{AD} for systems were the structure from the platinum cluster suffers great deformations due to the interaction with the support. Meanwhile, the formation energy E_{FOR} does not suffer from these ambiguities, and it is a quantity more suitable for comparisons.

Despite the amount of theoretical work which highlights the success of PBE based functionals to deal with transition metals, the lack of dispersion interactions from this functional, intrinsically important to describe the interaction between Pt clusters and carbon-based supports, is a problem that needs to be addressed to model the entire system. To deal with this problem, we decided to use the PBE, and RPBE functionals with two variations here called PBE-D2, RPBE-D2, which are constructed using the Grimme D2 empirical approach to include dispersion interactions. We have also simulated our systems with the rVV10 exchange-correlation functional, which is a vdW density functional available in ONETEP.

Figure 5.2 shows the formation energy per Pt atom for the simulated systems up to Pt_{55}, which allows us to compare the stability of different clusters in contact with the graphene support. For any Pt structure size, the three-dimensional structures present lower formation energies than the two-dimensional ones, i.e. for all the simulated systems, the 3D Pt clusters are more stable than the Pt monolayers when supported on graphene.

As the system size grows, the difference in the formation energies between two and three-dimensional clusters increases. This effect can be clearly observed in figure 5.2 by comparing the two plateaus formed for Pt_4 and Pt_{13} clusters and the decrease observed for Pt_{55} systems and this result becomes more evident when we take into account that the formation energies are being divided by the number of Pt atoms in the system. We see the same trend for all the simulated functionals. The inclusion of dispersion interactions decreases the formation energy for all the systems, and this effect increases with the cluster size, i.e., the difference in the formation energies between PBE and PBE-D2 is higher for Pt_{55} clusters than for Pt_4 clusters.

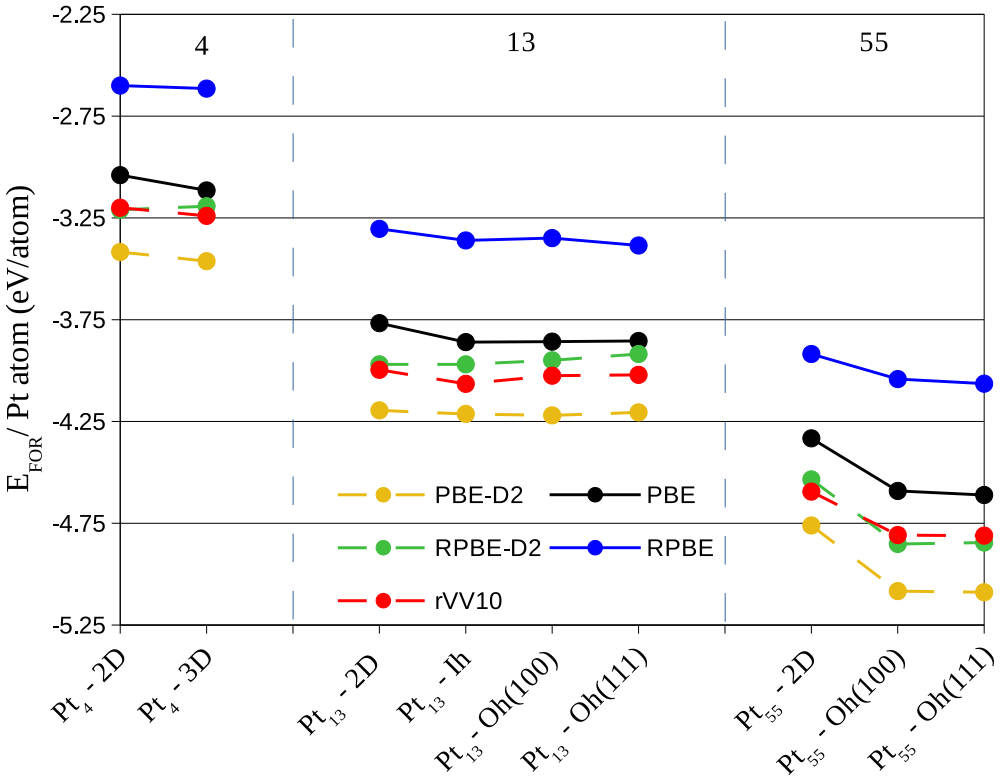

FIGURE 5.2: Formation energy per Pt atom, E_{FOR}/n, for different Pt clusters interacting with the graphene support. Ih (Oh) refers to Icosahedral (Cuboctahedral) symmetries. The cuboctahedral facet in contact with the graphene is indicated between brackets. Simulations containing dispersion interactions are represented by dashed lines. Vertical dashed lines were plotted to delimit the number of Pt atoms in the systems.

One of the reasons for the higher stability of three-dimensional supported clusters is the

stability of these clusters when isolated, which is presented through the cohesive energy of free Pt systems. In figure 5.3, we show the cohesive energies per Pt atom of Pt_n clusters (n = 4 - 55) obtained with different functionals. The trends obtained in figure 5.2 and figure 5.3 are very similar, showing that the stability of the Pt-graphene systems is determined to a great extent by the Pt-Pt interactions.

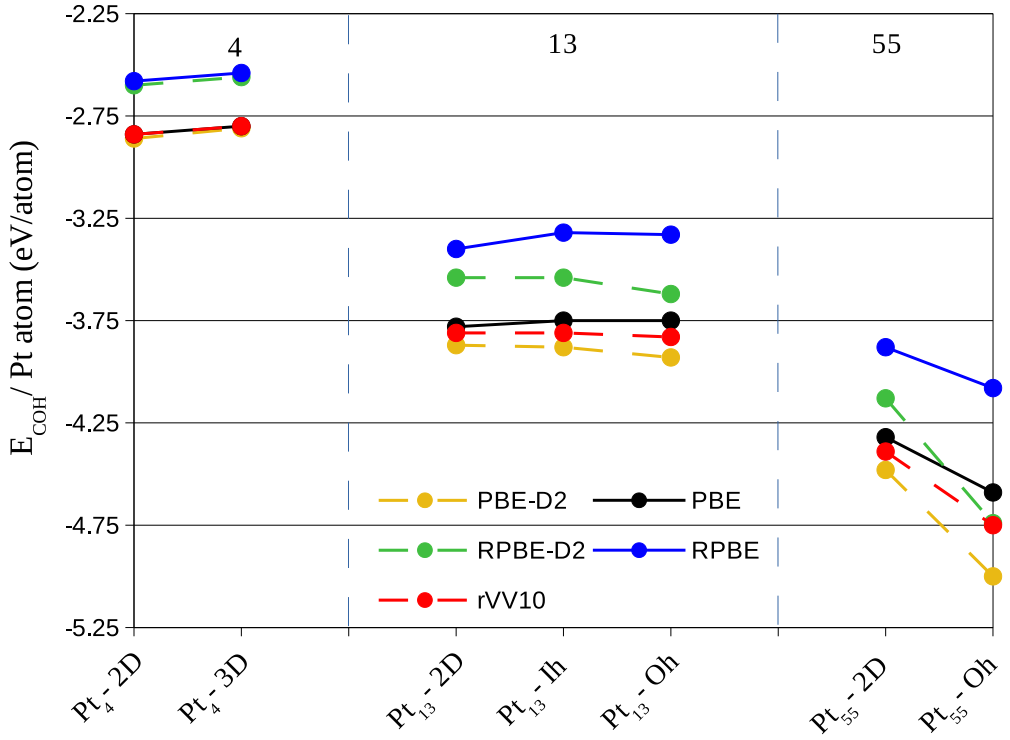

FIGURE 5.3: Cohesive energies, E_{COH}/n for different Pt clusters. Ih (Oh) refers to Icosahedral (Cuboctahedral) symmetries. Simulations containing dispersion interactions are represented by dashed lines. Vertical dashed lines were plotted to delimit the number of Pt atoms in the systems.

As previously said, several experimental and theoretical studies have shown that as the number of Pt atoms in contact with graphene increases the binding energy per contact atom decreases [155, 157, 164, 166]. Moreover, the dispersion interaction increases with the cluster size, therefore it is expected that for larger clusters the interactions between metal clusters and carbon-based supports will be dominated by dispersion interactions.

To illustrate both effects, the decrease in the binding energy per contact atom associated with the increase of Pt atoms in the interface region, and the importance of dispersion interactions to describe large systems, we present in figure 5.4 the adhesion energy divided by the number of Pt atoms in contact with the support for all the simulated functionals. To facilitate illustrating both effects, we have ordered the systems according to the number of Pt atoms in

the interface with the graphene support. We observe that the adhesion energy per contact atom weakens as we increase the system size, being almost negligible for larger systems. It is also interesting that the adhesion energy per contact atom strengthens for cuboctahedral clusters when the triangular (111) facet is close to the graphene. This decrease in Pt-C interaction associated with an increase in the number of Pt atoms in contact with graphene also helps to explain the difficulties to grow Pt monolayers over graphene supports.

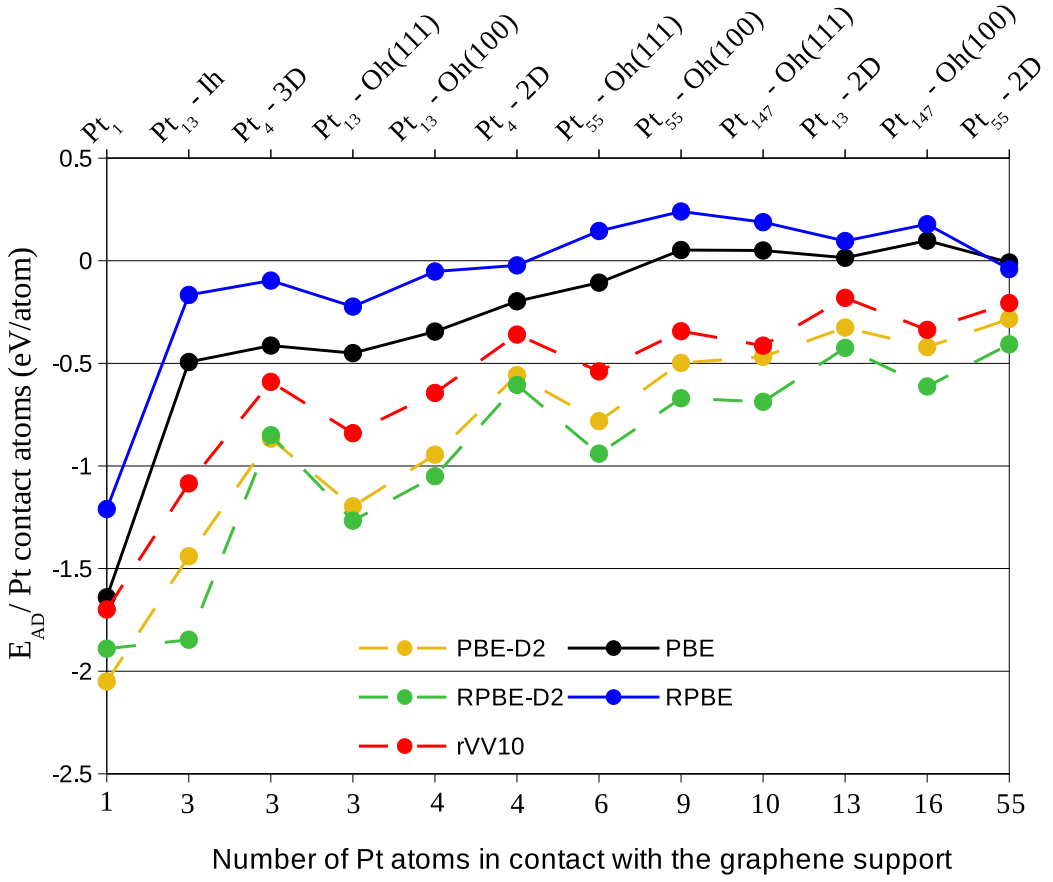

FIGURE 5.4: Adhesion energy per Pt atom in contact with the graphene support. The systems were ordered according to the number of Pt atoms in contact with the graphene. Ih (Oh) refers to Icosahedral (Cuboctahedral) symmetries, the cuboctahedral facet in contact with the graphene is indicated between brackets. Simulations containing dispersion interactions are represented by dashed lines.

As already observed for the formation energies, the dispersion interaction strengthens the interaction between Pt clusters and graphene for all the systems. It is important to emphasise that the inclusion of dispersion was able to provide negative adhesion energies for systems such as Pt_{55}, Pt_{147}, that are nanoparticles with a diameter close to 1.1nm and 1.7nm respectively, being nanoparticles with sizes closer to the ones used in experimental research [139, 142, 189, 190]. In calculations without dispersion corrections, we observe a positive (repulsive) adhesion energy. This result shows that the Pt-C interaction in large platinum nanoparticles is dominated

by dispersion, confirming the importance of including the dispersion interactions for a reliable description of these systems.

It is interesting to notice in figure 5.3 that the results obtained with the rVV10 functional for isolated clusters are close to the ones obtained with PBE. Meanwhile, for the calculations with Grimme D2 corrections, even the relative stabilities between different clusters for the same size changes. This trend favours choosing rVV10 as our functional to avoid the overestimation of dispersion interactions observed with the D2 correction. However, there is no optimum functional to describe the dispersion interactions for all types of systems, and it is difficult to clearly state which one has better accuracy without developing benchmarking tests with reliable experimental data. Still, it is interesting to observe that we obtain similar qualitative behaviour with rVV10 and with the two functionals with D2 correction. This similarity in the trends happens for all calculated values, which strengths our results.

The observed trends showing the weak interaction between Pt clusters and pristine graphene, the decrease of interaction per Pt atom with increasing nanoparticle size, and the dispersion interactions dominating the Pt/graphene adhesion energies agree with experimental findings in the area and can be used to strengthen observations from the literature. The negligible interaction between pristine graphene and nanoparticles larger than 1 nm, for example, agrees with experimental findings which indicate that the stability of Pt nanoparticles over graphene-based supports is mainly controlled by the presence of defects, edges, functional groups, or doping atoms that would increase the interaction metal-support as compared with a pristine graphene [167, 191, 192]. For example, Janowska *et al.* [167] observed with in situ transmission electron microscopy (TEM) a higher density of smaller Pt nanoparticles on edges of few-layer graphene supports as compared with the flat surface. Similarly, the concentration of a doping material such as B [192] or N [191] that can create defects and anchoring sites to the Pt clusters, was observed to correlate with the nanoparticle size, where a lower concentration would generate a surface with less anchoring sites and a tendency of larger nanoparticles, changing the catalytic activity per mass.

5.4 Geometrical and Electronic Effects of the Graphene Support on Platinum Clusters

So far we have investigated the stability of different Pt clusters over a graphene support and confirmed the importance of dispersion interactions to describe this interaction. Now, we

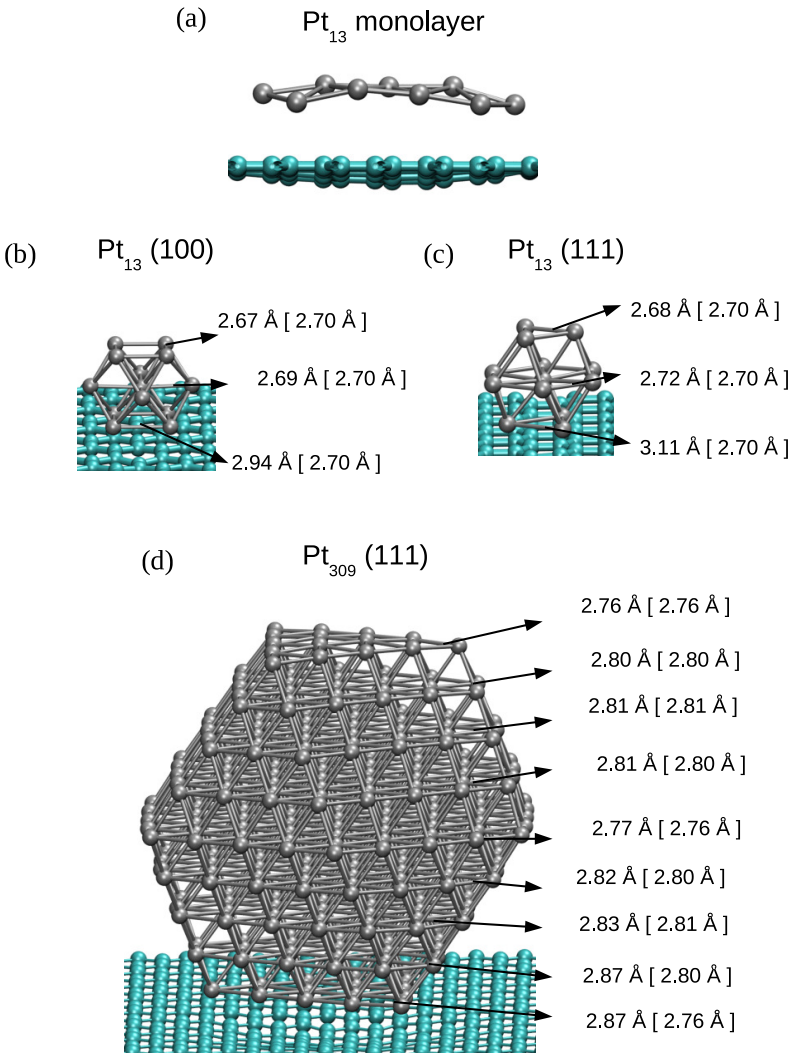

FIGURE 5.5: Optimised geometries for (a) Pt_{13} monolayer (b) Cuboctahedral Pt_{13} with the (100) facet and (c) the (111) facet interacting with graphene, and (d) Cuboctahedral Pt_{309} with the (111) facet in contact with the support. The numbers are the average Pt-Pt bond lengths for each Pt layer, while numbers between brackets represent the average bond lengths in the unsupported nanoparticles. Gray (green) spheres represent platinum (carbon) atoms.

can explore the geometrical and electronic effects that this interaction induces on Pt clusters. We start by showing in figure 5.5, the final geometries of Pt_{13} and Pt_{309} clusters interacting with the graphene support. It is possible to see that the interaction causes deformations on both geometries.

For the Pt_{13} monolayer a repulsion between the support and the cluster appears, which is illustrated in figure 5.5 (a), through the direction which the graphene support bends, providing a visual representation of the difficulties of growing Pt monolayers on graphene. Figures 5.5 (b) and (c) show the geometry optimised structures of a Pt_{13} cuboctahedral with the (100) and (111) facets in contact with the graphene support. The numbers in the figure 5.5 show the average

Pt-Pt bond lengths for different layers for each structure, illustrating how the Pt-Pt bond lengths in the closest (farthest) facets increase (decrease) in the supported cluster as compared with the 2.70 Å Pt-Pt average bond lengths obtained in isolated Pt_{13} clusters. Figure 5.5 (d) illustrates the same effect for cuboctahedral Pt_{309}, with almost no difference in the bond length averages of Pt layers far from the graphene support. Structural changes are also observed in the graphene sheet, with C-C bond lengths expanding from the isolated graphene value of 1.43 Å to values up to 1.45 Å in the closest regions to the metallic nanoparticle.

TABLE 5.2: Average Pt-Pt bond length for each Pt layer on cuboctahedral Pt nanoparticles with the (100) facet interacting with a graphene support. The results are presented for all the Pt layers, where the first one is the closest to the graphene support. Results in brackets were obtained for the same facets in an isolated nanoparticle.

	Pt_{13} (Å)	Pt_{55} (Å)	Pt_{147} (Å)	Pt_{309} (Å)
Layer 1	2.94 [2.70]	2.83 [2.71]	2.8 [2.75]	2.78 [2.75]
Layer 2	2.69 [2.70]	2.83 [2.79]	2.83 [2.79]	2.82 [2.78]
Layer 3	2.67 [2.70]	2.82 [2.79]	2.82 [2.79]	2.81 [2.79]
Layer 4		2.79 [2.79]	2.82 [2.79]	2.80 [2.79]
Layer 5		2.71 [2.71]	2.80 [2.79]	2.80 [2.79]
Layer 6			2.79 [2.79]	2.79 [2.79]
Layer 7			2.75 [2.75]	2.79 [2.79]
Layer 8				2.79 [2.78]
Layer 9				2.76 [2.75]

TABLE 5.3: Average Pt-Pt bond length for each Pt layer on cuboctahedral Pt nanoparticles with the (111) facet interacting with a graphene support. The results are presented for all the Pt layers, where the first one is the closest to the graphene support. Results in brackets were obtained for the same facets in an isolated nanoparticle.

	Pt_{13} (Å)	Pt_{55} (Å)	Pt_{147} (Å)	Pt_{309} (Å)
Layer 1	3.11 [2.70]	2.88 [2.75]	2.81 [2.75]	2.87 [2.76]
Layer 2	2.72 [2.70]	2.84 [2.80]	2.83 [2.81]	2.87 [2.80]
Layer 3	2.68 [2.70]	2.73 [2.73]	2.80 [2.80]	2.83 [2.81]
Layer 4		2.80 [2.80]	2.75 [2.75]	2.82 [2.80]
Layer 5		2.74 [2.75]	2.80 [2.80]	2.77 [2.76]
Layer 6			2.81 [2.81]	2.81 [2.80]
Layer 7			2.75 [2.75]	2.81 [2.81]
Layer 8				2.80 [2.80]
Layer 9				2.76 [2.76]

Tables 5.2 and 5.3 present the average Pt-Pt bond lengths for each layer of cuboctahedral Pt nanoparticles before and after the interaction with the graphene support. The data is given from the closest to the farthest Pt facet from the graphene layer. Table 5.2 presents the results for nanoparticles interacting with graphene via the (100) facet, while table 5.3 shows the same results for nanoparticles with the (111) facet is contact with the support. The numbers in brackets represent the results for the same facets in isolated Pt nanoparticles. In both cases, we observe Pt-Pt bond length expansions (contractions) in the closest (farthest) facets from graphene.

As also illustrated in figure 5.5, for smaller clusters this effect is more pronounced, while almost no change can be observed in the farthest facets of larger nanoparticles. The comparison of how this effect changes with the size of the cluster in contact with the support shows that increases in the size of the cluster reduces the changes in the Pt-Pt bond lengths. Such an effect is expected once the Pt-graphene interaction weakens as the number of Pt atoms in the interface increase. Moreover, as the nanoparticle size grows there are more intermediate layers that help to dilute the contractions of Pt-Pt bond lengths for the farthest facet, which helps explaining the results observed for Pt_{309} nanoparticles.

The average Pt-Pt bond lenghts for the closest Pt facet to the graphene support from tables 5.2 and 5.3 were used to obtain the average Pt-Pt bond lenght strain by comparing the values computed before and after the interaction. In figure 5.6 we plot the average Pt-Pt strain for the platinum facet in the interface with the graphene support against the adhesion energy per Pt atom in contact with the graphene support. This analysis shows that systems with more Pt-Pt bond length strain have stronger adhesion per contact atom. As indicated in table 5.2 and 5.3, larger deformations are present when the triangular facet (111) is in contact with the graphene system and the strain reduces as we increase the nanoparticle size.

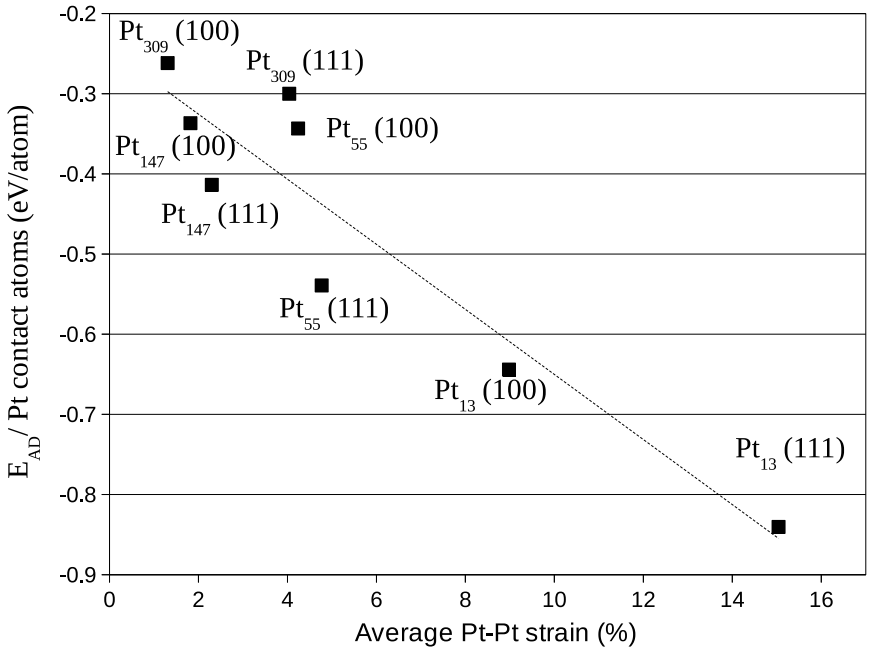

FIGURE 5.6: Adhesion energy per Pt atom in contact with the graphene support versus the average percentage of Pt-Pt bond length expansion in the nanoparticle facet in contact with the graphene sheet, where the black line is only a guide to the eye.

To understand the causes of the Pt-Pt deformations, we have investigated the electronic

changes in the graphene support and platinum clusters caused by the interaction. Figure 5.7 a) and b) show the charge rearrangements through electronic density differences plots of Pt_{55} cuboctahedral with the (100) and (111) facets interacting with graphene. The cuboctahedral with the (111) facet in contact with the graphene, which has a stronger adhesion energy per contact atom and a larger bond length expansion induced by the interaction, also shows larger charges redistributions. Figure 5.7 c), and d) show the Mulliken charges for each atom within a colour scale for the same systems, evidencing the interaction of the bottom facet with the graphene, with charge transfer from the metallic cluster to the support.

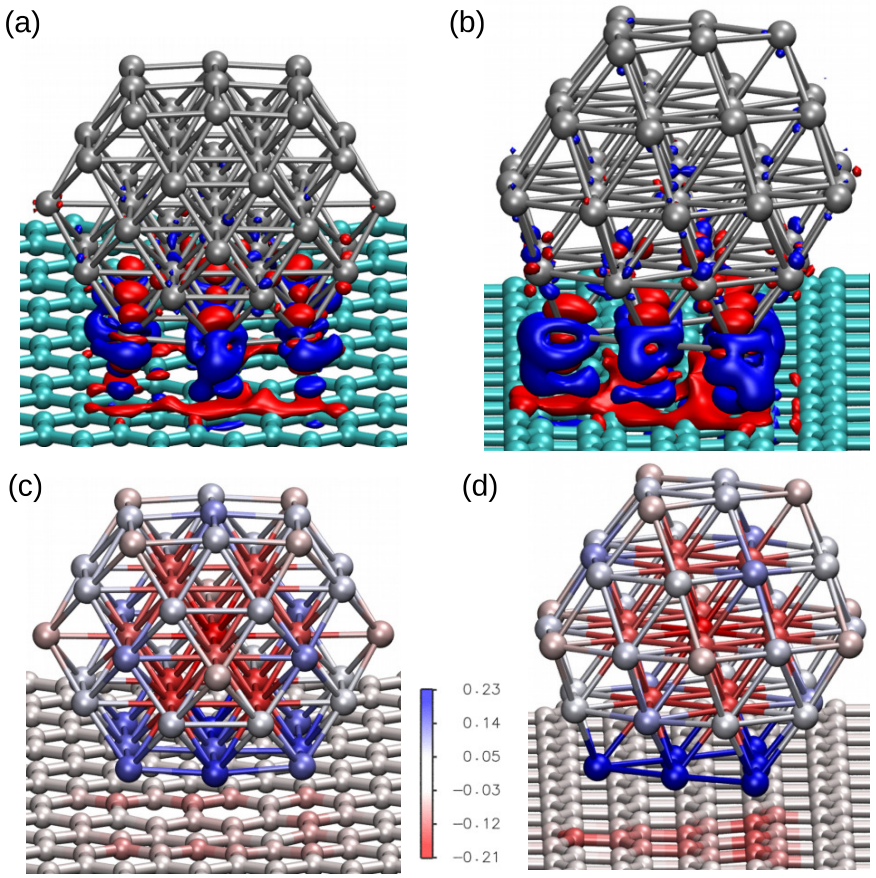

FIGURE 5.7: Changes in the electronic densities of supported Pt_{55} nanoparticles, where a) and b) show electronic density difference plots (Isosurface at 0.01e/Å^3), where blue (red) represents accumulation (depletion) of electrons, and c) and d) presents the Mulliken charges for each atom plotted as a colour scale. Figures a) and c) represent a cuboctahedral Pt_{55} with the (100) facet in contact with the graphene, while b) and d) represent the same system with the (111) facet interacting with the support. Green (gray) spheres represent carbon (platinum) atoms. Figure reproduced from ref. 9.

A quantitative analysis of the electronic rearrangement is performed in figure 5.8, where the charge difference per atom in the nearest Pt facet was calculated via Mulliken population

analysis and plotted against the average Pt-Pt strain. As also reported in previous studies [157–159, 161, 162, 184], electrons move from the Pt cluster to the support for small clusters interacting with the support. Moreover, a clear relation between the average Pt-Pt strain and the charge transferred per Pt atom in the Pt/graphene interface can be observed.

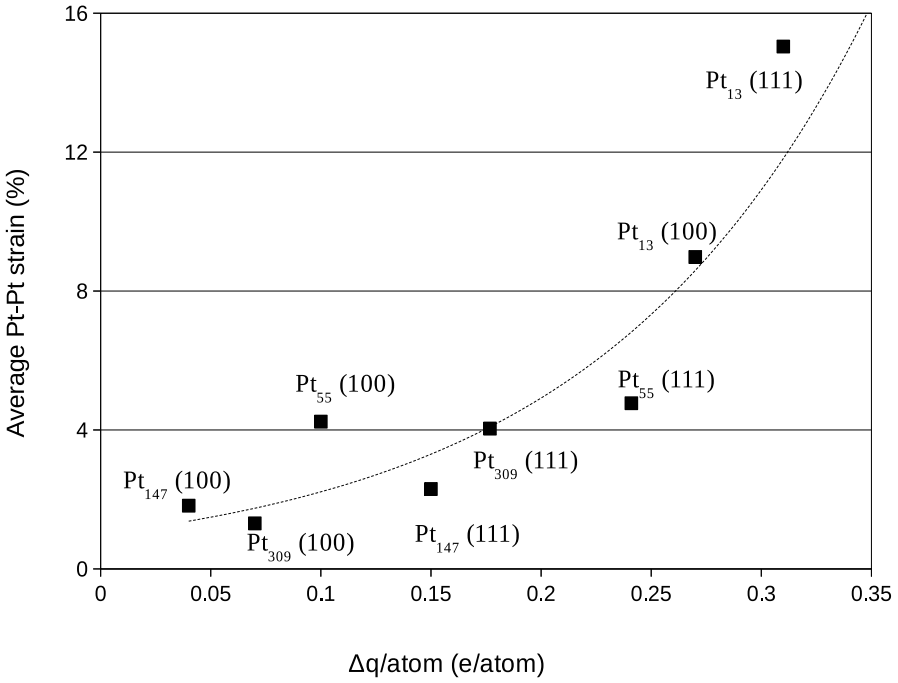

FIGURE 5.8: Average percentage of Pt-Pt bond length expansion in the nanoparticle facet in contact with the graphene versus the charge difference per Pt atom in the same nanoparticle facet, where the black line is only a guide to the eye.

We also plot in figure 5.9 the density of states normalised by the occupancies and projected on the d (p) angular momenta of Pt (C) atoms. As commented in previous chapters, changes in the d-band centre are commonly used as a descriptor of the catalytic activity of metallic clusters, where downshifts (upshifts) of the d-band centre in catalysts are usually associated with catalysts with weaker (stronger) interaction with adsorbates. Moreover, previous studies have discussed that bond lengths strains and electronic effects can change the d-band centre of metallic clusters and their catalytic activities [193], strengthening the idea that this type of results can be used as to create structure-property relationships.

The density of states was projected onto chosen Pt and C atoms. The p-band of carbon atoms was obtained only in the interacting region of the graphene sheet, which was plotted considering the system before and after the interaction with the Pt structures. Figure 5.9 (a), (b), (c), and (d) represents respectively, the interaction with the Pt_{13}, Pt_{55}, Pt_{147}, and Pt_{309} cuboctahedral nanoparticles. Meanwhile, figure 5.9 (e), (f), (g), and (h) represents the d-band of Pt_{13},

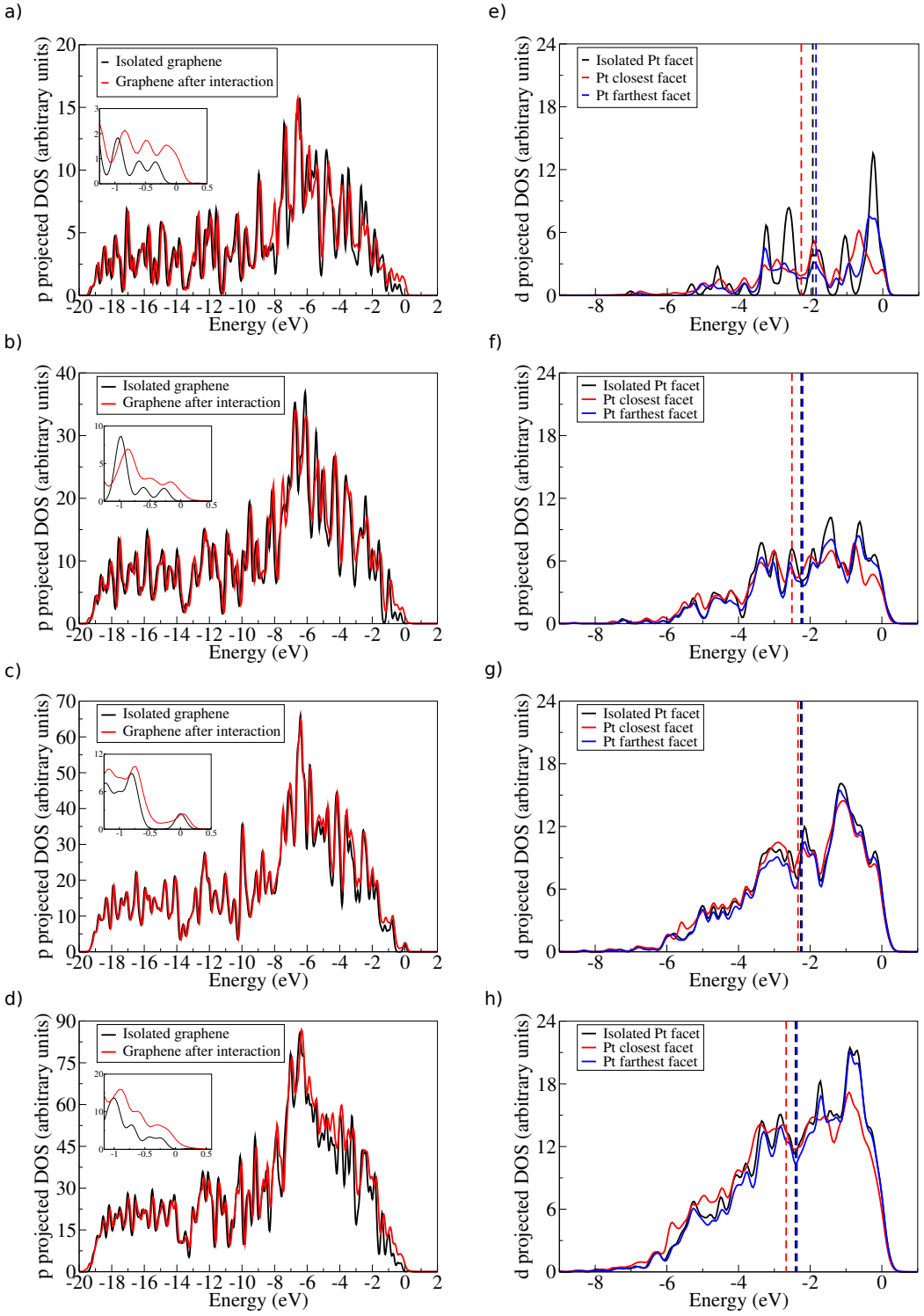

FIGURE 5.9: Atom and angular momentum projected density of states (l-p-DOS) plots for cuboctahedral nanoparticles interacting with the graphene support: (a), (b), (c), and (d) represents the p-bands of the graphene support interacting with Pt_{13}, Pt_{55}, Pt_{147}, and Pt_{309} cuboctahedral nanoparticles, while (e), (f), (g), and (h) represents the d-bands of different Pt facets for the same systems. Dashed lines indicate the d-band centre of each facet. For the plots of the p-band of graphene, black (red) lines indicate systems before (after) the interaction with the Pt cluster, with the inset showing in detail the occupied states with higher energy, i.e, close to the Fermi level. For the plots showing the d-band of platinum facets, black lines indicate the (111) facet in isolated Pt clusters, while red (blue) lines indicate the Pt (111) facets which are closest (farthest) from the support. Figure reproduced from ref 9.

Pt_{55}, Pt_{147}, and Pt_{309} cuboctahedral nanoparticles for isolated systems and for the closest and farthest facets from the graphene support. The projected densities of states were analysed only for nanoparticles with (111) facet interacting with the support.

The relation between changes in the d-band centre and the Pt-Pt bond lengths strain is explained in the literature with the Nørskov d-band centre model [99, 193]. According to this model, the changes in the d-band centre are related to the changes in the band width induced by the bond length strain, i.e., considering a constant number of electrons in the d-band, an expansive (compressive) strain would lead to a narrow (wider) band width which consequently should generate an upshift (downshift) in the d-band centre to preserve the band stretching. Meanwhile, ligand effects are related to the electronic changes caused by the interaction between catalytic material and support.

As previously said, we are presenting the density of states weighted by the occupancies with the Fermi level being set to zero for all the plots in figure 5.9. In the density of states, we observed a lowering in the intensity of the peaks for higher energy states of Pt facets close to the support after the interaction, while similar states in the graphene p-band increased, as shown in the insets in figure 5.9 (a), (b), (c), and (d). This effect, coupled with the electron density differences and the Mulliken population analysis, shows the existence of interaction between the p-band of the carbon atoms with the d-band of the Pt atoms, with charge redistribution from the Pt to the carbon atoms, followed by a C-C bond length expansion in the interface region of the graphene support. These effects are consistent with the Dewar-Chatt-Duncanson model [194], as also previously described by Mahmoodinia et al. [195] in the interaction of a Pt cluster and a polyaromatic hydrocarbon.

The d-band of the farthest Pt facet from the support shows different trends when compared with the isolated Pt and with the closest Pt facet, showing that the support affects each Pt facet differently. As we grow the system size, the differences between supported and isolated systems for the top facet starts to be negligible, as a direct result of the decrease in the Pt/support interaction per atom, and the increase in the number of Pt layers between this facet and the support. Figure 5.9 also shows downshifts in the d-band centre of the Pt facets close to the graphene, indicated by vertical dashed lines, which are much more intense than the changes observed for the Pt facets far from the support.

A more detailed analysis of the support effect on the d-band centre of Pt nanoparticles is presented in figure 5.10, which shows the d-band centre from closest (C) and farthest (F) Pt facets from the graphene sheet considering, respectively, a) the interaction of (100) and b)

(111) Pt facets with the support. To try to separate the electronic and geometrical effects caused by the interaction with the support, we have calculated the projected density of states using three different systems: i) isolated Pt clusters which are calculated with the structure obtained after geometry optimisations in vacuum, here called isolated Pt; ii) isolated Pt clusters using the structure obtained after the geometry optimisations of the Pt/graphene systems, here called deformed Pt and; iii) the whole Pt/graphene system, here called interacting Pt.

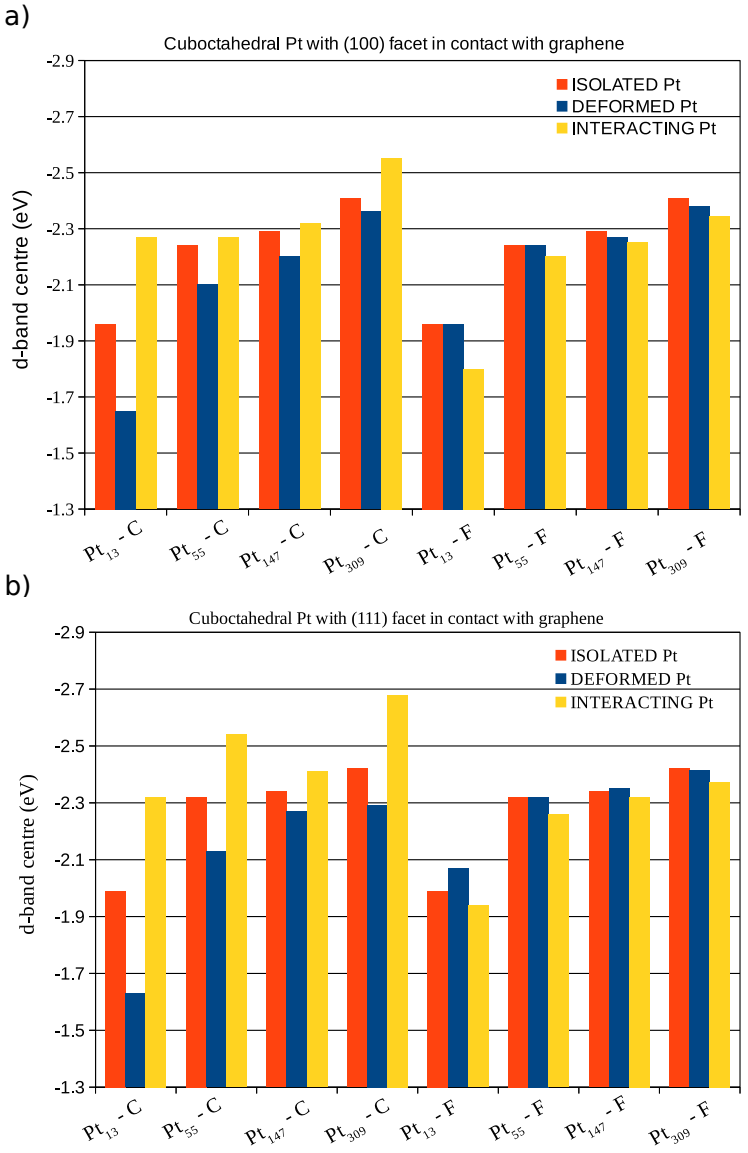

FIGURE 5.10: d-band centre from the closest (C) and farthest (F) Pt facets from the graphene support, considering Pt cuboctahedral nanoparticles with a) the (100) facet and b) the (111) facet in contact with the support. The results are presented for: i) isolated Pt systems: isolated Pt cluster with the geometry obtained during the optimisation in vacuum; ii) Deformed Pt systems: isolated Pt clusters with the geometry obtained after the interaction with the graphene support and; iii) Interacting Pt systems: the whole Pt/graphene system.

The comparison between the isolated Pt and the deformed Pt enables us to compute the

effects of geometrical changes on the d-band centre, while, the interacting Pt configuration includes all the support effects. In general, the interaction with the support leads to downshifts in the d-band centre of closest Pt facets from the graphene surface, which is the opposite effect that we should expect if the changes in the d-band centre were generated only due to the Pt-Pt bond lengths strains. We also observe small variations in the d-band centre of the facets far from the support, which rapidly decrease with the increase of the nanoparticle size.

In fact, the comparison between isolated Pt, deformed Pt, and interacting Pt, show the existence of two concurrent effects. The first one is the change in the d-band centre due to the Pt-Pt strain. This effect can be observed by comparing the d-band centre of deformed Pt and isolated Pt systems in figure 5.10 with the Pt-Pt bond lengths expansions from figure 5.6 leading to upshifts in the d-band centre. For all the studied sizes and different facets in contact with the graphene, larger expansions lead to greater upshifts in the d-band centre. The second effect is related to the changes in the high energy occupied states from the d-band of Pt due to the Pt-C interactions, which lowers the weight of high energy levels in the d-band centre calculation, generating the observed downshifts. This effect is clear when comparing the d-band centre of interacting Pt and deformed Pt systems in figure 5.10.

In practice, it is difficult to separate electronic and strain effects because both are a direct consequence of the same metal-support interaction. However, this strategy of computing strained or "deformed" structures can bring useful analysis. For example, a similar approach to try to separate the strain and electronic effects was performed by Tsai *et al.* [196] to study Os/Pt core-shell catalysts. As we do with the "Deformed Pt" clusters, they have simulated Pt slabs with compressed lattice parameters to mimic the strain effect of the Os core on the Pt surfaces. They have compared the results of compressed Pt slabs with simulations of relaxed Pt slabs and with Os slabs covered with 1 and 3 ML of Pt. They have observed, that the compressed Pt calculations provide results which are similar to the Pt_{3ML}/Os systems, and completely different results for the Pt_{1ML}/OS models. This observation points to the fact that the electronic effects are more relevant for the closest layers of Pt, and that for the layers far from the interface, the lattice changes should be the dominating effect.

In our case, we also see that the main differences from the "Deformed Pt" and "Interacting Pt", only happen for the facets close to the support and to a small extent for the farthest facet of Pt_{13}, which only has 3 Pt "layers". However, in our case, the weak interaction between the Pt nanoparticles and pristine graphene could also be the reason for the rapid vanishing of the electronic effects for Pt layers far from the support. The weak Pt/graphene interaction is also a

possible explanation for the small lattice changes for facets far from the support with increasing nanoparticle size. Thus, more studies with other supports could be helpful to compare and analyse to what extent each effect will control the ability of the nanoparticle to interact with adsorbates that are relevant to fuel cell catalysts.

The analysis of isolated systems also shows upshifts in the d-band centre associated with decreases in the system size, which is comparable to what we have presented in chapter 4. As illustrated in figure 5.10, the support effects in the d-band centre are size-dependent, being more pronounced in smaller clusters, which agrees with the weakening of Pt-C interaction as we increase the number of Pt atoms in contact to the support. These results indicate that it may be possible to search for optimum catalysts for specific reactions by linking support and size effects.

5.5 Conclusions

We have presented a DFT study of support and size effects of Pt nanoparticles on graphene, where we have simulated systems ranging from Pt_1 on 308 carbon atoms to Pt_{309} on 880 carbon atoms. We have compared two-dimensional and three-dimensional Pt clusters interacting with the graphene support, showing that nanoparticles are generally more stable than monolayers when supported on a graphene sheet. The differences between their stabilities increase with the size of the system, and the Pt-Pt interactions control the formation energies of such systems to a great extent.

The dispersion interactions were included in our simulations via a semi-empirical dispersion correction and a vdW functional. Our results show that the adhesion energy per Pt atom in contact with the support decreases as the number of Pt atoms in contact with graphene increases. Meanwhile, the analysis of the formation energies has indicated that the dispersion interaction grows with the system size. The combination of these two effects makes the inclusion of dispersion interactions important for an accurate description of the systems, especially for large Pt nanoparticles. Moreover, the weak interaction between Pt clusters and pristine graphene, specially for clusters and nanoparticles larger than 1 nm, helps to corroborate the idea that the presence of defects, functional groups, or doping atoms on graphene are necessary to strengthen the metal-support interaction and stabilise Pt nanoparticles over graphene-based supports [159, 167, 191, 192].

Additionally, we have studied the effects of the graphene support over the geometries and electronic properties of Pt clusters and nanoparticles. The Pt-Pt distances increase (decrease) in the closest (farthest) Pt facets from the graphene sheet, as a result of the electron redistribution between Pt and graphene. We were also able to correlate the Pt-Pt expansion in the closest facet with the adhesion energy per number of Pt atoms in contact with the graphene support, i.e., Pt systems with larger expansions showed more intense interactions with the graphene sheet.

In terms of electronic effects, which were analysed via electronic density difference plots, charge differences obtained with Mulliken populations and densities of states projected on the d-band of Pt atoms and p-band of carbon atoms, we have found considerable electron redistributions, with the overall charge being transferred from the platinum cluster to the graphene support. We have noticed that the Pt-Pt bond length strain and electron transfer from Pt to the graphene change the d-band centre, which is one descriptor for the catalytic activity of the metallic surfaces, indicating that is possible to modify the catalytic activity by combining support and size effects. We have tried to separate the strain and electronic effects from the metal-support interaction by simulating isolated Pt clusters with the geometry obtained after the interaction with the support. We observed, that the main differences in the d-band centres between the deformed Pt clusters and the supported ones happen for the facets directly interacting with the support, while for the farthest facets we only see differences for the Pt_{13} cluster. However, the weak Pt/-graphene interaction makes it difficult to define to what extent each effect controls the changes in d-band centres. As Pt nanoparticles supported on carbon-based supports are commonly used as catalysts in important technological applications such as fuel cells, we expect that the results of this study showing how the support affects geometric and electronic properties of the Pt clusters and the size-dependence of the support effects will be useful to other investigations on new catalysts.

Chapter 6

Adsorption Properties of Platinum Nanoparticles: Support and Size Effects

In this chapter, we compute adsorption energies for atomic oxygen, carbon monoxide and an ethanol molecule interacting with the isolated and supported platinum nanoparticles obtained in chapter 5. We perform these calculations for different nanoparticle sizes, trying to understand how the interplay between size and support effects could affect catalytic properties of the Pt nanoparticles. This work was published as a manuscript on "Physical Chemistry Chemical Physics - PCCP " [12].

L. G. Verga, A. E. Russell, and C.-K. Skylaris. Ethanol, O, and CO Adsorption on Pt Nanoparticles: Effects of Nanoparticle Size and Graphene support. Phys. Chem. Chem. Phys., 20:25918–25930, 2018.

in which, I participated in all the stages of the work. Prof. Chris-Kriton Skylaris and Prof. Andrea E. Russell participated with corrections and ideas for the manuscript, with the whole work being supervised by Prof. Chris-Kriton Skylaris.

Abstract

As previously commented, Pt nanoparticles dispersed over carbonaceous supports are

widely used as catalysts for different applications, making studies on the interplay between size and support effects indispensable for rational catalyst design. Here, we use DFT calculations to simulate the interaction of O, CO, and ethanol with free platinum cuboctahedral nanoparticles with up to 147 atoms and with the same Pt nanoparticles supported on a single layer of graphene with up to 720 carbon atoms. We compute adsorption energies for each adsorbate on different adsorption sites for supported and unsupported Pt nanoparticles. We show that as the Pt nanoparticle grows the adsorption energy decreases, and that the size effect is more important for O and CO adsorption than for ethanol. We observe that the generalised coordination number of each adsorption site controls the interaction strength for O and CO to a much larger extent than for ethanol. Electronic charge redistributions and density of states projected on the d band of the interacting Pt facets are used to obtain a better understanding of the differences between the electronic interactions for each adsorbate. For Pt nanoparticles supported on graphene, the presence of support weakens the adsorption energies for all the adsorbates, but this effect rapidly decreases with larger nanoparticles, and it is only significant for our smallest nanoparticle Pt_{13}. By demonstrating that the effects of nanoparticle size and support are different for ethanol as compared with O and CO, we conclude that it should be possible to modify different parameters in the catalyst design in order to tune the Pt nanoparticle to interact with specific adsorbates.

6.1 Background

Efficient anodic catalysts for ethanol fuel cells should be able to deal with the complicated task of breaking C-H, C-O, O-H, and C-C bonds [17, 18, 104, 197], while the cathodic catalyst should perform the oxygen reduction reaction to form water [104, 179]. An optimised catalyst should perform these reactions while being resistant to poisoning by molecules such as CO. As described in chapter 3, the size, shape, distribution, and composition of metallic nanoparticles as well as the composition, orientation and presence of defects on supports can be used to tune anodic and cathodic catalysts [18, 104, 179, 180, 198, 199].

Given the complexity of treating fuel cell catalysts with computational simulations, the theoretical studies are usually performed treating specific pieces of the problem, such as the interaction between adsorbed species and metallic surfaces. The adsorption of certain atoms and molecules on catalytic surfaces can provide information such as the changes induced in the molecules due to the interaction with the surface, adsorption sites preferences, and other characteristics of the interaction that can be useful to understand how a surface reacts as a catalyst. Performing these studies with a computational approach enables controlling catalyst's variables

which are more difficult to control experimentally. As an example, electronic and geometric changes due to size effects can be separated on theoretical studies by simply freezing the Pt nanoparticles of different sizes using the same Pt-Pt bond length, enabling the quantification of electronic effects induced by changing the nanoparticle's sizes [144, 200].

Studying the interaction of O, CO, and ethanol as adsorbed species can have important implications to fuel cell catalysts. The interaction of atomic oxygen with catalytic surfaces is widely studied in the literature and is commonly used as a predictive tool for reactivity in several chemical reactions. As illustrated in chapter 3, Nørskov *et al.* [4] used the Sabatier's Principle to correlate the activity of metallic surfaces for the oxygen reduction reaction to the adsorption energy of atomic oxygen in the format of a volcano plot, providing valuable insights for designing catalysts for this reaction. Activation energies for the bond breaking reaction of C-OH on an ethanol molecule were also correlated with atomic oxygen adsorption energies in the work of Sutton and Vlachos [71], with the activation energies for C-C and β C-H bond breaking also showing correlation with the O adsorption to a smaller extent.

Understanding the interaction of catalytic surfaces with ethanol molecules is also important to the design of new catalysts for ethanol fuel cells. First of all, the adsorption of ethanol is itself the first step in the ethanol oxidation reaction. Secondly, the ethanol adsorption can also be used as a descriptor for the first dehydrogenation step [201], which plays an important role in the ethanol oxidation reaction. Moreover, analysing the position of the molecule on top of the catalyst surface and how the electronic density of the molecule changes with the interaction can help to explain the dissociation steps of ethanol. In the literature, it is possible to find a few computational studies performed for ethanol molecules on metallic monolayers [202], slabs [203, 204], small nanoparticles [205], and core-shell M@Pt nanoparticles [206]. For Pt surfaces, all the computational results show adsorption energies lower than 1.0 eV, with a clear adsorption site preference for on top sites, and a crucial role of van der Waals interactions, which is responsible for changing the ethanol configuration adsorbed on metallic nanoparticles, favouring configurations with the C-C bond parallel to Pt surfaces [203, 207].

The chemisorption of carbon monoxide molecules is also a subject of great interest for ethanol fuel cell catalysts. Carbon monoxide can poison the catalyst surface by blocking active sites and decreasing the catalyst activity [17, 18, 104, 179] and can also work as a catalytic activity descriptor for other chemical reactions such as the CO oxidation [5, 7] that is important for a wide range of applications. However, the theoretical description of CO adsorption on Pt (111) sites via DFT with LDA or GGA exchange-correlation functionals is widely known to be

incompatible with experimental results.

The so-called "CO/Pt(111) puzzle" is characterised by DFT showing hollow sites as the preferred adsorption site, while experimental data show that CO is more stable on top sites [145]. The interaction of CO with a Pt surface is characterised by the bond of the CO σ HOMO, a lone pair in the sp hybrid orbital from the C atom, with a d orbital from the metallic surface, and a back-bonding from the metal to an unoccupied π^* orbital in the CO molecule [208]. As the CO LUMO energy is lower than it should be when calculated with GGA DFT, this piece of the interaction starts to be stronger, and as this interaction is more important for hollow sites than for top sites, the error in the adsorption site preference occurs [209, 210].

Several researchers have tried to different XC functionals to solve this problem [211–218]. Recently, the meta-GGA functional M06-L predicted the correct adsorption site for CO/Pt(111) [215], however, when dispersion interactions were included, the hollow site started to be the preferred site again, indicating that the success of M06-L could be related to error cancellations effects [216]. For Pt nanoparticles, the error is still present for adsorption sites in the centre of (111) facets, but less so near the edges, once finite size effects increase the adsorption strength, especially at on top and bridge adsorption sites near the edges of the nanoparticles [214, 219].

Here, we analyse via DFT simulations, how the adsorption of O, CO, and ethanol are affected by size effects for cuboctahedral Pt_n nanoparticles with (n = 13 - 147). Electronic and structural changes induced by the interaction are investigated trying to explain the differences in the effects of nanoparticle size for each molecule. Moreover, by adsorbing O, CO, and ethanol on Pt nanoparticles supported on pristine graphene, we assess how the interplay between size and support effects can change the adsorption of the same molecules. We finish with discussions about the observed phenomena, aiming to provide useful insights for rational catalyst design.

6.2 Computational Details

We have performed the simulations from this chapter using the ONETEP code [28] within the EDFT method [2]. We have adopted the vdW functional rVV10 [185, 186] as our exchange-correlation functional and used the projector augmented wave (PAW) method [24] to describe the core electrons. Similarly to the calculations from chapter 5, we set the psinc basis set [33] kinetic energy cutoff to 550 eV for geometry optimizations and 850 eV for total energy and properties calculations. Again, we have used the C-SWs method implemented in ONETEP to perform the l-p-DOS analysis. For each Pt atom, we have assigned 12 NGWFs, for C and O

atoms we allocated 4 NGWFs and H atoms were calculated with only 1 NGWF. For C atoms in the graphene sheet, we have assigned 8 NGWFs creating a more flexible basis set. For all NGWFs, we have used 9.0 a_0 radii. The NGWF conjugate gradient optimisation preconditioning parameter k_0 [188] used in our simulations was equal to 2.5 ${a_0}^{-1}$.

The initial isolated and supported cuboctahedral platinum nanoparticles are the geometry optimised structures obtained in chapter 5. Most of our analysis was performed only for cuboctahedral nanoparticles with the (111) facet interacting with the graphene sheet, as these were the most stable structures we have obtained. Again, we ensure that the orthorhombic and periodic simulation boxes allow periodicity to the graphene layer and a minimum gap of 10 Å between the borders of the simulation box and the Pt atoms. Here, only the adsorbates' geometries were relaxed, with a convergence threshold of 0.002 Ha/a_0 on the atomic forces, while atoms from the isolated and supported nanoparticles remained fixed.

To perform a more detailed analysis of support and size effects for Pt nanoparticles interacting with O, CO and ethanol, we have sampled different adsorption sites as illustrated in figure 6.1 for Pt_{147}. Figure 6.1 (a) illustrates adsorption sites for a (111) facet, where 1 to 3 and 4 to 6, respectively represent the adsorbates on top sites and bridge sites located in the vertex, edge and centre of the nanoparticle facet, while 7 and 8 are HCP sites in the vertex and edge of the nanoparticle and 9 is an FCC adsorption site. Figure 6.1 (b) shows the chosen sites for a (100) facet, with a similar ordering as that presented for the (111) facet.

For each adsorption site, we have calculated the generalised coordination number as introduced by Calle-Vallejo *et al.* [10], which we use in the following sections to encode the changes in adsorption energies on different adsorption sites. We present in figure 6.1 the GCN associated to each adsorption site for a Pt_{147} nanoparticle. As commented in chapter 3, the generalised coordination number accounts for changes in the coordination not only for the adsorption site but also for its first neighbours which are weighted based on their own coordination numbers as follows:

$$\overline{CN(i)} = \sum_{j=1}^{n_i} cn(j)/cn_{max} \tag{6.1}$$

where n_i is the number of nearest neighbours j from a site i, $cn(j)$ is the coordination number for each first neighbour and cn_{max} is the maximum number of first neighbours that this particular site should have in bulk. The generalised coordination number can also be computed for materials with different crystalline structures or different types of adsorption sites such as hollow and bridges by changing cn_{max}.

a) Adsorption sites for a Pt_{147} (111) facet

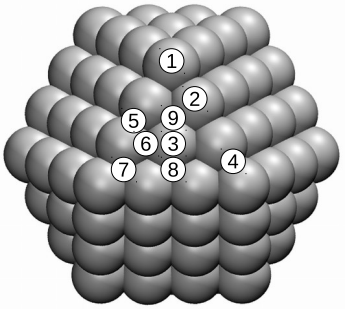

Adsorption Sites	GCN
1 Top – V	3.33
2 Top – E	5.00
3 Top – C	6.50
4 Bridge – V	3.83
5 Bridge – E	4.72
6 Bridge – C	5.33
7 HCP – V	4.05
8 HCP – E	5.18
9 FCC – E	4.41

b) Adsorption sites for a Pt_{147} (100) facet

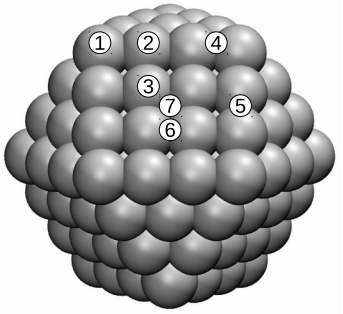

Adsorption Sites	GCN
1 Top – V	3.33
2 Top – E	5.00
3 Top – C	6.50
4 Bridge – V	3.83
5 Bridge – E	4.72
6 Bridge – C	6.44
7 Hollow – C	6.31

c)

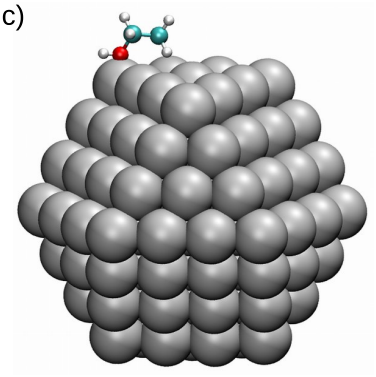

FIGURE 6.1: Adsorption sites for (a) Pt(111) facet of a Pt_{147}, where 1 to 3 represent top adsorption sites located on the vertex, edge and centre of the nanoparticle facet, 4 to 6 are bridge sites also located on the vertex, edge and centre of the (111) facet, and 7 and 8 are HCP sites locate on the vertex and edge of the Pt(111) facet and 9 is an FCC site. Figure (b) shows a similar adsorption site distribution for the (100) facet of a Pt_{147}, and (c) illustrates the initial configuration of an ethanol molecule on the Top-V site of Pt_{147}. For each adsorption site, we also present the generalised coordination number which was calculated as proposed by Calle-Vallejo *et al.* [10].

Meanwhile, figure 6.1 (c) shows the initial configuration of an ethanol molecule on a top-vertex adsorption site. The ethanol molecules were initialised in the trans-ethanol configuration with the oxygen atom on top of the adsorption site and with the C-C bond parallel to the studied Pt facet. This configuration follows the results obtained in the literature for ethanol adsorption on Pt(111) slabs and extended Pt surfaces [202–204]. Carbon monoxide molecules were placed with the C-O bond being perpendicular to the nanoparticle facet.

We have computed adsorption energies, E_{ADS}, to analyse the interaction between CO, O and ethanol with the catalyst model, i.e, supported or unsupported Pt nanoparticles, which is defined as follows:

$$E_{ADS} = E_{Adsorbate/Catalyst} - (E_{Catalyst} + E_{Adsorbate}) \tag{6.2}$$

where, $E_{Adsorbate}$ is the energy of an isolated O, CO, or ethanol, $E_{Catalyst}$ is the energy of the supported or unsupported Pt cluster used as our model catalysts, and $E_{Adsorbate/Catalyst}$ is the energy of the interacting system.

6.3 Adsorption on Isolated Pt Nanoparticles.

Here, we present the adsorption energies for ethanol, atomic oxygen, and a CO molecule interacting with Pt nanoparticles of different sizes in several adsorption sites for (111) and (100) facets. Figure 6.2 shows adsorption energies for each adsorbate in contact with a (111) facet for isolated Pt nanoparticles, with lower values of adsorption energies representing stronger interactions.

For atomic oxygen, the observed adsorption site hierarchy is similar to that obtained in the literature with Pt nanoparticles [65, 219–221]. In comparison with the results obtained for extended surfaces in the literature [219, 222, 223], the most stable adsorption site changes from the FCC site on Pt(111) slabs to HCP and bridge sites near the vertices of the Pt nanoparticle facets. Moreover, the hierarchy obtained with our calculations for the Pt_{55} cluster is similar to that demonstrated by Han, Miranda, and Ceder [220] with the adsorption energies ordered as follows: Bridge-V < HCP-V < Top-V < FCC-E < Bridge-C < Top-E. In addition to the adsorption site reordering, reducing the nanoparticle size strengthens the adsorption of oxygen on the nanoparticle surface, as previously demonstrated in the literature [144] and predicted via l-p-DOS analysis from chapter 4.

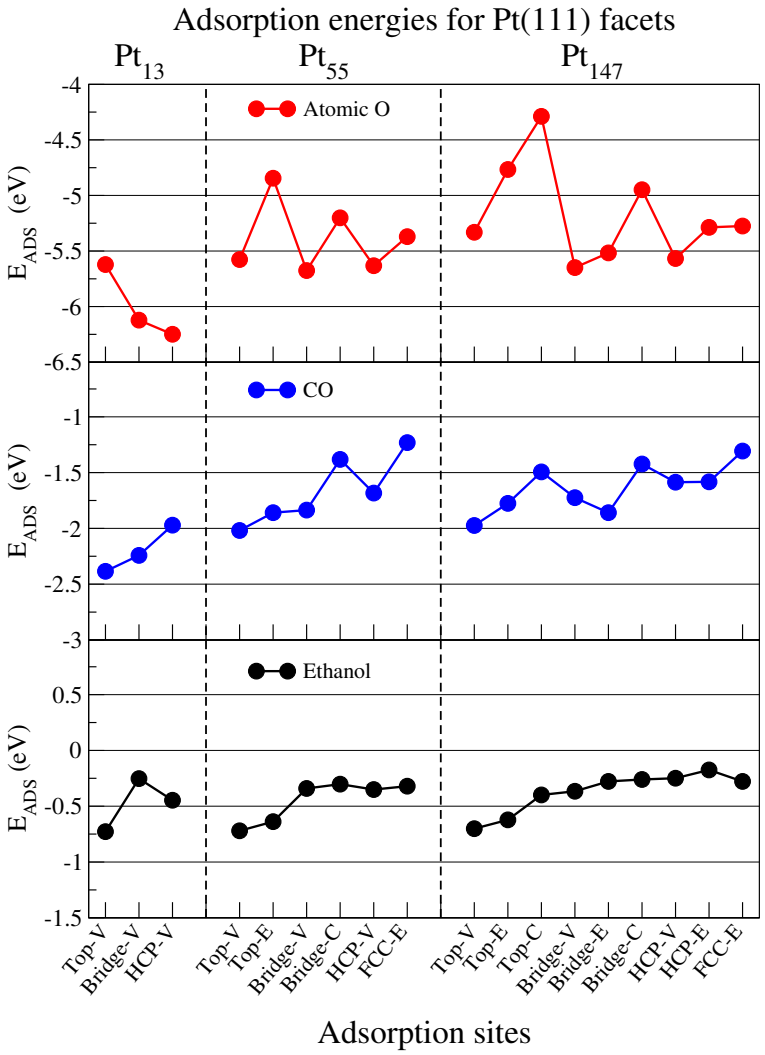

FIGURE 6.2: Adsorption energies for oxygen (red), carbon monoxide (blue), and ethanol (black) interacting with the (111) facet of Pt_{13}, Pt_{55}, and Pt_{147} on different adsorption sites. The letters V, E, and C represent adsorption sites in the vertex, edge and centre of a nanoparticle facet.

For the CO molecule, top and bridge sites near the edges and vertices of the nanoparticle facet are the favourable adsorption sites. A similar adsorption site preference was observed for icosahedral Pt_{55} nanoparticles [214] for adsorption energies computed with a vdW-DF functional and with the Grimme DFT+D3 [224] semiempirical approach. The CO/Pt(111) problem, which is the failure of DFT to reproduce the experimental result of top or bridge sites being preferred over hollow sites for a CO molecule interacting with a Pt(111) [145], is not as evident in our results as it is for Pt slabs. In nanoparticles, the adsorption energies are stronger near the edges and vertices, making the adsorption energies on Top-V, Top-E, B-V and B-E stronger than that obtained for HCP sites. However, for Pt_{147}, the adsorption energy for the HCP sites is stronger than that obtained for Top-C and Bridge-C sites, showing the same discrepancy that is

commonly obtained when comparing DFT results with experimental data for extended surfaces [145]. For CO molecules, we also observed that reducing the nanoparticle size strengthened the interaction between CO and the nanoparticle surface, which was also observed by Li *et al.* [144].

In contrast to O and CO adsorption, when ethanol interacts with Pt nanoparticles of different sizes, the adsorption site hierarchy and the strength of the adsorption remains almost constant. As an example, the adsorption energy of ethanol on a Top-V site only changed from -0.73 eV for a Pt_{13} to -0.70 eV for a Pt_{147}. In comparison, for oxygen atoms on HCP-V and CO on Top-V sites, we see differences in adsorption energies of about 0.68 eV and 0.41 eV when comparing similar adsorption sites for a Pt_{13} and a Pt_{147}. For all the studied sizes, ethanol preferentially adsorbs at Top-V and Top-E adsorption sites. For Bridge, HCP, and FCC sites, the interaction is weak, with Pt-O distances ranging from 2.8 Å to 3.1 Å. The preference for top sites in the adsorption of ethanol was also observed for Pt slabs [203, 204], extended Pt (111) monolayers [202], Pt_{13} [205] and core-shell M@Pt nanoparticles [206].

Figure 6.3 shows adsorption energies for adsorbates in contact with the (100) facet of isolated Pt nanoparticles. Again, our adsorption site hierarchy for atomic oxygen is comparable with previous studies for Pt nanoparticles [220, 221], showing a clear preference for bridge sites over top and hollow sites, and stronger adsorptions for sites near the vertices and edges of the nanoparticle. The same size effect is observed, with stronger adsorptions obtained for smaller nanoparticles.

For CO, there is a clear preference for bridge and top sites on (100) facets of Pt nanoparticles. The results for Pt_{55} and Pt_{147} are similar, showing weaker adsorptions as compared with Pt_{13}. Moreover, most of the adsorption sites on a (100) facet show comparable adsorption energies with the most stable ones observed in figure 6.2. For ethanol molecules, the top sites still are preferred over the bridge and hollow sites. However, the adsorption energies obtained for top sites on Pt(100) facets are around -0.5 eV being weaker than the -0.7 eV obtained for top sites on Pt(111).

In the literature, the catalytic activity for the ORR is commonly associated to the oxygen adsorption energy, where too weak adsorptions would hinder the molecular oxygen adsorption and dissociation, and too strong interaction would block adsorption sites and hinder the reaction. For the ORR, it is commonly suggested that the interaction of a Pt(111) slab and O is already too strong for an optimal catalyst [4, 8, 113, 179, 225, 226]. Our calculations show that the adsorption energies for sites near the edges and vertices of the nanoparticle are stronger than

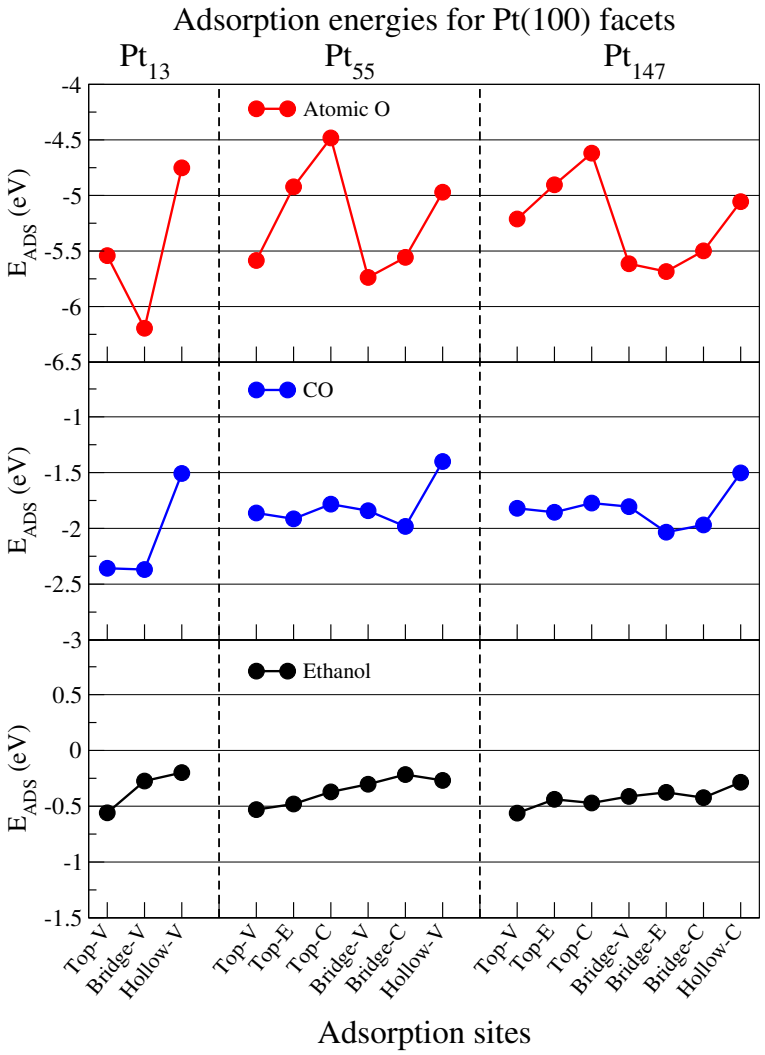

FIGURE 6.3: Adsorption energies for oxygen (red), carbon monoxide (blue), and ethanol (black) interacting with the (100) facet of Pt_{13}, Pt_{55}, and Pt_{147} on different adsorption sites. The letters V, E, and C represent adsorption sites in the vertex, edge and centre of a nanoparticle facet.

terrace-like sites and that, in the studied size range, the decrease of the nanoparticle size increases the strength of the adsorption. Moreover, as we decrease the nanoparticle size, the ratio between stronger (edges and vertices) and weaker (central) sites increases. The combination of these effects can suppress the benefits of decreasing the nanoparticle size, being also used in the literature to justify the ORR mass activity peak for Pt nanoparticles [135, 179].

For both Pt facets, we have observed that the nanoparticle size have less effects for the ethanol adsorption as compared to atomic oxygen and CO. Fajín *et al.* [81] also observed that the values of adsorption energies for water molecules interacting with Pt nanoparticles of different sizes were almost constant. In their work, the adsorption energy for a water molecule interacting with Pt_n nanoparticles in the range $13 \leq n \leq 140$ only changed from -0.58 eV to -0.47 eV,

while for coadsorbed OH and H the adsorption energies varied from -0.90 eV to -0.41 eV [81]. This effect was explained based on the changes in adsorption site preference of OH and H with nanoparticle size. Water molecules were adsorbed at on top sites for all the studied nanoparticles, while the most stable adsorption site for OH and H changed depending on the nanoparticle size. The authors concluded that the changes for adsorption energies of OH and H were not related just to size effects, but also with the changes in the optimum adsorption site of OH and H for different nanoparticles.

In our case, we cannot use the explanation proposed by Fajín *et al.* [81] to analyse the lack of size effects for ethanol adsorption energies. From our results, this effect happens even if we compare the same adsorption site for all the adsorbed species interacting with different Pt nanoparticles. Therefore, it is necessary a more in-depth investigation of the structural and electronic changes induced by the interaction of the adsorbed species with Pt nanoparticles of different sizes to explain why size effects seem to be less important in the adsorption of ethanol.

6.4 Structural and Electronic Analysis for Adsorbates Interacting with Isolated Pt Nanoparticles.

So far in this chapter, we have investigated the adsorption site preference and the adsorption energies of O, CO and ethanol interacting with Pt nanoparticles of different sizes. Here, we study this phenomenon in more detail by analysing structural and electronic changes happening in the nanoparticle and adsorbate after the interaction. We focus our attention on selected adsorption sites only for (111) facets. As the size effects for the (100) facets are similar to those obtained for (111) facets, we expect that the analysis and conclusions drawn from these results will be transferable to explain the size effects trends for the (100) facets.

Figure 6.4 shows the correlation between adsorption energies obtained for top sites placed on the (111) facet of different Pt nanoparticles and the generalised coordination numbers. We are first restraining our analysis to top sites on (111) facets to illustrate how the nanoparticle size affects the coordination for the same type of adsorption site. Moreover, ethanol adsorption is more stable on top sites, while dispersion interactions dominate the adsorption on bridge and hollow sites, as evidenced by the large Pt-O distances, ranging from 2.8 Å to 3.1 Å and by the adsorption energy values obtained in our calculations.

The correlation between adsorption energies and GCN illustrates how size effects can alter the interactions of the nanoparticle and adsorbates by modifying the environment around

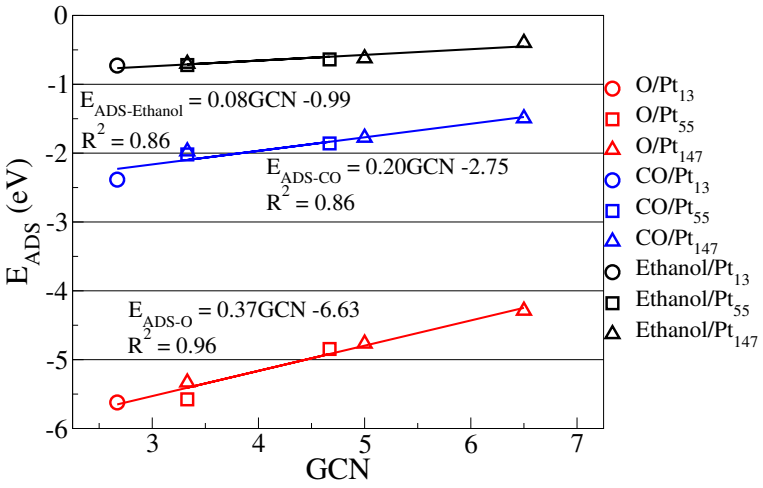

FIGURE 6.4: Adsorption energies for oxygen (red), carbon monoxide (blue), and ethanol (black) interacting with different top sites on (111) facets versus the generalised coordination number relative to each adsorption site. Circles, squares, and triangles represent Pt_{13}, Pt_{55}, and Pt_{147} nanoparticles.

adsorption sites. It also shows that the ethanol adsorption is less affected by changes in the generalised coordination number as compared with O and CO adsorptions. The equations obtained through the linear correlation between adsorption energies and generalised coordination numbers show a larger slope for the oxygen adsorption than for CO, which is different from the trends observed in the study performed by Jørgessen *et al.* [227], where the slopes for O and CO were respectively 0.22 eV and 0.25 eV.

Presenting the correlation only for top sites helps to illustrate how the nanoparticle size effects can be described to a certain extent via a purely geometrical descriptor. However, correlations between adsorption energies and the generalised coordination numbers can also be used as a predictive tool for catalyst activity in metallic nanoparticles enabling faster predictions about the interaction between a nanoparticle with a certain size and shape with adsorbates important for different chemical reactions[8, 226]. Thus, further comparisons between our findings and previous results from the literature might be interesting in that context. Figure 6.5 a), b), and c) present, respectively, the correlation between generalised coordination number and the adsorption energies obtained for adsorbates interacting with all sites on a (111) facet, and the correlations obtained only with bridge and hollow adsorption sites in the same facets.

The general trends observed for bridge and hollow adsorption sites, and consequently to the whole nanoparticle facet, are similar to that found for top adsorption sites, with the generalised coordination number of a given adsorption site controlling the adsorption energies of O and CO to a greater extent than for ethanol. For oxygen adsorption, we obtained high correlation coefficients for all the cases, while for CO, adding hollow sites worsen the correlation between

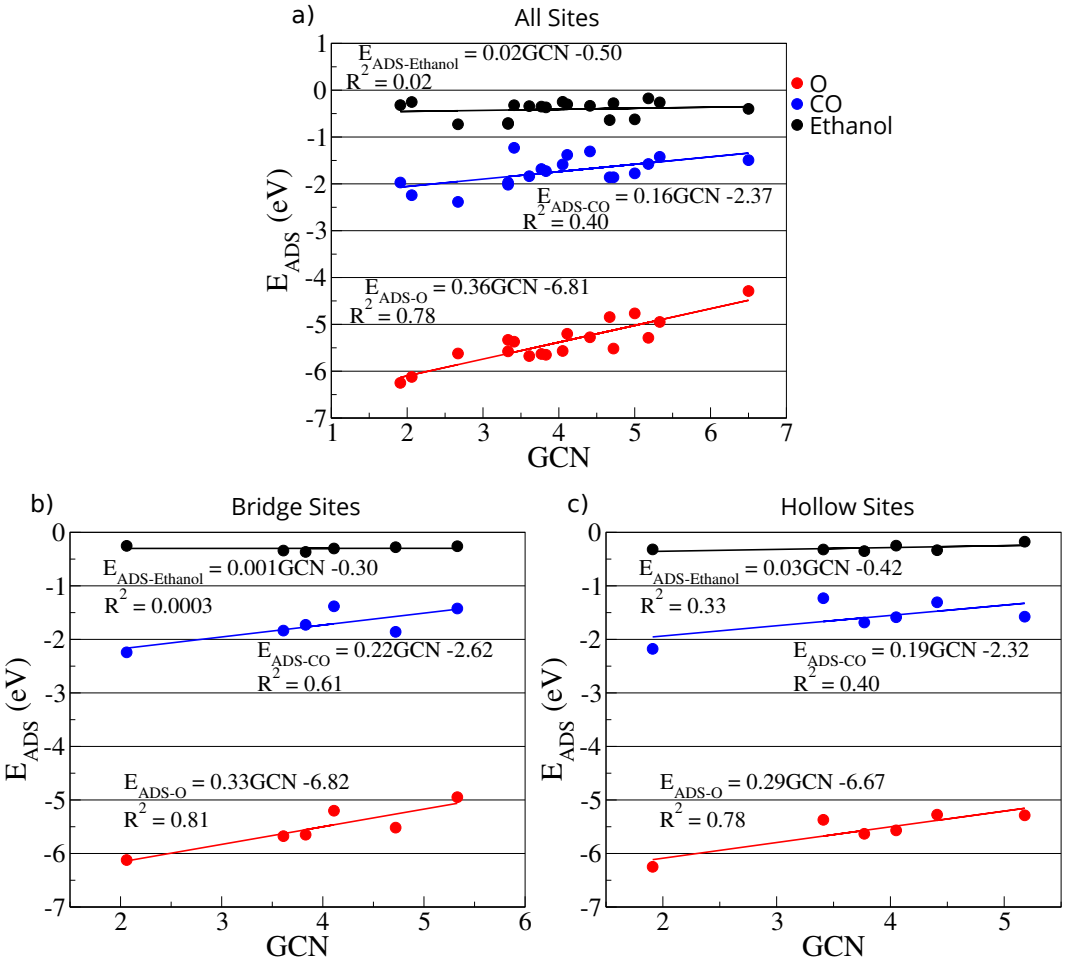

FIGURE 6.5: Adsorption energies for oxygen (red), carbon monoxide (blue), and ethanol (black) interacting with different adsorption sites on (111) facets versus the generalised coordination number relative to each adsorption site, where a) presents all adsorption sites on a (111) facet, while b) and c) presents bridge and hollow sites.

adsorption energies and the generalised coordination numbers. For the ethanol adsorption, the slopes of the linear equations and the correlation coefficients are considerably smaller for bridge and hollow sites as compared with the results for top sites. These findings are consistent with the results that show ethanol adsorption being favourable on top sites, with the adsorption energies for bridge and hollow sites being dominated by dispersion interactions.

Differently from our results, the work from Jørgessen *et al.* [227] obtained for CO and O adsorption that $E_{ADS-CO} = -1.36 + 0.252(GCN - 7.5)$ and $E_{ADS-O} = 0.95 + 0.218(GCN - 7.5)$. The differences between our results for the y-intercept and the ones from Jørgessen *et al.* can be explained by the usage of different codes, exchange-correlation functionals and strategies to obtain the adsorption energies. The main differences in the y-intercept are observed for the O adsorption due to the difference in the reference system used to calculate the adsorption energies. While we use an O atom as the reference system for the adsorption energies, the authors use half

of the energy of an O_2 molecule in the triplet state. Moreover, while we calculate the adsorption energies on rigid nanoparticles, the authors obtained their results on slab models, allowing two layers of Pt to relax during the interaction with the adsorbates, which can generate a shift in the adsorption energies as compared to our results.

Meanwhile, the differences in the slopes are caused by the methodology used to choose the adsorption sites and obtain the linear correlations. The authors obtained the correlations using the most stable adsorption sites for each adsorbate. More specifically, for CO, the authors used only top sites, and for O they use bridge sites on Pt(100), Pt(110), and Pt(211) and an FCC site for Pt(111). The slope we have obtained for top sites with CO is close to the one obtained by Jørgessen *et al.*, while the ones from atomic oxygen are different. As we change the selection of adsorption sites from top to bridge and hollow sites, the correlation slope becomes closer to the one Jørgessen *et al.*. These changes in the linear equations and correlation coefficients for each adsorbate depending on the type of adsorption site used to generate the correlation indicates the importance of a careful parametrisation when using linear equations from generalised coordination number correlations to predict adsorption energies.

This correlation between the Pt nanoparticle size effects and the level of coordination of an adsorption site is also compatible with the findings from Li *et al.* [144]. By studying size effects on Pt and Au nanoparticles ranging from 13 to 1415 atoms, Li *et al.* [144] observed that the spacing in the d-band projected density of states near the Fermi level, caused by quantum size effects, only played a role for Au_{13} clusters. For Pt clusters, the discreteness in the d-band DOS was much smaller, and the size effects observed for Pt were also explained in terms of the coordination numbers of the adsorption sites and as a consequence of the proximity to the edges of the nanoparticles.

Additionally to the changes in the level of coordination of adsorption sites, decreasing a nanoparticle size also generates changes in the bond lengths on the metallic surface. Strains in the bond lengths in the nanoparticle surface are also associated with changes in the strength of the interaction between nanoparticles and adsorbates. To assess the importance of these changes, we have constructed cuboctahedral nanoparticles created with Pt-Pt bond lengths similar to those obtained for experimental Pt bulk, with a lattice parameter of 3.92 Å[228, 229], and calculated O, CO and ethanol adsorption using these nanoparticles. Figure 6.6 shows the difference between adsorption energies obtained with the cuboctahedral Pt nanoparticles created with Pt-Pt bond lengths from experimental Pt bulk and the adsorption energies obtained with geometry

optimised Pt nanoparticles. The size effect decreases the Pt-Pt bond lengths, and these deformations change the adsorption energies. The results show that the deformation is not as important as other changes caused by altering the nanoparticle size, with the shifts in adsorption energies being closer or smaller than 0.1 eV in all the cases.

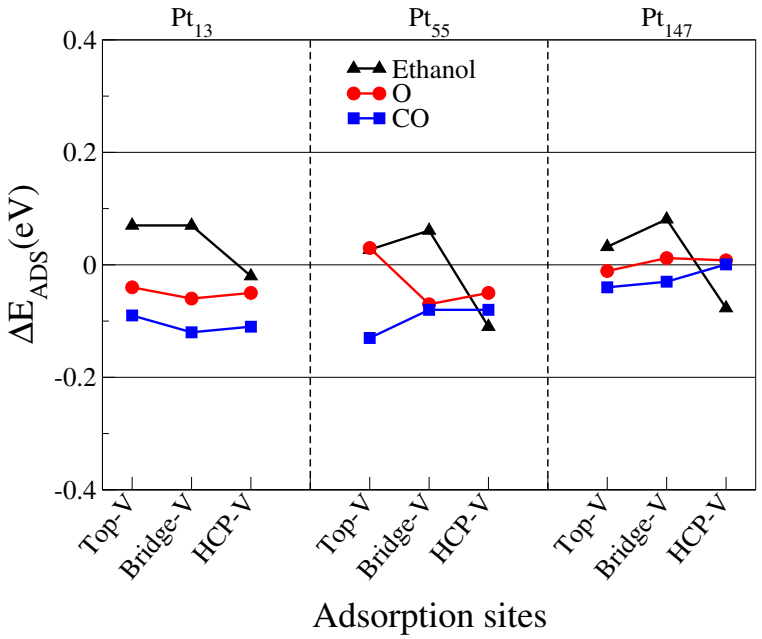

FIGURE 6.6: Differences between the adsorption energies of O, CO and ethanol obtained using geometry optimised nanoparticles and those obtained using unrelaxed Pt nanoparticles created with bond lengths from experimental Pt bulk. The letter V represents adsorption sites in the vertex of the nanoparticle facet.

Up to now, we have investigated the size effects for the adsorption of O, CO and ethanol on Pt nanoparticles, and encoded these results in terms of geometrical descriptors. We have observed that the interactions of O and CO with Pt nanoparticles are more affected by size effects than the interaction between ethanol and Pt. The difference in size effects is also evident in the slope of the correlation between adsorption energies and generalised coordination numbers, showing that, despite some similarities, the bonding mechanism for ethanol on Pt surfaces is different to O and CO. To assess the importance of dispersion interactions for each adsorbate, we have calculated the adsorption energies with the rPBE [22] functional and compared the results with our calculations with the vdW functional rVV10 [185, 186]. Figure 6.7 shows similar adsorption energy hierarchies obtained with rPBE and rVV10 for all adsorbates. The dispersion interactions are much more important for ethanol adsorption than for O and CO, being one of the main contributions for stabilising the ethanol molecule on Pt surfaces. This importance of the dispersion interactions for the ethanol adsorption was also observed by Tereschuck and Da Silva

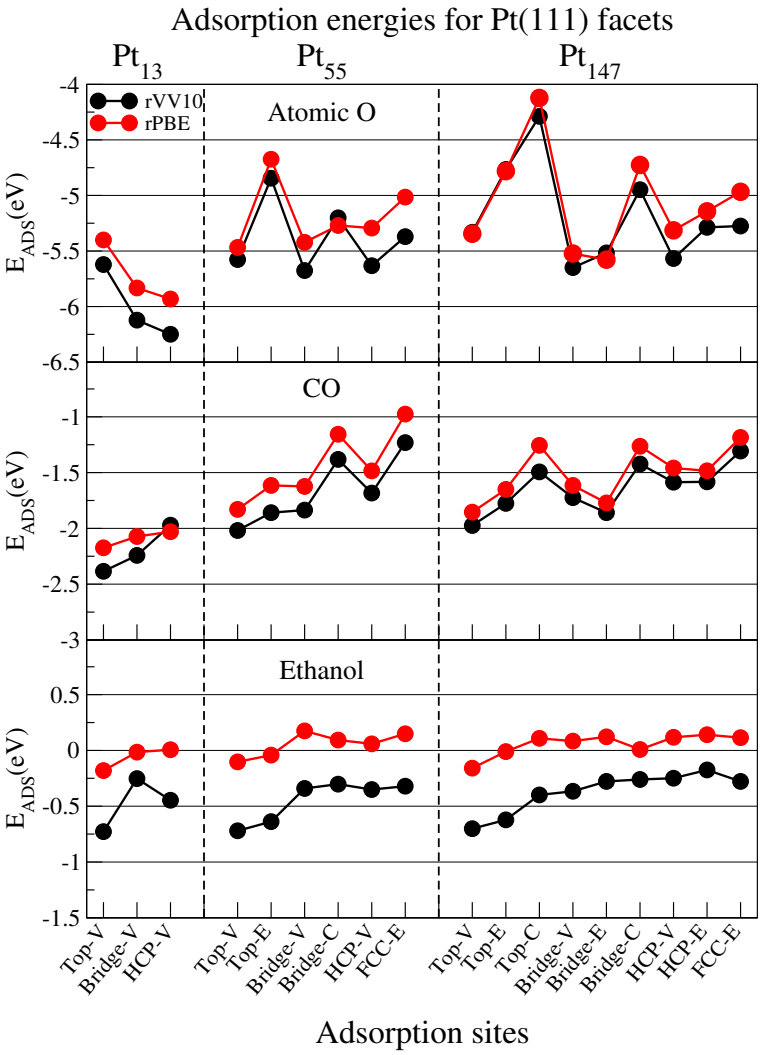

FIGURE 6.7: Adsorption energies for oxygen, carbon monoxide, and ethanol interacting with the (111) facet of Pt_{13}, Pt_{55}, and Pt_{147} on different adsorption sites. Red (black) circles are adsorption energies obtained with the rPBE (rVV10) functional. The letters V, E, and C represent adsorption sites in the vertex, edge and centre of a nanoparticle facet.

[203], where the ratio between the adsorption energies obtained with and without dispersion interaction was approximately 3.25 for ethanol molecules.

To obtain more information about how interactions between adsorbates and Pt surfaces occur, we show in figure 6.8 electronic density differences and Mulliken charge differences for each adsorbate interacting with Pt nanoparticles. For this analysis, we selected the energetically favoured sites for each adsorbate, namely HCP-V adsorption sites for O and Top-V for CO and ethanol.

For O and CO we see significant electronic rearrangements, with Mulliken charges indicating that electrons flow from the metallic surface to the adsorbates. The overall electronic density rearrangement does not change with the Pt nanoparticle size. For the atomic oxygen

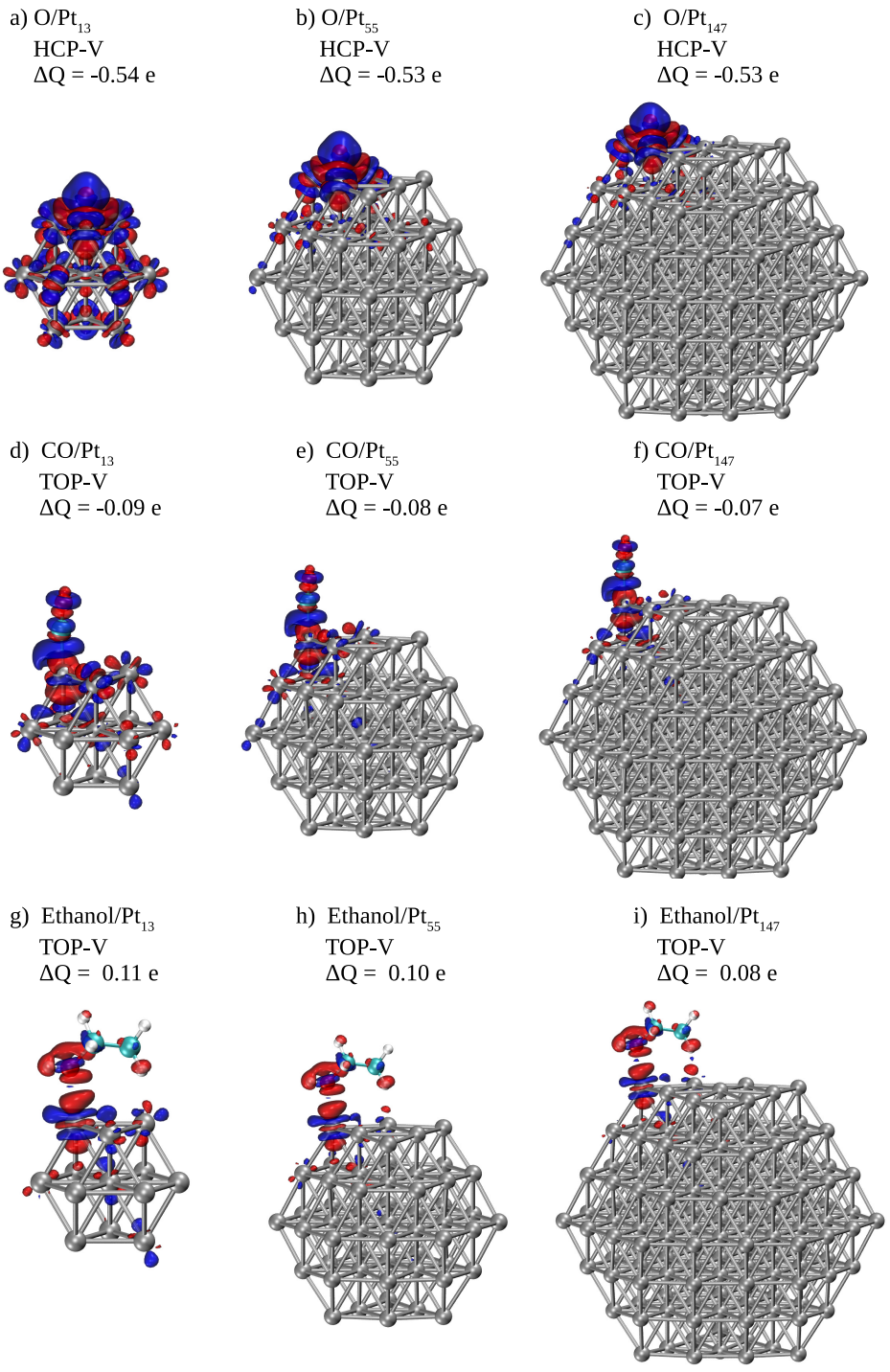

FIGURE 6.8: Electronic density differences plots for O, CO and ethanol interacting with Pt_{13}, Pt_{55}, and Pt_{147} nanoparticles (Isosurface at 0.02e/ $Å^3$), where blue (red) represents electron accumulation (depletion). The numbers associated with each plot are overall Mulliken charge differences calculated for each adsorbate, where a negative number represents adsorbate receiving electrons. We show the results for O interacting in the HCP-V adsorption site and CO and ethanol adsorbed on TOP-V sites.

adsorption, we observe that the electronic density change is more local for larger nanoparticles. The electronic density rearrangement caused by the adsorption is slightly smaller for ethanol than that observed for CO, and considerably smaller as compared to the changes caused by the interaction with O. Regarding the Mulliken charges, only two atoms in the ethanol molecule show considerable differences, the O atom in contact with the Pt surface and the H atom in the CH_3 group near the Pt surface. While the O atom loses electrons after the interaction, the H atom receives it, with an overall electron donation from ethanol to the Pt surface.

According to the d-band model [4, 99, 100], the interaction of adsorbates and a metallic surface can be separated in two terms. The first is the interaction of the adsorbate states with the s metallic states, which should be similar for different metallic surfaces due to the delocalisation character of the metallic s states. The second term is the interaction of the metallic d-states and the valence states from the adsorbate. The d-band, differently from the s states, is localised and considered to be the main reason for differences in the adsorption energies when comparing different metallic surfaces. According to this model, the centre of the d-band can also be used as a descriptor for the adsorption energies.

Figure 6.9 shows the density of states projected on the d-band of surface Pt atoms in the interacting region with the adsorbates. We show the density of states before and after the interaction with each adsorbate, using the adsorption sites presented in figure 6.8 for Pt_{13} and Pt_{147}. The analysis of the changes caused in the d-band after interaction with an adsorbate can provide qualitative information about how the adsorption happens, helping to explain the lack of size effects observed in the ethanol adsorption.

Figure 6.9 a), b, d), and e) shows new peaks in the density of states in the Pt facet after the interaction with O and CO, indicating the appearance of overlapping orbitals at the adsorbate/Pt interface. Atomic oxygen induces extra peaks around -6 eV, showing the overlap of p oxygen states with d states from the Pt surface. For the CO adsorption, extra peaks are observed around -10 eV and between -7 eV and -6 eV, arising from the overlap between the d-band of the Pt surface and CO orbitals. Other small peaks due to the interaction with the adsorbates are observed for lower values of energy. Such orbital overlaps were already observed and discussed in more details in previous theoretical studies, such as the work developed by Lynch and Hu [222].

For ethanol adsorption, the changes in the d-band density of states are much smaller as compared with the changes caused by O and CO adsorption. The main differences in the density of states are the intensity of the peaks due to the electronic repopulation and the appearance of small peaks that are not changing the overall d-band DOS. The results from the density of

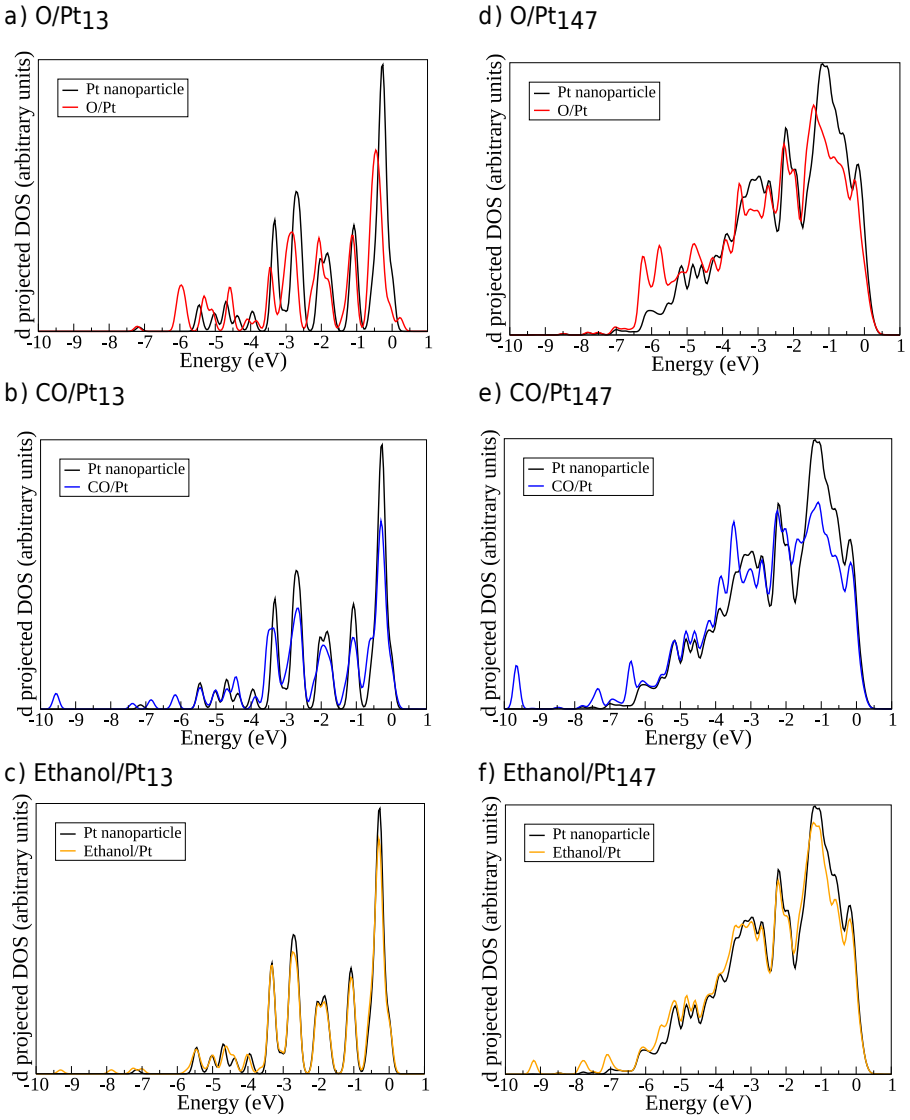

FIGURE 6.9: Local and angular momentum projected density of states (l-p-DOS) of the d-band of Pt atoms in the interacting region of the (111) facet. Figure a), b), and c) show the density of states for Pt_{13} interacting with O, CO, and ethanol. Figure d), e), and f) show O, CO, and ethanol interacting with Pt_{147}.

states show that the interaction between the d-band of the Pt surface with adsorbates states is much more relevant for O and CO adsorption than for ethanol. As changes in the d-band are consequences of altering the nanoparticle size and the coordination of the adsorption site, we should expect that the adsorbates with stronger interactions with the d-band would suffer more these effects, which also helps to explain the small slopes found for ethanol adsorption as compared with O and CO in figure 6.4.

Thus, as a large amount of the ethanol adsorption energy arises from dispersion interactions, which are not largely affected by the Pt nanoparticle size, and as we see a small interaction between ethanol and d-states from the Pt surface, it is expected that nanoparticle size effects are

TABLE 6.1: Atomic distances between Pt-O, Pt-C, C-O, and C-H, from the CH_3 group for O, CO, and Ethanol adsorbed on Pt nanoparticles.

System	Pt-O (Å)		
HCP-V O/Pt_{13}(111)	2.08		
HCP-V O/Pt_{147}(111)	2.10		
System	Pt-C (Å)	C-O (Å)	
CO Isolated	-	1.14	
Top-V CO/Pt_{13}(111)	1.85	1.16	
Top-V CO/Pt_{147} (111)	1.89	1.16	
System	Pt-O (Å)	C-O (Å)	C-H (Å)
Ethanol Isolated	-	1.45	1.10
Top-V Ethanol/Pt_{13}(111)	2.25	1.49	1.11
Top-V Ethanol/Pt_{147}(111)	2.24	1.50	1.12

less important for ethanol adsorption. Additionally, a recent work from Kakekhani *et al.* [230] demonstrated that the covalent contributions can be much less important for the adsorption energies of closed-shell adsorbates such as water, alcohols, ammonia, on metallic surfaces than for unsaturated intermediates such as O, OH, CO. The authors show that the correlation slope between adsorption energies of water and O is small, helping to explain the small slope in the correlation between ethanol adsorption energies and descriptors such as the generalised coordination number or d-band centres, which successfully describe the O adsorption.

Analysis of geometric changes in the adsorbate can also provide valuable information about the interaction and its effects. Table 6.1 shows atomic distances for Pt-O, Pt-C, C-O, and C-H, from the CH_3 group, after the interaction with the nanoparticles. For atomic oxygen and carbon monoxide, we observe a small increase in the distances between the metallic surface and the interacting atom from the adsorbate as we increase the nanoparticle size. These changes in bond lengths agree with the weakening in adsorption energies previously observed. For adsorbed ethanol, no substantial difference is observed in the Pt-O distances, which also agrees with the lack of size effects observed in the energetic profile.

For CO and ethanol adsorbed at Pt nanoparticles we also observe changes in the C-O bond lengths, increasing from 1.45 Å (1.14 Å) for isolated ethanol (CO) to up to 1.50 Å (1.16 Å). For the ethanol adsorption, most of the other internal bond lengths remain almost constant, with the C-H bond, increasing up to 0.02 Å due to the interaction of the hydrogen atom with the nanoparticle surface as evidenced in figure 6.8, and with the C-C bond decreasing 0.01 Å. However, the changes for C-H and C-C bonds are minimal when compared with the change in the C-O bond. We have also found small increases in CCO and HOC angles as compared with the isolated ethanol molecule.

6.5 O, CO, and Ethanol Interacting with Pt Nanoparticles Supported on Graphene

After studying size effects on the adsorption of O, CO, and ethanol on Pt nanoparticles, we have simulated the same Pt nanoparticles in contact with a pristine graphene sheet. These calculations aim to describe how the interplay between support and nanoparticle size affects the adsorption properties of the Pt nanoparticles. We focus our analysis for systems where the Pt nanoparticle interacts with the graphene support via the (111) facet, as this interaction is stronger than the one obtained when the (100) facet is in contact with the support.

Adsorption energies were calculated only for facets far from the support. Using this strategy we assess the effects of the support in the nanoparticle properties and avoid direct interactions between support and adsorbate. We have reduced the number of calculated adsorption sites for Pt_{147} nanoparticles due to the high computational demand of such simulations and due to the reduced support effect with increasing system size which was previously observed in chapter 5 and in the literature [161]. Figure 6.10 illustrates the effect of the support by showing adsorption energies for different adsorption sites on a Pt(111) facet.

In general, the presence of support weakens the interaction between adsorbates and the Pt surface. No meaningful change in the adsorption site preference due to the support effects was observed. In all the simulated cases, the change in adsorption energy due to the presence of the graphene support was smaller than 0.3 eV. The effect is smaller than the differences observed for isolated Pt nanoparticles when comparing different adsorption sites and smaller than the changes due to size effects for CO and O, but larger than the differences observed due to the size effects for ethanol molecules.

Similar effects were also observed by Lim and Wilcox [165] for an O_2 molecule, and by Fampiou and Ramasubramaniam [160] for CO molecules interacting with Pt_{13}/graphene systems. In both cases, the authors also included defects on the graphene support that enhanced the interaction between Pt and graphene and, consequently, the effects of the support in the interaction with the adsorbates. As commented in our previous chapter, the interaction with graphene causes changes in Pt-Pt bond length, in the d-band centres, and makes the Pt atoms more anionic.

Changes in bond lengths and d-band centres also happened due to the size effects in our analysis for isolated nanoparticles and can be used to explain the support effect for O and CO. For ethanol, our previous results for isolated nanoparticles demonstrated that the Pt-Pt bond lengths and d-band centre changes were not able to change the ethanol adsorption energies to this

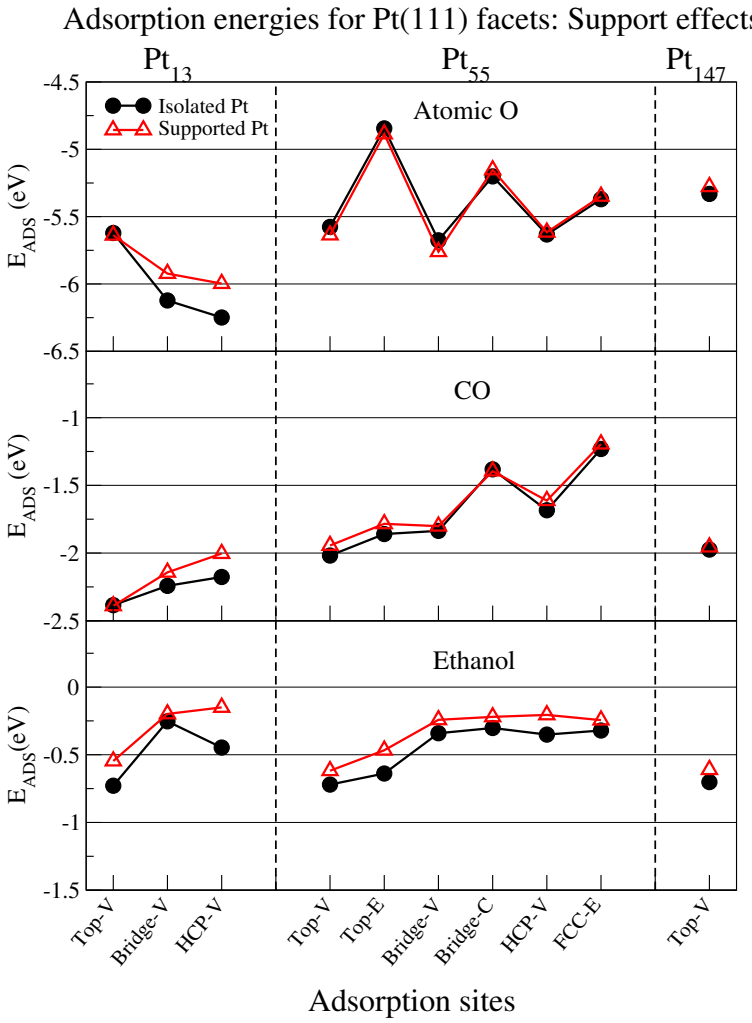

FIGURE 6.10: Adsorption energies for oxygen, carbon monoxide, and ethanol interacting with the (111) facet of Pt_{13}, Pt_{55}, and Pt_{147} on different adsorption sites. Black dots are adsorption energies obtained with isolated Pt nanoparticles and red triangles are the adsorption energies for Pt nanoparticles supported on graphene. The letters V, E, and C represent adsorption sites in the vertex, edge and centre of a nanoparticle facet.

extent. Recently, Seminovski *et al.* [231, 232] and Kakekhani *et al.* [230] demonstrated that the ethanol adsorption is stronger on cationic adsorption sites and that in some cases the electrostatic effects can be dominant [230]. Thus, a possible explanation for the support effect for ethanol adsorption can be the change in the atomic charges for the surface Pt atoms. However, additional results with different supports would be necessary to a more in-depth test of this explanation.

As previously observed, the interaction between Pt nanoparticles and the graphene support decreases with the Pt nanoparticle size. Moreover, as the Pt nanoparticle grows, more Pt layers are added between the interface Pt/graphene and the Pt facets far from the graphene. These effects decrease the graphene support effect on the adsorption properties of the Pt nanoparticle as we increase the Pt system size, being as small as 0.1 eV for Pt_{55} and Pt_{147}. Similar trends were

also obtained for adsorbates interacting with the Pt(100) facet of supported nanoparticles and for nanoparticles interacting with the (100) facet with the graphene support, which are described on appendix A.

Figure 6.11 shows how the correlation between adsorption energies and generalised coordination numbers changes for supported nanoparticles. As observed in figure 6.10, the support effects are more evident for adsorption sites on Pt_{13}, which are the three sites with lower generalised coordination numbers in figure 6.11 and analysis of this type of trend should be carefully performed. Thus, for more rigorous analysis, we show in figure 6.11 b) only the results for O adsorption and restrain our discussions to this adsorbate.

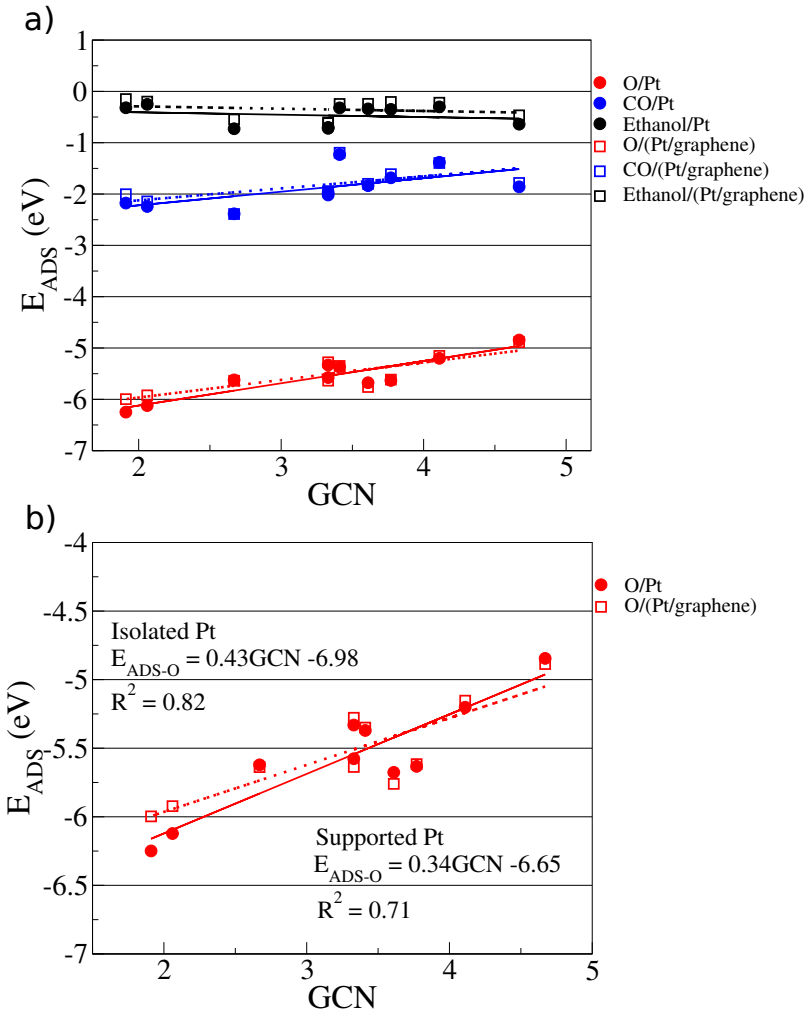

FIGURE 6.11: Adsorption energies for O (red), CO (blue) and ethanol (black) on isolated (filled circles) and supported (open squares) Pt nanoparticles. The adsorption sites used for these plots are the ones presented in figure 6.10. The continuous (segmented) lines are linear regressions obtained for isolated (supported) systems.

We observe that considerable changes only happen for two adsorption sites, which makes

the slope of the linear regression to drop from 0.43 eV for isolated nanoparticles to 0.34 eV on supported nanoparticles. These results can be misleading, showing changes in the slopes which are nothing but an artefact caused by the lack of support effects on larger nanoparticles and such relations should not be used to predict the support effect for other nanoparticles and adsorption sites. As an example, one might calculate with the obtained equations that the oxygen adsorption energy for a top site in the centre of a Pt_{309} nanoparticle (GCN=7.5) will be almost 0.2 eV stronger for the supported case, which contradicts the lack of support effects observed for larger nanoparticles.

We believe that to see how the linear dependence of adsorption energies on GCN changes due to the support effects, which would indicate if the support changes each adsorption site differently, it is necessary to simulate similar systems on supports with stronger interaction with nanoparticles, such as metal-oxides or supports with point defects. Supports with stronger influence on the nanoparticle would allow assessing these effects on larger nanoparticles with various adsorption sites and draw a better and more reliable correlation about the impact of the support on different adsorption sites. However, as these correlations rely solely on a geometrical descriptor, we do not expect them to be transferable to different nanoparticle sizes, shapes or to nanoparticles interacting with the support through different facets.

Ramos-Sánchez and Balbuena [163] also observed a similar decrease of support effect within the system size for Pt nanoparticles interacting with graphite supports. Furthermore, the small effect of the support for Pt facets far from the interface was recently observed for metal oxide supports [152], which have much stronger interactions with Pt nanoparticle than pristine graphene. However, even with a support with weak interaction, such as pristine graphene, we have managed to show that the support effects can be used to control the adsorption energies of ethanol, which is not strongly dependent on the nanoparticle size and shape, and that the support effect has a size dependency.

The size-dependency of the support effect could have interesting implications in terms of catalyst design and might be useful to explain some recent experimental findings. As commented before, the increase in the oxygen adsorption strength with decreasing nanoparticle size is commonly indicated as a reason for the decrease in mass activity with nanoparticles smaller than 2 - 2.5 nm [179]. However, recent experiments have been showing a remarkable increase in catalytic activity for ORR on size-selected subnanometer Pt clusters on carbon-based supports [142, 233]. There is intense debate around the reasons that could lead to this unusual behaviour. Possible explanations for this effect include the flexibility of such small clusters and the number

of isomers shapes that could adapt to break the linear-scaling relationships between the adsorbates and thus increase the activity [234, 235], and the changes in the cluster structure in this size range [233].

However, another possible explanation for this effect could be related to the size-dependency of the support effects on the adsorption properties of the metallic clusters. Our calculations show that the presence of the graphene support weakens the adsorption energies of atomic O, which would alleviate the drop in catalytic activity for smaller Pt nanoparticles and clusters. This effect is expected to be larger for graphene supports with point defects [160, 165], which are supposed to be the anchoring points for the metallic clusters [159, 167]. Thus, the increase in support effects with decreasing of nanoparticle size could be an additional factor to help to explain the ORR activity for subnanoclusters, pointing to the importance of controlling the nanoparticle size and support simultaneously to design catalysts for specific reactions.

6.6 Conclusions

We have performed DFT simulations to study how the presence of the support and the nanoparticle size can affect the adsorption strength of O, CO and ethanol on Pt surfaces. We have computed Pt cuboctahedral nanoparticles free and supported on graphene, where we have simulated nanoparticles with up to 147 atoms interacting with graphene with up to 720 carbon atoms. We sampled adsorption sites on (111) and (100) Pt facets for all nanoparticles, obtaining adsorption sites hierarchies similar to the ones observed in the literature for all the adsorbates.

The energetically favourable adsorption sites for atomic O were bridge and HCP sites near the edges of the nanoparticle facet. For the CO adsorption, bridge and top sites near the vertex of the nanoparticle presented stronger adsorption energies, while for ethanol, top sites near the edge and vertex of the nanoparticle are the most stable adsorption sites. For O and CO, as the Pt nanoparticle size increases the adsorption energies weaken. The same effect was not observed when ethanol interacted with Pt nanoparticles. We encoded the effects of size and the multiplicity of adsorption sites via a geometrical descriptor, showing a linear correlation between the adsorption energies and the generalised coordination number, which controlled the adsorption strength of O and CO to a greater extent as compared with ethanol.

We have analysed electronic density difference plots, charge differences obtained via Mulliken populations and densities of states projected on the d-band of interacting Pt atoms. The electronic redistributions due to the interaction with the adsorbate are much more local for

ethanol than for O and CO. In the density of states plots, we observed the appearance of extra peaks related to overlapping states between the Pt surface and adsorbate for O and CO, while the ethanol interaction only induced small changes in the d-band peaks intensities. These characteristics of the ethanol interaction and our observations regarding the importance of dispersion interaction in the adsorption energies of ethanol on Pt surfaces helped to explain the weaker size effect observed for ethanol on Pt nanoparticles as compared with O and CO.

Finally, we have observed weakening in the adsorption energies of O, CO and ethanol due to support effects. The weakening was attributed to the Pt lattice deformation, changes in the d-band centre, and electronic redistribution associated with the interaction between Pt nanoparticle and support. The support effect is also size dependent, and its influence on the adsorption energies was only significant for Pt_{13} nanoparticles, which could have impacts for catalyst design. For example, the weakening of the O adsorption energy can alleviate the negative effect that decreasing the nanoparticle size can have for the ORR. As we start decreasing the Pt nanoparticle size, from the optimum ORR mass activity obtained for nanoparticles with a diameter of around 2 nm, we generate an increase in adsorption energies that hinders the ORR. Below a certain size, the presence of the support starts affecting the nanoparticle and weakens the interaction between nanoparticle and oxygen, with the importance of the support effect increasing as we decrease the nanoparticle size. In that sense, the competition of support and size effects, together with the flexibility of small clusters [234, 235] and the different structures that small clusters can adopt [233] could be used to help to explain the unusual increase in ORR activity for size-selected subnanometer Pt clusters on carbon-based supports [142, 233].

The fact that the ethanol adsorption energies remained stable for different nanoparticle sizes, but were changed due to support effects also show possible ways of tuning the adsorption energies for specific adsorbates. As atomic oxygen adsorption is widely used as a descriptor for several chemical reactions; CO is a key contaminant for Pt catalysts; and ethanol adsorption is the first step in the ethanol oxidation reaction and can be used as a descriptor for ethanol dehydrogenation, we expect that our results will be useful for rational catalyst design, providing insights about the importance of controlling Pt nanoparticle size and support concurrently in order to develop better catalysts.

Chapter 7

DFT Calculation of Oxygen Adsorption on Platinum Nanoparticles: Coverage and Size Effects

In this chapter, we study how the oxygen adsorption changes due to the combination between nanoparticle size effects and changes in the adsorbate coverage for cuboctahedral platinum nanoparticles. This work was published as a manuscript on "Faraday Discussions" [13].

L. G. Verga, J. Aarons, M. Sarwar, D. Thompsett, A. E. Russell, and C.-K. Skylaris. DFT Calculation of Oxygen Adsorption on Platinum Nanoparticles: Coverage and Size Effects. Faraday Discuss., 208:497–522, 2018.

in which, I participated in all the stages of the work. Dr. J. Aarons contributed with the l-p-DOS method and with corrections in the manuscript. All the other authors participated with corrections and ideas for the manuscript, with the whole work being supervised by Prof. Chris-Kriton Skylaris.

Abstract

Catalysts made of Pt nanoparticles and Pt alloys are considered state-of-the-art catalysts

for anodic and cathodic reactions for different fuel cells architectures. The optimal size of such nanoparticles for each chemical reaction is a problem of constant debate. From a theoretical point of view, an approach to study these questions is observing how key adsorbates react with different nanoparticles in controlled conditions. In this chapter, we use large-scale DFT calculations to examine the interplay between the Pt nanoparticle size and the effect of changing the O coverage. We study the effect of oxygen coverage with varying fractions of O monolayer coverage, computing adsorption energies per O atom for Pt_{55}, Pt_{147}, and Pt_{309} nanoparticles. In general, the increase of O coverage lead to weaker adsorption energies per O, and when analysing the results in terms of oxygen monolayers, this effect is more pronounced for larger nanoparticles. We analyse the dependency of the adsorption energy per O atom on the O coverage in terms of the adsorbate distribution for each nanoparticle size and electronic changes that the adsorbed oxygen causes to the Pt nanoparticle. In studying nanoparticle size and oxygen coverage effects simultaneously, we offer insights with DFT accuracy to help heterogeneous catalyst design.

7.1 Background

As commented in the previous chapter, a deeper understanding of the interaction between catalyst surfaces and reactants, products and intermediates is fundamental in the study of new catalysts for different reactions. Thus, computational studies performed with density functional theory (DFT) and molecular dynamics (MD) on atomic and molecular adsorptions on catalytic surfaces are simple and powerful tools to provide insights for this area.

As we increase the adsorbate coverage, the system complexity and computational cost of such simulations grow. Thus, most of the computational studies on the interaction of atomic oxygen and metallic surfaces has been treating the problem in the low O coverage limit. However, adsorption energies depend on the adsorbate coverage. Usually, this effect is explained using the electronic and geometric changes that the catalytic surface suffers due to the presence of adsorbates and due to the presence of adsorbate-adsorbate interactions. For example, Miller and Kitchin [236] have studied the coverage effects for atomic oxygen interacting with Pt and Au fcc (111) surfaces, observing a weakening in the adsorption energies generated by the oxygen coverage increase. They have shown that oxygen coverage increases induce changes in electronic properties of the metallic surfaces, such as a downshift in the d-band centre energies

and a broadening of the d-band of surface atoms [236]. The dependency of the adsorption energies in the adsorbate's coverage has also been described for Pd (111) facets and atomic C, N and O [237], which has also been corroborated on different metallic slabs [238–240].

In another study, Bray, Skavdahl, McEwen, and Schneider [241] have shown that the changes in the O adsorption energies with different adsorbate coverages depends on the adsorbate cluster configuration formed on the catalyst surface. Treating different clusters configurations of adsorbates solely with DFT can be extremely expensive. Thus, the authors have explored the configuration of the adsorbates on the metallic surface with cluster expansions methods [241–245], showing that finding the minimum energy configuration can be a key step to reproduce temperature programmed desorption experiments with first principle calculations [241]. Getman and Schneider [243] and Frey, Schmidt, Wolverton, and Schneider [244] have also demonstrated the importance and non-uniformity of the coverage effects for the activation energies of reaction steps involved in the NO oxidation reaction. Bray, Smith and Schneider [245] have also simulated stepped, kinked Pt (321) surfaces as models for the catalytic activity of metallic nanoparticles, studying the interplay between the structural changes and the O coverage effects for the O adsorption. They have shown that on Pt (321) surfaces, bridge sites at the step edges are the prefered adsorption sites for atomic O on low O coverages and that the coverage increase makes O to adsorb on threefold hollow sites forming PtO_4-like structures.

As already mentioned in our previous chapters, most of the materials used for producing catalysts for fuel cells applications are expensive metals such as Pt, Pd, and Au and the usage of nanoparticles can help to alleviate the catalysts cost by increasing its surface area per mass. The usage of metallic nanoparticles introduces a rich variety of adsorption sites with dramatically different interactions to adsorbates as compared to the adsorption sites commonly observed on extended (111) or (100) facets. Similarly to what we have described for metallic surfaces, studying the adsorbate coverage effects on metallic nanoparticles with DFT calculations is a computationally demanding task. Thus, DFT-based studies with metallic nanoparticles are usually carried out in a low-coverage approximation.

However, it is still possible to highlight a few studies carried out both with DFT and MD calculations. An example of such studies is the work from Wei and Liu [136], which has shown with DFT calculations that the O coverage for Pt nanoparticles should be lower at terrace sites for the (111) facets than the one obtained for edge adsorption sites, indicating that the oxidation on Pt nanoparticles should start in the nanoparticle edges. They have also demonstrated that the coverage for the (100) facets should be higher than the one observed on (111) facets [136].

Jinnouchi, Suzuki, and Morimoto [246] have also studied the coverage effects with DFT calculations, showing that Pt electro-oxidation should start via the adsorption of OH adsorbates near the edges of the nanoparticles. The increase of the electrode potential would make O replace OH species in these adsorption sites, which will become fully covered by O and become inactive for the ORR. The authors have also indicated that the adsorption sites near the edges should be the starting point for corrosion, proposing the doping of the Pt nanoparticles with Au atoms as a solution to alleviate this problem [246]. Jinnouchi, Suzuki, and Morimoto [246] have also observed oxygen atoms moving to subsurface sites with increasing O coverage, which was also previously observed on experimental research [247, 248], with MD calculations [249], and with DFT calculations for Pt slabs [223]. Subsurface oxygen is an important phenomenon on catalysis research that is usually associated with the catalyst corrosion and to changes in the catalyst surface reactivity [247, 248, 250].

Recently, Gai *et al.* [249] have studied the coverage effects for Pt catalysts using molecular dynamics calculations on different Pt nanoparticles and Pt surfaces. For Pt spherical nanoparticles, they have observed that O adsorbs first on hollow sites, followed by O adsorption on subsurface sites. They have also observed that the size effect changes the necessary O pressure to form bulk oxides, with large nanoparticles requiring a higher pressure as compared with small clusters. They have explained these effects based on the decrease of the adsorption energies of O with increasing size and due to the change in the ratio between edge sites and terrace sites, which is higher for small nanoparticles. The effect of adsorption sites in the edges and corners of the nanoparticles was also tested by comparing different Pt nanoparticles shapes with similar sizes. They have observed that the octahedron models, which have a higher percentage of edges and corners, showed higher oxygen coverages when compared with cuboctahedral and cubic models in the same conditions [249].

Here, we show a detailed test of different methodologies used to tackle the oxygen coverage problem solely with DFT calculations, showing the limits of each approximation made to reduce the computational cost. The chosen methodology is then used to study the complicated combination between O coverage and Pt nanoparticle size. By computing different O coverages for three nanoparticle sizes, we expect to provide insights about these effects for practical catalyst design.

7.2 Computational Details

We have performed our DFT calculations with the ONETEP program [28] within the EDFT method [2]. We have adopted the rPBE functional [22] as our exchange-correlation functional, which is known to be particularly good for calculations of binding energies on surfaces [251], and the projector augmented wave (PAW) method [24, 174] to represent the core electrons.

The psinc basis kinetic energy cutoff has been set to 550 eV for geometry optimisations and 850 eV for total energy and properties calculations. We assigned 12 NGWFs for each Pt atom and 4 NGWFs for each O atom. For all NGWFs, we used 9.0 a_0 radii. The NGWF conjugate gradient optimisation preconditioning parameter k_0 [188] used in our simulations was equal to 2.5 ${a_0}^{-1}$. The Fermi-Dirac occupancy smearing scheme was used, with a 0.1 eV electronic temperature. Similarly to the other chapters, we have performed the l-p-DOS calculations using the C-SWs method implemented in ONETEP.

We have employed the BFGS method to optimise the geometries [252], using a convergence threshold of 0.002 Ha/a_0 on the atomic forces for the optimisation of O on Pt nanoparticles and 0.005 Ha/a_0 for the optimisation of isolated Pt nanoparticles. On the next sections, we discuss in details different geometry optimisations strategies to study the O adsorption for different nanoparticle sizes and O coverages. To assess the interaction between Pt nanoparticles and O atoms, we calculate the adsorption energies, E_{ADS} as follows:

$$E_{ADS} = E_{O/Pt_n} - E_{Pt_n} - \frac{1}{2}E_{O_2} \tag{7.1}$$

where, E_{O/Pt_n} is the energy for the system with O interacting with a Pt nanoparticle, E_{Pt_n} is the energy of the Pt nanoparticle, and E_{O_2} is the energy of an oxygen molecule in the triplet state.

We have used simulation cells obeying periodic boundary conditions with large vacuum gaps and with the spherical Coulomb-cutoff approach to eliminate interactions between periodic images [253]. We calculate the minimum Coulomb-cutoff radius r_{CC} with the following equation:

$$r_{CC} = rmax_{ij} + 2r_{NGWF} + a \tag{7.2}$$

where $rmax_{ij}$ is the maximum inter-atomic separation in our systems, r_{NGWF} is the NGWF

radius, and a is a constant value of at least 5 Å to account for Gibbs oscillations associated with the cut-off in the Coulomb operator. The following table shows how the adsorption energy changes with the Coulomb-cutoff radius for a short convergence test with O adsorption at a hollow site in a (111) facet of a cuboctahedral Pt_{55} nanoparticle. The nanoparticle has a diameter of approximately 11 Å. According to equation 7.2, we will use a cutoff radius of at least 25 Å, which is already under a 0.01 eV convergence threshold from larger radius sizes.

TABLE 7.1: Oxygen adsorption energies for different values of coulomb-cutoff radius.

r_{CC} (Å)	E_{ADS} (eV)
12	-11.68
24	-0.89
32	-0.89
36	-0.89
44	-0.89

7.3 Coverage Effect: Methodology Calibration

Studying the oxygen coverage effect with DFT calculations for Pt nanoparticles of different sizes is a computationally demanding task. In this section, we describe approximations made to reduce the computational effort and assess the effects of each one of them on our results. As previously described, finding the ground state arrangement of O atoms for a given coverage can be a complicated task. Some authors have tackled this problem in the literature using cluster expansion Hamiltonians for extended surfaces [241–245]. For nanoparticles, this task is even more complicated due to the higher number of distinct adsorption sites.

Here, we are not considering configurational effects, and we start all of our simulations with O atoms placed at hollow HCP and bridge sites near the edge of the nanoparticle for (111) and (100) facets respectively. These adsorption sites are the favourable ones for each nanoparticle facet if we ignore the adsorption sites in the edges and vertices of the nanoparticle. As the adsorption energies for HCP (111) and bridge (100) are similar, we increase the oxygen coverage on both facets in the same rate.

We study cuboctahedral platinum nanoparticles with up to 309 Pt atoms, covering the nanoparticles with up to 1ML of oxygen atoms, where we define 1 ML coverage if the number of O atoms is the same as the number of Pt atoms in the surface. To reduce the computational cost associated with the increasing number of O atoms, we test three assumptions for our O coverage calculations:

I) Constraining the movement of Pt nanoparticles.

The first assumption is commonly applied when studying the adsorption of atoms and molecules on metallic nanoparticles with DFT calculations. We assume that the change in the adsorption energies due to the nanoparticle's deformation induced by the interaction with the adsorbate should be small and that this effect would create an almost constant shift on adsorption energies, not changing the overall trends and main conclusions when comparing different systems.

To test this assumption, we compute the adsorption energies per O atom with two geometry optimisation strategies, here called "Relaxing Pt", when we geometry optimise all the Pt and oxygen atoms, and "Freezing Pt" when we optimise only O atoms with the Pt atoms constrained to the positions obtained after a geometry optimisation of isolated Pt nanoparticles.

We compute single O adsorption and multiple O adsorptions varying the oxygen coverage for Pt_{55} and Pt_{147} nanoparticles. For Pt_{55} nanoparticles we test the assumption for systems with the whole nanoparticle covered and with only one hemisphere covered, while for Pt_{147} we only consider hemispherical coverages. We calculate the adsorption energy as follows:

$$E_{ADS} = E_{O_m/Pt_n} - E_{Pt_n} - \frac{m}{2}E_{O_2} \tag{7.3}$$

$$^{\dagger}E_{ADS} = {}^{\dagger}E_{O_m/Pt_n} - E_{Pt_n} - \frac{m}{2}E_{O_2} \tag{7.4}$$

where E_{O_m/Pt_n} is the energy obtained for the interacting system when the Pt nanoparticle remains rigid during the optimisation of the adsorbates and $^{\dagger}E_{O_m/Pt_n}$ is the energy obtained for the interacting system if the Pt nanoparticle is allowed to relax during the oxygen adsorption. E_{O_2} is the energy of an O_2 molecule in the triplet state, E_{Pt_n} is the energy for Pt nanoparticles relaxed without O atoms, and m and n are the number of oxygen and Pt atoms.

Table 7.2 shows the computed adsorption energies for the "Relaxing Pt" and "Freezing Pt" approaches. In general, the differences in the adsorption energies with both strategies are around 0.2 eV per O atom. The overall trends in the adsorption energies with increasing oxygen coverage are very similar with both approaches, with the main differences between both strategies happening for high O coverages.

To assess how the nanoparticle relaxation due to the interaction with the adsorbate changes

TABLE 7.2: The effect of Pt nanoparticle relaxation: Adsorption energies for Pt nanoparticles interacting with atomic O with and without geometry optimising the Pt nanoparticles during the interaction with the adsorbate. In both cases, we present the adsorption energies per O atom for each coverage.

System	Relaxing Pt $^{\dagger}E_{ADS}/O(eV)$	Freezing Pt $E_{ADS}/O(eV)$
Pt_{55} O HCP (111)	-1.08	-0.88
Pt_{55} Hemisphere 0.33ML	-1.07	-0.84
Pt_{55} Hemisphere 0.66ML	-0.97	-0.80
Pt_{55} Hemisphere 1.00ML	-0.89	-0.74
Pt_{55} Nanoparticle 0.33ML	-1.06	-0.85
Pt_{55} Nanoparticle 0.66ML	-0.94	-0.74
Pt_{55} Nanoparticle 1.00ML	-0.82	-0.50
Pt_{147} O HCP (111)	-1.11	-0.85
Pt_{147} Hemisphere 0.15ML	-1.01	-0.84
Pt_{147} Hemisphere 0.46ML	-1.03	-0.86
Pt_{147} Hemisphere 0.91ML	-0.77	-0.55

the nanoparticle structure and the oxygen arrangement, we plot in figure 7.1 the radial distribution functions of Pt and O atoms using an atom in the centre of the nanoparticle as our reference. We present the atomic distribution functions for the "Relaxing Pt" and "Freezing Pt" approaches using three different oxygen coverages on a Pt_{55} nanoparticle.

For the "Freezing Pt" approach with 0.33ML coverage, we see the presence of six distinct peaks, with four peaks representing Pt atoms and the other two oxygen atoms. The peak at 2.74 Å in figure 7.1 shows the first Pt layer away from the centre of the nanoparticle. For the exposed Pt shell, the peak at 4.00 Å represents Pt atoms in the centre of the (100) facet, while peaks at 4.78 Å and 5.39 Å represent atoms in the edges and vertices of the nanoparticle. The oxygen peaks for bridge (100) and HCP (111) adsorption sites are respectively represented at 5.57 Å and 6.10 Å from the centre of the nanoparticle.

For the "Freezing Pt" approach, as we increase the oxygen coverage, the peak related to oxygen at the HCP (111) adsorption sites widens due to the change of O positions that start the geometry optimisations at HCP (111) sites and finish at bridge sites in the edges and vertices of the nanoparticle. According to Han, Miranda and Ceder [220] and with our calculations, the adsorption energies for these adsorption sites are similar, with bridge sites in edges of the nanoparticle being slightly stronger than HCP(111) near the vertices. The similarity of the adsorption energies for these adsorption sites is responsible for an easy O diffusion as pointed out by Peng *et al.* [219], which can explain why we observe O atoms moving between adsorption sites during the geometry optimisation. The peak for the bridge (100) site remains almost constant. Changing the adsorption site during the geometry optimisation is more difficult for these O atoms because bridge edge and top vertex sites are already being occupied by the O

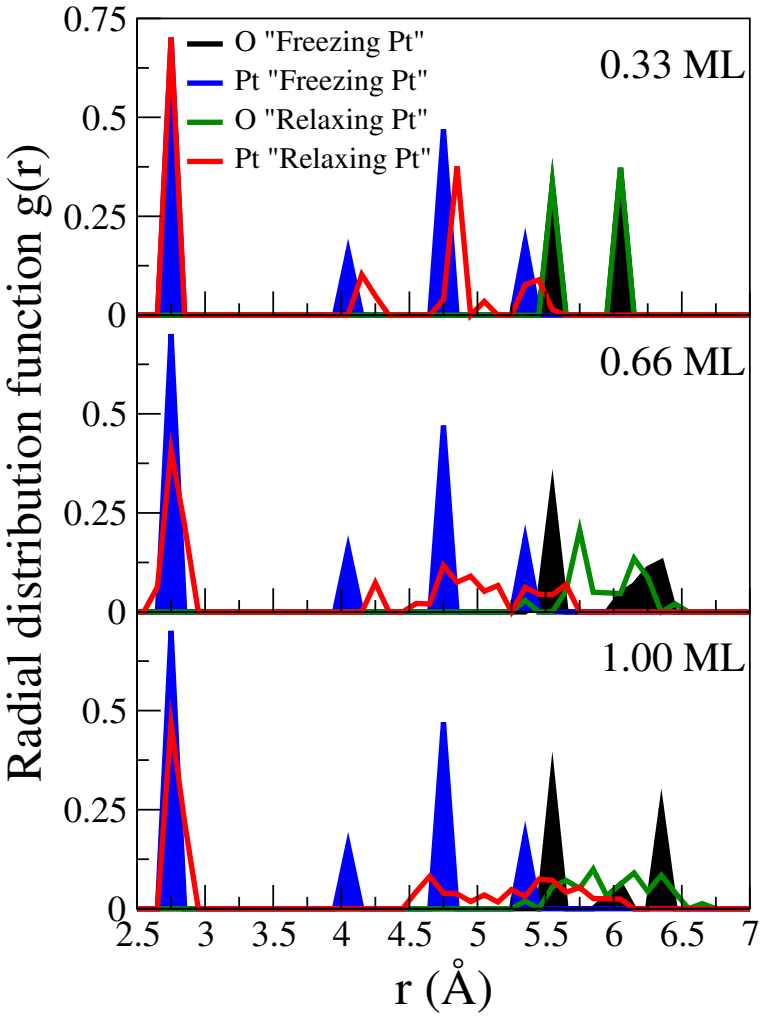

FIGURE 7.1: Radial distribution functions g(r) for "Relaxing Pt" and "Freezing Pt" approaches for 3 different oxygen coverages on Pt_{55}. Filled blue (black) curves represent Pt (O) g(r) functions for the "Freezing Pt" calculations. Red (green) curves represent Pt (O) g(r) functions for "Relaxing Pt" calculations. The atom in the centre of the Pt nanoparticle is used as the reference for the g(r) in all the calculations.

atoms from the (111) facet and because the remaining adsorption sites, namely top sites in the nanoparticle edges and centre of (100) facets present weaker interactions to oxygen.

For the "Relaxing Pt" approach, we see that while the first peak remains in the same position for all O coverages, the external Pt shell radially expands after the interaction with the adsorbates. For low coverages, such as 0.33ML, this expansion is the main modification and all the characteristics described before are present. As the O coverage increases, the change in the nanoparticle geometry becomes more visible, and the oxygen radial distribution also changes. For the 1 ML coverage, we stop having distinct peaks for both, Pt and O atoms and we see that a large overlapping region with Pt and O atoms appears, ranging from 5.25 Å to 6.25 Å, which might indicate the formation of a Pt-O external shell instead of the regular behaviour of O atoms

being at a certain distance away from the Pt shell. Thus, figure 7.1 helps to illustrate that the changes associated with the nanoparticle geometry deformation due to the interaction with the adsorbates is highly dependent on the oxygen coverage.

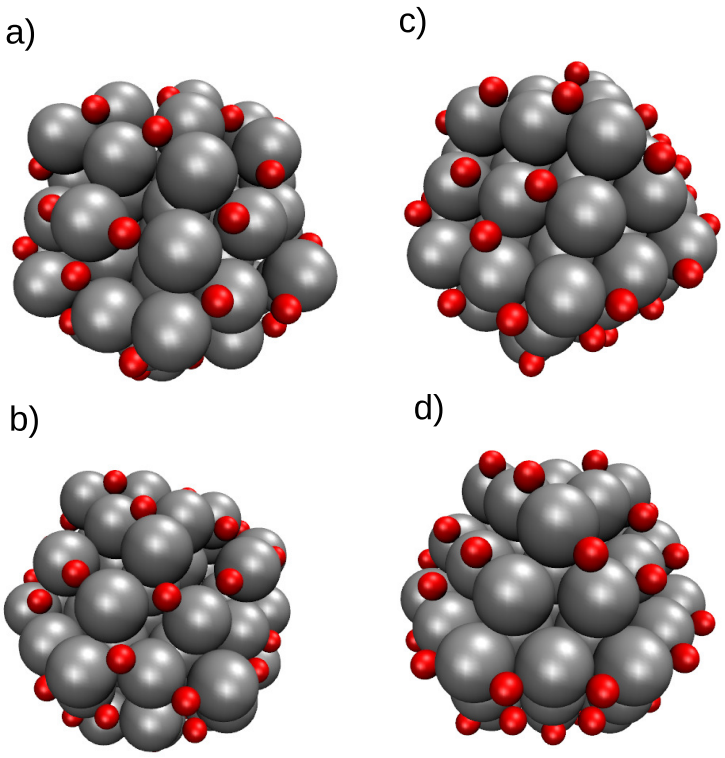

FIGURE 7.2: Final geometries for the 1 ML oxygen coverage on a Pt_{55} nanoparticle obtained with different geometry optimisation approaches, where a) and b) show the Pt nanoparticle covered with O from different angles for the "Relaxing Pt" strategy, while c) and d) show the same system from different angles for the "Freezing Pt" approach. Silver and red balls represent Pt and O atoms.

We also show in figure 7.2 the final configuration for the 1 ML coverage with the "Relaxing Pt" and "Freezing Pt" approaches from different angles. The results obtained with the "Relaxing Pt" approach show a sinking of the O atoms into the Pt nanoparticle structure for such O coverage. This result agrees with observations of subsurface O atoms with increasing oxygen coverage, already experimentally reported [247, 248] and observed in other computational studies for nanoparticles [246, 249] and slabs [223]. To accurately detect subsurface oxygen, our simulations would have to use a different approach and sample different initial configurations for the oxygen atoms.

Our results indicate that if one is interested in assessing subsurface oxygen, the "Relaxing Pt" approach should be more suitable. Moreover, with increasing O coverage, there are variations in the effects of Pt relaxation during the O adsorption. However, the main trends in

adsorption energies per O atom with different coverages are similar when calculated with both approaches. Thus, if one is mainly interested in the effect of the O coverage to the average bond strength between oxygen atoms and Pt nanoparticle and the calculations are focused on low and intermediate coverages, constrain the Pt atoms during the adsorbate relaxation seems a valid approach.

II) Hemispherical oxygen coverage.

The cuboctahedral nanoparticle is symmetric, and the changes in the nanoparticle caused by the O adsorption are relatively local. Thus, as our second assumption, we consider that we do not need to cover the whole nanoparticle surface with atomic O. Thus, we have added oxygen only to one hemisphere of the nanoparticle to test if that would be enough to represent the problem we want to study.

TABLE 7.3: Covering the whole nanoparticle vs hemispherical coverage: Adsorption energies per O atom for Pt_{55} interacting with atomic O at different coverages with the whole Pt_{55} surface and only one hemisphere covered with O

System	Nanoparticle Coverage $E_{ADS}/O(eV)$	Hemisphere Coverage $E_{ADS}/O(eV)$
Relaxing Pt 0.33ML	-1.06	-1.07
Relaxing Pt 0.66ML	-0.94	-0.97
Relaxing Pt 1.00ML	-0.82	-0.89
Freezing Pt 0.33ML	-0.85	-0.84
Freezing Pt 0.66ML	-0.74	-0.80
Freezing Pt 1.00ML	-0.50	-0.74

Table 7.3 shows the adsorption energies per O atom for the whole nanoparticle covered with O and for the hemispherical coverage. We compute these values using the "Relaxing Pt" and "Freezing Pt" approaches discussed before. In general, we see that this assumption does not change the behaviour of adsorption energies per O atom, being a valid approximation to reduce the computational cost.

The only significant change happens for our highest O coverage with the "Freezing Pt" approach, which should be treated carefully as previously demonstrated. For high O coverages, using a hemispherical coverage can induce an error in the final oxygen distribution on the free/-covered interface. For hemispherical coverages, the oxygens near the free/covered interface, which does not exist when the nanoparticle is fully covered, tend to move closer to facets free of oxygen and increase the distance between adsorbates, which in turn changes the adsorption energies per O atom as compared to the results obtained for the whole nanoparticle covered with O.

III) Relaxing O atoms only for one facet.

Finally, we test the effect of relaxing only a subset of O atoms. Here, we try to assess the O coverage effect for a single nanoparticle facet. We geometry optimise only the O atoms on a specific (111) facet, constraining the movement of all remaining O atoms.

We fix the O surrounding atoms in the stable positions obtained for the single oxygen adsorption, constraining the movement of Pt and surrounding O atoms. This strategy drastically reduces the degrees of freedom in the geometry optimisation. We calculate the adsorption energies ${}^{\star}E_{ADS}$, with a different methodology which is demonstrated in equation 7.5.

$$ {}^{\star}E_{ADS} = E_{O_m/Pt_n} - E_{REF} - \frac{mm}{2} E_{O_2} \tag{7.5} $$

where, E_{REF} is the energy for the reference system, which is defined by excluding O atom only for a single facet as illustrated in figure7.3, mm is the number of O atoms in the studied Pt facet, and m is the total number of O atoms in the system. The energy E_{O_m/Pt_n} can be calculated after the full geometry optimisation of all O atoms in the system or after the geometry optimisation of O atoms of one nanoparticle facet. In all the cases, we have covered only one hemisphere of the nanoparticle.

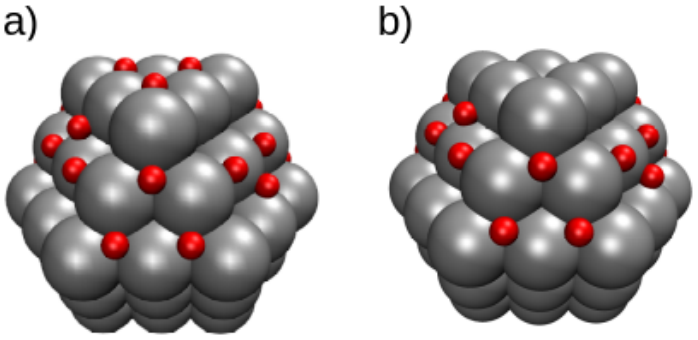

FIGURE 7.3: Illustration of the systems used to obtain a) E_{O_m/Pt_n} b) E_{REF}, where the E_{REF} structure is obtained by excluding the O atoms from the facet we are interested to study

Table 7.4 shows the adsorption energies per O atom computed by geometry optimising all O atoms or just the O atoms placed at a particular nanoparticle facet. For the calculations that we geometry optimise all O atoms, we show E_{ADS} calculated with equation 7.3 and ${}^{\star}E_{ADS}$ calculated with equation 7.5. The first two columns show that E_{ADS} and ${}^{\star}E_{ADS}$ are not comparable, as in

one case we are assessing the adsorption energies for the whole nanoparticle including (111) and (100) facets, and in the other case we assess a single (111) facet.

TABLE 7.4: Relaxing all O atoms vs Relaxing only the atoms on a specific facet: Adsorption energies per O atom for Pt nanoparticles interacting with atomic O at different coverages, where we show adsorption energies for all O atoms E_{ADS} calculated with equation 7.3 and adsorption energies for a single facet $^{\star}E_{ADS}$ calculated with equation 7.5

System	Relaxing all O $E_{ADS}/O(eV)$	Relaxing all O $^{\star}E_{ADS}/O(eV)$	Relaxing O in the (111) facet $^{\star}E_{ADS}/O(eV)$
Pt_{55} 0.33ML	-0.84	-0.72	-0.68
Pt_{55} 0.66ML	-0.80	-1.24	-0.72
Pt_{55} 1.00ML	-0.74	-0.93	-0.76
Pt_{147} 0.15ML	-0.84	-0.89	-0.91
Pt_{147} 0.46ML	-0.86	-1.01	-0.88
Pt_{147} 0.61ML	-0.87	-0.91	-0.76
Pt_{147} 0.91ML	-0.55	-0.38	-0.10

Comparing the final two columns, we see that relaxing only one nanoparticle facet is not enough to obtain the same behaviour for the oxygen coverage dependency in the adsorption energies as compared to the calculations relaxing the positions of all O atoms. When we allow all O atoms to relax, the increase in the oxygen coverage induces the change of adsorption sites for some O atoms, that leave the initial hollow (111) sites and occupy bridge and top sites in the edge and vertices of the nanoparticle as an artefact of our decisions for the initial O positions. Thus, if we are not allowing all O atoms to relax, the atoms in the studied facet will find a different oxygen configuration near the nanoparticle edges and vertices and the distance between oxygen atoms in the analysed facet and the other O atoms will also differ.

Thus, after our tests, we have decided to study the relation between the effect of oxygen coverage and Pt nanoparticle size using only the first two assumptions to create our methodology. In the next section, we present the adsorption energies per O atom for different coverages in three nanoparticle sizes. For all the calculations, we cover one hemisphere of the nanoparticle with oxygen and optimise all the oxygen positions, while keeping the Pt atoms frozen. Using this methodology, we are able to study the main trends in the adsorption energies per O atom for different oxygen coverages and nanoparticles sizes and analyse the electronic changes in the nanoparticle surface due to increasing O coverage.

7.4 Interplay Between Nanoparticle Size and O Coverage

So far we have assessed geometry optimisation methodologies to treat multiple oxygen adsorption with different coverages. Here, we employ the selected approach to study multiple

oxygen adsorptions on the Pt_{55}, Pt_{147}, and Pt_{309} nanoparticles with O coverages up to 1ML. The definition of coverage we have used so far considers 1ML when we have the same number of O and surface Pt atoms. As we are considering hemispherical coverage, the 1ML coverage is defined when the number of O atom is half of the number of Pt atoms in the surface of the nanoparticle.

We start our simulations with O atoms placed at hollow HCP near the vertices of (111) facets and bridge sites near the edge of (100) facets. We increase the O coverage by adding one atom per facet up to the maximum coverage treated for each nanoparticle. For Pt_{147} and Pt_{309} nanoparticles, after filling with oxygen the hollow HCP sites near the vertex, we start to use hollow HCP near the edges of the nanoparticle. For completeness, we present the initial and final (geometry optimised) O configuration for each nanoparticle size and O coverage in the appendix B.

As oxygen adsorption energies are highly dependent on the adsorption site [8, 10], we start our analysis showing in table 7.5 the number of O atoms on each adsorption site for each nanoparticle size and oxygen coverage. The numbers outside (inside) brackets in table 7.5 represent the number of O atoms in that particular adsorption site before (after) the geometry optimisations.

TABLE 7.5: Number of O atoms present on each type of adsorption site for different nanoparticle sizes and oxygen coverages. Numbers outside (inside) brackets represent the number of O atoms placed on a particular type of adsorption site before (after) the geometry optimisations.

	Adsorption sites in the (111) facet				Adsorption sites in the (100) facet		
	HCP-V	HCP-E	Bridge-V	Bridge-E	Bridge-NE	Bridge-V	Top-E
Pt_{55} 0.33ML	4 (4)	0 (0)	0 (0)	0 (0)	3 (3)	0 (0)	0 (0)
Pt_{55} 0.66ML	8 (1)	0 (0)	0 (7)	0 (0)	6 (6)	0 (0)	0 (0)
Pt_{55} 1.00ML	12 (2)	0 (0)	0 (10)	0 (0)	9 (6)	0 (2)	0 (1)
Pt_{147} 0.15ML	4 (4)	0 (0)	0 (0)	0 (0)	3 (3)	0 (0)	0 (0)
Pt_{147} 0.30ML	8 (8)	0 (0)	0 (0)	0 (0)	6 (6)	0 (0)	0 (0)
Pt_{147} 0.45ML	12 (12)	0 (0)	0 (0)	0 (0)	9 (9)	0 (0)	0 (0)
Pt_{147} 0.61ML	12 (3)	4 (2)	0 (9)	0 (2)	12 (12)	0 (0)	0 (0)
Pt_{147} 0.76ML	12 (3)	8 (0)	0 (9)	0 (8)	15 (15)	0 (0)	0 (0)
Pt_{147} 0.91ML	12 (0)	12 (0)	0 (12)	0 (12)	18 (16)	0 (0)	0 (2)
Pt_{309} 0.09ML	4 (4)	0 (0)	0 (0)	0 (0)	3 (3)	0 (0)	0 (0)
Pt_{309} 0.17ML	8 (8)	0 (0)	0 (0)	0 (0)	6 (6)	0 (0)	0 (0)
Pt_{309} 0.26ML	12 (12)	0 (0)	0 (0)	0 (0)	9 (9)	0 (0)	0 (0)
Pt_{309} 0.35ML	12 (12)	4 (4)	0 (0)	0 (0)	12 (12)	0 (0)	0 (0)
Pt_{309} 0.43ML	12 (12)	8 (8)	0 (0)	0 (0)	15 (15)	0 (0)	0 (0)
Pt_{309} 0.60ML	12 (11)	16 (10)	0 (1)	0 (6)	21 (21)	0 (0)	0 (0)
Pt_{309} 0.78ML	12 (3)	24 (8)	0 (9)	0 (16)	27 (27)	0 (0)	0 (0)

Table 7.5 shows two distinct effects related to the Pt nanoparticle size effect and O coverage. The first effect is related to the percentage of different adsorption sites on different nanoparticles. As the nanoparticle size grows, adsorption sites near the vertices and edges represent a

lower portion of the total number of sites. Thus, when comparing two nanoparticle sizes, the larger one will have a higher number of weaker adsorption sites being used to obtain the same O coverage. Consequently, when assessing the O coverage in terms of fractions of O monolayers, we should see a weakening in the adsorption energy per O atom due to the usage of weaker adsorption sites, which should be more relevant as we increase the nanoparticle size.

The second effect is the movement of oxygen atoms to different adsorption sites during the geometry optimisations that happened for certain coverages. For all nanoparticle sizes, we see oxygen atoms moving during the geometry optimisation from the initial adsorption sites when the coverages are higher than 0.6ML. For (111) facet, oxygen at the HCP (111) adsorption sites on the vertices and edges are destabilised with increasing coverages and are adsorbed at bridge sites in the vertices and edges of the nanoparticle. For (100) facet, oxygen remains stable for bridge sites near the edge for almost all coverages, with O atoms changing from the initial distribution of adsorption sites only for the highest O coverages in the covered/uncovered interface which is an artefact of adding O atoms to only one hemisphere. As explained in the previous section, changing the position of oxygen atoms in the (100) facets during the geometry optimisation is more difficult, because adsorption sites in the edges of the nanoparticle are already occupied by O atoms from the (111) facets and the remaining sites for the (100) facet bind oxygen much weaker than the initial position.

To assess how each effect contributes to the adsorption energy dependency on the oxygen coverage, we computed the oxygen adsorption for each adsorption site, considering a single O interacting with the nanoparticle, and used these values to calculate the average O adsorption for the initial, $Initial\overline{E}_{ADS}$ and final, $Final\overline{E}_{ADS}$, configurations, as follows:

$$\overline{E}_{ADS} = \frac{1}{m}\sum_{i}^{m} N_i E_{ADS}(i) \tag{7.6}$$

where m is the total number of O atoms, N_i is the number of O atoms on adsorption sites similar to the adsorption site i, and $E_{ADS}(i)$ is the adsorption energy computed for a single oxygen adsorbed at the site i. Table 7.6 shows the O adsorption energies for a single O atom interacting with the Pt nanoparticles on different adsorption sites which are present on initial and final O configurations for each nanoparticle sizes and O coverages. These values are used to compute the average adsorption energy as described in equation 7.4.

Figure 7.4 shows the average adsorption energy $\overline{E}_{ADS}$ obtained for the initial and final O configuration presented on table 7.5, and the adsorption energies E_{ADS} per O atom for all the

TABLE 7.6: Adsorption energies for a single O atom interacting on different adsorption sites and nanoparticle sizes, where NE and NC are non-existent and non-computed adsorption sites.

	Pt_{55} E_{ADS} (eV)	Pt_{147} E_{ADS} (eV)	Pt_{309} E_{ADS} (eV)
HCP-V (111)	-0.87	-0.85	-0.92
HCP-E (111)	NE	-0.61	-0.69
Bridge-V (111)	-1.13	-1.00	-1.08
Bridge-E (111)	NC	-0.90	-0.90
Bridge-NE (100)	-0.85	-0.83	-0.91
Bridge-V (100)	-0.98	NC	NC
Top-E (100)	-0.36	-0.28	NC

calculated O coverages and nanoparticle sizes.

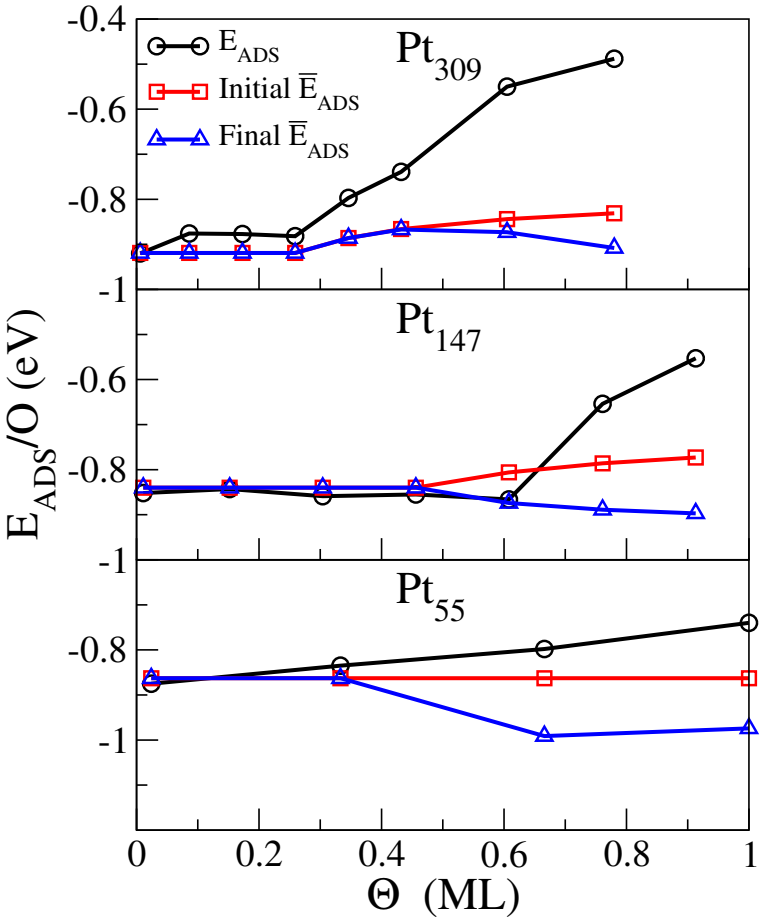

FIGURE 7.4: Adsorption energies per O atom E_{ADS} (black circles) and adsorption energy averages $\overline{E}_{ADS}$ for initial (red squares) and final (blue triangles) O configurations for several O coverages on Pt_{55}, Pt_{147}, and Pt_{309} nanoparticles.

The *Initial* $\overline{E}_{ADS}$ in figure 7.4 shows how the difference in the availability of adsorption sites for each nanoparticle size plays a role in the adsorption energy trend with increasing O coverage for each nanoparticle. For Pt_{55}, we achieve a 1ML O coverage using only HCP (111) sites at the vertex of the nanoparticle and bridge sites for the (100) facet. As a consequence, for

this nanoparticle size, we see a constant value for the *Initial* $\overline{E}_{ADS}$ result with all coverages. For Pt_{147} and Pt_{309}, we have to introduce weaker adsorption sites to obtain higher coverages, which in turn reduce the average adsorption energy.

As described in table 7.5, when the O coverage is higher than 0.6ML we see O atoms moving from the initial position at HCP (111) adsorption sites to bridge sites in the vertices and edges of the nanoparticles. This effect increases the average adsorption energy, as the bridge sites in the edges between (111) and (100) facets have stronger binding energies than the initial HCP positions. The oxygen preference for adsorption sites in the edges and vertices of the nanoparticle with increasing O coverage was also previously observed with DFT [136, 246] and MD [249] calculations, which similarly to our results, predicted a large concentration of oxygen in the edges of Pt nanoparticles and almost free terrace sites at (111) and (100) facets.

These changes in the oxygen distribution during the geometry optimisation observed in our calculations can be seen as an artefact of our simulation set-up. To reduce the computational cost in our investigation, we define the distribution of adsorbates across the nanoparticle surface based on arguments of the hierarchies of adsorption sites for a single oxygen interacting with the nanoparticle. We are not testing other configurations to properly search for the ground-state distribution of oxygen atoms over the nanoparticle surface. Thus, the movement of oxygen atoms to other adsorption sites observed after geometry optimisations might be only helping to correct some of the errors induced by the methodology to define the initial distribution of O on the nanoparticle surface.

The adsorption energies E_{ADS} per O atom in figure 7.4 includes the effects associated to the O distribution in different adsorption sites and the adsorbate-adsorbate interaction due to the increasing coverage, showing that the impact of increasing the O coverage grows with the nanoparticle size. For example, from figure 7.4, we see that the difference between E_{ADS} per O for the highest and lowest oxygen coverage for a Pt_{55} system is around 0.13 (eV/O), while for Pt_{147} the difference is 0.30 (eV/O), and for Pt_{309} it is 0.45 (eV/O). The fact that the decrease in the adsorption energies caused by the coverage effect is less intense for Pt_{55} agrees with the idea that catalytic activity in small nanoparticles size can be hindered by blocking active adsorption sites with strongly adsorbed species.

By computing the difference between *Final* $\overline{E}_{ADS}$ and the adsorption energy, E_{ADS}, per O atom with the covered nanoparticles, we can try to remove, to a certain extent, the contribution of using different adsorption sites and the problems with the initial oxygen configurations for each coverage from our simulation set-up. The comparison between the two quantities show

that the coverage effects are controlled to a larger extent by the electronic interactions between adsorbates and the modifications in the Pt surface that weaken the adsorption energy per oxygen. The difference between *Final* $\overline{E}_{ADS}$ and E_{ADS} for the highest oxygen coverage is 0.24 (eV/O) for Pt_{55}, 0.34 (eV/O) for Pt_{147} and 0.44 (eV/O) for Pt_{309}.

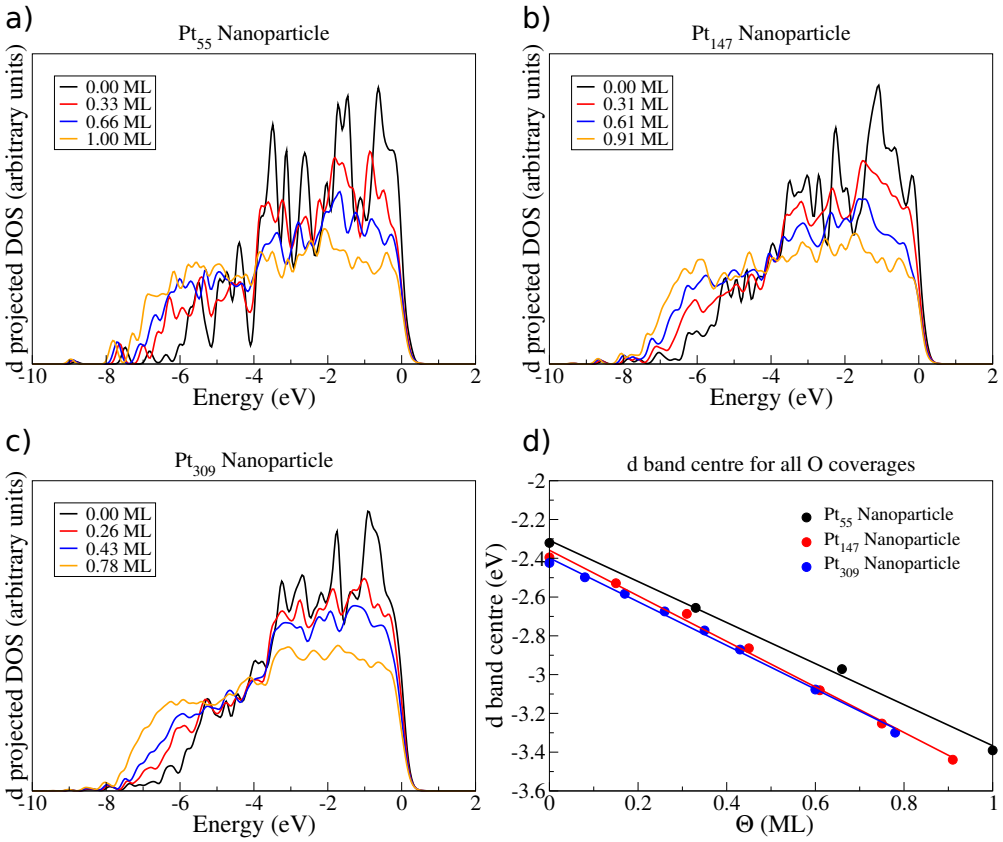

FIGURE 7.5: Density of states projected on the d-band of surface Pt atoms of cuboctahedral a) Pt_{55}, b) Pt_{147}, and c) Pt_{309} nanoparticles with different O coverages. Figure d) shows the calculated d-band centre for each nanoparticle size as a function of the O coverage.

To study how the presence of O atoms changes the nanoparticle surface, we show in figure 7.5 the d-band projected density of states for the surface Pt atoms on the covered hemisphere of Pt_{55}, Pt_{147}, and Pt_{309} nanoparticles interacting with different O coverages. For all nanoparticle sizes, as we increase the O coverage, the d-band states near the Fermi level are reduced in intensity and the intensity of the states near the -6.0 eV region increases. The peak near -6.0 eV corresponds to the overlapping orbitals between adsorbates and Pt surface. Additionally, to this effect, we see a widening of the d-band states, and consequently, a downshift of the d-band centre. Figure 7.5 d) shows how the d-band centres change with increasing O coverage. For all nanoparticle sizes, we observe a linear correlation between the O coverage and the lowering of the d-band centre. Similar changes in the d-bands and d-band centres due to the adsorbate

coverage were also observed for Pt, Pd, Au (111) slabs interacting with O, C, N, and used to explain the adsorption energy dependencies on the adsorbate coverage for different metallic surfaces and adsorbates [236–240].

For Pt nanoparticles, we observe that the downshifts in the d-band centres can be used to explain the weakening of the adsorption energies with increasing O coverage to some extent. When compared with the results obtained for metallic slabs [236–242], we obtain the same linear correlation between the d-band centres and adsorbate coverages, while for the adsorption energies per O atom we see a non-linear dependency on the O coverage. For Pt nanoparticles, we deal with a non-homogeneous O distribution through different adsorption sites and Pt facets, and we can use the d-band centre dependency on the O coverage only to qualitatively explain how the adsorbate coverage changes the electronic structure of the nanoparticle surface and consequently its bonding ability. However, it is not possible to use the d-band centre of the Pt surface for different O coverages to linearly correlate the adsorption energies per O or to accurately predict the changes with increasing O coverage, showing that the adsorbate-adsorbate interactions should be carefully considered when treating nanoparticles.

7.5 Conclusions

We carried out a study with large-scale DFT calculations on the combined action of Pt nanoparticle size and O coverage effects. We have performed a detailed analysis of different approaches of geometry optimisations used to study the oxygen coverage problem with DFT calculations, testing three approximations made to reduce the computational cost. We have conducted our tests with Pt_{55} and Pt_{147} nanoparticles and several O coverages. The first approximation is to maintain the Pt atoms in the optimised position found for an isolated nanoparticle. This approximation excludes the effects that the adsorbates create in the geometry of the nanoparticle, dramatically reducing the degrees of freedom and computational cost in the geometry optimisation.

We have shown that this approximation produces an almost constant shift in the adsorption energies, maintaining the overall trends in adsorption energies per O atom with increasing O coverages and different nanoparticle sizes. The most significant differences in adsorption energies happen for higher O coverages. For high O coverages, the results observed when relaxing all Pt and O atoms, show a sinking of O atoms into the nanoparticle surface and a considerable movement of oxygen atoms from their initial position during the geometry optimisation. When the same systems are computed with a rigid Pt nanoparticle structure, only the O movement

effect appears. These results show that the approximation is valid if one is mainly interested in studying the dependency of adsorption energy per O atom with the O coverage and nanoparticle size. For observing subsurface oxygen, a more rigorous study on Pt oxide formation, or higher O coverages studies the full relaxation should be more appropriate.

We have also shown that it is possible to reproduce the results of covering a Pt nanoparticle with O by only covering one hemisphere of the cuboctahedral nanoparticle. This simplification only changes the results for high O coverages, where we see a difference in the final distribution of used adsorption sites near the free/covered interface, which does not exist when the whole nanoparticle is covered. Our third approximation tested the effect of relaxing only a subset of O atoms, optimising the O atoms for a single (111) facet while keeping all the remaining O and Pt atoms in their initial positions. We have seen that relaxing only a fraction of the O atoms was not enough to reproduce the final O positions for that facet and consequently the adsorption energies and O coverage dependency.

After these tests, the selected methodology was used to study the interplay between Pt nanoparticle size and O coverage, by computing a selection of coverages on Pt_{55}, Pt_{147}, and Pt_{309} nanoparticles. We employed the first two assumptions, computing hemispherical O coverage and relaxing all O atoms with the Pt atoms frozen. We started our calculations placing O atoms at the hollow HCP near the vertices of (111) facets and bridge sites near the edges on (100) facets. As we increased the O coverage, we also used hollow HCP sites near the edges of (111) facets as initial positions for O atoms. In general, as we increase the O coverage the adsorption energy per O atom weakens and, when assessing the O concentration in terms of ML, this effect is more pronounced for larger nanoparticles. The fact that the O coverage seems to affect the adsorption energy per O atom on Pt_{55} to a smaller extent as compared to larger nanoparticles, reinforce the idea that the catalytic activity on these nanoparticles could be smaller due to the blocking of active adsorption sites due to the presence of strongly adsorbed species.

We show that the changes in the adsorption energies per O atom due to the combined effects of changing the nanoparticle size and O coverage have different causes. For nanoparticles of different sizes, the proportion between the number of adsorption sites near the vertices, edges and centre of each facet is different. Thus, for each nanoparticle size, the same O coverage will be achieved over a different distribution of adsorption sites. For larger nanoparticles, higher coverages will use a higher number of weaker binding sites as compared with smaller nanoparticles. Depending on the O coverage, we also observe oxygen atoms moving during the geometry optimisation, mainly from the HCP (111) adsorption sites to bridge sites in the vertices and edges of

the nanoparticles. This effect can be seen as an artefact of our initial distribution of oxygen over the nanoparticle, which was defined based on the adsorption site hierarchy for single oxygen adsorbed on different sites of metallic nanoparticles. Therefore, we can treat these changes in the O distribution over the nanoparticle as corrections to our initial guesses.

We have listed all the adsorption sites used in the initial configuration for all O coverages and the adsorption sites occupied by O atoms after the geometry optimisations. The adsorption energies of a single oxygen atom interacting with the nanoparticles on each one of these adsorption sites were also computed and used to calculate an average of the adsorption energy for the initial and final O configurations in a "single oxygen" coverage limit. We have compared the average adsorption energies for the initial and final O configurations to the adsorption energies per O atoms obtained with the covered nanoparticles.

We have observed that the adsorption site availability and the distribution of O atoms to different adsorption sites play a role in the changes in adsorption energies due to increasing O coverages. However, by analysing the difference between the average adsorption energy for the final O configuration and the adsorption energy per O atom for the covered Pt nanoparticles, we show that the main changes induced by the coverage effect are related to the interactions between adsorbates and the modifications that the O atoms create in the electronic structure of the Pt nanoparticles. We have presented the d-band projected density of states for the Pt atoms in the surface of the nanoparticles, showing a linear correlation between increases in the O coverage and downshifts in the d-band centre, which illustrates how the presence of adsorbates modify the metallic surface to weaken the adsorption energies per O atom. As the adsorption properties, which are key descriptors for catalytic systems, are dependent on the adsorbate coverage, we expect that an accurate description of adsorbate coverage effects will play an important role to predict catalytic properties of metallic nanoparticles. Thus, by bringing a detailed discussion about possible methodologies to tackle the problem with DFT calculations and by showing clear differences of the adsorbate coverage effect due to the nanoparticle size, we expect that our results will provide useful insights for further investigations in the computational catalysis field.

Chapter 8

Conclusions

The work from this thesis was focused on computationally studying platinum nanoparticles applied to heterogeneous catalysis. We have concentrated our studies on treating the interplay between nanoparticle size effects and other variables that are important for fuel cell catalysts such as the presence of support and the effects of changing the adsorbate coverage. We simulated the interaction of platinum clusters and nanoparticles with graphene and assessed the combination between size and support effects on the interaction between key adsorbates and the metallic surfaces. Moreover, we have studied possible strategies to computationally treating the interplay between nanoparticle size and coverage effects for Pt nanoparticles interacting with atomic oxygen and performed a study about how these effects change oxygen adsorption energies. We have also presented the theoretical framework that allowed the implementation of an atom-projected and angular momentum projected density of states (l-p-DOS), which is an invaluable tool for computational studies on metallic surfaces and nanoparticles applied to catalysis.

Together with the underlying theory for the implementation of local and angular momentum projected density of states (l-p-DOS) within ONETEP's formalism, we have presented in chapter 4 four options of angular momentum resolved bases that were implemented to obtain the l-p-DOS. We have tested three bases that are related to spherical waves, with a non-contracted set of spherical waves (SWs); a contracted set with unity contraction weights (C-SWs), and a contracted set where the contraction weights are determined via inner products with the NGWFs (CF-SWs). Additionally, we have tested pseudo-atomic orbitals (PAOs) as a fourth basis set option. We have applied all these methodologies to different systems and compared our results with similar calculations performed with the CASTEP code.

We have observed a similar trend for all systems in terms of charge spilling parameters,

with SWs $<$ PAOs $\leq$ CASTEP $<$ CF-SWs $<$ C-SWs. In general, the non-contracted SWs basis presented small charge spilling parameters, which was something expected given the large size of the SWs basis set. For the other bases, the charge spilling parameters were consistently larger than the ones obtained with SWs. The charge spilling parameters obtained with PAOs were almost identical in ONETEP and CASTEP. Meanwhile, for the contracted spherical waves, fitting the contraction weights to the NGWFs helped to reduce the spilling parameter. As a general rule, the differences in the charge spilling parameter did not cause substantial changes in the overall shape of the l-p-DOS plots and the implemented methods provided similar results to each other and to the ones obtained with CASTEP, which helped to validate the implementation of the code. For metallic systems, the trends about the d-band centres from different structures obtained with all the calculations were also similar, showing the robustness of the method for applications in the computational catalysis field. The implementation of l-p-DOS in a linear-scaling DFT code such as ONETEP produced an additional tool to analyse electronic properties using large-scale DFT calculations, which was used throughout this thesis.

The ONETEP code was used to study platinum nanoparticles interacting with graphene supports, where we have presented large-scale DFT calculations on systems ranging from a single Pt atom on graphene to a cuboctahedral Pt_{309} nanoparticle supported on 880 carbon atoms. In our calculations, we have considered two-dimensional and three-dimensional clusters and nanoparticles. The results show that three-dimensional structures are generally more stable than monolayers when supported on graphene and that the difference in stability between these two types of structures increases as the system grows. A large part of this difference in stability was associated with the Pt-Pt interactions, which also favoured the formation of 3D structures for any isolated cluster larger than 13 atoms.

We have observed that the dispersion interactions were extremely important to the description of our systems and a significant part of the Pt/graphene interaction for larger platinum nanoparticles. Moreover, the results have shown a decrease in the interaction strength per Pt atom for nanoparticles of increasing size. These trends agree with experimental findings in the area that indicate a weak interaction between pristine graphene and metallic nanoparticles, where the presence of doping atoms, defects, edges, or functional groups pointed as anchoring sites in the graphene-based supports, are responsible for the stability of nanoparticles supported on graphene [167, 191, 192]. Despite the weak interaction between graphene and the Pt nanoparticles, we have observed changes in the geometric and electronic properties of both structures.

In terms of geometries, the interatomic distances for Pt nanoparticles increased for the interacting facet and decreased for facets far from the support, while the carbon-carbon distances in the graphene sheet increased in the region near the Pt nanoparticle. In terms of electronic changes, we have observed electronic redistribution in the interacting region, with electrons flowing from the nanoparticle to the graphene.

The changes in the geometries and electronic properties were correlated with the interaction strength between nanoparticles and support. Systems with larger interatomic expansions in the Pt facet near the support presented stronger interactions and larger electronic redistributions. The changes in the interatomic distances and the electronic redistributions altered the d-band centres calculated on both facets, indicating that the support, as well as the nanoparticle size, could change the catalytic activity of metallic nanoparticles. We have attempted to separate the electronic and strain effects that caused the changes in the nanoparticle d-band centres by calculating this property on isolated nanoparticles constructed with the same geometry of the nanoparticles supported on graphene, which we have named "Deformed Pt". We have observed that the main differences from the "Deformed Pt" and the Pt nanoparticles supported on graphene appeared only for the facets in contact with the support, while for the farthest facets we only see differences for the Pt_{13} cluster. However, due to the weak interaction between Pt nanoparticle and graphene, it was not possible to conclusively define to what extent each effect controls the changes in the d-band centres for Pt facets far from the support. Interestingly, we have observed that the effect of the support also depends on the nanoparticle size, showing the importance of considering both effects together for a more realistic modelling of metallic nanoparticles applied to heterogeneous catalysis.

Using the structures obtained in our study about the Pt/graphene interaction, we have calculated how the size and support effects affect the adsorption properties of the platinum nanoparticles. We have performed our DFT calculations for three probe adsorbates, namely O, CO and ethanol. The adsorption energies calculations were performed on multiple adsorption sites on isolated and supported Pt nanoparticles. The adsorption site hierarchies obtained with isolated nanoparticles were similar to the ones previously observed in the literature, with atomic O preferentially binding on bridge and HCP sites near the edges of the nanoparticle facet and CO adsorption being favoured on bridge and top sites near the vertex of the nanoparticles. For ethanol, top sites near the edge and vertex of the nanoparticle were the most stable adsorption sites for all nanoparticle sizes.

In terms of size effects, we have observed that the adsorption energies of O and CO

weaken with increasing nanoparticle sizes, which can have significant implications in terms of catalytic activity. For example, in the context of catalytic activity towards the oxygen reduction reaction, the adsorption energy of atomic oxygen is commonly used as a catalytic descriptor and, for Pt catalysts, it is commonly indicated that the interaction of Pt(111) slabs and O is too strong for optimal ORR catalysis [4, 8, 113, 179, 225, 226]. Thus, the fact that the adsorption energies are stronger near the vertices and edges of nanoparticles, which represent a larger proportion of the available sites for small nanoparticles, and the increase in adsorption energies with decreasing nanoparticle sizes, can help explain why the ORR activity decreases for nanoparticles smaller than 2-3 nm, and the peak of mass activity found in this size range [179].

Meanwhile, for the ethanol adsorption, almost no size effect was observed. To explain these differences in the size effect for ethanol as compared with O and CO, we have performed an in-depth DFT investigation on the differences of the interaction for each adsorbate. We encoded size effects and the multiplicity of adsorption sites using the generalised coordination number and discussed how the linear equations can change depending on the adsorption sites used for its parametrisations. We have also demonstrated, that the changes in the adsorption site coordination controlled the adsorption of O and CO to a much greater extent than for ethanol. The analysis of how the electronic densities of platinum surfaces and adsorbates change with the interaction has shown that the electronic redistributions due to the interaction are much more local for ethanol than for O and CO and that overlapping states between surface and adsorbate are more noticeable for O and CO than for ethanol. These findings, coupled to observations that the dispersion interactions for ethanol adsorption are a larger fraction of the interaction as compared for O and CO, helped explain why the nanoparticle size affects the adsorption energies of ethanol to a smaller extent as compared with O and CO.

We have also observed a weakening in the adsorption energies of O, CO and ethanol due to the support effects. The weakening happens due to the Pt lattice deformation, d-band centre changes and electronic redistribution associated with interactions between Pt nanoparticle and support. The support effect was also size dependent, being only significant for Pt_{13} nanoparticles and this effect can also have interesting implications in terms of catalyst design. The adsorption energy of O being too strong is pointed as a reason for the poorer activity for the ORR in nanoparticles smaller than 2 nm. Thus, the decrease in the O adsorption energy caused by the interaction of the nanoparticle with the support, which is more important for small nanoparticles, can help to mitigate the strengthening in adsorption energy which is caused by the decrease of the nanoparticle size. In that sense, the competition of the size and support effects on small

clusters could be an additional reason to explain the unusual increase in activity experimentally observed for size-selected subnanometer Pt clusters on carbon-based supports [142, 233]. We have also observed that the ethanol adsorption energies remained almost stable for different nanoparticle sizes, but were changed due to the support effects, showing that the combination of support and size brings possible ways of tuning the adsorption energies for specific adsorbates.

In our final study, we have investigated the interplay between the Pt nanoparticle size and O coverage effects. We have tested three approximations to reduce the computational cost of the simulations and assessed their impact on our study. In our first approximation, we maintain the Pt atoms fixed in the optimised positions obtained for isolated Pt nanoparticles, allowing further optimisations only for the positions of the adsorbed oxygen atoms. This approximation significantly reduces the computational time by restraining the number of degrees of freedom for the geometry optimisations. For low and intermediate coverages, the results obtained with fully relaxed systems and with this approximation were qualitatively similar, i.e., we have obtained similar trends with almost constant shifts in the adsorption energies. However, for higher O coverages, the relaxation of the Pt atoms has allowed the oxygen atoms to accommodate almost in the same plane as the Pt nanoparticle surface, which was not possible for rigid nanoparticle structures. These results have demonstrated that rigid nanoparticles are a valid approximation for such studies when the main interests are the O adsorption trends with low and intermediate coverages. For high coverages or for studies where subsurface oxygen is the main interest, full relaxation of the structure should aid more reliable results.

The second approximation was made trying to use symmetry arguments to justify covering only one hemisphere of the cuboctahedral nanoparticles. Again, the approximation was valid for low and intermediate coverages, showing significant differences only for high coverages, where the O atoms in the interface between free and covered hemispheres have shown different behaviours as compared to the same calculations for fully covered nanoparticles. A final approximation that we have tested was allowing only the O atoms in one facet to relax while fixing the position of all other O and Pt atoms. This strategy generated different results as compared to calculations where all O atoms are allowed to move, and we were not able to reproduce the final O positions for the studied facet and consequently the coverage dependency for the adsorption energies. Thus, we have selected the first two approximations to perform a study on coverage effects for different Pt nanoparticle sizes.

The increase in O coverage weakened the adsorption energies per oxygen atom; however, this trend was different depending on the nanoparticle size. The decrease in adsorption energy

per O with increasing coverage was much more evident for larger nanoparticles than for the Pt_{55}, which strengthen the idea that small nanoparticles could have the catalytic activity hindered due to the blocking of adsorption sites made by strongly adsorbed species. We have managed to separate the differences in the coverage dependency for each nanoparticle size into three parts. First of all, the ratio between edge, vertex and terrace sites is size dependent, i.e., for small nanoparticles edge and vertex adsorption sites are a larger fraction of the available sites as compared to terrace sites. Thus, the distribution of adsorption sites used for a certain O coverage on each nanoparticle will depend on the nanoparticle size, i.e., larger nanoparticles will use a higher number of weaker (terrace-like) sites than small nanoparticles for the same oxygen coverage.

Secondly, we have observed that the oxygen atoms move from HCP(111) sites to bridge sites for coverages higher than 0.6ML during the geometry optimisation, which also depends on the availability of adsorption sites and which is connected to size effects. This second effect can be seen as an artefact of our simulation set-up. For all the calculations, we have defined the initial distribution of adsorbates on nanoparticle facets based on arguments of adsorption site hierarchies obtained in the low-coverage limit, i.e., without considering configurational contributions to the total energies. Thus, the oxygen atoms moving to other adsorption sites during geometry optimisations helped to correct some of the errors induced by the initial guesses. For a more thorough investigation of coverage effect, we would indicate considering several different initial guesses to search for the ground-state distribution of adsorbates via a brute-force approach or with other approaches such as parametrisations of cluster-expansion Hamiltonians [241–245].

To quantify the influence of the availability of different adsorption sites in the adsorption energies, we have listed the adsorption sites for each coverage and nanoparticle size in the initial configuration and the sites occupied by oxygen in the configuration after the geometry optimisation. For each adsorption site, we have calculated the O adsorption energy for single oxygen interacting with the nanoparticle and used these values to compute the average adsorption energy for the final and initial configuration of each coverage. By analysing how these average adsorption energies for the initial and final configurations compare with the adsorption energy per O in the covered nanoparticles, we have observed that the distribution of O atoms to different sites play a smaller role to the overall coverage effect as compared to the adsorbate-adsorbate interactions and to the modifications that the O atoms create in the electronic structure of the Pt nanoparticles. We have observed that the increase in coverage changes the d-band centre of

metallic surfaces, and obtained a linear correlation between the increase in coverage and down-shifts in the d-band centres, which has also been observed for extended surfaces [236–242] and helps to explain the weakening in the interaction strength per O atom.

In general, our work demonstrates that the nanoparticle size can affect the catalytic activity in many different ways. The nanoparticle size effects played an important part in controlling the interaction strength between the nanoparticle surface and probe adsorbates such as atomic oxygen which is an important descriptor for chemical reactions and carbon monoxide that is a key contaminant for Pt catalysts in many applications, which helps to explain the decrease in catalytic activity with smaller nanoparticles. Meanwhile, for interaction with ethanol molecules, the nanoparticle size effects were not as significant. At the same time, the nanoparticle size was an essential factor to control the interaction between nanoparticles and graphene. The nanoparticle size affects how the support alters the geometric and electronic properties of the nanoparticles, including the ability of the nanoparticles to interact with probe adsorbates. In that sense, we have demonstrated that controlling the nanoparticle size concurrently with the support is a route that can be investigated in the search for better catalysts and that the size effect for the support interactions could be an additional explanation to the unusual high ORR activity of small clusters. Finally, we have also shown that the adsorption strengths, which are important descriptors for catalytic systems, are dependent on the adsorbate coverage and that this dependency also varies with the nanoparticle size. By showing the many impacts that the nanoparticle size can have on metallic nanoparticles applied to heterogeneous catalysis and by investigating the non-trivial combination of different effects important to the area, we expect to have provided insights that could be used in future researches to understanding and developing more efficient catalysts.

8.1 Further Work

Further work in similar problems to the ones treated in this thesis is necessary and is already happening inside and outside of our group. Similar to other areas in computational modelling, the main challenges in the field of heterogeneous catalysis are related to the trade-off between the accuracy of the calculations employed in the research and the similarity of the model to the investigated phenomenon. Additional work in both areas is desirable, where, for example, our group is contributing with the development and improvement of new linear-scaling DFT methods applied to metallic systems which can become useful in the near future for investigations of more realistic nanoparticle sizes. In particular to the questions treated in

this thesis, further work in the interplay between nanoparticle size and support is an interesting option, including investigations on metal-oxides and metal-carbides supports or other carbon-based supports such as defected graphene or other variations of two-dimensional carbon-based structures. Additionally, as we have observed that the size and support effects in adsorption energies change depending on the adsorbate, assessing how these effects control reaction mechanisms for the ethanol oxidation reaction could be a continuation for the work developed in this thesis. Particularly, studies with transition state search algorithms about how the combination between nanoparticle size and presence of support affects the first dehydrogenation step of ethanol molecules and reaction steps involved in the ethanol C-C bond break could be interesting continuations for our work. We also understand that more accurate investigations of the combination between nanoparticle size and adsorbate coverage effects, including the role of the adsorbates distributions for different nanoparticle sizes and shapes using, for example, cluster expansion Hamiltonians, could also provide new insights for the area. Finally, generating more accurate models including, for example, solvation and pH effects could drive insights from computational studies such as the one developed in this thesis to more realistic conditions, helping to develop new and more efficient catalysts.

Appendix A

Adsorption of O, CO, and Ethanol on Support Nanoparticles: Additional Results

A.1 O, CO, and Ethanol interacting with the Pt (100) facet of supported Pt nanoparticles

In chapter 6 we show how the support affects the adsorption properties of Pt nanoparticles interacting with O, CO and ethanol for adsorption sites in the (111) facet. Here, we show similar results obtained for the adsorbates interacting with the (100) facet. Again, the Pt nanoparticles are bound to the graphene via the (111) facet. Figure A.1 shows how the presence of the graphene support changes the interaction between nanoparticles and adsorbates.

Figure A.1 shows that the support effects for adsorption on the (100) facet of the Pt nanoparticles are similar to the ones obtained for the (111) facet which were discussed in chapter 6. Again, the presence of support weakens the adsorption of O, CO and ethanol on the Pt surface. In all the simulated cases, the change in adsorption energy due to the presence of graphene was lower than 0.3 eV, and the effect of the graphene support decreases as we increase the nanoparticle size. As we observed the same trend in the support effect with increasing nanoparticle size, we have decided to avoid calculations with Pt_{147} nanoparticles, as these effects should also be negligible.

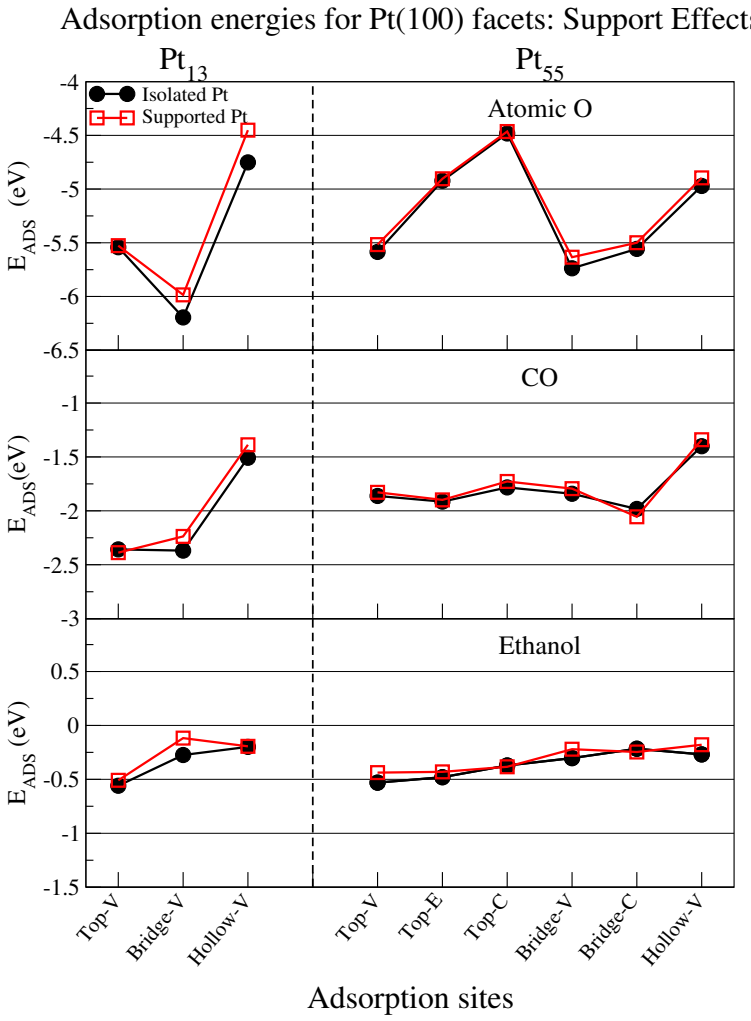

FIGURE A.1: Adsorption energies for O, CO, and ethanol interacting with the (100) facet of Pt_{13}, Pt_{55}, and Pt_{147} on different adsorption sites. The letters V, E, and C represent adsorption sites in the vertex, edge and centre of a nanoparticle facet. Black dots are adsorption energy values calculated for isolated nanoparticles and red open squares are the same values calculated for Pt nanoparticles supported on pristine graphene.

A.2 Binding the Pt (100) facet on graphene

The majority of the analysis of support effects performed in our thesis considered Pt nanoparticles interacting with pristine graphene via the (111) facet. However, we have also calculated the adsorption energies for atomic oxygen interacting with a smaller number of adsorption sites on (111) and (100) facets for Pt nanoparticles bound to graphene via the (100) facet.

Paz-Borbón and Baletto [254] recently showed that the adsorption energies of O_2 on PtNi, Pt and Ni nanoparticles can suffer considerable changes when the clusters are bound to MgO supports via the (111) or (100) facets. In our case, the support effect for Pt_{13} interacting with graphene via the (111) and (100) facet is quite similar, being as small as 0.3 eV. For larger

clusters, we also see a similar decrease in the support effect with increasing nanoparticle sizes. A possible reason for the similarities between the support effect for both facets could be the weak Pt-graphene interaction, which does not lead to significant changes as the ones observed by Paz-Borbón and Baletto [254].

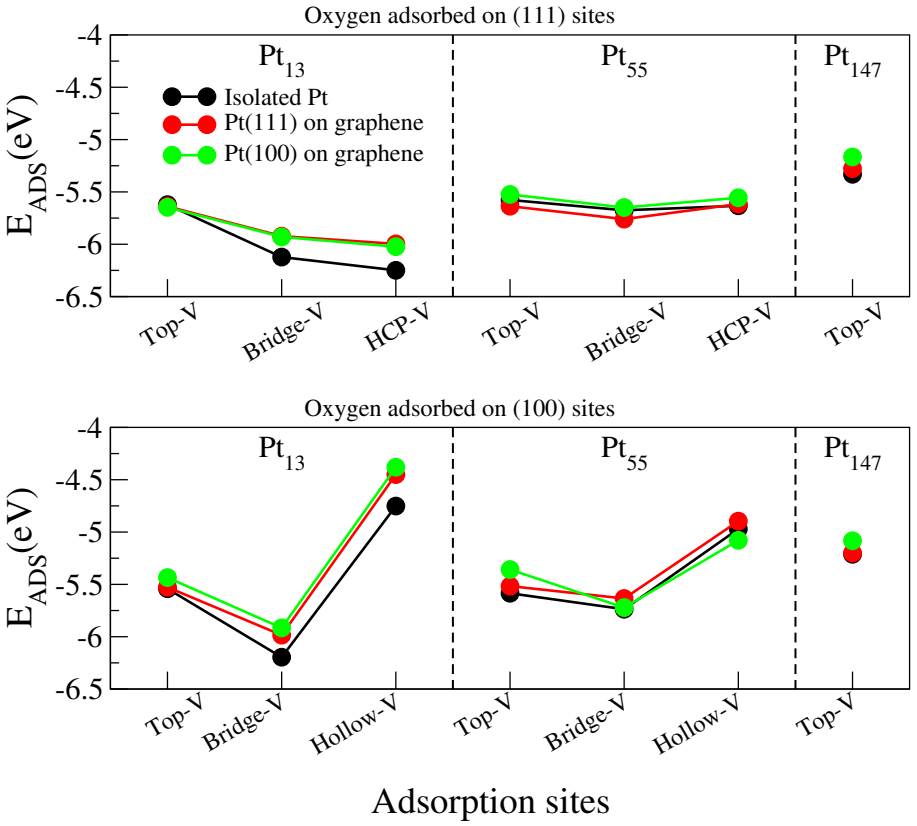

FIGURE A.2: Adsorption energies for oxygen interacting with the adsorption sites in the (111) and (100) facets of Pt_{13}, Pt_{55}, and Pt_{147}, where the letter V represents adsorption sites in the vertices of a nanoparticle facet. Black dots are adsorption energy values calculated for isolated nanoparticles. Red and green dots are the adsorption energies calculated for Pt nanoparticles bound to graphene via the (111) and (100) facet.

Appendix B

Structures for Different Adsorbate Coverages and Nanoparticle Sizes

As discussed in chapter 7, the initial O distribution with a given O coverage is different for each nanoparticle size. Figure B.1 shows the initial and final O configuration for Pt_{55} with three different values of O coverage. At this nanoparticle size, we reach a 1.00ML coverage using only HCP vertex sites for (111) facets and Bridge sites near the edges for (100) facets. For 0.66ML and 1.00ML coverages, we clearly see O atoms moving from the initial HCP (111) adsorption sites to bridge sites in the vertices of the nanoparticle after the geometry optimisation.

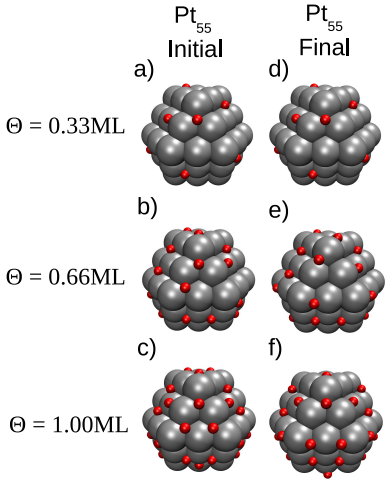

FIGURE B.1: Pt_{55} nanoparticle interacting with different coverages of atomic oxygen, where a), b), c) show initial O configuration and d), e), f) show the O configuration after geometry optimisations. Silver (red) balls represent Pt (O) atoms.

Figure B.2 shows the initial and final O configuration for Pt_{147} nanoparticles with different O coverages. Increasing O coverage, up to 0.46ML, is obtained by adding one O atom to a HCP

vertex (111) site and one O atom to a Bridge site near the edge of (100) facet. For higher O coverages, we also use HCP edges (111) adsorption sites. Similarly to the results obtained for Pt_{55}, we only see oxygen movement between adsorption sites for systems with O coverages equal or higher than 0.60ML.

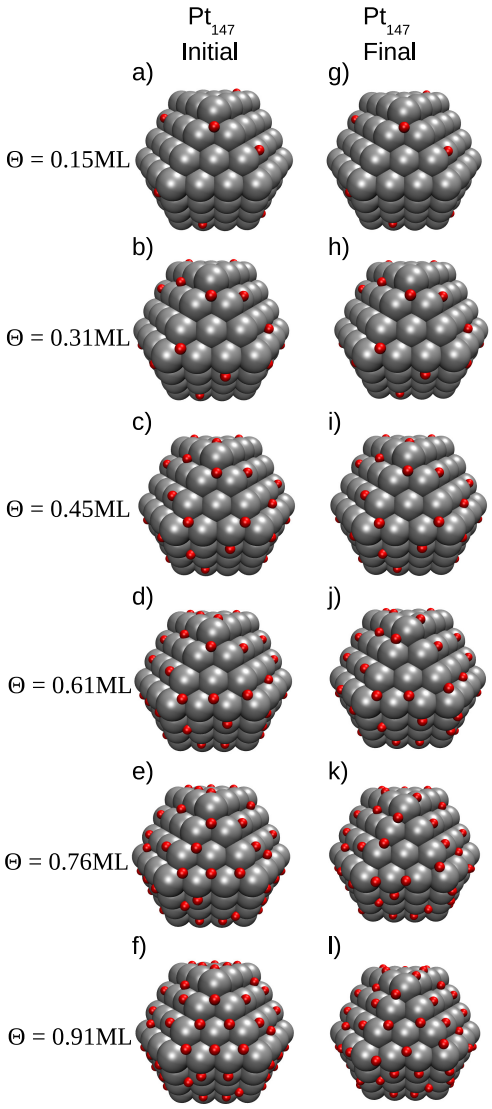

FIGURE B.2: Pt_{147} nanoparticle interacting with different coverages of atomic oxygen, where a), b), c), d), e), and f) show initial O configuration and g), h), i), j), k), and l) show the O configuration after geometry optimisation. Silver (red) balls represent Pt (O) atoms.

For Pt_{309} nanoparticles, as illustrated in figure B.3, we see significant changes between initial and final O configuration only for the systems with 0.78ML O coverage. For 0.6ML, we see small changes between initial and final O configurations, while for systems with lower coverage the initial and final O configuration are identical.

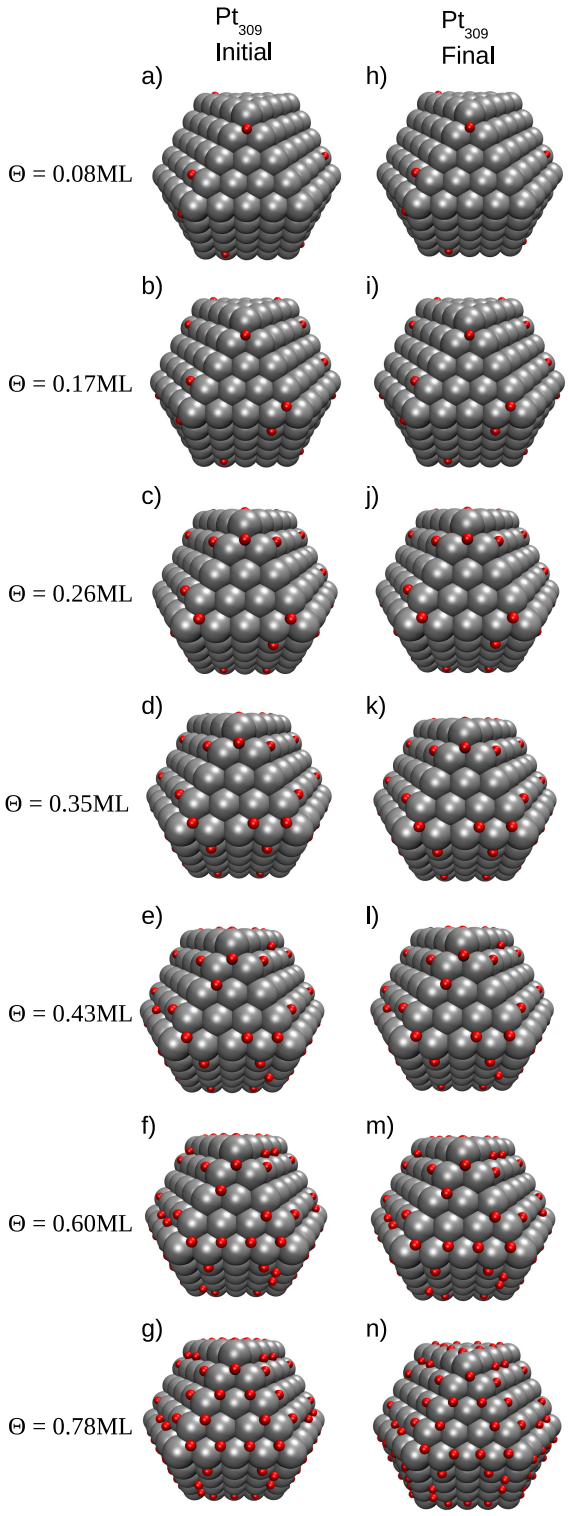

FIGURE B.3: Pt_{309} nanoparticle covered with atomic oxygen on different coverages, where a) to g) show initial O configuration and h) to n) show the O configuration after geometry optimisation. Silver (red) balls represent Pt (O) atoms.

Bibliography

[1] John P. Perdew and Karla Schmidt. Jacob's Ladder of Density Functional Approximations for the Exchange-correlation Energy. *AIP Conference Proceedings*, 577(1):1–20, 2001. Cited on pages viii and 10.

[2] Álvaro Ruiz-Serrano and Chris-Kriton Skylaris. A Variational Method for Density Functional Theory Calculations on Metallic Systems with Thousands of Atoms. *The Journal of Chemical Physics*, 139(5):054107, 2013. Cited on pages viii, 22, 23, 59, 72, 93, and 120.

[3] Lars C. Grabow, Amit A. Gokhale, Steven T. Evans, James A. Dumesic, and Manos Mavrikakis. Mechanism of the Water Gas Shift Reaction on Pt: First Principles, Experiments, and Microkinetic Modeling. *The Journal of Physical Chemistry C*, 112(12):4608–4617, 2008. Cited on pages viii, 27, 28, and 29.

[4] J. K. Nørskov, J. Rossmeisl, A. Logadottir, L. Lindqvist, J. R. Kitchin, T. Bligaard, and H. Jónsson. Origin of the Overpotential for Oxygen Reduction at a Fuel-Cell Cathode. *The Journal of Physical Chemistry B*, 108(46):17886–17892, 2004. Cited on pages viii, 29, 30, 31, 33, 36, 92, 98, 107, and 140.

[5] Liang Zhang and Graeme Henkelman. Computational Design of Alloy-Core@Shell Metal Nanoparticle Catalysts. *ACS Catalysis*, 5(2):655–660, 2015. Cited on pages viii, 37, 38, and 92.

[6] Lin Li, Frank Abild-Pedersen, Jeff Greeley, and Jens K. Nørskov. Surface Tension Effects on the Reactivity of Metal Nanoparticles. *The Journal of Physical Chemistry Letters*, 6(19):3797–3801, 2015. PMID: 26722873. Cited on pages viii, 43, and 44.

[7] T. Jiang, D. J. Mowbray, S. Dobrin, H. Falsig, B. Hvolbæk, T. Bligaard, and J. K. Nørskov. Trends in CO Oxidation Rates for Metal Nanoparticles and Close-Packed, Stepped, and Kinked Surfaces. *The Journal of Physical Chemistry C*, 113(24):10548–10553, 2009. Cited on pages viii, 45, and 92.

[8] Jolyon Aarons, Lewys Jones, Aakash Varambhia, Katherine E. MacArthur, Dogan Ozkaya, Misbah Sarwar, Chris-Kriton Skylaris, and Peter D. Nellist. Predicting the Oxygen-Binding Properties of Platinum Nanoparticle Ensembles by Combining High-Precision Electron Microscopy and Density Functional Theory. *Nano Letters*, 17(7):4003–4012, 2017. PMID: 28644034. Cited on pages ix, 34, 46, 47, 98, 101, 129, and 140.

[9] L. G. Verga, J. Aarons, M. Sarwar, D. Thompsett, A. E. Russell, and C.-K. Skylaris. Effect of Graphene Support on Large Pt Nanoparticles. *Phys. Chem. Chem. Phys.*, 18:32713–32722, 2016. Cited on pages x, xv, 69, 82, and 84.

[10] Federico Calle-Vallejo, José I. Martínez, Juan M. García-Lastra, Philippe Sautet, and David Loffreda. Fast Prediction of Adsorption Properties for Platinum Nanocatalysts with Generalized Coordination Numbers. *Angewandte Chemie International Edition*, 53(32):8316–8319, 2014. Cited on pages xi, 33, 94, 95, and 129.

[11] Lucas Garcia Verga and Chris-Kriton Skylaris. Chapter 8 - DFT Modeling of Metallic Nanoparticles. In Stefan T. Bromley and Scott M. Woodley, editors, *Computational Modelling of Nanoparticles*, volume 12 of *Frontiers of Nanoscience*, pages 239 – 293. Elsevier, 2018. Cited on pages xv, 5, and 24.

[12] L. G. Verga, A. E. Russell, and C.-K. Skylaris. Ethanol, O, and CO Adsorption on Pt Nanoparticles: Effects of Nanoparticle Size and Graphene Support. *Phys. Chem. Chem. Phys.*, 20:25918–25930, 2018. Cited on pages xv and 90.

[13] L. G. Verga, J. Aarons, M. Sarwar, D. Thompsett, A. E. Russell, and C.-K. Skylaris. DFT Calculation of Oxygen Adsorption on Platinum Nanoparticles: Coverage and Size Effects. *Faraday Discuss.*, 208:497–522, 2018. Cited on pages xv and 116.

[14] L. Carrette, K. A. Friedrich, and U. Stimming. Fuel Cells - Fundamentals and Applications. *Fuel Cells*, 1(1):5–39, 2001. Cited on page 1.

[15] Rajesh K. Ahluwalia and X. Wang. Direct Hydrogen Fuel Cell Systems for Hybrid Vehicles. *Journal of Power Sources*, 139(1–2):152 – 164, 2005. Cited on page 1.

[16] C.E Thomas, Brian D James, Frank D Lomax Jr, and Ira F Kuhn Jr. Fuel Options for the Fuel Cell Vehicle: Hydrogen, Methanol or Gasoline? *International Journal of Hydrogen Energy*, 25(6):551 – 567, 2000. Cited on page 1.

[17] M.Z.F. Kamarudin, S.K. Kamarudin, M.S. Masdar, and W.R.W. Daud. Review: Direct Ethanol Fuel Cells. *International Journal of Hydrogen Energy*, 38(22):9438 – 9453, 2013. Cited on pages 2, 91, and 92.

[18] Di Li, Xinyu Li, and Jinlong Gong. Catalytic Reforming of Oxygenates: State of the Art and Future Prospects. *Chemical Reviews*, 116(19):11529–11653, 2016. PMID: 27527927. Cited on pages 3, 91, and 92.

[19] P. Hohenberg and W. Kohn. Inhomogeneous Electron Gas. *Phys. Rev.*, 136:B864–B871, Nov 1964. Cited on page 6.

[20] W. Kohn and L. J. Sham. Self-Consistent Equations Including Exchange and Correlation Effects. *Phys. Rev.*, 140:A1133–A1138, Nov 1965. Cited on page 6.

[21] John P. Perdew, Kieron Burke, and Matthias Ernzerhof. Generalized Gradient Approximation Made Simple. *Phys. Rev. Lett.*, 77:3865–3868, Oct 1996. Cited on pages 11, 59, and 72.

[22] B. Hammer, L. B. Hansen, and J. K. Nørskov. Improved Adsorption Energetics within Density-Functional Theory Using Revised Perdew-Burke-Ernzerhof Functionals. *Phys. Rev. B*, 59:7413–7421, Mar 1999. Cited on pages 11, 72, 104, and 120.

[23] John P. Perdew, Adrienn Ruzsinszky, Gábor I. Csonka, Oleg A. Vydrov, Gustavo E. Scuseria, Lucian A. Constantin, Xiaolan Zhou, and Kieron Burke. Restoring the Density-Gradient Expansion for Exchange in Solids and Surfaces. *Phys. Rev. Lett.*, 100:136406, Apr 2008. Cited on page 11.

[24] P. E. Blöchl. Projector Augmented-Wave Method. *Phys. Rev. B*, 50:17953–17979, Dec 1994. Cited on pages 14, 59, 72, 93, and 120.

[25] W. Kohn. Density Functional and Density Matrix Method Scaling Linearly with the Number of Atoms. *Phys. Rev. Lett.*, 76:3168–3171, Apr 1996. Cited on page 15.

[26] Stefan Goedecker. Linear Scaling Electronic Structure Methods. *Rev. Mod. Phys.*, 71:1085–1123, Jul 1999. Cited on page 15.

[27] D R Bowler and T Miyazaki. O(n) Methods in Electronic Structure Calculations. *Reports on Progress in Physics*, 75(3):036503, 2012. Cited on page 15.

[28] Chris-Kriton Skylaris, Peter D. Haynes, Arash A. Mostofi, and Mike C. Payne. Introducing ONETEP: Linear-scaling Density Functional Simulations on Parallel Computers. *The Journal of Chemical Physics*, 122(8):084119, 2005. Cited on pages 15, 59, 72, 93, and 120.

[29] José M Soler, Emilio Artacho, Julian D Gale, Alberto García, Javier Junquera, Pablo Ordejón, and Daniel Sánchez-Portal. The SIESTA Method for Ab Initio Order-N Materials Simulation. *Journal of Physics: Condensed Matter*, 14(11):2745, 2002. Cited on page 15.

[30] T. Ozaki and H. Kino. Efficient Projector Expansion for the Ab Initio LCAO Method. *Phys. Rev. B*, 72:045121, Jul 2005. Cited on page 15.

[31] M.J. Gillan, D.R. Bowler, A.S. Torralba, and T. Miyazaki. Order-N First-Principles Calculations with the Conquest Code. *Computer Physics Communications*, 177(1):14 – 18, 2007. Proceedings of the Conference on Computational Physics 2006. Cited on page 15.

[32] Luigi Genovese, Alexey Neelov, Stefan Goedecker, Thierry Deutsch, Seyed Alireza Ghasemi, Alexander Willand, Damien Caliste, Oded Zilberberg, Mark Rayson, Anders Bergman, and Reinhold Schneider. Daubechies Wavelets as a Basis Set for Density Functional Pseudopotential Calculations. *The Journal of Chemical Physics*, 129(1):014109, 2008. Cited on page 15.

[33] Chris-Kriton Skylaris, Arash A. Mostofi, Peter D. Haynes, Chris J. Pickard, and Mike C. Payne. Accurate Kinetic Energy Evaluation in Electronic Structure Calculations with Localized Functions on Real Space Grids. *Computer Physics Communications*, 140(3):315 – 322, 2001. Cited on pages 16, 60, and 93.

[34] N. David Mermin. Thermal Properties of the Inhomogeneous Electron Gas. *Phys. Rev.*, 137:A1441–A1443, Mar 1965. Cited on page 17.

[35] S. Goedecker. Decay Properties of the Finite-temperature Density Matrix in Metals. *Phys. Rev. B*, 58:3501–3502, Aug 1998. Cited on page 18.

[36] M J Gillan. Calculation of the Vacancy Formation Energy in Aluminium. *Journal of Physics: Condensed Matter*, 1(4):689, 1989. Cited on page 19.

[37] M. Methfessel and A. T. Paxton. High-precision Sampling for Brillouin-zone Integration in Metals. *Phys. Rev. B*, 40:3616–3621, Aug 1989. Cited on page 19.

[38] Nicola Marzari, David Vanderbilt, Alessandro De Vita, and M. C. Payne. Thermal Contraction and Disordering of the Al(110) Surface. *Phys. Rev. Lett.*, 82:3296–3299, Apr 1999. Cited on page 19.

[39] Péter Pulay. Convergence Acceleration of Iterative Sequences. The Case of SCF Iteration. *Chemical Physics Letters*, 73(2):393 – 398, 1980. Cited on page 20.

[40] P. Pulay. Improved SCF Convergence Acceleration. *Journal of Computational Chemistry*, 3(4):556–560, 1982. Cited on page 20.

[41] G. Kresse and J. Furthmüller. Efficient Iterative Schemes for Ab initio Total-energy Calculations Using a Plane-Wave Basis Set. *Phys. Rev. B*, 54:11169–11186, Oct 1996. Cited on page 20.

[42] Nicola Marzari, David Vanderbilt, and M. C. Payne. Ensemble Density-Functional Theory for Ab Initio Molecular Dynamics of Metals and Finite-Temperature Insulators. *Phys. Rev. Lett.*, 79:1337–1340, Aug 1997. Cited on pages 21 and 22.

[43] Christoph Freysoldt, Sixten Boeck, and Jörg Neugebauer. Direct Minimization Technique for Metals in Density Functional Theory. *Phys. Rev. B*, 79:241103, Jun 2009. Cited on pages 21 and 22.

[44] Stewart J. Clark, Matthew D. Segall, Chris J. Pickard, Phil J. Hasnip, Matt I. J. Probert, Keith Refson, and Mike C. Payne. First Principles Methods Using CASTEP. *Zeitschrift für Kristallographie - Crystalline Materials*, 220(5/6):567–570, 2005. Cited on pages 22, 54, and 59.

[45] S. Goedecker and L. Colombo. Efficient Linear Scaling Algorithm for Tight-Binding Molecular Dynamics. *Phys. Rev. Lett.*, 73:122–125, Jul 1994. Cited on page 23.

[46] Jolyon Aarons, Misbah Sarwar, David Thompsett, and Chris-Kriton Skylaris. Perspective: Methods for Large-scale Density Functional Calculations on Metallic Systems. *The Journal of Chemical Physics*, 145(22):220901, 2016. Cited on page 23.

[47] Jolyon Aarons and Chris-Kriton Skylaris. Electronic Annealing Fermi Operator Expansion for DFT Calculations on Metallic Systems. *The Journal of Chemical Physics*, 148(7):074107, 2018. Cited on page 23.

[48] Cynthia M. Friend and Bingjun Xu. Heterogeneous Catalysis: A Central Science for a Sustainable Future. *Accounts of Chemical Research*, 50(3):517–521, 2017. PMID: 28945397. Cited on page 24.

[49] H. Bernhard Schlegel. Geometry Optimization. *Wiley Interdisciplinary Reviews: Computational Molecular Science*, 1(5):790–809, 2011. Cited on page 25.

[50] HANNES JÓNSSON, GREG MILLS, and KARSTEN W. JACOBSEN. *Nudged Elastic Band Method for Finding Minimum Energy Paths of Transitions*, pages 385–404. WORLD SCIENTIFIC, 2011. Cited on pages 25 and 26.

[51] Greg Mills and Hannes Jónsson. Quantum and Thermal Effects in H_2 Dissociative Adsorption: Evaluation of Free Energy Barriers in Multidimensional Quantum Systems. *Phys. Rev. Lett.*, 72:1124–1127, Feb 1994. Cited on pages 25 and 26.

[52] Gregory Mills, Hannes Jónsson, and Gregory K. Schenter. Reversible Work Transition State Theory: Application to Dissociative Adsorption of Hydrogen. *Surface Science*, 324(2):305 – 337, 1995. Cited on pages 25 and 26.

[53] Graeme Henkelman, Blas P. Uberuaga, and Hannes Jónsson. A Climbing Image Nudged Elastic Band Method for Finding Saddle Points and Minimum Energy Paths. *The Journal of Chemical Physics*, 113(22):9901–9904, 2000. Cited on pages 25 and 26.

[54] Graeme Henkelman and Hannes Jónsson. A Dimer Method for Finding Saddle Points on High Dimensional Potential Surfaces Using Only First Derivatives. *The Journal of Chemical Physics*, 111(15):7010–7022, 1999. Cited on pages 25 and 26.

[55] Thomas A. Halgren and William N. Lipscomb. The Synchronous-Transit Method for Determining Reaction Pathways and Locating Molecular Transition States. *Chemical Physics Letters*, 49(2):225 – 232, 1977. Cited on pages 25 and 26.

[56] Niranjan Govind, Max Petersen, George Fitzgerald, Dominic King-Smith, and Jan Andzelm. A Generalized Synchronous Transit Method for Transition State Location. *Computational Materials Science*, 28(2):250 – 258, 2003. Proceedings of the Symposium on Software Development for Process and Materials Design. Cited on pages 25 and 26.

[57] Cheng Shang and Zhi-Pan Liu. Constrained Broyden Minimization Combined with the Dimer Method for Locating Transition State of Complex Reactions. *Journal of Chemical Theory and Computation*, 6(4):1136–1144, 2010. Cited on page 25.

[58] Hui-Fang Wang and Zhi-Pan Liu. Comprehensive Mechanism and Structure-Sensitivity of Ethanol Oxidation on Platinum: New Transition-State Searching Method for Resolving the Complex Reaction Network. *Journal of the American Chemical Society*, 130(33):10996–11004, 2008. PMID: 18642913. Cited on pages 25 and 41.

[59] H. Bernhard Schlegel. Exploring Potential Energy Surfaces for Chemical Reactions: An Overview of Some Practical Methods. *Journal of Computational Chemistry*, 24(12):1514–1527, 2003. Cited on page 26.

[60] Daniel Sheppard, Rye Terrell, and Graeme Henkelman. Optimization Methods for Finding Minimum Energy Paths. *The Journal of Chemical Physics*, 128(13):134106, 2008. Cited on page 26.

[61] Frank. Jensen. *Introduction to Computational Chemistry*. Wiley, 2007. Cited on page 26.

[62] Alejandro J. Garza, Alexis T. Bell, and Martin Head-Gordon. Mechanism of CO_2 Reduction at Copper Surfaces: Pathways to C_2 Products. *ACS Catalysis*, 8(0):1490–1499, 2018. Cited on page 27.

[63] Vladimir Tripković, Egill Skúlason, Samira Siahrostami, Jens K. Nørskov, and Jan Rossmeisl. The Oxygen Reduction Reaction Mechanism on Pt(111) from Density Functional Theory Calculations. *Electrochimica Acta*, 55(27):7975 – 7981, 2010. EMERGING TRENDS AND CHALLENGES IN ELECTROCHEMISTRY. Cited on page 27.

[64] Shizhong Liu, Michael G. White, and Ping Liu. Mechanism of Oxygen Reduction Reaction on Pt(111) in Alkaline Solution: Importance of Chemisorbed Water on Surface. *The Journal of Physical Chemistry C*, 120(28):15288–15298, 2016. Cited on page 27.

[65] Paul C. Jennings, Hristiyan A. Aleksandrov, Konstantin M. Neyman, and Roy L. Johnston. DFT Studies of Oxygen Dissociation on the 116-atom Platinum Truncated Octahedron Particle. *Phys. Chem. Chem. Phys.*, 16:26539–26545, 2014. Cited on pages 27 and 96.

[66] Paul C. Jennings, Hristiyan A. Aleksandrov, Konstantin M. Neyman, and Roy L. Johnston. A DFT Study of Oxygen Dissociation on Platinum Based Nanoparticles. *Nanoscale*, 6:1153–1165, 2014. Cited on page 27.

[67] Jeff Greeley and Manos Mavrikakis. A First-Principles Study of Methanol Decomposition on Pt(111). *Journal of the American Chemical Society*, 124(24):7193–7201, 2002. PMID: 12059245. Cited on page 27.

[68] Jeff Greeley and Manos Mavrikakis. Competitive Paths for Methanol Decomposition on Pt(111). *Journal of the American Chemical Society*, 126(12):3910–3919, 2004. PMID: 15038745. Cited on page 27.

[69] Zhao-Xu Chen, Konstantin M. Neyman, Kok Hwa Lim, and Notker Rösch. CH_3O Decomposition on PdZn(111), Pd(111), and Cu(111). A Theoretical Study. *Langmuir*, 20(19):8068–8077, 2004. PMID: 15350074. Cited on page 27.

[70] R. Alcalá, M. Mavrikakis, and J.A. Dumesic. DFT Studies for Cleavage of C-C and C-O Bonds in Surface Species Derived from Ethanol on Pt(111). *Journal of Catalysis*, 218(1):178 – 190, 2003. Cited on page 27.

[71] Jonathan E. Sutton and Dionisios G. Vlachos. Ethanol Activation on Closed-Packed Surfaces. *Industrial & Engineering Chemistry Research*, 54(16):4213–4225, 2015. Cited on pages 27 and 92.

[72] Bin Liu and Jeffrey Greeley. Density Functional Theory Study of Selectivity Considerations for C–C Versus C–O Bond Scission in Glycerol Decomposition on Pt(111). *Topics in Catalysis*, 55(5):280–289, Jun 2012. Cited on page 27.

[73] Jonathan E. Sutton, Paraskevi Panagiotopoulou, Xenophon E. Verykios, and Dionisios G. Vlachos. Combined DFT, Microkinetic, and Experimental Study of Ethanol Steam Reforming on Pt. *The Journal of Physical Chemistry C*, 117(9):4691–4706, 2013. Cited on page 27.

[74] Ming Li, Wenyue Guo, Ruibin Jiang, Lianming Zhao, Xiaoqing Lu, Houyu Zhu, Dianling Fu, and Honghong Shan. Density Functional Study of Ethanol Decomposition on Rh(111). *The Journal of Physical Chemistry C*, 114(49):21493–21503, 2010. Cited on page 27.

[75] C.J. Houtman and M.A. Barteau. Divergent Pathways of Acetaldehyde and Ethanol Decarbonylation on the Rh(111) Surface. *Journal of Catalysis*, 130(2):528 – 546, 1991. Cited on page 27.

[76] John P. Clay, Jeffrey P. Greeley, Fabio H. Ribeiro, W. Nicholas Delgass, and William F. Schneider. DFT Comparison of Intrinsic WGS Kinetics over Pd and Pt. *Journal of Catalysis*, 320:106 – 117, 2014. Cited on pages 27 and 29.

[77] Chia-Hao Lin, Chung-Liang Chen, and Jeng-Han Wang. Mechanistic Studies of Water-Gas-Shift Reaction on Transition Metals. *The Journal of Physical Chemistry C*, 115(38):18582–18588, 2011. Cited on page 27.

[78] Shih-Chang Huang, Chia-Hao Lin, and J.-H. Wang. Trends of Water Gas Shift Reaction on Close-Packed Transition Metal Surfaces. *The Journal of Physical Chemistry C*, 114(21):9826–9834, 2010. Cited on page 27.

[79] José L. C. Fajín, M. Natália D. S. Cordeiro, and José R. B. Gomes. Density Functional Theory Study of the Water Dissociation on Platinum Surfaces: General Trends. *The Journal of Physical Chemistry A*, 118(31):5832–5840, 2014. PMID: 24547954. Cited on pages 27 and 42.

[80] Andrey S. Bazhenov, Leon Lefferts, and Karoliina Honkala. Adsorption and Activation of Water on Cuboctahedral Rhodium and Platinum Nanoparticles. *The Journal of Physical Chemistry C*, 121(8):4324–4331, 2017. Cited on page 27.

[81] José L. C. Fajín, Albert Bruix, Maria Natália D. S. Cordeiro, José R. B. Gomes, and Francesc Illas. Density Functional Theory Model Study of Size and Structure Effects on Water Dissociation by Platinum Nanoparticles. *The Journal of Chemical Physics*, 137(3):034701, 2012. Cited on pages 27, 42, 99, and 100.

[82] Rengin Peköz and Davide Donadio. Dissociative Adsorption of Water at (211) Stepped Metallic Surfaces by First-Principles Simulations. *The Journal of Physical Chemistry C*, 121(31):16783–16791, 2017. Cited on page 27.

[83] George G. Olympiou, Christos M. Kalamaras, Constantinos D. Zeinalipour-Yazdi, and Angelos M. Efstathiou. Mechanistic Aspects of the Water–Gas shift Reaction on Alumina-Supported Noble Metal Catalysts: In situ DRIFTS and SSITKA-mass Spectrometry Studies. *Catalysis Today*, 127(1):304 – 318, 2007. I.A. Vasalos Festschrift. Cited on page 29.

[84] Alexandre Goguet, Frederic C. Meunier, Daniele Tibiletti, John P. Breen, and Robbie Burch. Spectrokinetic Investigation of Reverse Water-Gas-Shift Reaction Intermediates over a Pt/CeO_2 Catalyst. *The Journal of Physical Chemistry B*, 108(52):20240–20246, 2004. Cited on page 29.

[85] Gary Jacobs, Syed Khalid, Patricia M. Patterson, Dennis E. Sparks, and Burtron H. Davis. Water-Gas Shift Catalysis: Kinetic Isotope Effect Identifies Surface Formates in Rate Limiting Step for Pt/ceria Catalysts. *Applied Catalysis A: General*, 268(1):255 – 266, 2004. Cited on page 29.

[86] F.C. Meunier, D. Tibiletti, A. Goguet, S. Shekhtman, C. Hardacre, and R. Burch. On the Complexity of the Water-Gas Shift Reaction Mechanism over a Pt/CeO_2 Catalyst: Effect of the Temperature on the Reactivity of Formate Surface Species Studied by Operando DRIFT During Isotopic Transient at Chemical Steady-State. *Catalysis Today*, 126(1):143 – 147, 2007. Operando Spectroscopy. Cited on page 29.

[87] Andrew J. Medford, Aleksandra Vojvodic, Jens S. Hummelshøj, Johannes Voss, Frank Abild-Pedersen, Felix Studt, Thomas Bligaard, Anders Nilsson, and Jens K. Nørskov. From the Sabatier Principle to a Predictive Theory of Transition-Metal Heterogeneous Catalysis. *Journal of Catalysis*, 328:36 – 42, 2015. Special Issue: The Impact of Haldor Topsøe on Catalysis. Cited on pages 30 and 33.

[88] J. N. Bronsted. Acid and Basic Catalysis. *Chemical Reviews*, 5(3):231–338, 1928. Cited on page 31.

[89] M. G. Evans and M. Polanyi. Inertia and Driving Force of Chemical Reactions. *Trans. Faraday Soc.*, 34:11–24, 1938. Cited on page 31.

[90] Hèctor Prats, Francesc Illas, and Ramón Sayós. General Concepts, Assumptions, Drawbacks, and Misuses in Kinetic Monte Carlo and Microkinetic Modeling Simulations Applied to Computational Heterogeneous Catalysis. *International Journal of Quantum Chemistry*, 118(9):e25518, 2018. Cited on page 31.

[91] A Logadottir, T.H Rod, J.K Nørskov, B Hammer, S Dahl, and C.J.H Jacobsen. The Brønsted-Evans-Polanyi Relation and the Volcano Plot for Ammonia Synthesis over Transition Metal Catalysts. *Journal of Catalysis*, 197(2):229 – 231, 2001. Cited on page 31.

[92] J.K. Nørskov, T. Bligaard, A. Logadottir, S. Bahn, L.B. Hansen, M. Bollinger, H. Bengaard, B. Hammer, Z. Sljivancanin, M. Mavrikakis, Y. Xu, S. Dahl, and C.J.H. Jacobsen. Universality in Heterogeneous Catalysis. *Journal of Catalysis*, 209(2):275 – 278, 2002. Cited on page 31.

[93] Shengguang Wang, Burcin Temel, Juan Shen, Glenn Jones, Lars C. Grabow, Felix Studt, Thomas Bligaard, Frank Abild-Pedersen, Claus H. Christensen, and Jens K. Nørskov. Universal Brønsted-Evans-Polanyi Relations for C–C, C–O, C–N, N–O, N–N, and O–O Dissociation Reactions. *Catalysis Letters*, 141(3):370–373, Mar 2011. Cited on page 31.

[94] S. Wang, V. Petzold, V. Tripkovic, J. Kleis, J. G. Howalt, E. Skulason, E. M. Fernandez, B. Hvolbaek, G. Jones, A. Toftelund, H. Falsig, M. Bjorketun, F. Studt, F. Abild-Pedersen, J. Rossmeisl, J. K. Nørskov, and T. Bligaard. Universal Transition State Scaling Relations for (De)hydrogenation Over Transition Metals. *Phys. Chem. Chem. Phys.*, 13:20760–20765, 2011. Cited on page 31.

[95] Jonathan E. Sutton and Dionisios G. Vlachos. Effect of Errors in Linear Scaling Relations and Brønsted-Evans-Polanyi Relations on Activity and Selectivity Maps. *Journal of Catalysis*, 338:273 – 283, 2016. Cited on page 32.

[96] F. Abild-Pedersen, J. Greeley, F. Studt, J. Rossmeisl, T. R. Munter, P. G. Moses, E. Skúlason, T. Bligaard, and J. K. Nørskov. Scaling Properties of Adsorption Energies for Hydrogen-Containing Molecules on Transition-Metal Surfaces. *Phys. Rev. Lett.*, 99:016105, Jul 2007. Cited on page 32.

[97] Bin Liu and Jeffrey Greeley. Decomposition Pathways of Glycerol via C-H, O-H, and C-C Bond Scission on Pt(111): A Density Functional Theory Study. *The Journal of Physical Chemistry C*, 115(40):19702–19709, 2011. Cited on page 32.

[98] Bin Liu and Jeffrey Greeley. A Density Functional Theory Analysis of Trends in Glycerol Decomposition on Close-Packed Transition Metal Surfaces. *Phys. Chem. Chem. Phys.*, 15:6475–6485, 2013. Cited on page 32.

[99] B. Hammer and J.K. Nørskov. Theoretical Surface Science and Catalysis-Calculations and Concepts. In *Impact of Surface Science on Catalysis*, volume 45 of *Advances in Catalysis*, pages 71 – 129. Academic Press, 2000. Cited on pages 33, 65, 85, and 107.

[100] Jens K. Nørskov, Frank Abild-Pedersen, Felix Studt, and Thomas Bligaard. Density Functional Theory in Surface Chemistry and Catalysis. *PNAS*, 108(3):937–943, 2011. Cited on pages 33, 65, and 107.

[101] Federico Calle-Vallejo, Jakub Tymoczko, Viktor Colic, Quang Huy Vu, Marcus D. Pohl, Karina Morgenstern, David Loffreda, Philippe Sautet, Wolfgang Schuhmann, and Aliaksandr S. Bandarenka. Finding Optimal Surface Sites on Heterogeneous Catalysts by Counting Nearest Neighbors. *Science*, 350(6257):185–189, 2015. Cited on pages 33 and 34.

[102] Xianfeng Ma and Hongliang Xin. Orbitalwise Coordination Number for Predicting Adsorption Properties of Metal Nanocatalysts. *Phys. Rev. Lett.*, 118:036101, Jan 2017. Cited on page 34.

[103] Ye Wang, Shouzhong Zou, and Wen-Bin Cai. Recent Advances on Electro-Oxidation of Ethanol on Pt- and Pd-Based Catalysts: From Reaction Mechanisms to Catalytic Materials. *Catalysts*, 5(3):1507–1534, 2015. Cited on page 35.

[104] M.A.F. Akhairi and S.K. Kamarudin. Catalysts in Direct Ethanol Fuel Cell (DEFC): An Overview. *International Journal of Hydrogen Energy*, 41(7):4214 – 4228, 2016. Cited on pages 35, 36, 91, and 92.

[105] Ermete Antolini. Catalysts for Direct Ethanol Fuel Cells. *Journal of Power Sources*, 170(1):1 – 12, 2007. Cited on pages 35 and 36.

[106] Liang Ma, Deryn Chu, and Rongrong Chen. Comparison of Ethanol Electro-oxidation on Pt/C and Pd/C Catalysts in Alkaline Media. *International Journal of Hydrogen Energy*, 37(15):11185 – 11194, 2012. Hydrogen Enriched Methane. Cited on pages 35 and 36.

[107] Lam Wing H. Leung and Michael J. Weaver. Real-time FTIR Spectroscopy as a Quantitative Kinetic Probe of Competing Electrooxidation Pathways of Small Organic Molecules. *The Journal of Physical Chemistry*, 92(14):4019–4022, 1988. Cited on page 35.

[108] H. Wang, Z. Jusys, and R. J. Behm. Ethanol Electrooxidation on a Carbon-Supported Pt Catalyst: Reaction Kinetics and Product Yields. *The Journal of Physical Chemistry B*, 108(50):19413–19424, 2004. Cited on pages 35 and 36.

[109] M.H. Shao and R.R. Adzic. Electrooxidation of Ethanol on a Pt Electrode in Acid Solutions: in situ ATR-SEIRAS Study. *Electrochimica Acta*, 50(12):2415 – 2422, 2005. Cited on pages 35 and 36.

[110] Flavio Colmati, Germano Tremiliosi-Filho, Ernesto R. Gonzalez, Antonio Berna, Enrique Herrero, and Juan M. Feliu. Surface Structure Effects on the Electrochemical Oxidation of Ethanol on Platinum Single Crystal Electrodes. *Faraday Discuss.*, 140:379–397, 2009. Cited on pages 35, 36, and 41.

[111] Stanley C.S. Lai, Steven E.F. Kleijn, Fatma T.Z. Öztürk, Vivienne C. van Rees Vellinga, Jesper Koning, Paramaconi Rodriguez, and Marc T.M. Koper. Effects of Electrolyte pH and Composition on the Ethanol Electro-oxidation Reaction. *Catalysis Today*, 154(1):92 – 104, 2010. Catalytic Surface Science. Cited on pages 35 and 36.

[112] Richard Kavanagh, Xiao-Ming Cao, Wen-Feng Lin, Christopher Hardacre, and P. Hu. Origin of Low CO_2 Selectivity on Platinum in the Direct Ethanol Fuel Cell. *Angewandte Chemie International Edition*, 51(7):1572–1575, 2012. Cited on page 35.

[113] J. Greeley, I. E. L. Stephens, A. S. Bondarenko, T. P. Johansson, H. A. Hansen, T. F. Jaramillo, J. Rossmeisl, I. Chorkendorff, and J. K. Nørskov. Alloys of Platinum and Early Transition Metals as Oxygen Reduction Electrocatalysts. *Nature Chemistry*, 1:552–556, 2009. Cited on pages 36, 98, and 140.

[114] Ifan E. L. Stephens, Alexander S. Bondarenko, Francisco J. Perez-Alonso, Federico Calle-Vallejo, Lone Bech, Tobias P. Johansson, Anders K. Jepsen, Rasmus Frydendal, Brian P. Knudsen, Jan Rossmeisl, and Ib Chorkendorff. Tuning the Activity of Pt(111) for Oxygen Electroreduction by Subsurface Alloying. *Journal of the American Chemical Society*, 133(14):5485–5491, 2011. PMID: 21417329. Cited on page 36.

[115] Paul C. Jennings, Hristiyan A. Aleksandrov, Konstantin M. Neyman, and Roy L. Johnston. O_2 Dissociation on M@Pt Core-Shell Particles for 3d, 4d, and 5d Transition Metals. *The Journal of Physical Chemistry C*, 119(20):11031–11041, 2015. Cited on page 36.

[116] Benjamin Corona, Marco Howard, Liang Zhang, and Graeme Henkelman. Computational Screening of Core@Shell Nanoparticles for the Hydrogen Evolution and Oxygen Reduction Reactions. *The Journal of Chemical Physics*, 145(24):244708, 2016. Cited on page 37.

[117] Beatriz Roldan Cuenya and Farzad Behafarid. Nanocatalysis: Size- and Shape-dependent Chemisorption and Catalytic Reactivity. *Surface Science Reports*, 70(2):135 – 187, 2015. Cited on page 39.

[118] Sven Heiles and Roy L. Johnston. Global Optimization of Clusters Using Electronic Structure Methods. *International Journal of Quantum Chemistry*, 113(18):2091–2109, 2013. Cited on page 39.

[119] Edoardo Aprà, Riccardo Ferrando, and Alessandro Fortunelli. Density-Functional Global Optimization of Gold Nanoclusters. *Phys. Rev. B*, 73:205414, May 2006. Cited on page 40.

[120] De-en Jiang and Michael Walter. Au_{40}: A Large Tetrahedral Magic Cluster. *Phys. Rev. B*, 84:193402, Nov 2011. Cited on page 40.

[121] Oliver D. Häberlen, Sai-Cheong Chung, Mauro Stener, and Notker Rösch. From Clusters to Bulk: A Relativistic Density Functional Investigation on a Series of Gold Clusters Au_n, n = 6, ..., 147. *The Journal of Chemical Physics*, 106(12):5189–5201, 1997. Cited on page 40.

[122] Lichang Wang and Qingfeng Ge. Studies of Rhodium Nanoparticles Using the First Principles Density Functional Theory Calculations. *Chemical Physics Letters*, 366(3):368 – 376, 2002. Cited on page 40.

[123] Yusuke Nanba, Takayoshi Ishimoto, and Michihisa Koyama. Structural Stability of Ruthenium Nanoparticles: A Density Functional Theory Study. *The Journal of Physical Chemistry C*, 121(49):27445–27452, 2017. Cited on page 40.

[124] Sven Krüger, Stefan Vent, Folke Nörtemann, Markus Staufer, and Notker Rösch. The Average Bond Length in Pd Clusters Pd_n, n=4-309: A Density-Functional Case Study on the Scaling of Cluster Properties. *The Journal of Chemical Physics*, 115(5):2082–2087, 2001. Cited on page 40.

[125] Wenqin Zhang, Qingfeng Ge, and Lichang Wang. Structure Effects on the Energetic, Electronic, and Magnetic Properties of Palladium Nanoparticles. *The Journal of Chemical Physics*, 118(13):5793–5801, 2003. Cited on page 40.

[126] Francesc Viñes, Francesc Illas, and Konstantin M. Neyman. Density Functional Calculations of Pd Nanoparticles Using a Plane-Wave Method. *The Journal of Physical Chemistry A*, 112(38):8911–8915, 2008. Cited on page 40.

[127] Li Xiao and Lichang Wang. Structures of Platinum Clusters: Planar or Spherical? *The Journal of Physical Chemistry A*, 108(41):8605–8614, 2004. Cited on pages 40, 71, and 72.

[128] Maurício J. Piotrowski, Crina G. Ungureanu, Polina Tereshchuk, Krys E. A. Batista, Anderson S. Chaves, Diego Guedes-Sobrinho, and Juarez L. F. Da Silva. Theoretical Study of the Structural, Energetic, and Electronic Properties of 55-Atom Metal Nanoclusters: A DFT Investigation within van der Waals Corrections, Spin-Orbit Coupling, and PBE+U of 42 Metal Systems. *The Journal of Physical Chemistry C*, 120(50):28844–28856, 2016. Cited on page 40.

[129] Geng Sun and Philippe Sautet. Metastable Structures in Cluster Catalysis from First-Principles: Structural Ensemble in Reaction Conditions and Metastability Triggered Reactivity. *Journal of the American Chemical Society*, 140(8):2812–2820, 2018. PMID: 29424224. Cited on page 41.

[130] Si Chung. Chang, Lam Wing H. Leung, and Michael J. Weaver. Metal Crystallinity Effects in Electrocatalysis as Probed by Real-time FTIR Spectroscopy: Electrooxidation of Formic Acid, Methanol, and Ethanol on Ordered Low-index Platinum Surfaces. *The Journal of Physical Chemistry*, 94(15):6013–6021, 1990. Cited on page 41.

[131] X.H. Xia, H.-D. Liess, and T. Iwasita. Early Stages in the Oxidation of Ethanol at Low Index Single Crystal Platinum Electrodes. *Journal of Electroanalytical Chemistry*, 437(1):233 – 240, 1997. Cited on page 41.

[132] Carlos Busó-Rogero, Sylvain Brimaud, Jose Solla-Gullon, Francisco J. Vidal-Iglesias, Enrique Herrero, R. Jürgen Behm, and Juan M. Feliu. Ethanol Oxidation on Shape-controlled Platinum Nanoparticles at Different pHs: A Combined in situ IR Spectroscopy and Online Mass Spectrometry Study. *Journal of Electroanalytical Chemistry*, 763:116 – 124, 2016. Cited on page 41.

[133] Adolfo Ferre-Vilaplana, Carlos Buso-Rogero, Juan M. Feliu, and Enrique Herrero. Cleavage of the C–C Bond in the Ethanol Oxidation Reaction on Platinum. Insight from Experiments and Calculations. *The Journal of Physical Chemistry C*, 120(21):11590–11597, 2016. Cited on page 41.

[134] Joelma Perez, Valdecir A. Paganin, and Ermete Antolini. Particle Size Effect for Ethanol Electro-Oxidation on Pt/C Catalysts in Half-cell and in a Single Direct Ethanol Fuel Cell . *Journal of Electroanalytical Chemistry*, 654(1–2):108 – 115, 2011. Cited on page 42.

[135] K. Kinoshita. Particle Size Effects for Oxygen Reduction on Highly Dispersed Platinum in Acid Electrolytes. *Journal of The Electrochemical Society*, 137(3):845–848, 1990. Cited on pages 42 and 99.

[136] Guang-Feng Wei and Zhi-Pan Liu. Optimum Nanoparticles for Electrocatalytic Oxygen Reduction: The Size, Shape and New Design. *Phys. Chem. Chem. Phys.*, 15:18555–18561, 2013. Cited on pages 42, 118, and 132.

[137] Venkatasubramanian Viswanathan and Frank Yi-Fei Wang. Theoretical Analysis of the Effect of Particle Size and Support on the Kinetics of Oxygen Reduction Reaction on Platinum Nanoparticles. *Nanoscale*, 4:5110–5117, 2012. Cited on page 42.

[138] Vladimir Tripković, Isotta Cerri, Thomas Bligaard, and Jan Rossmeisl. The Influence of Particle Shape and Size on the Activity of Platinum Nanoparticles for Oxygen Reduction Reaction: A Density Functional Theory Study. *Catalysis Letters*, 144(3):380–388, 2014. Cited on page 42.

[139] Minhua Shao, Amra Peles, and Krista Shoemaker. Electrocatalysis on Platinum Nanoparticles: Particle Size Effect on Oxygen Reduction Reaction Activity. *Nano Letters*, 11(9):3714–3719, 2011. PMID: 21806027. Cited on pages 42 and 77.

[140] Sebastian Proch, Mark Wirth, Henry S. White, and Scott L. Anderson. Strong Effects of Cluster Size and Air Exposure on Oxygen Reduction and Carbon Oxidation Electrocatalysis by Size-Selected Ptn ($n \leq 11$) on Glassy Carbon Electrodes. *Journal of the American Chemical Society*, 135(8):3073–3086, 2013. PMID: 23398572. Cited on page 42.

[141] Rikson Siburian, Takahiro Kondo, and Junji Nakamura. Size Control to a Sub-Nanometer Scale in Platinum Catalysts on Graphene. *The Journal of Physical Chemistry C*, 117(7):3635–3645, 2013. Cited on page 42.

[142] Takane Imaoka, Hirokazu Kitazawa, Wang-Jae Chun, Saori Omura, Ken Albrecht, and Kimihisa Yamamoto. Magic Number Pt_{13} and Misshapen Pt_{12} Clusters: Which One is the Better Catalyst? *Journal of the American Chemical Society*, 135(35):13089–13095, 2013. PMID: 23902457. Cited on pages 42, 77, 113, 115, and 141.

[143] J. Kleis, J. Greeley, N. A. Romero, V. A. Morozov, H. Falsig, A. H. Larsen, J. Lu, J. J. Mortensen, M. Dułak, K. S. Thygesen, J. K. Nørskov, and K. W. Jacobsen. Finite Size Effects in Chemical Bonding: From Small Clusters to Solids. *Catalysis Letters*, 141(8):1067–1071, Aug 2011. Cited on page 43.

[144] Lin Li, Ask H. Larsen, Nichols A. Romero, Vitali A. Morozov, Christian Glinsvad, Frank Abild-Pedersen, Jeff Greeley, Karsten W. Jacobsen, and Jens K. Nørskov. Investigation of Catalytic Finite-Size-Effects of Platinum Metal Clusters. *The Journal of Physical Chemistry Letters*, 4(1):222–226, 2013. PMID: 26291235. Cited on pages 43, 92, 96, 98, and 103.

[145] Peter J. Feibelman, B. Hammer, J. K. Nørskov, F. Wagner, M. Scheffler, R. Stumpf, R. Watwe, and J. Dumesic. The CO/Pt(111) Puzzle†. *J. Phys. Chem. B*, 105(18):4018–4025, 2001. Cited on pages 44, 93, 97, and 98.

[146] Ilya V. Yudanov, Riadh Sahnoun, Konstantin M. Neyman, Notker Rösch, Jens Hoffmann, Swetlana Schauermann, Viktor Johánek, Holger Unterhalt, Günther Rupprechter, Jörg Libuda, and Hans-Joachim Freund. CO Adsorption on Pd Nanoparticles: Density Functional and Vibrational Spectroscopy Studies. *The Journal of Physical Chemistry B*, 107(1):255–264, 2003. Cited on page 44.

[147] Ilya V. Yudanov, Riadh Sahnoun, Konstantin M. Neyman, and Notker Rösch. Metal Nanoparticles as Models of Single Crystal Surfaces and Supported Catalysts: Density Functional Study of Size Effects for CO/Pd(111). *The Journal of Chemical Physics*, 117(21):9887–9896, 2002. Cited on page 44.

[148] Ilya V. Yudanov, Alexander Genest, Swetlana Schauermann, Hans-Joachim Freund, and Notker Rösch. Size Dependence of the Adsorption Energy of CO on Metal Nanoparticles: A DFT Search for the Minimum Value. *Nano Letters*, 12(4):2134–2139, 2012. PMID: 22468882. Cited on pages 44 and 45.

[149] Svetlana S. Laletina, Mikhail Mamatkulov, Elena A. Shor, Vasily V. Kaichev, Alexander Genest, Ilya V. Yudanov, and Notker Rösch. Size-Dependence of the Adsorption Energy

of CO on Pt Nanoparticles: Tracing Two Intersecting Trends by DFT Calculations. *The Journal of Physical Chemistry C*, 121(32):17371–17377, 2017. Cited on pages 44 and 45.

[150] Takeshi Daio, Aleksandar Staykov, Limin Guo, Jianfeng Liu, Masaki Tanaka, Matthew Stephen Lyth, and Kazunari Sasaki. Lattice Strain Mapping of Platinum Nanoparticles on Carbon and SnO_2 Supports. *Scientific Reports*, 5:13126, 2015. Cited on pages 48, 50, and 71.

[151] Peng Zhang, Sheng-Yang Huang, and Branko N. Popov. Mesoporous Tin Oxide as an Oxidation-Resistant Catalyst Support for Proton Exchange Membrane Fuel Cells. *Journal of The Electrochemical Society*, 157(8):B1163–B1172, 2010. Cited on page 48.

[152] Ashkan Moradabadi, Shideh Ahmadi, and Payam Kaghazchi. Evidence of a Strong Effect of Defect-free Metal Oxide Supports on Pt Nanoparticles. *Nanoscale*, 9:4478–4485, 2017. Cited on pages 48, 49, and 113.

[153] Xin Xia, Glenn Jones, Misbah Sarwar, Qian Tang, Ian Harkness, and David Thompsett. A DFT Study of Pt Layer Deposition on Catalyst Supports of Titanium Oxide, Nitride and Carbide. *J. Mater. Chem. A*, 3:24504–24511, 2015. Cited on page 49.

[154] Xin Xia, Jane L. R. Yates, Glenn Jones, Misbah Sarwar, Ian Harkness, and David Thompsett. Theoretical Exploration of Novel Catalyst Support Materials for Fuel Cell Applications. *J. Mater. Chem. A*, 4:15181–15188, 2016. Cited on page 49.

[155] Sergio Navalon, Amarajothi Dhakshinamoorthy, Mercedes Alvaro, and Hermenegildo Garcia. Metal Nanoparticles Supported on Two-Dimensional Graphenes as Heterogeneous Catalysts. *Coordination Chemistry Reviews*, 312:99 – 148, 2016. Cited on pages 50, 70, 71, and 76.

[156] Brian H Morrow and Alberto Striolo. Platinum Nanoparticles on Carbonaceous Materials: The Effect of Support Geometry on Nanoparticle Mobility, Morphology, and Melting. *Nanotechnology*, 19(19):195711, 2008. Cited on pages 50 and 71.

[157] Xiaojie Liu, Yong Han, James W. Evans, Albert K. Engstfeld, R. Juergen Behm, Michael C. Tringides, Myron Hupalo, Hai-Qing Lin, Li Huang, Kai-Ming Ho, David Appy, Patricia A. Thiel, and Cai-Zhuang Wang. Growth Morphology and Properties of Metals on Graphene . *Progress in Surface Science*, 90(4):397 – 443, 2015. Cited on pages 50, 71, 76, and 83.

[158] K. Okazaki-Maeda, Y. Morikawa, S. Tanaka, and M. Kohyama. Structures of Pt Clusters on Graphene by First-Principles Calculations. *Surface Science*, 604(2):144 – 154, 2010. Cited on pages 50, 71, and 83.

[159] Ioanna Fampiou and Ashwin Ramasubramaniam. Binding of Pt Nanoclusters to Point Defects in Graphene: Adsorption, Morphology, and Electronic Structure. *The Journal of Physical Chemistry C*, 116(11):6543–6555, 2012. Cited on pages 50, 71, 74, 83, 88, and 114.

[160] Ioanna Fampiou and Ashwin Ramasubramaniam. CO Adsorption on Defective Graphene-Supported Pt_{13} Nanoclusters. *The Journal of Physical Chemistry C*, 117(39):19927–19933, 2013. Cited on pages 50, 71, 110, and 114.

[161] Hongbo Shi, Scott M. Auerbach, and Ashwin Ramasubramaniam. First-Principles Predictions of Structure-Function Relationships of Graphene-Supported Platinum Nanoclusters. *The Journal of Physical Chemistry C*, 120(22):11899–11909, 2016. Cited on pages 50, 83, and 110.

[162] G. Rámos-Sanchez and P. B. Balbuena. Interactions of Platinum Clusters with a Graphite Substrate. *Phys. Chem. Chem. Phys.*, 15:11950–11959, 2013. Cited on pages 50, 71, 72, and 83.

[163] G. Ramos-Sánchez and P.B. Balbuena. CO Adsorption on Pt Clusters Supported on Graphite. *Journal of Electroanalytical Chemistry*, 716:23 – 30, 2014. Special Issue in Honour of Kingo Itaya. Cited on pages 50 and 113.

[164] Amitesh Maiti and Alessandra Ricca. Metal-Nanotube Interactions - Binding Energies and Wetting Properties. *Chemical Physics Letters*, 395(1):7 – 11, 2004. Cited on pages 50, 71, and 76.

[165] Dong-Hee Lim and Jennifer Wilcox. DFT-Based Study on Oxygen Adsorption on Defective Graphene-Supported Pt Nanoparticles. *The Journal of Physical Chemistry C*, 115(46):22742–22747, 2011. Cited on pages 50, 71, 110, and 114.

[166] Wolfgang B. Schneider, Udo Benedikt, and Alexander A. Auer. Interaction of Platinum Nanoparticles with Graphitic Carbon Structures: A Computational Study. *ChemPhysChem*, 14(13):2984–2989, 2013. Cited on pages 50, 71, and 76.

[167] Izabela Janowska, Maria-Simona Moldovan, Ovidiu Ersen, Hervé Bulou, Kambiz Chizari, Marc J. Ledoux, and Cuong Pham-Huu. High Temperature Stability of Platinum Nanoparticles on Few-layer Graphene Investigated by In Situ High Resolution Transmission Electron Microscopy. *Nano Research*, 4(5):511–521, May 2011. Cited on pages 50, 78, 88, 114, and 138.

[168] Lifeng Dong, Raghavendar Reddy Sanganna Gari, Zhou Li, Michael M. Craig, and Shifeng Hou. Graphene-supported Platinum and Platinum–Ruthenium Nanoparticles with High Electrocatalytic Activity for Methanol and Ethanol Oxidation. *Carbon*, 48(3):781 – 787, 2010. Cited on page 50.

[169] Xiaomei Chen, Genghuang Wu, Jinmei Chen, Xi Chen, Zhaoxiong Xie, and Xiaoru Wang. Synthesis of "Clean" and Well-Dispersive Pd Nanoparticles with Excellent Electrocatalytic Property on Graphene Oxide. *Journal of the American Chemical Society*, 133(11):3693–3695, 2011. PMID: 21348468. Cited on pages 50 and 51.

[170] Daniel Sanchez-Portal, Emilio Artacho, and Jose M Soler. Projection of Plane-wave Calculations into Atomic Orbitals. *Solid State Communications*, 95(10):685 – 690, 1995. Cited on page 53.

[171] Daniel Sánchez-Portal, Emilio Artacho, and José M Soler. Analysis of Atomic Orbital Basis Sets from the Projection of Plane-Wave Results. *Journal of Physics: Condensed Matter*, 8(21):3859, 1996. Cited on pages 53 and 61.

[172] Stefan Maintz, Volker L. Deringer, Andrei L. Tchougréeff, and Richard Dronskowski. LOBSTER: A Tool to Extract Chemical Bonding from Plane-Wave Based DFT. *Journal of Computational Chemistry*, 37(11):1030–1035, 2016. Cited on page 54.

[173] Alvaro Ruiz-Serrano, Nicholas D. M. Hine, and Chris-Kriton Skylaris. Pulay Forces from Localized Orbitals Optimized in situ Using a psinc Basis Set. *The Journal of Chemical Physics*, 136(23):234101, 2012. Cited on page 56.

[174] Nicholas D M Hine. Linear-Scaling Density Functional Theory Using the Projector Augmented Wave Method. *Journal of Physics: Condensed Matter*, 29(2):024001, nov 2016. Cited on pages 59 and 120.

[175] David Vanderbilt. Soft Self-Consistent Pseudopotentials in a Generalized Eigenvalue Formalism. *Phys. Rev. B*, 41:7892–7895, Apr 1990. Cited on page 59.

[176] Kevin F. Garrity, Joseph W. Bennett, Karin M. Rabe, and David Vanderbilt. Pseudopotentials for High-Throughput DFT Calculations. *Computational Materials Science*, 81:446 – 452, 2014. Cited on page 59.

[177] Andrew J. Morris, Rebecca J. Nicholls, Chris J. Pickard, and Jonathan R. Yates. OptaDOS: A Tool for Obtaining Density of States, Core-level and Optical Spectra from Electronic Structure Codes. *Computer Physics Communications*, 185(5):1477 – 1485, 2014. Cited on page 59.

[178] Jochen Friedl and Ulrich Stimming. Model Catalyst Studies on Hydrogen and Ethanol Oxidation for Fuel Cells . *Electrochimica Acta*, 101:41 – 58, 2013. Cited on page 70.

[179] Minhua Shao, Qiaowan Chang, Jean-Pol Dodelet, and Regis Chenitz. Recent Advances in Electrocatalysts for Oxygen Reduction Reaction. *Chemical Reviews*, 116(6):3594–3657, 2016. PMID: 26886420. Cited on pages 70, 91, 92, 98, 99, 113, and 140.

[180] Marc T. M. Koper. Structure Sensitivity and Nanoscale Effects in Electrocatalysis. *Nanoscale*, 3:2054–2073, 2011. Cited on pages 70 and 91.

[181] Piotr Błoński and Jürgen Hafner. Geometric and Magnetic Properties of Pt Clusters Supported on Graphene: Relativistic Density-Functional Calculations. *The Journal of Chemical Physics*, 134(15), 2011. Cited on page 71.

[182] Yasuharu Okamoto. Density-Functional Calculations of Icosahedral {M13} (M = Pt and Au) Clusters on Graphene Sheets and Flakes. *Chemical Physics Letters*, 420(4–6):382 – 386, 2006. Cited on page 71.

[183] Carlos F. Sanz-Navarro, Per-Olof Åstrand, De Chen, Magnus Rønning, Adri C. T. van Duin, Timo Jacob, , and William A. Goddard. Molecular Dynamics Simulations of the Interactions between Platinum Clusters and Carbon Platelets. *The Journal of Physical Chemistry A*, 112(7):1392–1402, 2008. PMID: 18217729. Cited on page 71.

[184] Qiaofang Qi, Huiling Liu, Wei Feng, Hongwei Tian, Haixia Xu, and Xuri Huang. Theoretical Investigation on the Interaction of Subnano Platinum Clusters with Graphene Using DFT Methods. *Computational Materials Science*, 96, Part A:268 – 276, 2015. Cited on pages 71 and 83.

[185] Oleg A. Vydrov and Troy Van Voorhis. Nonlocal van der Waals Density Functional: The Simpler the Better. *The Journal of Chemical Physics*, 133(24), 2010. Cited on pages 72, 93, and 104.

[186] Riccardo Sabatini, Tommaso Gorni, and Stefano de Gironcoli. Nonlocal van der Waals Density Functional Made Simple and Efficient. *Phys. Rev. B*, 87:041108, Jan 2013. Cited on pages 72, 93, and 104.

[187] Stefan Grimme. Semiempirical GGA-type Density Functional Constructed with a Long-Range Dispersion Correction. *Journal of Computational Chemistry*, 27(15):1787–1799, 2006. Cited on page 72.

[188] Arash A. Mostofi, Peter D. Haynes, Chris-Kriton Skylaris, and Mike C. Payne. Preconditioned Iterative Minimization for Linear-scaling Electronic Structure Calculations. *The Journal of Chemical Physics*, 119(17):8842–8848, 2003. Cited on pages 72, 94, and 120.

[189] Xiaoxia Li, Xinping Qiu, Huiping Yuan, Liquan Chen, and Wentao Zhu. Size-Effect on the Activity of Anodic Catalysts in Alcohol and CO Electrooxidation . *Journal of Power Sources*, 184(2):353 – 360, 2008. Selected papers from the: {INTERNATIONAL BATTERY MATERIALS ASSOCATION 2007 CONFERENCE}. In Memoriam of Juergen Besenhard. Cited on page 77.

[190] K. J. J. Mayrhofer, B. B Blizanac, M. Arenz, V. R. Stamenkovic, P. N. Ross, and N. M. Markovic. The Impact of Geometric and Surface Electronic Properties of Pt-Catalysts on the Particle Size Effect in Electrocatalysis. *The Journal of Physical Chemistry B*, 109(30):14433–14440, 2005. PMID: 16852816. Cited on page 77.

[191] Qizhong Sun and Seok Kim. Synthesis of Nitrogen-Doped Graphene Supported Pt Nanoparticles Catalysts and their Catalytic Activity for Fuel Cells. *Electrochimica Acta*, 153:566 – 573, 2015. Cited on pages 78, 88, and 138.

[192] H.N. Yang and W.J. Kim. Effect of Boron-Doping Levels in Pt-B-Graphene on the Electrochemical Properties and Cell Performance of High Temperature Proton Exchange Membrane Fuel Cells. *Electrochimica Acta*, 209:430 – 439, 2016. Cited on pages 78, 88, and 138.

[193] T. Bligaard and J.K. Nørskov. Ligand Effects in Heterogeneous Catalysis and Electrochemistry. *Electrochimica Acta*, 52(18):5512 – 5516, 2007. Surface Imaging/Spectroscopy at Solid/Liquid Interface (ISSIS)Selection of papers from the International Symposium on Surface Imaging/Spectroscopy at Solid/Liquid Interface (ISSIS) , May 28 to June 1, 2006, Krakow, Poland. Cited on pages 83 and 85.

[194] D.Michael P. Mingos. A Historical Perspective on Dewar's Landmark Contribution to Organometallic Chemistry. *Journal of Organometallic Chemistry*, 635(1–2):1 – 8, 2001. Cited on page 85.

[195] Mehdi Mahmoodinia, Mahsa Ebadi, Per-Olof Astrand, De Chen, Hong-Ye Cheng, and Yi-An Zhu. Structural and Electronic Properties of the Pt_n-PAH Complex (n = 1, 2) from Density Functional Calculations. *Phys. Chem. Chem. Phys.*, 16:18586–18595, 2014. Cited on page 85.

[196] Ho-Cheng Tsai, Yu-Chi Hsieh, Ted H. Yu, Yi-Juei Lee, Yue-Han Wu, Boris V. Merinov, Pu-Wei Wu, San-Yuan Chen, Radoslav R. Adzic, and III William A. Goddard. DFT Study of Oxygen Reduction Reaction on Os/Pt Core–Shell Catalysts Validated by Electrochemical Experiment. *ACS Catalysis*, 5(3):1568–1580, 2015. Cited on page 87.

[197] Daniela Zanchet, Joao Batista O. Santos, Sonia Damyanova, Jean Marcel R. Gallo, and José Maria C. Bueno. Toward Understanding Metal-Catalyzed Ethanol Reforming. *ACS Catalysis*, 5(6):3841–3863, 2015. Cited on page 91.

[198] Francesca Baletto and Riccardo Ferrando. Structural Properties of Nanoclusters: Energetic, Thermodynamic, and Kinetic Effects. *Rev. Mod. Phys.*, 77:371–423, May 2005. Cited on page 91.

[199] Ermete Antolini. Structural Parameters of Supported Fuel Cell Catalysts: The Effect of Particle Size, Inter-Particle Distance and Metal Loading on Catalytic Activity and Fuel Cell Performance. *Applied Catalysis B: Environmental*, 181:298 – 313, 2016. Cited on page 91.

[200] Federico Calle-Vallejo, Philippe Sautet, and David Loffreda. Understanding Adsorption-Induced Effects on Platinum Nanoparticles: An Energy-Decomposition Analysis. *The Journal of Physical Chemistry Letters*, 5(18):3120–3124, 2014. PMID: 26276322. Cited on page 92.

[201] Hao Li and Graeme Henkelman. Dehydrogenation Selectivity of Ethanol on Close-Packed Transition Metal Surfaces: A Computational Study of Monometallic, Pd/Au, and Rh/Au Catalysts. *The Journal of Physical Chemistry C*, 121(49):27504–27510, 2017. Cited on page 92.

[202] Aline O. Pereira and Caetano R. Miranda. Atomic Scale Insights into Ethanol Oxidation on Pt, Pd and Au Metallic Nanofilms: A DFT with van der Waals Interactions. *Applied Surface Science*, 288:564 – 571, 2014. Cited on pages 92, 96, and 98.

[203] Polina Tereshchuk and Juarez L. F. Da Silva. Ethanol and Water Adsorption on Close-Packed 3d, 4d, and 5d Transition-Metal Surfaces: A Density Functional Theory Investigation with van der Waals Correction. *The Journal of Physical Chemistry C*, 116(46):24695–24705, 2012. Cited on pages 92, 96, 98, and 105.

[204] Rafael L. H. Freire, Adam Kiejna, and Juarez L. F. Da Silva. Adsorption of Water and Ethanol on Noble and Transition-metal Substrates: A Density Functional Investigation within van der Waals Corrections. *Phys. Chem. Chem. Phys.*, 18:29526–29536, 2016. Cited on pages 92, 96, and 98.

[205] Larissa Zibordi-Besse, Polina Tereshchuk, Anderson S. Chaves, and Juarez L. F. Da Silva. Ethanol and Water Adsorption on Transition-Metal 13-Atom Clusters: A Density Functional Theory Investigation within van der Waals Corrections. *The Journal of Physical Chemistry A*, 120(24):4231–4240, 2016. PMID: 27269477. Cited on pages 92 and 98.

[206] Vagner A. Rigo, Caetano R. Miranda, and Francesca Baletto. Ethanol Chemisorption on Core-Shell Pt-Nanoparticles: An Ab Initio Study. *The European Physical Journal B*, 92(2):24, Feb 2019. Cited on pages 92 and 98.

[207] Wei Liu, Alexandre Tkatchenko, and Matthias Scheffler. Modeling Adsorption and Reactions of Organic Molecules at Metal Surfaces. *Accounts of Chemical Research*, 47(11):3369–3377, 2014. PMID: 24915492. Cited on page 92.

[208] George Blyholder. Molecular Orbital View of Chemisorbed Carbon Monoxide. *The Journal of Physical Chemistry*, 68(10):2772–2777, 1964. Cited on page 93.

[209] G. Kresse, A. Gil, and P. Sautet. Significance of Single-Electron Energies for the Description of CO on Pt(111). *Phys. Rev. B*, 68:073401, Aug 2003. Cited on page 93.

[210] Alfred Gil, Anna Clotet, Josep M. Ricart, Georg Kresse, Maite García-Hernández, Notker Rösch, and Philippe Sautet. Site Preference of CO Chemisorbed on Pt(111) from Density Functional Calculations. *Surface Science*, 530(1):71 – 87, 2003. Cited on page 93.

[211] Ilya Grinberg, Yashar Yourdshahyan, and Andrew M. Rappe. CO on Pt(111) Puzzle: A Possible Solution. *The Journal of Chemical Physics*, 117(5):2264–2270, 2002. Cited on page 93.

[212] Alessandro Stroppa, Konstantinos Termentzidis, Joachim Paier, Georg Kresse, and Jürgen Hafner. CO Adsorption on Metal Surfaces: A Hybrid Functional Study with Plane-wave Basis Set. *Phys. Rev. B*, 76:195440, Nov 2007. Cited on page 93.

[213] A. Stroppa and G. Kresse. The Shortcomings of Semi-Local and Hybrid Functionals: What We Can Learn from Surface Science Studies. *New J. Phys.*, 10:063020, 2008. Cited on page 93.

[214] Jack B. A. Davis, Francesca Baletto, and Roy L. Johnston. The Effect of Dispersion Correction on the Adsorption of CO on Metallic Nanoparticles. *The Journal of Physical Chemistry A*, 119(37):9703–9709, 2015. PMID: 26320360. Cited on pages 93 and 97.

[215] Sijie Luo, Yan Zhao, and Donald G. Truhlar. Improved CO Adsorption Energies, Site Preferences, and Surface Formation Energies from a Meta-Generalized Gradient Approximation Exchange–Correlation Functional, M06-L. *The Journal of Physical Chemistry Letters*, 3(20):2975–2979, 2012. PMID: 26292236. Cited on page 93.

[216] Patanachai Janthon, Francesc Viñes, Jakkapan Sirijaraensre, Jumras Limtrakul, and Francesc Illas. Adding Pieces to the CO/Pt(111) Puzzle: The Role of Dispersion. *The Journal of Physical Chemistry C*, 121(7):3970–3977, 2017. Cited on page 93.

[217] Yu-Wei Huang and Shyi-Long Lee. Hybrid DFT and Hyper-GGA DFT Studies of the CO Adsorption on Pt Nanoclusters: Effects of the Cluster Size and Better CO LUMO Description. *Chemical Physics Letters*, 492(1):98 – 102, 2010. Cited on page 93.

[218] Thomas M. Soini, Alexander Genest, and Notker Rösch. Assessment of Hybrid Density Functionals for the Adsorption of Carbon Monoxide on Platinum Model Clusters. *The Journal of Physical Chemistry A*, 119(17):4051–4056, 2015. PMID: 25876734. Cited on page 93.

[219] Guowen Peng and Manos Mavrikakis. Adsorbate Diffusion on Transition Metal Nanoparticles. *Nano Letters*, 15(1):629–634, 2015. PMID: 25422876. Cited on pages 93, 96, and 123.

[220] B. C. Han, C. R. Miranda, and G. Ceder. Effect of Particle Size and Surface Structure on Adsorption of O and OH on Platinum Nanoparticles: A First-Principles Study. *Phys. Rev. B*, 77:075410, Feb 2008. Cited on pages 96, 98, and 123.

[221] Liya Wang, Ata Roudgar, and Michael Eikerling. Ab Initio Study of Stability and Site-Specific Oxygen Adsorption Energies of Pt Nanoparticles. *The Journal of Physical Chemistry C*, 113(42):17989–17996, 2009. Cited on pages 96 and 98.

[222] M Lynch and P Hu. A Density Functional Theory Study of CO and Atomic Oxygen Chemisorption on Pt(111). *Surface Science*, 458(1):1 – 14, 2000. Cited on pages 96 and 107.

[223] Zhihui Gu and Perla B. Balbuena. Absorption of Atomic Oxygen into Subsurfaces of Pt(100) and Pt(111): Density Functional Theory Study. *The Journal of Physical Chemistry C*, 111(27):9877–9883, 2007. Cited on pages 96, 119, and 125.

[224] Stefan Grimme, Jens Antony, Stephan Ehrlich, and Helge Krieg. A Consistent and Accurate Ab Initio Parametrization of Density Functional Dispersion Correction (DFT-D) for the 94 Elements H-Pu. *The Journal of Chemical Physics*, 132(15):154104, 2010. Cited on page 97.

[225] Vojislav Stamenkovic, Bongjin Simon Mun, Karl J. J. Mayrhofer, Philip N. Ross, Nenad M. Markovic, Jan Rossmeisl, Jeff Greeley, and Jens K. Nørskov. Changing the Activity of Electrocatalysts for Oxygen Reduction by Tuning the Surface Electronic Structure. *Angewandte Chemie International Edition*, 45(18):2897–2901, 2006. Cited on pages 98 and 140.

[226] Tom Ellaby, Jolyon Aarons, Aakash Varambhia, Lewys Jones, Peter Nellist, Dogan Ozkaya, Misbah Sarwar, David Thompsett, and Chris-Kriton Skylaris. Ideal Versus Real: Simulated Annealing of Experimentally Derived and Geometric Platinum Nanoparticles. *Journal of Physics: Condensed Matter*, 30(15):155301, 2018. Cited on pages 98, 101, and 140.

[227] Mikkel Jørgensen and Henrik Grönbeck. Scaling Relations and Kinetic Monte Carlo Simulations To Bridge the Materials Gap in Heterogeneous Catalysis. *ACS Catalysis*, 7(8):5054–5061, 2017. Cited on pages 101 and 102.

[228] J. W. Arblaster. Crystallographic Properties of Platinum. *Platinum Metals Review*, 41(1):12–21, 1997. Cited on page 103.

[229] J. W. Arblaster. Crystallographic Properties of Platinum. *Platinum Metals Review*, 50(3):118–119, 2006. Cited on page 103.

[230] Arvin Kakekhani, Luke T. Roling, Ambarish Kulkarni, Allegra A. Latimer, Hadi Abroshan, Julia Schumann, Hassan AlJama, Samira Siahrostami, Sohrab Ismail-Beigi, Frank Abild-Pedersen, and Jens K. Nørskov. Nature of Lone-Pair-Surface Bonds and Their Scaling Relations. *Inorganic Chemistry*, 57(12):7222–7238, 2018. PMID: 29863849. Cited on pages 109 and 111.

[231] Yohanna Seminovski, Rafael C. Amaral, Polina Tereshchuk, and Juarez L.F. Da Silva. The Role of the Anionic and Cationic Pt Sites in the Adsorption Site Preference of Water and Ethanol on Defected Pt4/Pt(111) Substrates: A Density Functional Theory Investigation Within the D3 van der Waals Corrections. *Surface Science*, 667:84 – 91, 2018. Cited on page 111.

[232] Yohanna Seminovski, Polina Tereshchuk, Adam Kiejna, and Juarez L. F. Da Silva. The Role of the Cationic Pt Sites in the Adsorption Properties of Water and Ethanol on the Pt_4/Pt(111) and Pt_4/CeO_2(111) substrates: A Density Functional Theory Investigation. *The Journal of Chemical Physics*, 145(12):124709, 2016. Cited on page 111.

[233] Takane Imaoka, Hirokazu Kitazawa, Wang-Jae Chun, and Kimihisa Yamamoto. Finding the Most Catalytically Active Platinum Clusters With Low Atomicity. *Angewandte Chemie International Edition*, 54(34):9810–9815, 2015. Cited on pages 113, 114, 115, and 141.

[234] Kasumi Miyazaki and Hirotoshi Mori. Origin of High Oxygen Reduction Reaction Activity of Pt12 and Strategy to Obtain Better Catalyst Using Sub-nanosized Pt-alloy Clusters. *Scientific Reports*, 7:45381, 2017. Cited on pages 114 and 115.

[235] Borna Zandkarimi and Anastassia N. Alexandrova. Dynamics of Subnanometer Pt Clusters Can Break the Scaling Relationships in Catalysis. *The Journal of Physical Chemistry Letters*, 10(3):460–467, 2019. Cited on pages 114 and 115.

[236] Spencer D. Miller and John R. Kitchin. Relating the Coverage Dependence of Oxygen Adsorption on Au and Pt FCC(111) Surfaces Through Adsorbate-Induced Surface Electronic Structure Effects. *Surface Science*, 603(5):794 – 801, 2009. Cited on pages 117, 118, 134, and 143.

[237] John R. Kitchin. Correlations in Coverage-Dependent Atomic Adsorption Energies on Pd(111). *Phys. Rev. B*, 79:205412, May 2009. Cited on pages 118, 134, and 143.

[238] Zhongnan Xu and John R. Kitchin. Probing the Coverage Dependence of Site and Adsorbate Configurational Correlations on (111) Surfaces of Late Transition Metals. *The Journal of Physical Chemistry C*, 118(44):25597–25602, 2014. Cited on pages 118, 134, and 143.

[239] Nilay İnoğlu and John R. Kitchin. Simple Model Explaining and Predicting Coverage-Dependent Atomic Adsorption Energies on Transition Metal Surfaces. *Phys. Rev. B*, 82:045414, Jul 2010. Cited on pages 118, 134, and 143.

[240] Mohammad J. Eslamibidgoli and Michael H. Eikerling. Atomistic Mechanism of Pt Extraction at Oxidized Surfaces: Insights from DFT. *Electrocatalysis*, 7(4):345–354, Jul 2016. Cited on pages 118, 134, and 143.

[241] J.M. Bray, I.J. Skavdahl, J.-S. McEwen, and W.F. Schneider. First-Principles Reaction Site Model for Coverage-Sensitive Surface Reactions: Pt(111)-O Temperature Programmed Desorption. *Surface Science*, 622(Supplement C):L1 – L6, 2014. Cited on pages 118, 121, 134, 142, and 143.

[242] David J. Schmidt, Wei Chen, C. Wolverton, and William F. Schneider. Performance of Cluster Expansions of Coverage-Dependent Adsorption of Atomic Oxygen on Pt(111). *Journal of Chemical Theory and Computation*, 8(1):264–273, 2012. PMID: 26592887. Cited on pages 118, 121, 134, 142, and 143.

[243] Rachel B. Getman and William F. Schneider. DFT-Based Coverage-Dependent Model of Pt-Catalyzed NO Oxidation. *ChemCatChem*, 2(11):1450–1460, 2010. Cited on pages 118, 121, and 142.

[244] Kurt Frey, David J. Schmidt, C. Wolverton, and William F. Schneider. Implications of Coverage-Dependent O Adsorption for Catalytic NO Oxidation on the Late Transition Metals. *Catal. Sci. Technol.*, 4:4356–4365, 2014. Cited on pages 118, 121, and 142.

[245] J. M. Bray, J. L. Smith, and W. F. Schneider. Coverage-Dependent Adsorption at a Low Symmetry Surface: DFT and Statistical Analysis of Oxygen Chemistry on Kinked Pt(321). *Topics in Catalysis*, 57(1):89–105, Feb 2014. Cited on pages 118, 121, and 142.

[246] Ryosuke Jinnouchi, Kensaku Kodama Takahisa Suzuki, and Yu Morimoto. DFT Calculations on Electro-Oxidations and Dissolutions of Pt and Pt-Au Nanoparticles. *Catalysis Today*, 262(Supplement C):100 – 109, 2016. Electrocatalysis. Cited on pages 119, 125, and 132.

[247] Noah McMillan, Tanmay Lele, Christopher Snively, and Jochen Lauterbach. Subsurface Oxygen Formation on Pt(100): Experiments and Modeling. *Catalysis Today*, 105(2):244 – 253, 2005. Oscillatory Behaviour of Heterogeneous Catalytic Reactions. Cited on pages 119 and 125.

[248] M. Teliska, W. E. O'Grady, and D. E. Ramaker. Determination of O and OH Adsorption Sites and Coverage in Situ on Pt Electrodes from Pt L23 X-ray Absorption Spectroscopy. *The Journal of Physical Chemistry B*, 109(16):8076–8084, 2005. PMID: 16851943. Cited on pages 119 and 125.

[249] Lili Gai, Yun Kyung Shin, Muralikrishna Raju, Adri C. T. van Duin, and Sumathy Raman. Atomistic Adsorption of Oxygen and Hydrogen on Platinum Catalysts by Hybrid Grand Canonical Monte Carlo/Reactive Molecular Dynamics. *The Journal of Physical Chemistry C*, 120(18):9780–9793, 2016. Cited on pages 119, 125, and 132.

[250] Angel A. Topalov, Ioannis Katsounaros, Michael Auinger, Serhiy Cherevko, Josef C. Meier, Sebastian O. Klemm, and Karl J. J. Mayrhofer. Dissolution of Platinum: Limits for the Deployment of Electrochemical Energy Conversion? *Angewandte Chemie International Edition*, 51(50):12613–12615, 2012. Cited on page 119.

[251] Ke Yang, Jingjing Zheng, Yan Zhao, and Donald G Truhlar. Tests of the RPBE, revPBE, τ-HCTHhyb, ωB97X-D, and MOHLYP Density Functional Approximations and 29 Others Against Representative Databases for Diverse Bond Energies and Barrier Heights in Ccatalysis. *The Journal of chemical physics*, 132(16):164117, 2010. Cited on page 120.

[252] Nicholas D. M. Hine, Mark Robinson, Peter D. Haynes, Chris-Kriton Skylaris, Mike C. Payne, and Arash A. Mostofi. Accurate Ionic Forces and Geometry Optimization in Linear-Scaling Density-Functional Theory with Local Orbitals. *Phys. Rev. B*, 83:195102, May 2011. Cited on page 120.

[253] Nicholas DM Hine, Jacek Dziedzic, Peter D Haynes, and Chris-Kriton Skylaris. Electrostatic Interactions in Finite Systems Treated with Periodic Boundary Conditions: Application to Linear-Scaling Density Functional Theory. *The Journal of chemical physics*, 135(20):204103, 2011. Cited on page 120.

[254] Lauro Oliver Paz-Borbón and Francesca Baletto. A DFT Study on the O_2 Adsorption Properties of Supported PtNi Clusters. *Inorganics*, 5(3):43, 2017. Cited on pages 146 and 147.

PhD Data Directory Tree

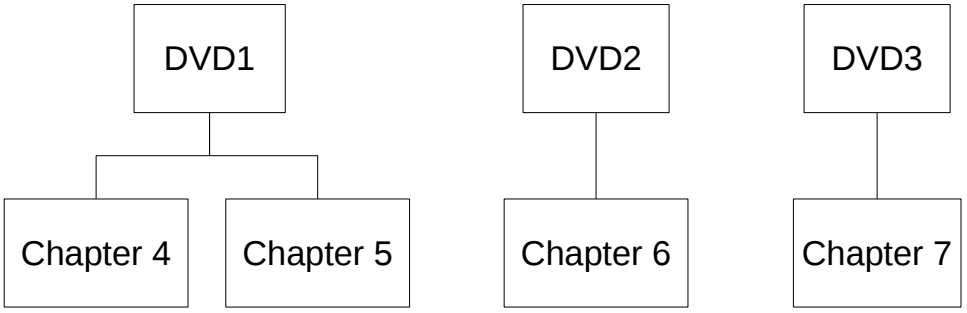

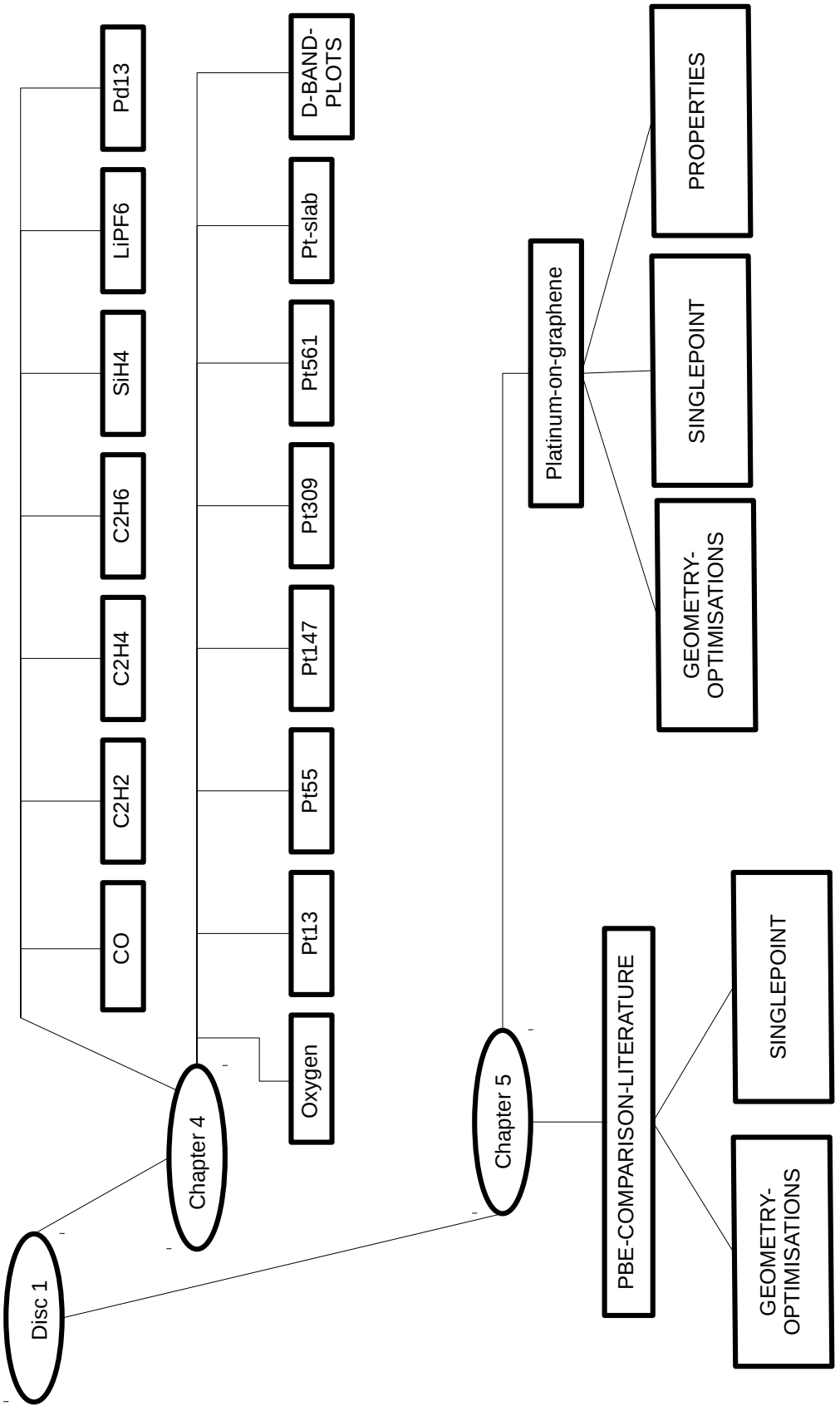
Disc 1
Chapter 4
CO
C2H2
C2H4
C2H6
SiH4
LiPF6
Pd13
Oxygen
Pt13
Pt55
Pt147
Pt309
Pt561
Pt-slab
D-BAND-PLOTS
Chapter 5
Platinum-on-graphene
GEOMETRY-OPTIMISATIONS
SINGLEPOINT
PROPERTIES
PBE-COMPARISON-LITERATURE
GEOMETRY-OPTIMISATIONS
SINGLEPOINT

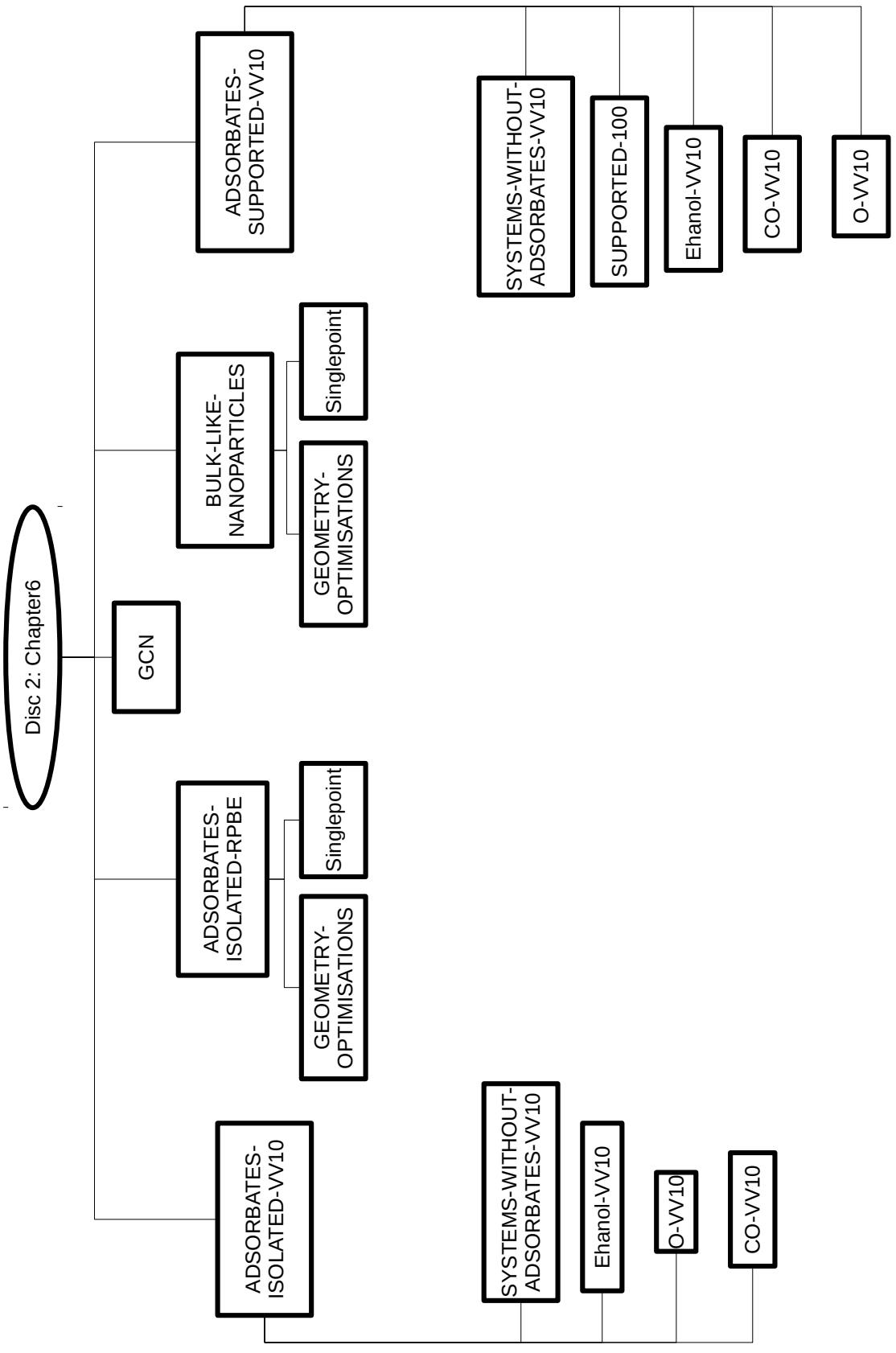
Disc 2: Chapter6
GCN
BULK-LIKE-NANOPARTICLES
Singlepoint
GEOMETRY-OPTIMISATIONS
ADSORBATES-ISOLATED-RPBE
Singlepoint
GEOMETRY-OPTIMISATIONS
ADSORBATES-ISOLATED-VV10
SYSTEMS-WITHOUT-ADSORBATES-VV10
Ehanol-VV10
O-VV10
CO-VV10
ADSORBATES-SUPPORTED-VV10
SYSTEMS-WITHOUT-ADSORBATES-VV10
SUPPORTED-100
Ehanol-VV10
CO-VV10
O-VV10

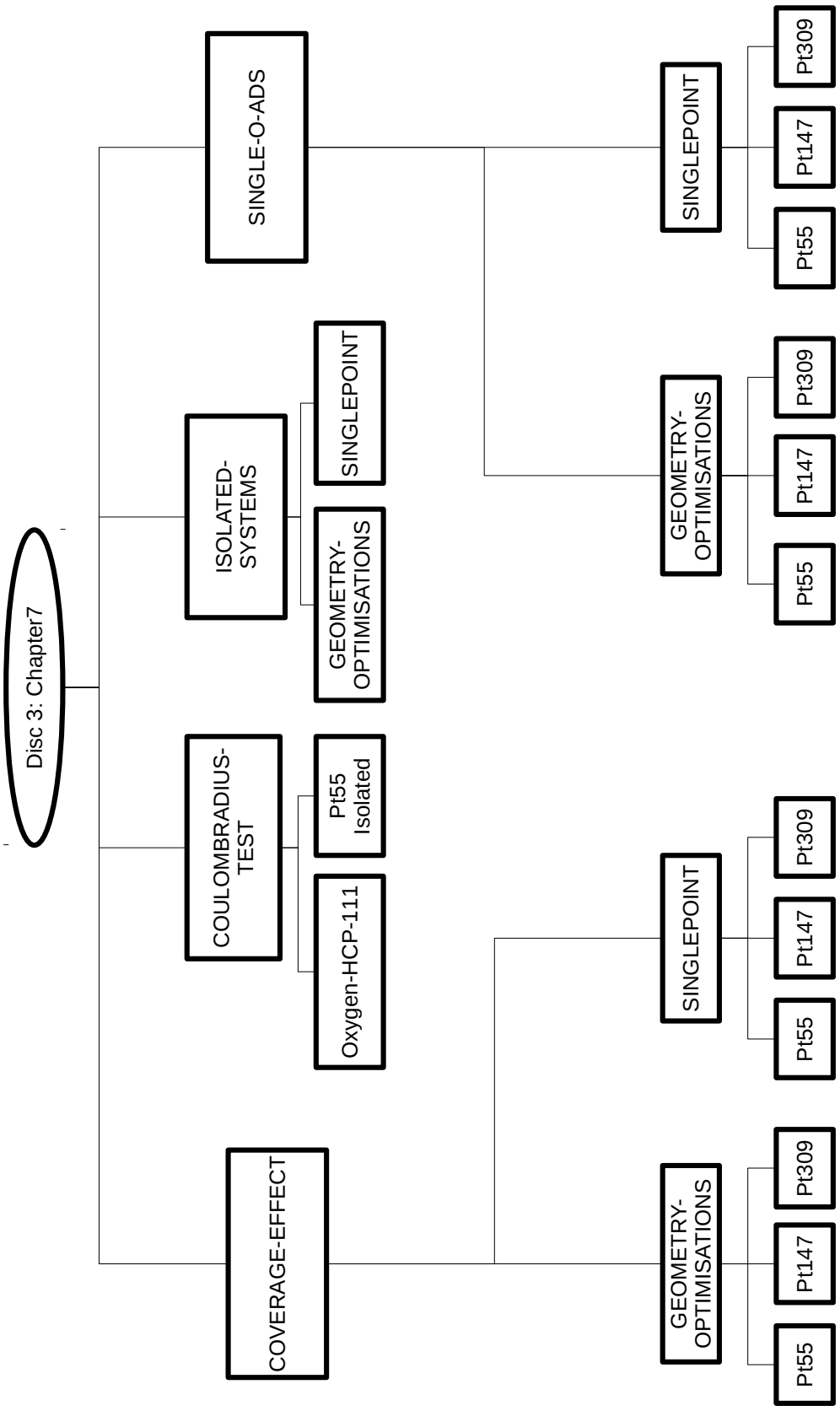
Disc 3: Chapter7
SINGLE-O-ADS
ISOLATED-SYSTEMS
SINGLEPOINT
GEOMETRY-OPTIMISATIONS
COULOMBRADIUS-TEST
Pt55 Isolated
Oxygen-HCP-111
COVERAGE-EFFECT
SINGLEPOINT
Pt55
Pt147
Pt309
GEOMETRY-OPTIMISATIONS
Pt55
Pt147
Pt309
SINGLEPOINT
Pt55
Pt147
Pt309
GEOMETRY-OPTIMISATIONS
Pt55
Pt147
Pt309